SCUOLA DI DOTTORATO

UNIVERSITÀ DEGLI STUDI "MEDITERRANEA" DI REGGIO CALABRIA

DIPARTIMENTO DI INGEGNERIA CIVILE, DELL'ENERGIA, DELL'AMBIENTE E DEI MATERIALI
DICEAM

DOTTORATO DI RICERCA IN
INGEGNERIA CIVILE, AMBIENTALE E DELLA SICUREZZA

CURRICULUM
INGEGNERIA IDRAULICA,
COSTRUZIONI IDRAULICHE E MARITTIME,
IDROLOGIA E ENERGIA DALLE ACQUE

XXXIII CICLO

PERFORMANCE OPTIMIZATION OF U-OWC WAVE ENERGY CONVERTERS

DOTTORANDO:
ANDREA SCIALÒ

[redacted]

TUTOR:
PROF. FELICE ARENA, PROF. JOÃO CARLOS DE CAMPOS HENRIQUES,
PROF. GIOVANNI MALARA

[redacted]

[redacted]

COORDINATORE:
PROF. FELICE ARENA

[redacted]

REGGIO CALABRIA, OTTOBRE 2021

ANDREA SCIALÒ

PERFORMANCE OPTIMIZATION OF U-OWC WAVE ENERGY CONVERTERS

Sommario

La tesi tratta dell'ottimizzazione di convertitori di tipo U-Oscillating Water Column (U-OWC) integrati in dighe a parete verticale. Il caso studio considerato in questo lavoro è un impianto di energia dal moto ondoso nel Mar Mediterraneo. In particolare, la configurazione geometrica ottimale di un U-OWC è stata ottenuta per il porto di Roccella Jonica, Italia. In questo contesto, la tecnica della linearizzazione statistica è stata utilizzata in combinazione con algoritmi di ottimizzazione per identificare la configurazione ottimale dell'U-OWC con un costo computazionale ridotto. Successivamente, le performance dell'impianto sono state valutate e ottimizzate utlizzando un modello non lineare wave-to-wire nel dominio del tempo. Questo modello numerico ha permesso di testare differenti strategie di controllo del PTO con l'obiettivo di massimizzare la conversione di energia dell'impianto di Roccella Jonica. I risultati del capture width ratio per turbine di Wells monoplana e multi-stage sono stati confrontati con la turbina biradiale. É stata anche valutata la possibilità di connettere una singola turbina a diverse camere d'aria per ridurre il costo complessivo dei PTO. Un sistema di valvole di sfogo è stato introdotto per controllare la velocità rotazionale del PTO durante gli stati di mare più energetici senza la necessità di spegnere l'impianto per ragioni di sicurezza. I risultati presentati hanno dimostrato che l'efficienza dell'U-OWC dipende dalla geometria del dispositivo, dal sistema di power take-off (PTO) utilizzato e dalla strategia di controllo selezionata. Infine, è stata anche studiata una classe di sistemi power take-off innovativi, i generatori ad elastomero dielettrico (DEG). Le performance di un U-OWC con DEG sono state valutate attraverso una campagna sperimentale condotta su un prototipo in piccola scala installato nel laboratorio NOEL di Reggio Calabria senza attivazione elettrica. Inoltre, una simulazione hardware-in-the-loop (HIL) è stata effettuata per replicare le condizioni operative reali con un carico sperimentale ridotto e meno rischi rispetto a test in vasche di laboratorio o in mare.

Parole chiave:

Oscillating Water Column, ottimizzazione, linearizzazione statistica, Power Take-Off, controllo

Abstract

The thesis deals with the optimisation of U-Oscillating Water Columns (U-OWC) integrated into vertical breakwaters. The case study considered in the present work was a wave power plant installed in the Mediterranean Sea. Specifically, the optimal geometrical configuration of a U-OWC was computed for the port of Roccella Jonica, Italy. In this context, the statistical linearisation technique was used in combination with optimisation algorithms to identify the optimal U-OWC configuration with reduced computational cost. Next, the power plant's performance was assessed and optimised using a non-linear time-domain wave-to-wire model. This numerical model allowed the testing of different PTO control strategies aiming to maximise the power conversion of the Roccella Jonica power plant. Capture width ratio results for single and multi-stage Wells turbines were compared with the biradial turbine. The possibility of connecting one turbine to several air chambers was also investigated to reduce the overall PTO costs. A bypass relief valve system was introduced to control the PTO rotational speed during the most energetic sea states without turning off the power plant for safety reasons. The presented results demonstrated that the U-OWC efficiency depends on the device's geometry, the adopted power take-off (PTO) system and the selected control strategy. Finally, an innovative class of power take-off systems – the dielectric elastomer generators (DEGs) – was also studied. The performance of a U-OWC with DEGs was estimated through an experimental campaign conducted on a small scale prototype installed at the NOEL laboratory of Reggio Calabria without electrical activation. In addition, a hardware-in-the-loop (HIL) simulation was conducted to replicate real operating conditions with reduced experimental burden and fewer risks than wave tank or field tests.

Key-words:

Oscillating Water Column, optimization, statistical linearization, Power Take-Off, control

Contents

List of Figures

List of Tables

Acknowledgements

Very special thanks to my masters:
Prof. Felice Arena
Prof. João C. C. Henriques
Dr. Giovanni Malara

Nomenclature

Romans

a	generator control law constant	
A_1	U-duct cross sectional area	[m^2]
A_3	air chamber cross sectional area	[m^2]
A_m	wave amplitude	[m]
A_v	valve area	[m^2]
b_1	width of the U-duct	[m]
b_2	width of the air chamber	[m]
b_3	transverse width of the U-OWC chamber	[m]
c	speed of sound	[m/s]
C	capacitance	[F]
c_v	discharge coefficient	[-]
$\mathrm{CWR}_\mathrm{elec}$	electrical capture width ratio (3.36)	[-]
D	turbine rotor diameter	[m]
d_v	valve diameter	[m]
e	DEG radius in the pre-stretched configuration	[m]
e_0	DEG radius in the undeformed configuration	[m]
E_BD	break-down electric field	[MW/m]
f_o	frequency of occurrence of a sea state	[%]
g	acceleration of gravity	[m/s^2]
h	submergence of the U-duct opening	[m]
h_c	height of the air chamber	[m]
H_s	significant wave height	[m]
h_t	displacement of the membrane tip	[m]
I	turbine/generator set moment of inertia	[kg m^2]

ℓ	air chamber width	[m]
l_{12}	length of the U-duct	[m]
$\dot{m}_{\mathrm{tot}}$	total mass flow rate (3.39)	[kg/s]
$\dot{m}_{\mathrm{turb}}$	air mass flow rate through the turbine	[kg/s]
$\dot{m}_{\mathrm{v}}$	air mass flow rate through the valve	[kg/s]
$\tilde{m}$	inertia related quantity	[kg/m^4]
$\tilde{m}_{\infty}$	added mass-like term at	
	infinite frequency	[kg/m^4]
$\mathrm{Ma}_{\mathrm{tip}}$	blade tip Mach number	[-]
n_{c}	number of connected chambers	[-]
n_{l}	number of dielectric layers	[-]
n_{ss}	number of sea states	[-]
n_{v}	number of valves	[-]
p	absolute air chamber pressure	[Pa]
p_{exc}	excitation pressure	[Pa]
p_{atm}	absolute atmospheric pressure	[Pa]
P_{elec}	electrical power (3.38)	[W]
P_{ctrl}	generator electromagnetic power (3.28)	[W]
$P_{\mathrm{gen}}^{\mathrm{rated}}$	generator rated power	[W]
P_{pneu}	pneumatic power	[W]
P_{turb}	turbine aerodynamic power (3.24)	[W]
$\hat{P}_{\mathrm{wave}}$	wave energy flux per unit	
	wave-crest length (3.1)	[W/m]
Q_{turb}	turbine volumetric flow rate at	
	inlet conditions	[m^3/s]
t	time	[s]
t_0	DEG thickness in the undeformed configuration	[m]
T_{p}	peak period	[s]
V_{c}	instantaneous air chamber volume	[m^3]

Greek symbols

γ	specific heat ratio of air, $C_{\mathrm{p}}/C_{\mathrm{v}}$	[-]
Γ	Gamma function	
Δp	turbine pressure head, $p - p_{\mathrm{atm}}$	[Pa]

Δt	time interval	[s]
$\Delta\Omega$	range of turbine rotational speed	[s]
η_{turb}	turbine efficiency (3.25)	[-]
η_{elec}	electrical efficiency	[-]
λ_{p}	membrane pre-stretch coefficient	[-]
λ_{u}	maximum admissible membrane stretch	[-]
ξ	distance between the instantaneous inner free surface and the top of the chamber	[m]
Π	turbine dimensionless power (3.21)	[-]
ρ	density	[kg/m^3]
σ	standard deviation	[-]
Φ	turbine dimensionless flow rate (3.20)	[-]
Ψ	turbine dimensionless pressure head (3.19)	[-]
ω	wave frequency	[rad/s]
Ω	turbine/generator set rotational speed	[rad/s]
Ω_{max}	maximum rotational speed recorded for all sea states	[rad/s]
Ω_{thr}	maximum allowed rotational speed (3.31)	[rad/s]
$\Omega_{\mathrm{v}}^{\mathrm{open}}$	rotational speed threshold for opening the first relief valve	[rad/s]

Subscripts

1	relative to section (1)
3	relative to section (3)
atm	atmospheric quantity
bep	best efficiency point
c	air chamber
eq	equivalent terms
in	turbine inlet stagnation conditions
v	valve
w	water

Acronyms

BR	biradial turbine

CD-DEG	circular diaphragm dielectric elastomer generator
DEG	dielectric elastomer generator
GA	genetic algorithm
HIL	Hardware-In-the-Loop
MWL	mean water level
OWC	oscillating water column
PS	parameter sweep
PT	pressure transducer
PTO	power take-off
WEC	wave energy converter
WT1	single-stage turbine
WT2	two-stage turbine
WT3	three-stage turbine

Chapter 1

Introduction

Wave energy is increasing its importance among the renewable sources of energy. Waves are generated by winds blowing on the surface of seas and oceans and propagate for large distances with small energy losses. The contribution of wave energy as a clean source is due to its abundance and its energy density which is higher compared with solar and wind energy. The global wave energy power is estimated to be approximately 2 TW [11], which is a value close to the world electricity consumption. However, a portion from 10 to 25 % of this available wave energy can be extracted [12] to be converted into electrical energy. In 1974, after the beginning of the oil crisis of 1973, the potential of wave energy was emphasized by Stephen Salter, professor at University of Edinburgh, who published the paper "Wave Power" on the prestigious journal Nature [13]. Already in those years, the author found a hundred of proposals of devices for extracting energy from the waves among the British Patents. Different prototypes were mentioned, making use of flaps, floating devices, channels and liquid pistons. In that work Salter proposed a device known as Salter's Duck or the Edinburgh Duck, a floating body rotating about its centre under the action of the incoming waves. From the 70's more than a thousand of patents were registered and hundreds of them were built and tested, reaching different stages of development up to the full-scale construction. Wave energy converters (WECs) can be classified according to different criteria: the working principle, the deployment location or the size. One of the most accredited classifications can be found in [4], which is essentially based on the working principles of the devices, as shown in Fig. 1.1. The main types of WECs are the Oscillating Water Columns (OWCs), the oscillating bodies and the overtopping devices.

1.1 Overtopping devices

Overtopping devices collect the water of the wave crests in reservoirs that are located above the mean water level. The gathered water then returns to the sea by activating low-head hydraulic turbines with vertical axis. The water can be captured through channels such as the case of the Tapchan (Tapered

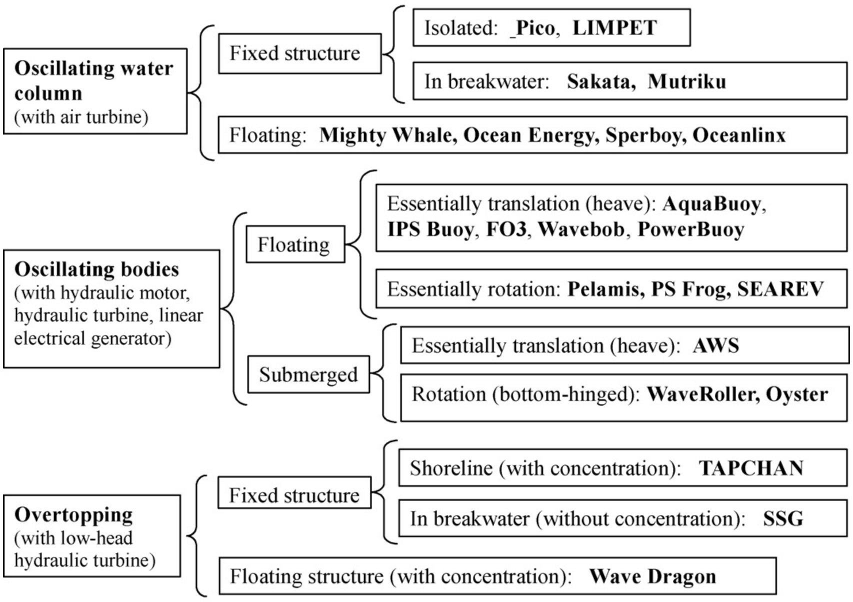

Fig. 1.1: Classification of wave energy converters

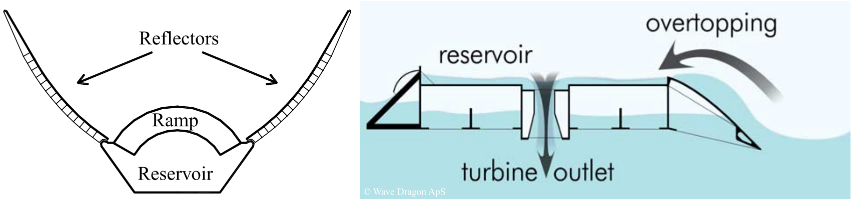

Fig. 1.2: Scheme of the Wave Dragon. From Ref. [1]

Channel Wave Power Device) [14] where the collector is carved into a rocky cliff and becomes gradually narrower having the effect of amplifying the wave height which overcomes the walls of the collector filling the reservoir.

In the offshore floating device Wave Dragon [1] the water is directed to the reservoir through two reflectors and a ramp. A 1:4.5 scale prototype was installed in Denmark and tested.

The SSG (Seawave Slot-Cone Generator) [2] is an overtopping device integrated into a breakwater, with three reservoirs at three different levels. The water enters the reservoirs through openings located in the sloped wall of the breakwater. A multi-stage hydraulic turbine is installed to produce energy from the three different potential energy levels (see Fig. 1.3). The major drawback of this type of devices is the use of low head turbines.

1.2 Oscillating bodies

Oscillating bodies are wave energy converters which exploit the relative motion of two or more components to produce energy. They can be floating structures or completely submerged devices. Oscillating bodies can be installed in deep water where the waves are more energetic. Nevertheless, the

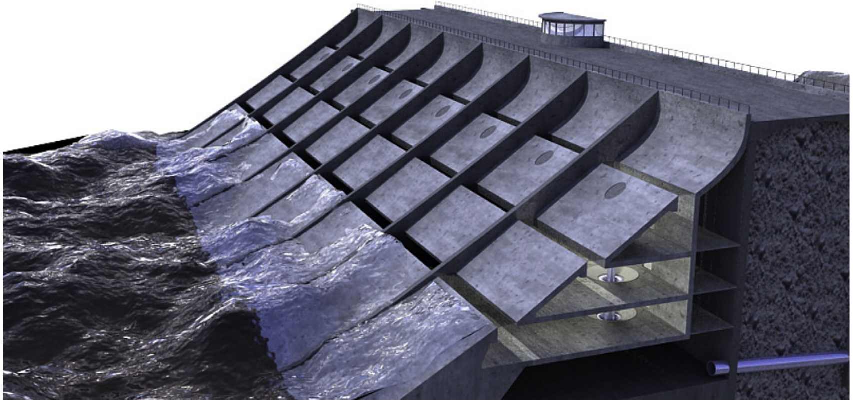

Fig. 1.3: Schematic view of the SSG. From Ref. [2]

Fig. 1.4: Installation of the AWS pilot plant. From Ref. [3]

distance from the main land implies difficulties related to the maintenance, the mooring systems and the electrical cables to deliver energy to the grid. Most of the oscillating bodies make use of the heave motion to harvest energy. This is the case of the single-body systems, represented by a buoy which moves with respect to a fixed plane, such as the sea bottom. Alternatively, the floating body can be connected to a bottom-fixed structure by a cable. The PTO can be represented by a piston pump connected to an hydraulic turbine or a linear electrical generator. Other kinds of oscillating bodies are represented by the two-body point absorbers. The IPS buoy [15] includes a floater connected to a piston which oscillates inside a tube open at both ends. The relative motion between the floater and the tube, caused by the waves action, drives a PTO. Devices with a similar working principle are the AquaBuoy [16], the Wavebob and the PowerBuoy. The Archimedes Wave Swing (AWS) [17] is a completely submerged heaving system which includes a floater that is moved by the motion of crests and troughs and a bottom-fixed part called basement. The AWS was installed and tested in the North of Portugal in 2004, see Fig. 1.4.

Fig. 1.5: Pelamis WECs installed off the coast in the North of Portugal. From Ref. [4]

In some oscillating bodies the energy production is obtained through relative rotation instead of translation. The most famous pitching system was the Salter Duck which was studied and tested at different scales for many years. The Pelamis is a WEC composed of four cylindrical sections hinged together and aligned according to the wave direction [18]. The relative motion between the parts pumps high-pressure oil through hydraulic motors activating three electrical generators. Three full-size Pelamis, each one with a rated power of 750 kW, were installed off the coast in the North of Portugal in 2008, see Fig. 1.5.

Other oscillating bodies comprise a body which is submerged and another part which is above the mean water level or enclosed and protected inside a hull [19, 20]. Oscillating bodies can exploit the motion in pitch by being hinged at the sea bed in shallow waters (less than 20 m). The Oyster (see Fig. 1.6) was developed by the company Aquamarine Power in 2005 [21]. It is a flap whose motion around the sea bottom hinge pumps high pressure sea water to a Pelton turbine located onshore. The moving flap covers the entire water depth, from the water surface to the sea bed. An Oyster device was installed in the Orkney Islands in 2009 and connected to the national grid of UK.

Similar to the Oyster is the WaveRoller device which comprises moving panels pumping high pressure oil to an hydraulic motor. WaveRoller panels can be fully or mostly submerged. A WaveRoller prototype was installed at Peniche, in Portugal, in 2008.

1.3 Oscillating Water Columns (OWCs)

OWCs are considered as one of the most studied and tested wave energy converters. This is due to their simple working principle. OWCs comprise a hollow structure made of concrete or steel which shows an opening located at the bottom below the mean water level. The incident waves interact with the structure through the big opening causing the free water surface inside the chamber to oscillate. The air trapped in the upper part of the structure is alternatively compressed and expanded and flows out to the

Fig. 1.6: Oyster prototype. From Ref. [4]

atmosphere and back to the chamber. The airflow drives the rotor of a turbine connected to an electrical generator. Turbines are usually self-rectifying, i.e. the rotational direction of the rotor does not change with the direction of the air flow. OWCs are versatile devices that can be deployed both as fixed structures, also integrated in breakwaters, or as floating bodies.

1.3.1 History of OWCs

The first OWC device was designed in the late 40's by the Japanese navy officer Yoshio Masuda, who developed a navigation buoy, which included a tube opened at the bottom, powered by an air turbine connected to a generator [22]. The system was provided with rectifying valves. A schematic view of the so called Masuda's buoy is shown in Fig. 1.7 a). A number of buoys were produced by the Japanese company Ryokuseisha (see Fig. 1.7 b)). The navigation buoy was not the only WEC developed by Yoshio Masuda. His research included also large scale wave energy converters. The first concept was a circular ring buoy with diameters greater than the wave length. This idea was developed by the Japan Marine Science and Technology (JAMSTEC) in 1975. Masuda adapted a ship, the KAIMEI, to a wave energy converter by creating OWC chambers in the hull. The ship was 80 m long, 12 m wide and was moored on 40 m water depth. The KAIMEI was an attenuator-type device, floating along the wave direction. Unidirectional and self-rectifying air turbines were tested over the years. A shore-fixed OWC was built at Sanje Turuoka city in 1983. This kind of WECs were thought for island use. The OWC measured 8 m in width, 5 m in length and 5 m in height. Two Wells turbine were installed on the shaft of a generator with 40 kW rated power. However, the water depth at the OWC opening was just 2 m, thus the energy available to the chamber was small.

Meanwhile in Europe during the years 1970's government programs began to fund research in the wave

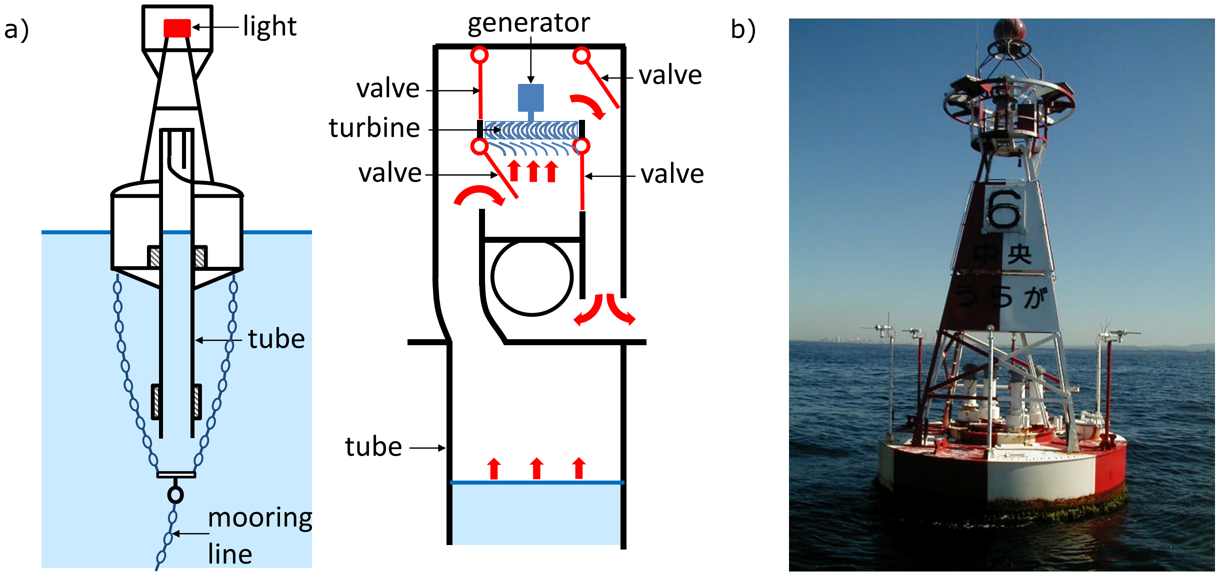

Fig. 1.7: a) Sketch of Masuda’s navigation buoy. From Ref. [5]. b) Ryokuseisha light buoy (From Ref. [6])

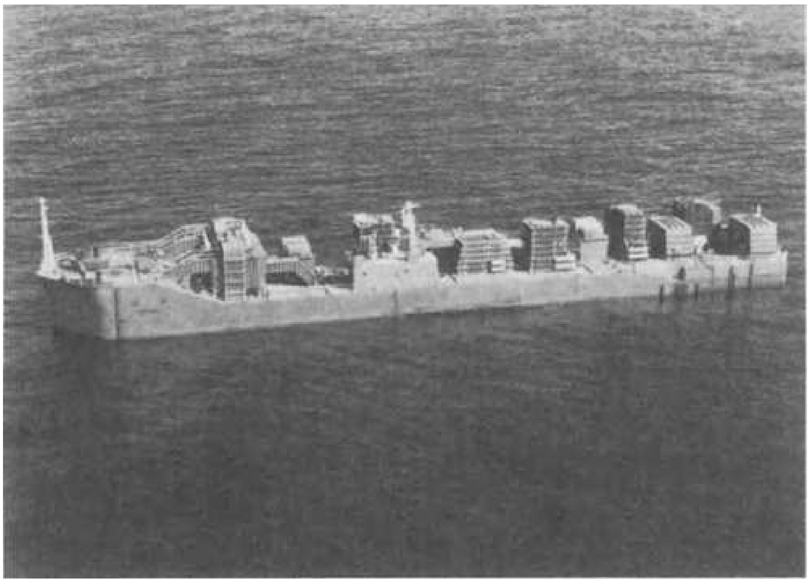

Fig. 1.8: Picture of the KAIMEI ship

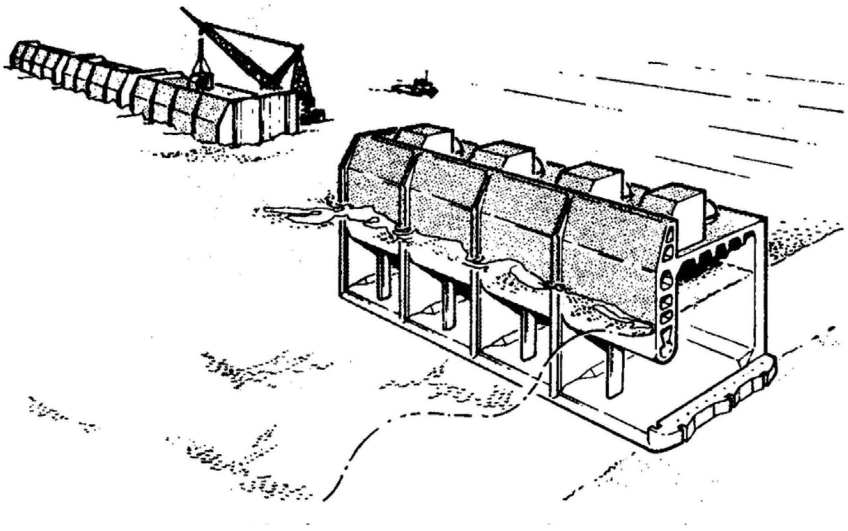

Fig. 1.9: The NEL OWC breakwater

energy field. This is the case of UK [23], where the Department of Energy commissioned the National Engineering Laboratory (NEL) to carry out an economic and technical feasibility study on large-scale wave energy devices. Among the different devices, there was the NEL Oscillating Water Column: a breakwater provided with multiple OWC chambers (Fig. 1.9). In the report "Wave Energy Studies at the U.K. National Engineering Laboratory" several shapes for OWCs were tested and the relative efficiencies were computed. Both floating and fixed OWCs are described, emphasizing the advantages to build a fixed structure in shallow water, such as: the utilization of less space between the devices, the higher efficiency conversion, the easier maintenance, the lower maximum wave height that can occur.

In the same years, after 1977, a wave energy program started in Norway funded by the Ministry of Petroleum and Energy [24]. This research conducted to the installation of a 0.5 MW OWC between 1984 and 1985 on a steep cliff at Toftestallen, near Bergen. The structure was built in concrete (the lower part close to the mean water level) and steel (the upper part). The opening of the OWC was 10 m wide and 3.5 m high and the chamber had a water plane area of 50 m^2. A vertical-axis self-rectifying Wells turbine was installed. However, during the winter of 1988 a storm destroyed the steel part of the OWC, while the concrete part survived.

Until the first years of the 1990's the activity on Oscillating Water Columns in Europe was conducted by universities, such as the Queen's University of Belfast that developed a shoreline OWC prototype with a rated power of 75 kW in 1991 [25]. The plant was built at the island of Islay in Scotland. From 1982 the Japanese Ministry of Transport, together with the First District Port Construction Bureau, the Port and Harbour Research Institute and the Coastal Development Institute of Technology and several companies started a research for the development of a prototype of OWC integrated in a composite breakwater in the port of Sakata in Yamagata Prefecture [26]. The test breakwater was built in the summer of 1989 and began to produce energy in the winter of the same year. The caisson was 20 m long and the air chamber

Fig. 1.10: OWC at Toftestallen, Norway

was 7 m wide. Two Wells turbines with a diameter of about 1.4 m were connected to a generator with a rated power of 60 kW and maximum rotational speed of 3000 rpm. The results of the experiment and the recorded efficiencies (hydrodynamic, turbine and generator efficiencies) were used to predict the performance of a full-scale wave power plant with larger turbine diameter and generator. The wave power plant of the Sakata port can be considered as the first case of OWC integrated into a breakwater, with the aim of sharing the costs between the civil building and the wave energy converter. The research on wave energy in India began in 1983 at the Indian Institute of Technology (IIT) in Madras, funded by the Department of Ocean Development of the Government of India. The studies led to the class of OWCs and a demonstration plant with rated power of 150 kW was designed and installed at Vizhinjam, near Trivandrum, on the South West Coast of India in 1991 [27]. The chamber was integrated on a caisson with size 17 m×21 m equipped with a Wells turbine with a rotor diameter of 2 m. After the tests of the first OWC prototypes which allowed to assess the reliability of the technology, a number of devices based on the working principle of the oscillating water column were designed and tested.

1.3.2 Fixed OWCs

An important boost to the development of WECs in Europe was given by the decision of the European Commission to fund R&D programs on wave energy. A European Pilot Plant Study was funded by the FP2-JOULE 1 program on renewable energies from 1992 to 1993. The project was coordinated by the Instituto Superior Técnico of Lisbon, together with researchers from UK and Ireland, with the aim of investigating a location for the design and installation of a medium scale shoreline OWC wave power plant. The pilot plant was intended to allow research related to practical aspects, such as constructional methods, testing of air turbines, control systems and grid connection. In particular, two sites were identified: the island of Pico in the Azores and the island of Islay in Scotland. The Pico plant was the first wave energy plant designed and built to provide electrical energy to the grid in a permanent way [28]. The concrete structure, measuring 12 m x 12 m, was mainly cast in-situ. The top of the chamber was 11.5 above the mean water level, while the opening of the OWC was located 3.7 m below the water surface. The plant was built by exploiting a natural gully, see Fig. 1.11. Its construction began in 1996 and finished in 1998. However, it began to produce energy for the first time after summer 1999. The plant was equipped with a monoplane Wells turbine with guide vanes and an outer diameter of 2.3 m, connected to a 400 kW generator and able to operate with variable rotational speed. A relief valve was installed between the atmosphere and the air chamber in order to control the flow rate through the turbine. The plant operated from 1999 to 2018, but with long periods of inactivity due to the frequent need of repairing or replacing mechanical components and to the excessive distance from the main land. After the decision took in 2017 to dismantle the plant, the foundation of the structure partially collapsed during a severe storm in 2018.

Fig. 1.11: The Pico OWC wave power plant in the Azores. (Courtesy of J. C. C. Henriques)

Fig. 1.12: LIMPET OWC wave power plant, Island of Islay, Scotland

The OWC of Pico was a useful structure, not only to produce and deliver energy to the grid, but also as a research and training centre for many researchers.

The plant installed on the island of Islay was called LIMPET (Land Installed Marine Powered Energy Transformer) and is a shoreline OWC with inclined water column (see Fig. 1.12) to improve the hydrodynamic performance [29]. The construction was completed in September 2000 and was funded by the Joule III programme of the EU. The device was 21 m wide and the collector was divided into three separate columns. It was equipped with two contra-rotating Wells turbines with a rotor diameter of 2.6 m connected to generators with total rated power of 500 kW. The plant was provided with relief valves installed for safety reasons. The performance of the plant were poor, less than one third, with respect to the expected average power output, estimated to be about 150 kW. It turned out that this falling in terms of energy was due to a change in the profile of the seabed and a water depth one meter less than predicted was detected, with consequences on the reduction of the energy delivered by the incoming waves.

Shoreline OWCs were developed also in China. After the tests conducted on a 20 kW wave power plant in 1996, a 100 kW OWC was built in 2001 and connected to the electric grid at Zhelang Town, Shanwei City of Guangdong Province [30].

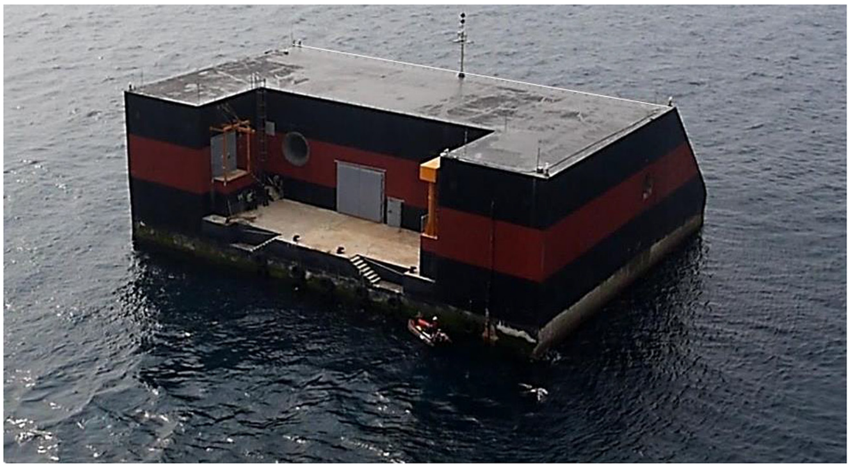

Fig. 1.13: Bottom-standing OWC installed at Yongsoo (Korea)

The project was supported by the China's National Key Technologies R&D Program. The company Wavegen of Inverness designed the nearshore OWC wave energy converter called OSPREY (Ocean Swell Powered Renewable EnergY), which includes a collector chamber and a wind turbine [31]. Two contra-rotating Wells turbines were installed and each one of these was connected to a 500 kW generator. The device was designed to be installed on a water depth of about 15 m. The OSPREY was built and towed near Dounreay in Scotland, but it was destroyed before being installed. In 2013, the prototype GreenWAVE was built by the company Oceanlinx and funded by the Australian Government. It was a 1 MW bottom-standing OWC 24 m long and 21 m large. In 2014 the device was towed to Port Macdonnel in South Australia but the airbags supporting the device were damaged and the structure sank. In the years 2003-2012 a bottom-standing OWC was installed in Korea, at Yongsoo near the Jeju island [32]. It is a 500 kW wave power plant funded by KORDI. The device is 37 m long, 31.2 m wide and 27.5 m high. It has a rated power of 500 kW and is equipped with an impulse turbine with 1.8 m of rotor diameter, see Fig. 1.13.

In 1984 a way to increase the hydrodynamic performance of a wave energy converter was theoretically demonstrated [33]. The study proposed the idea to build a harbour, made of two thin sidewalls projected from the device towards the incoming waves. The theory could also be applied to OWCs. This was the case of the full-scale prototype Oceanlinx of size 36 m x 35 m built by the Australian company Energetech and installed and tested near Port Kembla, in Australia, in 2005. A parabolic wall was employed to focus the energy of the waves towards the chamber, see Fig. 1.14.

1.3.3 OWCs integrated into a breakwater

The experience of the wave power plant installed at Pico showed that the aspects related to the civil structure in fixed OWCs are the most critical and expensive. These aspects are, for example, the construction of the underwater part of the device, the employed materials and the relative distance from

Fig. 1.14: Oceanlinx prototype, Port Kembla, Australia

the building site, etc. The idea to integrate the OWC chamber into harbour breakwaters allows to share the costs between the civil structure and the plant. Apart from the economical issue, the other advantages of a combination of breakwater and OWC are the reduction of loads and wave heights in front of the breakwater due to the absorbed energy, the easier access for operation and maintenance of the WEC and the possibility to employ infrastructures and utilities of the harbour. The first case of integration of a brekawater and an OWC is represented by the Sakata plant (1991), in Japan [26]. The chamber is embodied in the central caisson of the breakwater structure. The choice to make the breakwater "electrically active" with an oscillating water column was evaluated by the Basque Government's Department of Transport and Public Works and the Ente Vasco de la Energía when a new breakwater had to be built at the port of Mutriku in the years 2008-2010 [34]. The construction of the OWCs involved a length of 100 m, in a curved section, of the total breakwater, see Fig. 1.15.

The Mutriku wave energy plant consists of 16 chambers, each one connected to a Wells turbine with a rated power of 18.5 kW. The total capacity of the plant is 296 kW. The Mutriku plant served also as a research centre where different air turbines were tested [35]. In Italy the OWCs technology was integrated into the vertical breakwater of the port of Civitavecchia, Rome [36]. 17 caissons, for a total length of 578 m, were built, each one with 8 independent chambers, see Fig. 1.16. Currently, no turbines are installed. The OWCs are of U-type, where a U-shaped duct connects the inner chamber to the open wave field and the opening of the duct is horizontal. The so-called U-OWC or REWEC3 (REsonant Wave Energy Converter, realization number 3) was patented by Boccotti in 2003 [37]. Other breakwaters in Italy are designed to host U-OWC caissons, such as in the port of Salerno (under construction in January 2021) and port of Roccella Jonica [38].

Fig. 1.15: OWC integrated into Mutriku's breakwater, Spain

Fig. 1.16: U-OWC breakwater in Civitavecchia, Rome, Italy

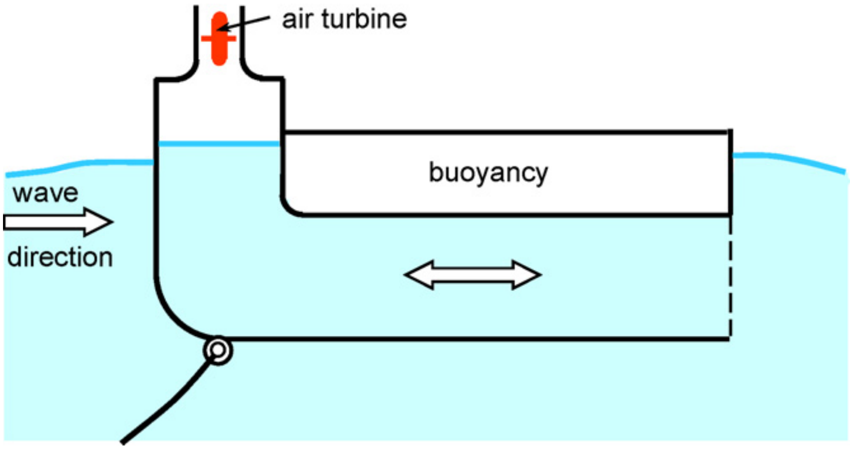

Fig. 1.17: Sketch of the Backward Bent Duct Buoy (BBDB)

1.3.4 Floating OWCs

The study conducted by Yoshio Masuda on wave-activated buoys was followed by the research of McCormick [39] in 1974, who modelled a buoy with a circular floating body and a tube located in the centre and open on both ends, communicating with sea at the bottom and with the atmosphere at the top, where a turbine is connected. McCormick showed that the length of the central tube can be dimensioned to obtain the maximum power for a certain resonant wave period. The OWC spar buoy absorbs energy from the waves due to its heaving oscillation. The shape of this device was studied and optimized and it was found out that a non-uniform cross section of the tube may result in an improvement of the performance [40].

Tests conducted on the KAIMEI plant demonstrated the good efficiencies of the air turbines. However, the efficiency of the conversion from wave energy to pneumatic energy was much less than expected. Hence, the necessity to design a floating wave energy converter to improve the efficiencies. The wave-activated buoys have the drawback of the central tube that needs installations in deep water and are subjected to ocean currents. The Backward Bent Duct Buoy (BBDB), [41], was designed to overcome such limits. The BBDB include an air chamber that is bent backward with respect to the wave direction as shown in Fig. 1.17. The lack of the vertical pipe allows the device to be installed at any depth greater than the draft of the buoy. Several tests were conducted in tanks to compare the performance of the BBDB and the wave-activated buoy with the central pipe. In a tank test performed at the Japan Ship Research Institute, the electric generation of the BBDB proved to be three times larger than that of the center pipe buoy. After first tests, the BBDB device began to become popular Europe, Asia and USA. Sandia National Laboratory, funded by the U.S. Department of Energy's (DOE) Wind and Water Power Technologies Program Office (WWPTO), adopted a BBDB device, called RM6, as the OWC reference model for the marine energy programme [42].

Several numerical studies and tests were conducted to investigate the dynamics and performance of

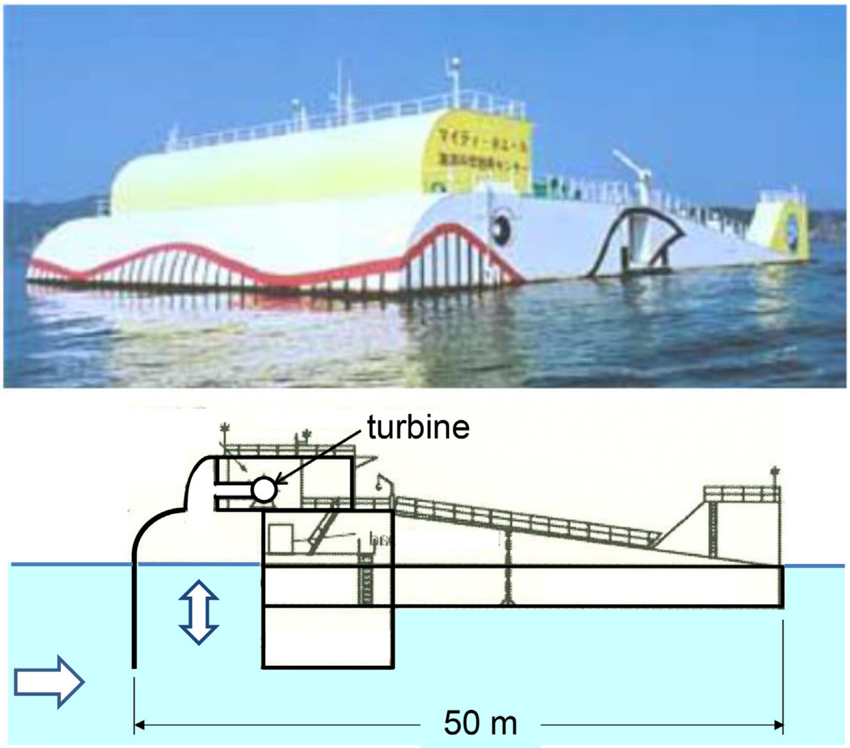

Fig. 1.18: Mighty Whale

the BBDB [43, 44, 45, 46].

In 1987 JAMSTEC began a study on a floating OWC called Mighty Whale, with the dual purpose of converting wave energy into electricity and dissipating wave heights behind it [47]. Mighty Whale was installed and tested from September 1998 in Gokasho Bay, Nansei Town, in Mie Prefecture. The WEC was a 50 m × 30 m floating structure with three air chambers connected to Wells turbines for a total rated power of 110 kW, see Fig. 1.18.

The Orecon wave energy buoy was a floating OWC with chambers with different drafts in order to generate electricity from several sea states. The device was tension moored to the sea bed [48].

A 1:15 model of a large multipurpose floating platform [49] is currently tested in Italy, in the Mediterranean Sea, funded by the European project “The Blue Growth Farm”. The platform includes a wind turbine and several chambers based on the U-OWC working principle installed on the wave-exposed side.

1.3.5 OWCs key advantages

The design and tests of a wave energy converter aim to develop a device able to withstand the wave loads and to effectively produce electrical energy to be delivered to the electrical grid. The conversion process from wave energy to electrical energy occurring in WECs involves forces of hundreds of tons and small velocities. The power take-off system is to be designed to cope with these conditions. Besides, large PTO forces imply high costs for the structure. The advantage of oscillating water columns devices resides in the fact that the air chamber carries out the task of converting the large force of the waves and the low velocity of the inner free water surface into higher air velocity and smaller forces that interact with the air turbine. The turbine blades rotate at rotational speeds ranging from hundreds to few thousand revolutions per minute. This is the range of velocities allowed by commercial low-cost electrical generators. A simple computation showing a comparison between different WECs with respect to the forces required to obtain the same amount of power output is described in Ref. [50]. Specifically, a classic wave energy converter comprising a floater connected to a PTO system with a damping and a spring is compared to a floating OWC equipped with an air turbine. The peak forces on the rotor blades of the turbine in the OWC are two orders of magnitude smaller than the forces on the hydraulic PTO. In OWCs the PTO is not hit directly by the wave forces. Indeed, forces are transmitted from the waves to a compressible medium, the air in the chamber, which delivers the power to the turbine, thus reducing the peak loads. Another important aspect to be considered relates to the peak-to-average ratio of the power output. For most of the WECs, this ratio reaches high values. The control of the peak-to-average power ratio, called peak shaving, results to be a generally difficult operation due to the low capability of PTOs to dissipate the excess of energy during the most energetic sea states. High values of the peak-to-average ratio of the power output implies oversized generators to operate the PTO during the most energetic sea states, with consequences on the related costs. Besides, an electrical generator sized for high sea states shows poor efficiencies when operating in milder waves. This problem can be easily addressed in OWCs thanks to the possibility to dissipate energy on the PTO. This can be achieved by limiting the pneumatic power available to the turbine through the installation of relief valves in parallel with the turbine or high-speed stop valve (HSSV) in series with the turbine as shown in Ref. [51].

1.3.6 Air turbines

One of the most important advantages of the OWCs technology is represented by the fact that the only moving mechanism is the rotor of an air turbine that is located far from the waves' action, in the upper part of the chamber. A self-rectifying air turbine can extract the energy related to the air flux that goes out from the chamber to the atmosphere and back always rotating in the same direction. The most common self-rectifying air turbine equipped in OWCs is the Wells turbine, invented by A. Wells in 1976 [52]. This type of turbine has a rotor, whose blades are symmetrical with respect to a plane normal to the rotational axis. Due to the shape of the blades, the reciprocating air flow produces a unidirectional torque. The behaviour of the air flow through the rotor blades can be observed in a two-dimensional plane where V is the absolute flow velocity, W is the relative flow velocity and $U = \Omega r$ is the blade speed, where Ω is the angular velocity of the rotor and r is the radius. The two-dimensional cascade flow of a monoplane Wells turbine without guide vanes is shown in Fig. 1.19 where the incoming flow is axial.

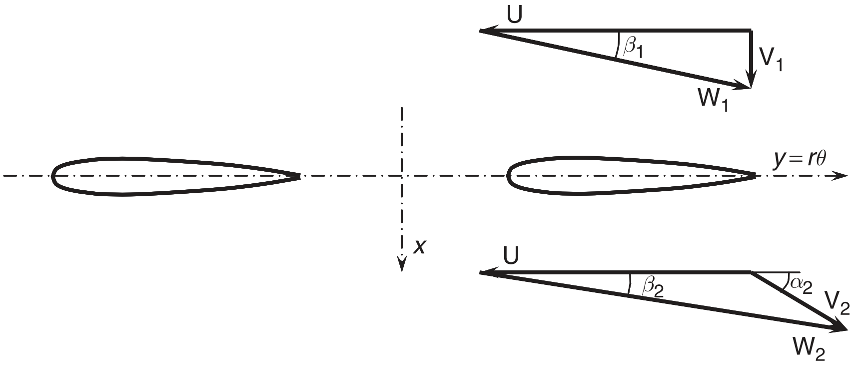

Fig. 1.19: Two-dimensional cascade flow for a monoplane Wells turbine without guide vanes [7]

The absence of guide vanes induces losses relative to the kinetic energy at the exit of the rotor due to swirl flow. Losses can be reduced by introducing a set of properly designed guide vanes on both sides of the rotor. Alternatively, a contra-rotating turbine can be adopted, where two rows of identical rotor blades rotate with the same speed but in opposite direction. However, this solution is mechanically complex and expensive due to the presence of two power electronics system to control the two turbine-generator rotating sets. A less complex way to reduce the swirl losses is to consider the biplane turbine, where two identical rows of blades, rotating in the same direction, are mounted in the same shaft at a certain distance between them. The biplane turbine can be found in the version without guide vanes, with guide vanes between the two rotors [54] or with guide vanes on both rotors. Besides, the biplane turbine allows to reduce the pressure head per rotor, mitigating the sudden drop in the stall region of the efficiency curve [55] typical of the Wells turbine, thus increasing the average efficiency of the machine. The sharp fall of the curve of the efficiency as function of the flow rate coefficient occurs when the angle of incidence at the entrance of the rotor blades exceeds the stall-free limit. The rotor blades stalling causes aerodynamic losses with consequences on the reduction of the operational range of the Wells turbine.

The most popular alternative to the Wells tubine is represented by the axial-flow impulse turbine [56]. An impulse turbine comprises a rotor with a set of twin guide vanes. The guide vanes and the blades are placed near one another forming a channel for the flow. The blades have sharp edges and the inlet angle is equal to the exit angle for symmetrical purpose. The two-dimensional cascade flow for an impulse turbine with guide vanes is shown in Fig. 1.20.

Due to the losses between the rotor blades and the downstream guide vanes, the efficiency of the impulse turbines shows peaks lower than those achieved with the Wells turbines. Nevertheless, the efficiency curve of the impulse turbine does not present the sudden drop when stall conditions occur. However, the performance of the impulse turbine can be increased by adopting pivoting guide vanes instead of fixed ones [57]. In this way the flow coming from the rotor can enter the downstream guide vanes with a smaller angle of incidence reducing the losses due to the boundary layer separation. Recently a novel turbine was proposed to overcome both the backwards of the Wells and the axial-flow impulse

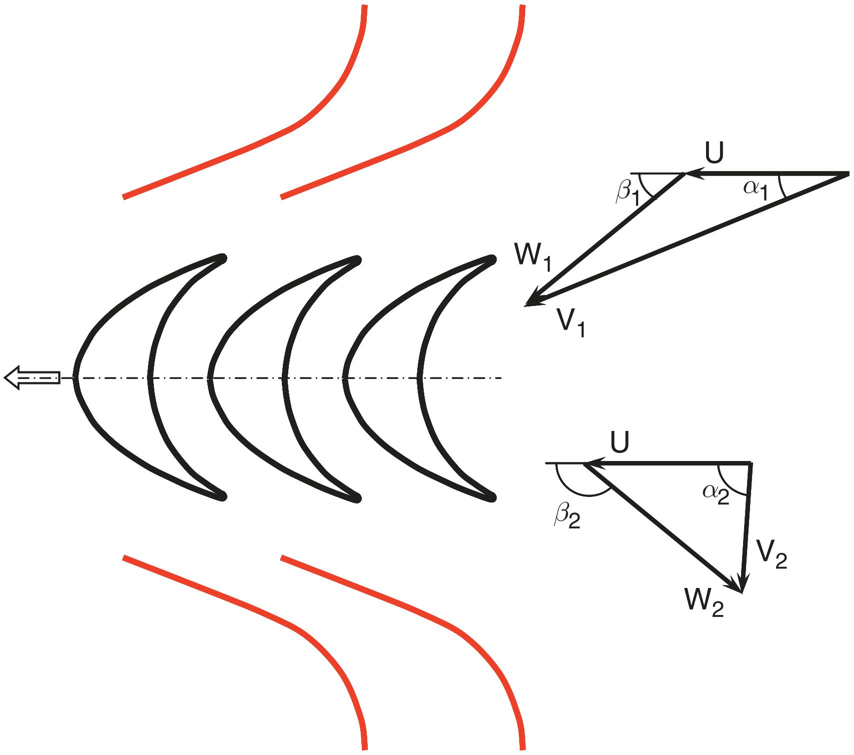

Fig. 1.20: Two-dimensional cascade flow for an impulse turbine with guide vanes

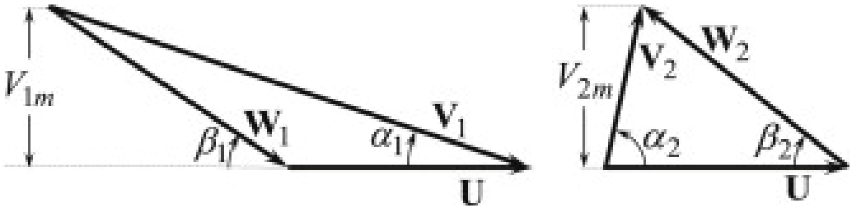

Fig. 1.21: Velocity diagram of the biradial turbine. From left to right: rotor blades entry and exit. From Ref. [8]

turbine. The biradial turbine [8] is symmetrical with respect to a plane perpendicular to the rotor axis of rotation. The flow gets in to, and out from, the rotor through the two openings which are axially spaced. The flow entering to the rotor is centripetal, while the outgoing flow is centrifugal.

The guide vanes rows are connected to the corresponding rotor through semicircular ducts. The velocity diagram of the biradial turbine is shown in Fig. 1.21 where the two conditions, at the entry to the rotor blades and at the exit from the rotor blades are described. The diagram is obtained for best efficiency conditions, when $W_1 \approx W_2$. The biradial turbine shows peaks in the efficiency curve higher than those presented by the Wells turbine. Besides the efficiency curve does not present the sharp drop typical of the Wells turbines in the stall region.

1.3.7 U-type Oscillating Water Columns (U-OWCs)

In the last decades researches were conducted to increase the efficiency of the OWCs. The performance are the highest when the oscillations inside the chamber are in phase with the excitation force of the waves. Phase control was implemented to cope with this problem [58] in the case of OWC equipped with a turbine with controllable blade setting angles. However, devices for phase control require the knowledge of wave field time history and the prediction of the incident wave field for the phase control of each individual wave.

In 2002 Boccotti [37] proposed a new configuration of the OWC structure (totally or partially submerged) by adding a vertical duct on the wave-beaten side with the submerged horizontal opening facing upwards. This device was called U-OWC due to the U-shape of the vertical duct.

Boccotti found that a natural resonance between the irregual waves and the WEC could be obtained by setting some geometrical parameters of the structure instead of using mechanical devices for the phase control. From a comparison study between a traditional OWC and a U-OWC, both integrated into a breakwater, Boccotti stated that the additional vertical duct could increase the performance of the device. This was due to essentially two reasons: the eigenperiod of the U-OWC is greater than the eigenperiod of the OWC and the amplitudes of the pressure fluctuations on the horizontal opening of the U-OWC are larger than those on the opening of the OWC. Since the opening of the vertical duct is higher with respect to the opening of the traditional OWC, the U-OWC performs better also with small wind waves [59].

The presence of a higher opening with respect to the OWCs, makes the U-OWCs an optimal choice for installations in the Mediterranean Sea, where waves are smaller compared to the sea states occurring in the oceans.

The mathematical model used for the description of the water column oscillations in the U-OWC is based on the application of the extended Bernoulli theorem for unsteady flow. The model was validated and improved through small-scale field experiments [60, 61, 62] on a model of U-OWC installed in benign natural basin exposed to random incident waves at the NOEL (Natural Ocean Engineering Laboratory) in Reggio Calabria, Italy. The first full-scale U-OWC integrated into a breakwater was built in the Mediterranean Sea in the harbour of Civitavecchia, Italy [63] for the building of a new dock in 2015. A total of 17 U-OWC caissons were constructed, each one comprising 8 independent chambers. Each chamber has a vertical duct which is 6 m long and 1.6 m wide, while the inner chamber is 3.2 m wide and 9.4 m tall above the mean water level. The caissons are installed at a water depth of 15 m. During a sea storm in November 2015 the plant absorbed from 70 to over 90 % of the average incident wave power.

Two smaller plants are under construction in Italy: one in the port of Salerno and one in the port of Roccella Jonica.

Specifically, most of the present study is focused on the performance optimization of the U-OWC plant of the marina "Porto delle Grazie" of Roccella Jonica, located in the southern part of Italy.

1.4 Contributions of the thesis to the state of the art

This thesis's main contribution is developing and implementing approaches for optimizing the energy-wise performance of a particular type of oscillating water column device, namely the U-OWC. A critical feature of the present analysis is that the considered optimization problems involved U-OWCs operating in low energy areas, which are barely considered in similar studies.

From a computational perspective, the energetic performance of the U-OWC was so far investigated by considering the sensitivity analysis related to just one or few parameters at a time. Herein, several geometrical parameters are taken into account to find the optimal configuration of a chamber of U-OWC. In this context, considering all the possible combinations would be computationally too expensive or even prohibitive with the common computational resources. Therefore, the first contribution relates to adopting the statistical linearization technique to solve the equations describing the dynamics of the U-OWC. An approximation of the U-OWC response is obtained with a considerable reduction of the computational time. This latter aspect allows coupling the statistical linearization with established optimization algorithms adopted to search for the optimal geometrical configuration of a U-OWC chamber.

Another contribution of this work is selecting an optimal turbine (in terms of type and size) to be installed on a U-OWC wave power plant for the Mediterranean Sea. The selection was conducted by considering both Wells turbines (including multi-stage configurations) and biradial turbines. The control of the turbine and a relief valves system was proposed to maximize the plant's energy production for the particular local wave climate.

The thesis also covers the possible utilization of a new type of PTO for the U-OWC, the dielectric elastomer generators (DEGs), through two different tests. A first field experiment was conducted to study the DEG coupling on the U-OWC without electrical control. Afterwards, and hardware-in-the-loop simulation was conducted to evaluate the power production of the coupled system. The obtained data show promising results for further future tests.

1.5 Thesis structure

The main goal of this work is the optimization of the performance of U-OWCs integrated into a breakwater. The efficiency of the U-OWC chamber is strongly connected with the design of the geometrical parameters of the device and with the power take-off system. The influence of the width of the vertical duct opening on the performance of the plant was investigated by Boccotti by letting all the remaining parameters (length of the duct, width and heigth of the inner chamber, diameter of the turbine) constant [64]. A recent study included in the optimization process not just the width of the vertical duct but also its length and the thickness of the wall [65].

Chapter 2 deals with the problem of designing an optimal geometrical configuration of a U-OWC chamber for the port of Roccella Jonica, Italy. The dynamics of the U-OWC is described by a system of two non-linear differential equations with no closed-form solution. The problem can be solved numerically. However, this implies a time consuming and computanionally expensive process. When dealing with optimization problems several parameters should be considered and the use of numerical approaches can become prohibitive for the computations. For circumventing this problem, the statistical linearization technique is employed to find an approximate solution of the U-OWC response. Thus, the statistical linearization is coupled to optimiziation algorithms, specifically the genetic algorithms, to find the optimal configuration for the chamber of U-OWC to be constructed in the Roccella Jonica port. The method of the coupled statistical linearization and the genetic algorithms is validated through parameter sweep and a significant reduction of the computational time has been observed. Two approaches are proposed and compared: an optimization based on the design sea state, and an optimization based on the wave climate. Clearly, the latter approach resulted in better performance. This work was published in a conference proceedings:

- **A. Scialò**, G. Malara, F. Arena, *Geometrical optimization of U-Oscillating Water Columns in random waves*. In: Proceedings of the 38th International Conference on Ocean, Offshore and Arctic Engineering. Glasgow, Scotland, UK: OMAE 2019; 2019. https://doi.org/10.1115/OMAE2019-95973.

In passing, note that the geometrical optimization was conducted by considering a Wells turbine installed in the U-OWC chamber with fixed rotational speed. This is not an optimal solution since the rotational speed is to be controlled during the different sea states of the local wave climate in order to maximize the power conversion. Therefore, a time-domain model was required for the optimal selection and control of the PTO.

Chapter 3 describes the implementation of a time-domain wave-to-wire model to evaluate the performance of the Roccella Jonica wave power plant during the year. Configurations with several chambers sharing a single turbine are explored in order to reduce the costs of the PTO while maximizing the performance. The optimal turbine type, turbine diameter and generator rated power are selected based on the electrical capture width ratio. For the purpose, Wells turbines, both monoplane and two/three-stages, and biradial turbine were compared. The introduction of a bypass relief valve system was considered to control the PTO rotational speed during the most energetic sea states in order to satisfy the imposed rotational speed constraints without the need of turning the power plant off for safety reasons. This work was published in a conference proceedings and in a journal:

- **A. Scialò**, G. Malara, F. Arena, J. C. C. Henriques, L. M. C. Gato, *Selection of a PTO system and a relief valve for the Roccella Jonica wave power plant*. Proceedings of the 4th International

Conference on Renewable Energies Offshore - RENEW 2020, Lisbon, Portugal, October 12 – 15, 2020.

- **A. Scialò**, J. C. C. Henriques, G. Malara, A. F. O. Falcão, L. M. C. Gato, F. Arena, *Power take-off selection for a fixed U-OWC wave power plant in the Mediterranean Sea: The case of Roccella Jonica*, Energy 215 (2021) 119085. doi:10.1016/j.energy.2020.119085.

Finally, in Chapter 4 an innovative class of power take-off systems, namely the dielectric elastomer generators (DEGs), is described. An experimental campaign was conducted on a small scale prototype of U-OWC installed at the NOEL laboratory of Reggio Calabria. Firstly, the purely mechanical response of the coupled system (U-OWC and DEG) was investigated without electrical activation. The collected data were used to validate the mathematical model and to predict the performance of a full-scale U-OWC power plant equipped with DEGs. As an intermediate step between the mechanical test and a further test at sea with electrical activation, a hardware-in-the-loop (HIL) simulation was considered to replicate the realistic operating conditions of a U-OWC equipped with DEGs in a laboratory with a smaller experimental burden and less risks with respect to wave tank or sea tests. Besides, HIL tests allow repeatability in a controlled environment which is not possible in field experiments. This work was published in two conference proceedings and in two journals:

- F. Arena, L. Daniele, V. Fiamma, M. Fontana, G. Malara, G. Moretti, A. Romolo, G. P. Rosati Papini, **A. Scialò**, R. Vertechy, *Field experiments on dielectric elastomer generators integrated on a U-OWC wave energy converter*. Proceedings of the ASME 37th International Conference on Ocean, Offshore and Arctic Engineering – OMAE 2018, Madrid, Spain, June 17-22 2018.
- Moretti G., Malara G., **Scialò A.**, Daniele L., Romolo A., Vertechy R., Fontana M., Arena F., *Modelling and field testing of a breakwater-integrated U-OWC wave energy converter with dielectric elastomer generator*, Renewable Energy, Volume 146, 2020, Pages 628-642, ISSN 0960-1481, https://doi.org/10.1016/j.renene.2019.06.077.
- **Scialò A.**, Moretti, G., Malara, G., Fontana M., Romolo A., Arena F., *Hardware in the loop test of a U-Oscillating Water Column converter coupled with a Dielectric Elastomer Generator*. Proceedings of the 13th European Wave and Tidal Energy Conference – EWTEC 2019, Naples, Italy, September 1st – 6th 2019.
- Moretti G., **Scialò A.**, Malara G. et al. *Hardware-in-the-loop simulation of wave energy converters based on dielectric elastomer generators*. Meccanica (2021). https://doi.org/10.1007/s11012-021-01320-8.

The conclusions of this research work are provided in Chapter 5, where future perspectives and developments are outlined as well.

The Appendix is dedicated to the description of the method employed to obtain the computation of the hydrodyanmic coefficients for a U-OWC chamber.

Chapter 2

Geometrical optimization of a U-OWC chamber by using the statistical linearization technique and genetic algorithms

2.1 Introduction

A number of Wave Energy Converter (WEC) concepts have been proposed and tested so far. The Oscillating Water Column (OWC) devices are amongst the few that have reached the stage of full-size prototype and are considered as the most effective for producing energy [4]. In a nutshell, an OWC operates by exploiting the principle of the oscillating water column inside an hollow chamber with a bottom opening in the wave beaten side. The air pocket located in the upper part of the chamber is alternatively compressed and decompressed by the sequence of crests and troughs. The generated airflow drives a turbine linked to the chamber through an orifice and a duct. The turbine installed in a OWC is usually a self-rectifying Wells turbine [5], which rotates in the same direction regardless of the air flow direction.

On the basis of the OWC working principle, Boccotti proposed the so-called U-Oscillating Water Column (U-OWC) by adding a vertical element with an upward opening that connects the open wave field with the chamber through a U-shaped duct [37]. This novelty provides an additional inertia to the system that can be used to modify the eigenperiod of the U-OWC by tuning it to a given value, thus increasing the performance in terms of absorbed and produced power. A comparison between the traditional OWC and the novel U-shaped Oscillating Water Columns, given identical geometrical dimensions of the inner chamber, was carried out by Boccotti [59]. Since then, several improvements were made. The theoretical model for the U-OWC dynamics was originally proposed by Boccotti [66]. Next, Malara and Arena derived the equations of motion of the system by including memory effects previously neglected [67]. Experimental activities were performed to assess the dynamic response of the system to real operating conditions and to measure the power output [60]. The first full scale breakwater embodying U-OWC devices was built in Civitavecchia (Rome, Italy). The plant is composed by 124 independent chambers with a total length of 524 m. In the future the plant could produce about 2.5 MW by installing turbines with a rated power of 18-20 kW. Successively, an experimental campaign was conducted in order to test a U-OWC device equipped with a closed air chamber holding a set of Circular Diaphragm Dielectric Elastomer Generators (CD-DEGs) [68]. The first study was promising, though, further investigations are required to assess the amount of energy that can be produced by replacing the classical Wells turbine with a DEG-Power Take-Off (The coupled system of U-OWC and DEG will be presented in Chapter 5).

Optimization is a crucial issue in the design of these devices. In this regard, several studies were conducted to investigate the geometrical optimization of different wave energy converters. A detailed analysis on geometry optimization of wave energy converters is reported in Ref. [69] where different approaches are considered and compared. Methods like the Constructal Design and the design of experiments (DOE) were employed to find the optimal shape of a OWC [70] and a point absorber [71], respectively. In the last years some authors applied a class of optimization algorithms, the Genetic Algorithms (GAs), to wave energy converters with the aim of seeking the optimal shape which maximizes the power output and minimizes the costs [72, 73]. Originally proposed by John Holland [74] in 1975, Genetic Algorithms are stochastic search techniques developed on the basis of living beings evolutionary process and they proved to be a powerful tool to solve optimization problems in a variety of fields. Concisely, GAs evolve the solution given by an initial population by employing the operations of selection and recombination. More recently, other authors proposed a comparison between two different algorithms applied to a floating OWC geometry. They employed a Constraint Optimization BY Linear Approximation (COBYLA), that is a direct search method, and a Differential Evolution (DE) algorithm, based on genetic operations [75]. They proved that DE, despite requiring a larger computational time, shows higher probability to converge to a global optimum. Different heuristic optimization approaches were tested on renewable energy systems [76]. Specifically, the authors noted that GAs outperform other methods in the optimization of wave energy converter arrays. In Ref. [77] genetic algorithms are adopted to find both opitmal individual dimensions (radii and drafts) and array layout of cylindrical buoys with heave motion. Other researchers conducted a techno-economic optimization by applying Genetic Algorithms to a pendulum wave energy converter aiming at minimizing the ratio between the capital cost and the annual energy production [78]. They included geometrical and PTO parameters and costs of the different materials.

In the work reported here a Genetic Algorithm is used to optimize the geometry of a U-OWC integrated into a breakwater. Wave data off the coast of Roccella Jonica (Reggio Calabria, Italy) are employed for the study. Specifically, two different optimizations are performed: an approach based on the design sea state; and an approach based on an optimal design in a wave climate. In the former case, the optimization function is the power produced by the U-OWC in the considered sea state. In the latter case, the objective function is the average energy converted in a year by the wave power plant. A validation of the proposed Genetic Algorithm is presented by adopting the Parameter Sweep (PS) method, as in Ref. [79], exploring every possible combination in the parameters space.

The hydrodynamic parameters of the system, the added mass and the retardation function, are calculated by a semi-analytical approach. Besides, in order to reduce the computational time of the GA, the statistical linearization technique is employed to complute approximately the solution of the coupled nonlinear differential equations governing the U-OWC dynamics [80].

2.2 Preliminary remarks on the efficient calculation of the U-OWC response

A schematic view of a U-OWC is shown in Fig. 2.1 where the dimensions of the device are depicted. The symbols b_1 and b_2 represent, respectively, the width of the vertical duct and of the pneumatic chamber, while b_3 (not shown in the figure) is the transverse width of the chamber. The external duct has an horizontal opening with a submergence h below the mean water level and is l_i long. The height of the chamber is h_c. Finally, an orifice is located in the upper part of the chamber with a diameter of dimension D designed to install an air turbine.

2.2.1 U-OWC equations of motion

The equation governing the water column oscillations is obtained by applying an energy balance between the points (1) and (2) of Fig. 2.1 through the Bernoulli theorem. Specifically, it is seen that:

$$M(x)\ddot{x}+C(\dot{x},x)\dot{x}+x+\frac{1}{\rho g}\left(p_\mathrm{c}-p_\mathrm{atm}\right)+\frac{b_2}{g b_1}\int_{-\infty}^{t}K(t-\tau)\dot{x}(\tau)d\tau=\frac{\Delta p^{(D)}}{\rho g} \tag{2.1}$$

where dot denotes differentiation with respect to time; ρ is the water density; g is the acceleration due to gravity; p_atm is the atmospheric pressure; $K(t)$ is the retardation function and describes the memory effects. The equation is expressed as a function of $x(t)$, that is the vertical distance between the free surface inside the chamber and the mean water level (positive upwards), and $p_\mathrm{c}(t)$, that is the pressure of the air in the chamber. The free surface of the water column is assumed to translate rigidly along the

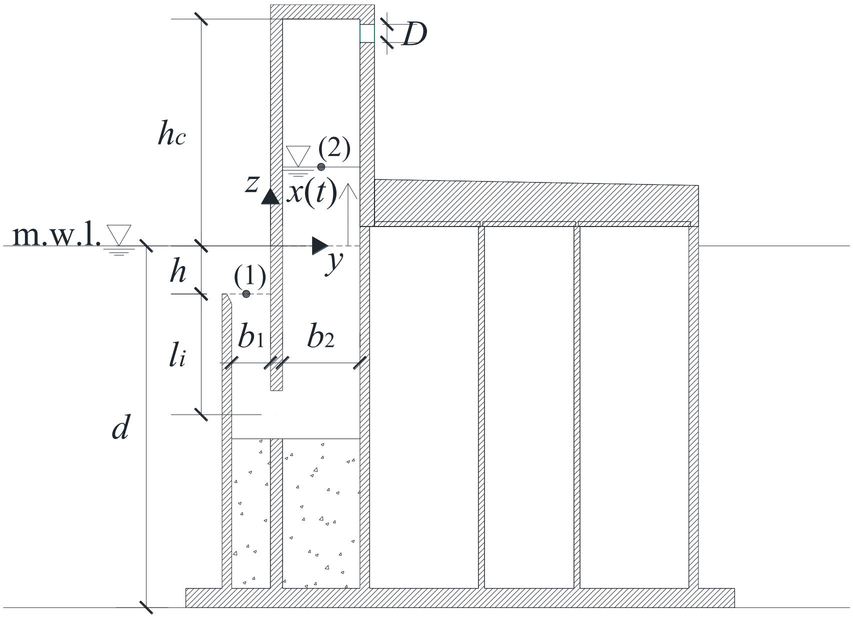

Fig. 2.1: Cross-section of a U-OWC caisson. The geometrical parameters are marked by symbols. The numbers in brackets represent the points for the application of Bernoulli theorem.

vertical direction. The system is excited by the wave pressure $\Delta p^{(D)}$ calculated in a diffracted wave field at the center of the external opening. The nonlinear terms of mass and damping are respectively expressed according to the relations:

$$M(x) = \frac{1+C_{\mathrm{in}}}{g}\left(\frac{b_2}{b_1}l_{\mathrm{i}} + l_{\mathrm{i}} + h + x\right) + \frac{b_2}{gb_1}H(\infty) \tag{2.2}$$

and

$$C(\dot{x},x) = \frac{1}{2g}\left\{1 + C_{\mathrm{dg}}\left[\frac{l_{\mathrm{i}}}{R_{h1}}\left(\frac{b_2}{b_1}\right)^2 + \frac{l_{\mathrm{i}}+h+x}{R_{h2}}\right]\right\}|\dot{x}|, \tag{2.3}$$

in which $H(\infty)$ represents the infinite frequency added mass and R_{h1} and R_{h2} are the hydraulic radii of the external vertical duct and of the inner chamber, respectively.

This equation is related to the air chamber equation derived by assuming an isentropic thermodynamic process. Thus, the resulting equation is

$$C_{\mathrm{p}}(x)\dot{p}_{\mathrm{c}} + C_{\mathrm{x}}\left(p_{\mathrm{c}}\right)\dot{x} + K_{\mathrm{p}}\left(p_{\mathrm{c}}\right)p_{\mathrm{c}} = 0, \tag{2.4}$$

where the nonlinear damping and stiffness terms are expressed as follow

$$C_{\mathrm{p}}(x) = b_2 b_3\left(h_{\mathrm{c}} - x\right), \tag{2.5}$$

$$C_{\mathrm{x}}(p_{\mathrm{c}}) = -\gamma b_2 b_3 p_{\mathrm{c}} \tag{2.6}$$

and

$$K_{\mathrm{p}}(p_{\mathrm{c}}) = \gamma \left(\frac{p_{\mathrm{atm}}}{p_{\mathrm{c}}}\right)^{1/\gamma} \frac{\dot{m}_{\mathrm{t}}}{\rho_{\mathrm{atm}}}, \tag{2.7}$$

where γ is the ratio of the specific heat at constant pressure over the specific heat at constant volume and ρ_{atm} is the atmospheric density. The air mass rate is related to the pressure drop through the dimensionless turbine coefficient Λ [61]

$$\dot{m}_{\mathrm{t}} = \frac{\Lambda D}{\Omega}(p_{\mathrm{c}} - p_{\mathrm{atm}}), \tag{2.8}$$

Ω being the turbine rotational speed. Note that eq. (2.8) is valid only for quantifying the air flow rate through Wells turbines.

2.2.2 Statistical linearization solution

The equations governing the dynamics of a U-OWC have no closed-form solution. Numerical approaches offer straightforward tools for computing numerically the system response. However, they are quite time consuming and computationally expensive during the design process. On the other hand, other approaches are available for analyzing such nonlinear problems. In this regard, the statistical linearization technique proved to be one of the most effective approximate methods [81]. The application of this technique to wave energy converter was demonstrated for several WECs. Statistical linearization was applied to approximate the response of a point absorber [82], an oscillating wave surge and an oscillating water column [83]. Particular emphasis was given to OWC devices, such as in Ref. [84], where the reliability of the technique is assessed for an array of oscillating water column chambers.

The statistical linearization technique is implemented by replacing the original system of nonlinear equations by a surrogate equivalent linear system with unknown system parameters. Further, since the nonlinearities exhibit an asymmetric behavior, the response of the system has a non-zero mean. To take into account this offset, the response components are computed as:

$$x = x_0 + m_{\mathrm{x}} \tag{2.9}$$

and

$$\Delta p_{\mathrm{c}} = \Delta p_0 + m_{\mathrm{p}}. \tag{2.10}$$

The terms m_{x} and m_{p}, appearing in (2.9) and (2.10) are the mean offsets of the water displacement and the air pressure inside the chamber, respectively; Δp_{c} is the pressure drop; x_0 and Δp_0 are the zero-mean processes of the two time-dependent variables. Under this assumption, the equivalent set of equations is

$$\left(M + M_{\mathrm{eq}}^{(1)}\right)\ddot{x}_0 + C_{\mathrm{eq}}^{(1)}\dot{x}_0 + \left(1 + K_{\mathrm{eq}}^{(1)}\right)x_0 + \frac{\Delta p_0}{\rho g} + \frac{b_2}{g b_1}\int_{-\infty}^{t} K(t-\tau)\dot{x}_0(\tau)\mathrm{d}\tau = \frac{\Delta p^{(D)}}{\rho g} \tag{2.11}$$

and

$$\left(C_{\mathrm{p}}^{(2)} + C_{\mathrm{p,eq}}^{(2)}\right)\Delta\dot{p}_0 + \left(C_{\mathrm{x}}^{(2)} + C_{\mathrm{x,eq}}^{(2)}\right)\dot{x}_0 + K_{\mathrm{p,eq}}^{(2)}\Delta p_0 + K_{\mathrm{x,eq}}^{(2)}x_0 = 0, \tag{2.12}$$

where the subscript eq denotes the unknown equivalent mass, damping and stiffness terms. The other terms appearing in equations (2.11) and (2.11) are

$$M = \frac{1 + C_{\mathrm{in}}}{g}\left(\frac{b_2}{b_1}l_{\mathrm{i}} + l_{\mathrm{i}} + h + m_{\mathrm{x}}\right) + \frac{b_2}{g b_1}H(\infty), \tag{2.13}$$

$$C_{\mathrm{p}}^{(2)} = b_2 b_3\left(h_{\mathrm{c}} - m_{\mathrm{x}}\right) \tag{2.14}$$

and

$$C_{\mathrm{x}}^{(2)} = -\gamma b_2 b_3\left(m_{\mathrm{p}} + p_{\mathrm{atm}}\right). \tag{2.15}$$

The values of the equivalent coefficients are determined by minimizing the mean square error of the response vector ε, that is the difference between the original and the approximate response. That is, they are determined by solving the equations:

$$\begin{aligned}\frac{\partial}{\partial M_{\mathrm{eq}}^{(1)}}E\left(\varepsilon^2\right) &= \frac{\partial}{\partial C_{\mathrm{eq}}^{(1)}}E\left(\varepsilon^2\right) = \frac{\partial}{\partial K_{\mathrm{eq}}^{(1)}}E\left(\varepsilon^2\right) = \frac{\partial}{\partial C_{\mathrm{p,eq}}^{(2)}}E\left(\varepsilon^2\right)\\ &= \frac{\partial}{\partial C_{\mathrm{x,eq}}^{(2)}}E\left(\varepsilon^2\right) = \frac{\partial}{\partial K_{\mathrm{p,eq}}^{(2)}}E\left(\varepsilon^2\right) = \frac{\partial}{\partial K_{\mathrm{x,eq}}^{(2)}}E\left(\varepsilon^2\right) = 0\end{aligned} \tag{2.16}$$

Applying equation (2.16), it is seen that the mass and stiffness terms of the equivalent system, $M_{\mathrm{eq}}^{(1)}$ and $K_{\mathrm{eq}}^{(1)}$, are equal to zero. In carrying out the computations of the problem described in equation (2.16), a system of 5 equations, containing the equivalent coefficients, is obtained:

$$2C_{\mathrm{eq}}^{(1)}\sigma_{\dot{x}0}^{2} = \frac{1}{g}\left\{1 + C_{\mathrm{dg}}\left[\frac{l_{\mathrm{i}}}{R_{h1}}\left(\frac{b_2}{b_1}\right)^{2} + \frac{l_{\mathrm{i}} + h + m_{\mathrm{x}}}{R_{h2}}\right]\right\} E\left[|\dot{x}_0|\dot{x}_0^{2}\right], \tag{2.17}$$

$$C_{\mathrm{p,eq}}^{(2)}\sigma_{\dot{\Delta}p_0}^{2} + C_{\mathrm{x,eq}}^{(2)}E\left[\dot{x}_0\dot{\Delta}p_0\right] + K_{\mathrm{x,eq}}^{(2)}E\left[x_0\dot{\Delta}p_0\right] = 0, \tag{2.18}$$

$$C_{\mathrm{x,eq}}^{(2)}\sigma_{\dot{x}0}^{2} + K_{\mathrm{p,eq}}^{(2)}E\left[\Delta p_0\dot{x}_0\right] + C_{\mathrm{p,eq}}^{(2)}E\left[\dot{\Delta}_{p0}\dot{x}_0\right] = \gamma p_{\mathrm{atm}}^{\frac{1}{\gamma}}\frac{1}{\rho_{\mathrm{atm}}}E\left[\left(\Delta p_0 + m_{\mathrm{p}} + p_{\mathrm{atm}}\right)^{1-\frac{1}{\gamma}}\dot{m}_{\mathrm{t}}\dot{x}_0\right], \tag{2.19}$$

$$C_{\mathrm{x,eq}}^{(2)}E[\dot{x}_0\Delta p_0] + K_{\mathrm{p,eq}}^{(2)}\sigma_{\Delta p_0}^{2} + K_{\mathrm{x,eq}}^{(2)}E[x_0\Delta p_0] = \gamma p_{\mathrm{atm}}^{\frac{1}{\gamma}}\frac{1}{\rho_{\mathrm{atm}}}E\left[\left(\Delta p_0 + m_{\mathrm{p}} + p_{\mathrm{atm}}\right)^{1-\frac{1}{\gamma}}\dot{m}_{\mathrm{t}}\Delta p_0\right], \tag{2.20}$$

and

$$C_{\mathrm{p,eq}}^{(2)}E\left[\dot{\Delta}p_0x_0\right] + K_{\mathrm{p,eq}}^{(2)}E[\Delta p_0x_0] + K_{\mathrm{x,eq}}^{(2)}\sigma_{x0}^{2} = \gamma p_{\mathrm{atm}}^{\frac{1}{\gamma}}\frac{1}{\rho_{\mathrm{atm}}}E\left[\left(\Delta p_0 + m_p + p_{\mathrm{atm}}\right)^{1-\frac{1}{\gamma}}\dot{m}_t x_0\right], \tag{2.21}$$

where the symbol σ denotes the standard deviation of a variable. The variances and the expected values are related to the response spectra and cross-spectra.

The response of the equivalent system is sought in the frequency domain, where the equations (2.11) and (2.12) becomes

$$\left[-\omega^{2}M + i\omega C_{\mathrm{eq}}^{(1)} + 1 + i\omega\frac{b_2}{gb_1}\widetilde{K}(\omega)\right]X(\omega) + \frac{1}{\rho g}\widetilde{\Delta p}(\omega) = \frac{1}{\rho g}\widetilde{\Delta p}^{(D)}, \tag{2.22}$$

and

$$\left[i\omega\left(C_{\mathrm{p}}^{(2)} + C_{\mathrm{p,eq}}^{(2)}\right) + K_{\mathrm{p,eq}}^{(2)}\right]\widetilde{\Delta p}(\omega) + \left[i\omega\left(C_{\mathrm{x}}^{(2)} + C_{\mathrm{x,eq}}^{(2)}\right) + K_{\mathrm{x,eq}}^{(2)}\right]X(\omega) = 0. \tag{2.23}$$

By solving this system of algebraic equations, the response spectral components are computed as

$$S_{xx} = |X(\omega)|^{2}, \tag{2.24}$$

$$S_{x\Delta p} = X(\omega)(\Delta p(\omega))^{*}, \tag{2.25}$$

$$S_{\Delta px} = \Delta p(\omega)(X(\omega))^*, \tag{2.26}$$

and

$$S_{\Delta p\Delta p} = |\Delta p(\omega)|^2, \tag{2.27}$$

with $*$ denoting complex conjugation. Once the spectral components are obtained, they can be employed for the evaluation of the response statistics. Specifically, the variances of the response components are computed by the equations

$$\sigma_{x0}^2 = \int_{-\infty}^{+\infty} S_{xx} \mathrm{d}\omega, \tag{2.28}$$

$$\sigma_{\dot{x}0}^2 = \int_{-\infty}^{+\infty} \omega^2 S_{xx} \mathrm{d}\omega, \tag{2.29}$$

and

$$\sigma_{\ddot{x}0}^2 = \int_{-\infty}^{+\infty} \omega^4 S_{xx} \mathrm{d}\omega. \tag{2.30}$$

The expected values involved in the solution of eq. (2.17)-(2.21) are calculated by the following relationships:

$$E[x_0 \Delta p_0] = \int_{-\infty}^{+\infty} S_{x\Delta p} \, \mathrm{d}\omega, \tag{2.31}$$

$$E[\Delta p_0 x_0] = \int_{-\infty}^{+\infty} S_{\Delta px} \mathrm{d}\omega, \tag{2.32}$$

$$E[x_0 \ddot{x}_0] = \int_{-\infty}^{+\infty} -\omega^2 S_{xx} \mathrm{d}\omega, \tag{2.33}$$

$$E\left[x_0\dot{\Delta p}_0\right] = \int_{-\infty}^{+\infty} \omega S_{x\Delta p} \mathrm{d}\omega, \tag{2.34}$$

$$E[\Delta p_0 \dot{x}_0] = \int_{-\infty}^{+\infty} \omega S_{\Delta p x} \mathrm{d}\omega, \tag{2.35}$$

$$E[\dot{x}_0 \Delta p_0] = \int_{-\infty}^{+\infty} \omega S_{x\Delta p} \mathrm{d}\omega, \tag{2.36}$$

$$E\left[\dot{x}_0\dot{\Delta p}_0\right] = \int_{-\infty}^{+\infty} \omega^2 S_{x\Delta p} \mathrm{d}\omega, \tag{2.37}$$

and

$$E\left[|\dot{x}_0|\,\dot{x}_0^2\right] = \frac{\left(2\sigma_{\dot{x}0}^2\right)^3 \Gamma(3)}{4\sqrt{2\pi}\left(\sqrt{\sigma_{\dot{x}0}^2}\right)^3}, \tag{2.38}$$

where Γ denotes the Gamma function [85]. The analytical expressions for the expectation of the remaining terms are not known. Therefore, they are computed numerically. The offsets are determined by considering the equations (2.11) and (2.12) on the average, by taking the expected value of the terms containing the variables x_0 and Δp_0. This yelds:

$$\frac{1+C_{\mathrm{in}}}{g} E[x_0\ddot{x}_0] + m_{\mathrm{x}} + \frac{m_{\mathrm{p}}}{\rho g} = 0 \tag{2.39}$$

and

$$-b_2 b_3 E\left[x_0 \dot{\Delta p}_0\right] - \gamma b_2 b_3 E[\Delta p_0 \dot{x}_0] + \frac{\gamma}{\rho_{\mathrm{atm}}} E\left[p_{\mathrm{atm}}^{1/\gamma} \dot{m}_{\mathrm{t}} \left(\Delta p_0 + m_{\mathrm{p}} + p_{\mathrm{atm}}\right)^{1-\frac{1}{\gamma}}\right] = 0. \tag{2.40}$$

The computation of the coefficients of the equivalent linear system depends on the response statistics, which are unknown. Therefore, an iterative procedure is employed, by assuming initial values for the equivalent coefficients and the mean offsets as shown in Table 2.1.

Table 2.1: Initial values of the equivalent coefficients and mean offsets

$C_{\text{eq}}^{(1)}$	$C_{\text{x,eq}}^{(2)}$	$C_{\text{p,eq}}^{(2)}$	$K_{\text{x,eq}}^{(2)}$	$K_{\text{p,eq}}^{(2)}$	m_{x}	m_{p}
0	0	0	1	1	0	0

2.3 U-OWC optimization via genetic algorithm

In the last decades Genetic Algorithms have been broadly employed to solve many optimization problems in the engineering field. Genetic Algorithms are heuristic techniques for stochastic search based on the concepts of natural selection and adaptation. The basic idea comes from the field of biology, where the term adaptation relates to a process whose structure is repeatedly modified to increase its performance. The GAs start from an initial set of random solutions called population. The individuals in the population are called chromosomes and represent a potential solution to the optimization problem. They are progressively modified from one generation to another. The evolution occurs mainly through two different genetic processes: the crossover and the mutation. The crossover involves two chromosomes at a time by combining their features. A cut-point is randomly chosen and a portion of a chromosome, its genes, is replaced by the corresponding part of the other chromosome and vice versa. The mutation operation acts upon a single chromosome by changing the value of one or more genes. Thus, a feature lost during the selection process can be recovered, or a gene that was not present in the initial population can be subsequently added. Another feature is elitism, a process whereby the individuals with the best fitness value in each iteration are guaranteed to move to the next generation without undergoing crossover or mutation. Next, a new generation, called offspring, is obtained. During each iteration, the fitness of the chromosomes is evaluated through the maximization/minimization of the objective function. The chromosomes are sorted according to their fitness function and are ready to be selected for the next generation. In this work, a stochastic sampling mechanism is adopted, which selects chromosomes according to their selection probability. The optimization process runs as long as a better solution is found, or until some stopping criterion is reached, such as a predetermined number of generations without an improved solution, or a time limit. The iterative sequence followed by the GA is shown in Fig. 2.2.

2.4 Numerical results

In this study the design parameters of a U-OWC are analyzed with the purpose to maximize its performance. Wave data off the coast of Roccella Jonica are considered for the characterization of the site where the U-OWC wave power plant is going to be built. The marina "Porto delle Grazie" of Roccella Jonica is located in the southern part of Italy, in the Ionian Sea. Currently, the basin is protected by a rubble-mound breakwater. A project funded by "Regione Calabria" foresees the expansion of the harbor

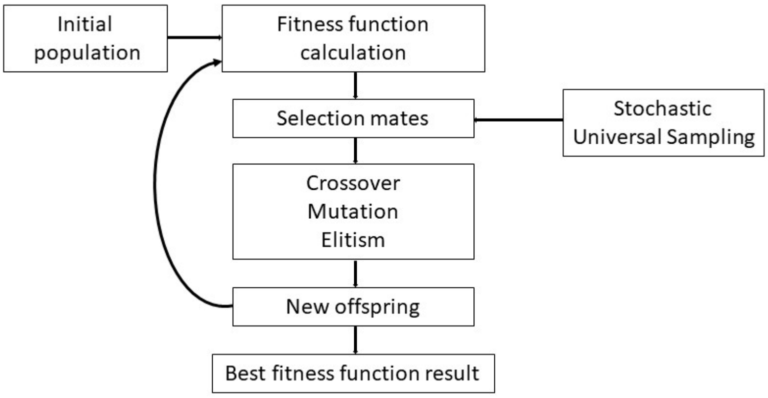

Fig. 2.2: Steps followed by the Genetic Algorithm iterative process

Table 2.2: Lower and upper bounds of the design parameters.

b_1[m]		b_2[m]		l_i[m]		D[m]	
min	max	min	max	min	max	min	max
0.1	4.00	0.1	4.00	0.1	5.00	0.4	1.00

by constructing a breakwater embodying U-OWC type caissons at a water depth of about 7 m with a total length of 20 m. The current layout of the port is shown in Fig. 2.3.

The incident wave power per unit length was first computed by considering a JONSWAP spectral model and by adopting the equation proposed by Arena et al. [86], who expressed the average flux of energy as

$$\Phi = \frac{\rho g^2}{64\pi} \alpha_{f_2} {H_s}^2 T_p, \tag{2.41}$$

where $\alpha_{f_2} = 0.91$ for the mean JONSWAP spectrum. The frequency of occurrence of the sea states is obtained by the UKMO numerical model, which has been used for extrapolating offshore meteorological data. Next, the offshore wave data have been propagated at the U-OWC location via the MIKE21 numerical code. Such a procedure allowed determining a mean available energy of 25675 kWh/m. Further, by analyzing the data with directions ranging from 85° to 225°, the most energetic sea state turned out to be that one coming from 185°, with $H_s = 2.25$ m and $T_p = 6$ s. The performance of a U-OWC depends on some geometrical parameters. Referring to the U-OWC shown in Fig. 2.1, the vector of the design parameters which are considered for the optimization contains 4 elements: b_1, b_2, l_i, D. Specifically, for each element of the vector, a lower and upper bound is given in order to restrict the computation only to reasonable geometrical values and to avoid unfeasible cases. Further, it is introduced the constraint $b_1 + b_2 = 6.00$ m associated with the limited available width of the breakwater layout.

Table 2.2 shows upper and lower bounds of the design variables. The opening of the vertical duct

Fig. 2.3: Aerial view of the current state of the Roccella Jonica Harbour (Courtesy of marina "Porto delle Grazie")

is located 2.00 m below the MWL, that is an effective value for the sea states of the Mediterranean Sea. Nevertheless, the optimization is conducted also for different submergences of the opening under the mean water level. In this regard, note that uncovering periods are accounted for via the cumulative distribution function of the free surface displacement. Specifically, the produced powers are reduced proportionally to the fraction of time in which the water column remains uncovered. The height of the chamber, h_c, is set at 6.00 m above the MWL, consistently with the pre-existing breakwater, while the transversal width of the chamber, b_3, measures 4.00 m, thus covering the total length of the extension with 5 independent chambers. The dimensionless turbine coefficient Λ is set to a constant value of 0.30 and it is supposed connected to a generator with a rated power of 20 kW. The U-OWC caissons will be built at a water depth of 7 m and they will be oriented at 148° with respect to the northern direction. The GA was implemented via the Matlab Optimization Tool. An initial population of 40 vectors was employed. The elite count, that is the number of individuals that survive by default at each iteration, was set to 2. The use of elitism prevents solutions with the fittest values from being left out by the stochastic selection process. A fraction of 0.8 of the population, after excluding the elite children, was established to undergo the crossover operator. The remaining individuals are subjected to mutation. A validation of the GA method applied to a U-OWC and the results of the two cases are depicted in the following sections.

2.4.1 Validation through Parameter Sweep

Initially, a comparison between the results of the proposed method and the global maximum of the power produced by the turbine obtained by investigating all possible configurations was considered in order to evaluate the reliability and the accuracy of the GA algorithm. For this purpose, three geometrical parameters were considered, b_1, l_i and D. Specifically, in each simulation, the value of a parameter was

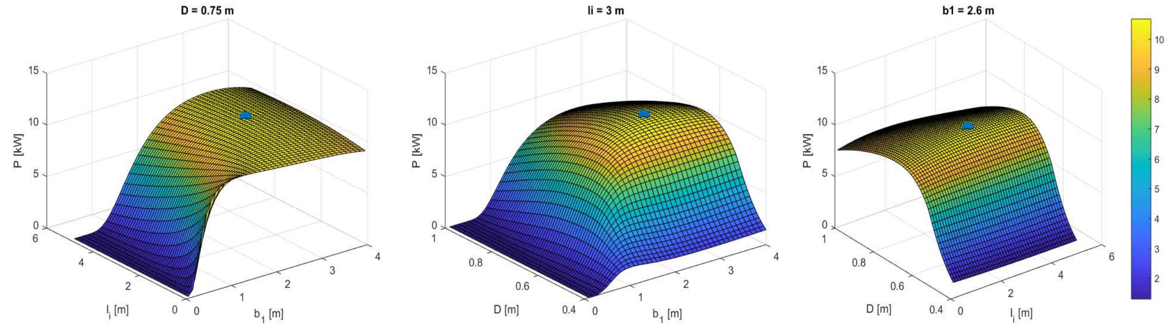

Fig. 2.4: Comparison between the Genetic Algorithm optimal solutions and the parameter sweep results, in terms of power production. From left to right, the surfaces represent the values obtained through the PS for a given value of diameter $D = 0.75\,\text{m}$, of the length of the vertical duct $l_\text{i} = 3\,\text{m}$, and of the width of the vertical duct $b_1 = 2.6\,\text{m}$. The blue round marks identify the global maximum value found by the GA.

held fixed and the computation was carried out by iteratively modifying the remaining two parameters. The vectors b_1 and l_i were computed with a step of 0.1 m, while the diameter D was changed with a step of 0.01 m. Clearly, both the GA and the PS were run under the same domain and over identical grids. Results are shown in Fig. 2.4, where the surfaces represent the power output obtained for each possible combination of the parameters, while the blue round mark on the surface stands for the optimal value found by the Genetic Algorithm. It is seen that the Genetic Algorithm finds the global maximum in any of the three above-mentioned cases.

2.4.2 Sea state based optimization

The optimization of the chamber with respect to a design sea state was first considered [37]. As mentioned previously, it has a significant wave height of 2.25 m, a peak period of 6 s and a direction of 185° with respect to the North. The optimization objective is the maximization of the power produced by the Wells turbine. The experimental curves of Curran and Gato [87] were employed for describing the performance of the turbine. Note that the curves show that the turbine works effectively in a restricted range of pressures. Thus, a variation in the rotational speed should be considered to account for this characteristic. However, in this example, this aspect is not taken into account within the optimization problem. Indeed, the value of the turbine rotational speed, Ω, has been set to a constant value of 3200 rpm for each iteration. The average power converted by the Wells turbine can be calculated, according to the relationship expressed in Ref. [40] and reminding the value of the air mass rate, as

$$P = \frac{\Lambda D}{\Omega \rho_{atm}} \left(\Delta p_0 + m_p\right)^2 . \tag{2.42}$$

Table 2.3: Optimization results

RUN	b_1[m]	b_2[m]	l_i[m]	D[m]	P[kW]	ITER.
$1(\mathrm{h}=-2.00\,\mathrm{m})$	2.80	3.20	3.20	0.69	10.7034	53
$2(\mathrm{h}=-1.50\,\mathrm{m})$	3.00	3.00	3.50	0.71	11.0719	60
$3(\mathrm{h}=-1.00\,\mathrm{m})$	3.20	2.80	3.80	0.74	11.5042	59

Though Genetic Algorithms demonstrated high likelihood to find the best solution in the solution space of an optimization problem with three variables, also in this case a comparison with the parameter sweep was considered. Here again, the GA found the exact global maximum of the power produced by the turbine. The results pertaining to different submergences of the vertical duct opening are listed in Table 2.3. It is seen that, the value of the produced power increases as the submergence of the opening is closer to the mean water level. In particular, the width of the external vertical duct, its length, and the diameter tends to increase as the submergence of the opening decreases, while the width of the inner chamber shows the opposite behavior. The computational time was evaluated and compared. The parameter sweep method took 12 hours, while each optimization of the Genetic Algorithm required a number of generations which varies from 53 to 60 with a time ranging from 47 to 54 minutes employing a function evaluation running in parallel. The saving in terms of time is significant. The algorithm terminated because the average relative change in the best fitness function value was less than or equal to the function tolerance that was set to 10^{-6}.

2.4.3 Wave climate based optimization

Although the previous approach to the optimization problem is rather simple, it does not account for the variability of the whole set of sea states. Thus, another approach was adopted based on the wave climate off the coast of Roccella Jonica. For this purpose, sea states from 15 relevant directions have been considered and sorted according to their significant wave heights and peak periods. A frequency of occurrence, f_o, has been assigned to each direction, from 85° to 225°, and for each $H_\mathrm{s}-T_\mathrm{p}$ pair. The annual incident energy matrix is achieved by multiplying each frequency of occurrence by the average flux of energy (Table 2.4). The objective function for this optimization problem is the maximization of the annual energy produced by the U-OWC converter expressed as follows

$$\max\left(\sum_i\sum_j P_{i,j} f_{o_{i,j}}\Delta t\right) \tag{2.43}$$

where the subscrits i, j denote a specific sea state, and Δt is the number of hours in a year. For each sea state a constant turbine rotational speed, Ω, was adopted and set to 3200 rpm. This is a rotational speed limit allowed by the commercial electrical generators related to maximum centrifugal stresses. The

Table 2.4: Annual incident energy matrix. The values are expressed in kWh/m

T_p[s] / H_s[m]	0.25	0.75	1.25	1.75	2.25	2.75	3.25	3.75	TOT
3	9.7	389.8	0	0	0	0	0	0	399.5
4	0	336.2	298.2	0	0	0	0	0	634.5
5	0	0.4	2076.9	892.6	0	0	0	0	2969.9
6	0	0	109.1	197.3	5568.1	0	0	0	5874.5
7	0	0	0	5.6	0.8	366.6	10768.8	0	11141.9
8	0	0	0	0	0	0	2.8	4652.6	4655.4
TOT	9.7	726.4	2484.3	1095.5	5568.9	366.6	10771.6	4652.6	25675.7

Table 2.5: Optimization values for wave climate approach

RUN	b_1[m]	b_2[m]	l_i[m]	D[m]	E[kWh]	ITER.
A($\mathrm{h} = -2.00\,\mathrm{m}$)	2.50	3.50	1.60	0.67	22371.9	60
B($\mathrm{h} = -1.50\,\mathrm{m}$)	2.60	3.40	1.80	0.68	24046.5	55
C($\mathrm{h} = -1.00\,\mathrm{m}$)	2.70	3.30	2.20	0.70	25906.9	62

optimization based on wave climate was carried out for the above-mentioned three cases of the vertical duct opening submergence. The values of the design parameters and of the objective function resulting from the computation are listed in Table 2.5.

The optimization processes terminated after a number of generations between 55 and 62, which required approximately from 8 to 9 hours. Here again, the trend of b_1, b_2, l_i and D is confirmed, noting that the width of the vertical duct, its length and the diameter increase their values with the reduction of the submergence of the vertical duct opening. This is essentially due to the fact that mild sea states are prevailing in the Roccella Jonica wave climate. Therefore, a submergence located in close proximity to the mean water level, that is 1 m below the water surface, encourages wave energy absorption from smaller sea states.

2.4.4 Comparison

A comparison was proposed between the two methods. For this purpose, the parameters of the sea state based optimization are utilized for estimating the average annual energy produced by the plant. As an example, the set of design parameters obtained with RUN number 1 was considered (see Table 2.3). In this numerical example the average annual wave energy was 21437 kWh against 22371.9 kWh produced by taking into account the wave climate optimization, as shown in Table 2.5. The optimization based on a wave climate guarantees obviously better performances as it takes into account the variability of the whole set of sea states. Indeed, the optimization based on the wave climate increases the power production by 4.36 %. However, this small difference makes the algorithm based on the design sea state a good option when a faster computation is required.

Chapter 3

Power take-off selection for the U-OWC wave power plant of Roccella Jonica

3.1 Introduction

The importance of wave energy as an alternative renewable source of energy was put in evidence in Ref. [13]. The global wave energy resource available in the oceans is estimated to be about 2.11 TW/yr [11]. A wide variety of devices with different working principles were designed and tested by companies and research institutions to convert wave energy into electrical energy [4]. Only a few concepts successfully reached the full-scale deployment.

Even though there is no clear convergence towards a specific technology [88], wave energy converters (WECs) based on the oscillating water column (OWC) principle are showing robustness in the harsh marine environment and good efficiency in absorbing the energy delivered by the incoming waves [89]. OWCs are versatile devices that can be employed in floating offshore plants [47, 41], in nearshore/shoreline installations [29, 28] or embedded in vertical breakwaters [90, 66, 34, 91, 92], thus sharing the cost with the coastal protection structure.

Extensive descriptions of the various OWC configurations and implementations can be found in [5, 6]. One of the main advantages of OWCs is their simple operating principle. An OWC comprises a hollow structure open to the sea at its submerged part. Air enclosed above the inner free surface is alternately compressed and decompressed by wave action. The resulting pressure difference between the inner air and the atmosphere is used to drive an air turbine.

In 2003 Boccotti [37] proposed a new configuration of the OWC structure whose submerged opening faces upwards rather than downwards horizontally, leading to the so-called U-OWC. This configuration allows a longer water column and consequently a lower resonant frequency, without the penalty of a deeply submerged opening. Performance gains in the wave-to-pneumatic power can be achieved by matching the resonance frequency to the wave climate of the deployment site [59, 93]. The first full-scale U-OWC plant was built in the Mediterranean Sea by integrating the caissons on a vertical breakwater in the harbour of Civitavecchia, Italy [63]. The numerical model of the U-OWC was validated through small-scale field experiments [60, 61, 62].

The Wells turbine, with several variants, is the most frequently used turbine in OWC applications [52, 94, 95, 96, 7, 5, 97, 98]. The Wells turbine is characterized by a narrow operating range that ensures high efficiencies. Two or more rotor blades planes (biplane or multi-plane turbines) should be considered for OWCs operating with relatively large pressure heads [53, 99]. Alternatively, axial impulse turbines [56] were also studied and tested in OWC devices [100, 101]. These turbines do not show the hard-stall characteristics of the Wells turbine but have the disadvantage of significant losses in the exit guide-vanes [98]. A new impulse turbine of radial-flow type was developed to overcome the shortcomings of the Wells and axial impulse turbines [8]. Recently, a new type of PTO based on dielectric elastomeric generators was tested on a small U-OWC model [102].

OWC-breakwater converters may be located in highly energetic oceanic areas as is the case of Mutriku [103, 34]. This solution can also be interesting in less energetic regions as is the case of the Mediterranean Sea. In Italian coastal areas, the average wave energy flux ranges from about 3 kW/m in the Ionian and the Adriatic Seas to 12 kW/m in the western coast of Sardinia [104].

The objective of this chapter is to assess the viability of installing OWCs in areas of low wave energy. The present case study is a U-OWC type caisson embedded in a breakwater in a marina in the Ionian Sea, Italy. The construction of the wave power plant is motivated by the need to expand the existing harbour basin for touristic purposes. In this context, the challenge is to identify the optimal PTO system from a technical perspective.

A large variability characterizes the wave climate off Roccella Jonica coast in terms of energy availability and frequency of occurrence. The prevailing of sea states of low energy content are interspersed with Mediterranean storms. These storms are mild in comparison with the more severe Atlantic storms and they occur during the winter season. Despite their relatively rare occurrence, the energy from these storms represents a considerable fraction of the total annual wave energy. The PTO system to be installed at the Roccella Jonica U-OWC has to effectively harvest energy in this wave climate, where the turbine closure time usually associated with storms needs to be minimized. The implementation of algorithms for the turbine rotational speed control was proposed by several authors to significantly improve the efficiency of a OWC wave power plant according to different strategies [105, 106, 107, 108].

The instantaneous rotational speed of the turbine may be regulated through the generator electromagnetic torque only in sea states with small energy content. In Mediterranean storms, the generator rated power may not be sufficient to limit the rotational speed of the PTO system. The OWCs are one of the few wave energy converters where it is rather simple to dissipate energy. The easiest solution is to install a bypass relief pressure valve in parallel with the turbine [109, 110, 111]. Another option only available to the biradial turbine, is the use of a high-speed safety valve (HSSV) installed in series with the turbine. The valve can be operated in a on/off mode [112] or using a sophisticated and promising control type called peak-shaving [113].

The contribution of this work is to select and effectively operate the PTO of an OWC wave power plant in a wave climate with high peak-to-annual average wave power, minimizing the need to turn off the plant for safety reasons. The work was divided into the following tasks:

- assess the Roccella Jonica wave power plant performance;
- explore a configuration with several chambers sharing a turbine to reduce PTO costs;
- select the turbine diameter and generator rated power for a Wells turbine and a biradial turbine;
- control the rotational speed of both types of turbines under mild Mediterranean storm conditions;
- evaluate the effect of using multistage Wells turbine configurations to cope with the over-speed problem;
- assess the effectiveness of introducing a bypass relief valve system to control the PTO rotational speed;
- performance comparison of multi-stage Wells turbines with a biradial turbine satisfying the imposed rotational speed constraints;
- technical selection of the optimal power take-off system.

The economic feasibility analysis of the selected PTO configurations was out of scope of the present study.

The work is organized as follows. The description of the U-OWC wave power plant and the wave climate is reported in Section 3.2. The U-OWC governing equations are presented in Section 3.3, while Section 3.4 is devoted to the model of the turbine/generator set. Results of the power plant performance are presented and discussed in Section 3.5.

3.2 Case study: Roccella Jonica U-OWC breakwater

This section provides a description of the U-OWC breakwater project for the Roccella Jonica marina and a detailed analysis of the local wave climate.

Fig. 3.1: Aerial view of Roccella Jonica marina showing the planned location of the U-OWC breakwater. Courtesy of Marina di Roccella - Porto delle Grazie S.r.l..

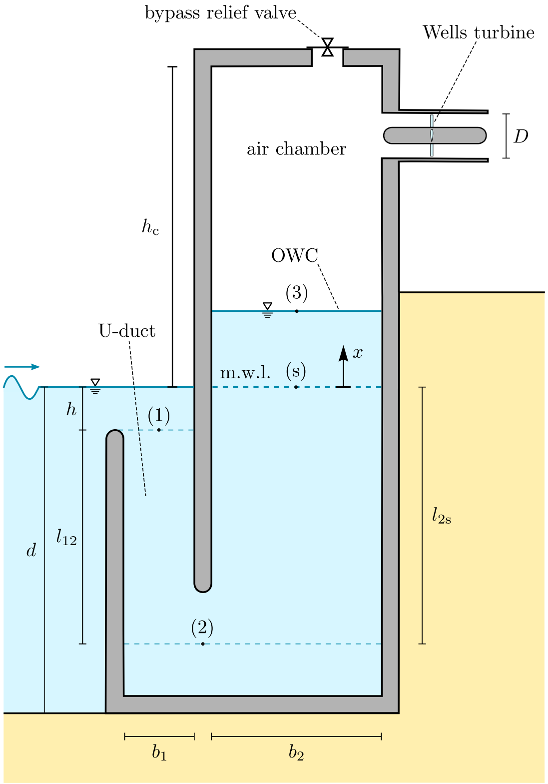

Fig. 3.2: Schematic cross section view of one of the chambers of the Roccella Jonica wave power plant with a Wells turbine installed.

3.2.1 U-OWC plant overview

Roccella Jonica is a small village of the province of Reggio Calabria (Italy), facing the Ionian Sea. The case study for this work is represented by the marina “Porto delle Grazie” whose docks are protected by a rubble-mound breakwater. The aerial picture shows the current status and configuration of the harbour (Fig. 3.1). A forthcoming expansion of the current breakwater is planned to increase the harbour receptivity. The project includes the adoption of two U-OWC caissons to be embedded on the new breakwater.

Each caisson has an overall length of about 15 m and is designed to incorporate four chambers: two central chambers with a transverse width $b_3 = 3.20\,\mathrm{m}$ and two side-chambers 3.15 m wide. The U-OWCs

Table 3.1: Sea states representing Roccella Jonica local wave climate [10].

n_{ss} -	H_{s} [m]	T_{p} [s]	$\hat{P}_{\text{wave}}$ [kW/m]	f_{o} [%]	$\hat{P}_{\text{wave}}\, f_{\text{o}}$ [kW/m]
1	0.25	3	0.1	2.55	0.002
2	0.75	3	0.7	10.81	0.079
3	0.75	4	1.1	6.17	0.065
4	1.25	4	2.9	1.37	0.040
5	1.25	5	3.9	10.08	0.388
6	1.25	6	4.6	0.67	0.031
7	1.75	5	7.5	1.82	0.138
8	1.75	6	9.1	0.30	0.027
9	1.75	7	10.3	0.01	0.001
10	2.25	6	15.0	5.53	0.830
11	2.75	7	25.4	2.48	0.631
12	3.25	7	35.5	1.65	0.585
13	3.75	8	51.5	1.16	0.596

are constrained to have a total width of about 6 m to respect the existing breakwater layout. Indeed, the vertical duct has a width $b_1 = 2$ m, while the inner chamber width is $b_2 = 4$ m (Fig. 3.2). The top of the air chambers is positioned at a height $h_{\text{c}} = 5.5$ m above the mean water level. Besides, the vertical duct has a length $l_{12} = 3.95$ m and its opening is located at a distance $h = 2$ m below the mean water level to allow a continuous absorption of the power of the incoming waves during a variety of different sea states, thus avoiding time intervals during which the duct opening could remain uncovered. The turbines are installed inside a duct with a diameter D, located at the top of the air chambers. The caissons are to be installed at a water depth $d = 7.2$ m from the mean water level. The tide amplitude at Roccella Jonica does not exceed 0.3 m.

3.2.2 Wave climate off Roccella Jonica coast

The wave resource for the Roccella Jonica power plant was obtained from offshore meteorological data, processed and propagated to the coastal area by using the numerical code MIKE21 SW [10]. The wave resource was described by a discrete spectrum composed of N components of frequency ω_m. The mean energy flux per unit crest length is given by [114]

$$\hat{P}_{\text{wave}} = \frac{1}{2}\rho_{\text{w}} g \sum_{m=1}^{N} A_m^2 \frac{c_m}{2}\left(1+\frac{2k_m d}{\sinh(2k_m d)}\right), \tag{3.1}$$

with A_m the wave amplitudes, c_m the phase speed, k_m the wave number and d the water depth. The wave climate of interest for electricity production is represented by 13 sea states characterized by a significant wave height H_{s}, a peak wave period T_{p} and a frequency of occurrence f_{o}, Table 3.1. These sea states contribute to the annual average energy flux per unit crest length for 3.41 kW/m. It should be noted that

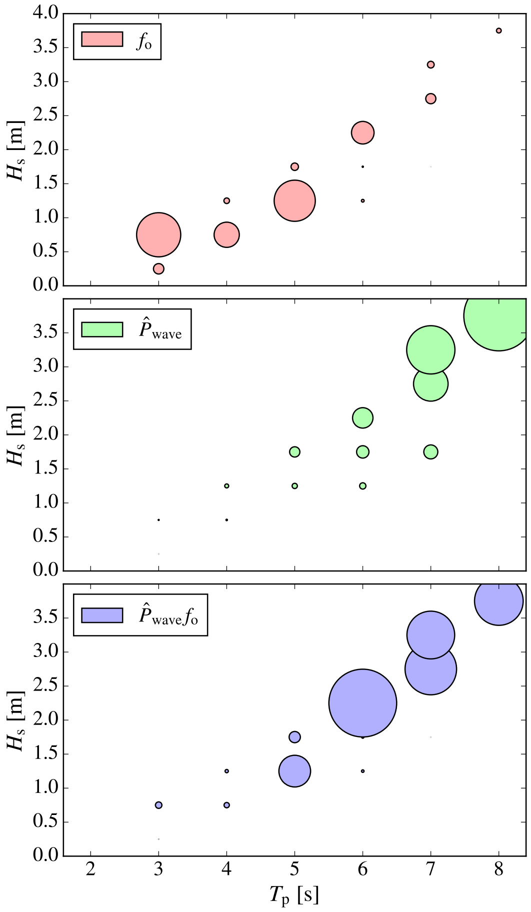

Fig. 3.3: Frequency of occurrence f_o, wave power per unit crest length $\hat{P}_{wave}$, and $\hat{P}_{wave} f_o$, for each sea state, versus significant wave height H_s and peak wave period T_p. The size of the bubbles is proportional to the values of the variables presented in Table 3.1.

the sum of the frequencies of occurrence related to the considered sea states is 44.6%. The other sea states, not included here, have directions such that they do not affect the power plant or whose frequency of occurrence is negligible.

The site of Roccella Jonica is characterized by a wave climate with predominant sea states where the significant wave heights are smaller than 1.75 m. However, the energy associated with these sea states is relatively small in comparison with the annual averaged power. On the other hand, sea states with H_s between 2.25 and 3.75 m and T_p between 6 and 8 s occur less frequently but represent a large share of the energy. The flux of energy per unit crest length and the relative frequency of occurrence for each sea state can be observed in Fig. 3.3.

3.3 U-OWC governing equations

3.3.1 U-OWC model

The free surface motion inside the air chamber was modelled applying the extended Bernoulli equation for unsteady flow between section (1), located at the opening of the U-duct, and section (3), on the inner free surface, Fig. 3.2.

$$\int_1^3 \rho_\mathrm{w} \frac{\partial v}{\partial t} \mathrm{d}s + \frac{1}{2}\rho_\mathrm{w}\left(v_3^2 - v_1^2\right) + (p_3 - p_1) + \rho_\mathrm{w} g\,(x_3 - x_1) + \Delta p_\mathrm{loss} = 0, \tag{3.2}$$

where v is the velocity, p is the pressure, x is the vertical position with respect to the mean water level, ρ_w is the water density, g is the acceleration due to gravity and Δp_loss are the pressure losses between the duct and the chamber. The integral can be split into two terms by considering the intermediate section (2) at the interface between the U-duct and the chamber

$$\int_1^2 \rho_\mathrm{w} \frac{\partial v}{\partial t} \mathrm{d}s + \int_2^3 \rho_\mathrm{w} \frac{\partial v}{\partial t} \mathrm{d}s + \frac{1}{2}\rho_\mathrm{w}\left(v_3^2 - v_1^2\right) + (p_3 - p_1) + \rho_\mathrm{w} g\,(x_3 - x_1) + \Delta p_\mathrm{loss} = 0. \tag{3.3}$$

Changing from variable v to the volumetric flow rate Q in the OWC, the following result is obtained

$$\frac{1}{A_1}\int_1^2 \rho_\mathrm{w} \frac{\partial Q}{\partial t} \mathrm{d}s + \frac{1}{A_3}\int_2^3 \rho_\mathrm{w} \frac{\partial Q}{\partial t} \mathrm{d}s + \frac{1}{2}\rho_\mathrm{w}\left(\frac{Q^2}{A_3^2} - \frac{Q^2}{A_1^2}\right) + (p_3 - p_1) + \rho_\mathrm{w} g\,(x_3 - x_1) + \Delta p_\mathrm{loss} = 0, \tag{3.4}$$

where $A_1 = b_1 b_3$ and $A_3 = b_2 b_3$ are the cross sectional areas of the vertical duct and the inner chamber, respectively. Denoting by l_{12} the vertical distance from section (1) to section (2), and by $l_{2\mathrm{s}} + x_3$ the vertical distance between section (2) and section (3) (Fig. 3.2), results in

$$\tilde{m}\dot{Q} + \beta Q^2 + (p_3 - p_1) + \rho_\mathrm{w} g\,(x_3 - x_1) + \Delta p_\mathrm{loss} = 0, \tag{3.5}$$

with

$$\tilde{m} = \rho_\mathrm{w}\left(\frac{l_{12}}{A_1} + \frac{l_{2\mathrm{s}} + x_3}{A_3}\right), \tag{3.6}$$

$$\beta = \frac{1}{2}\rho_\mathrm{w}\left(\frac{1}{A_3^2} - \frac{1}{A_1^2}\right). \tag{3.7}$$

The pressure at section (1) is expressed by

$$p_1 = p_\mathrm{atm} + \rho_\mathrm{w} g h - \rho_\mathrm{w} \frac{\partial \phi}{\partial t}, \tag{3.8}$$

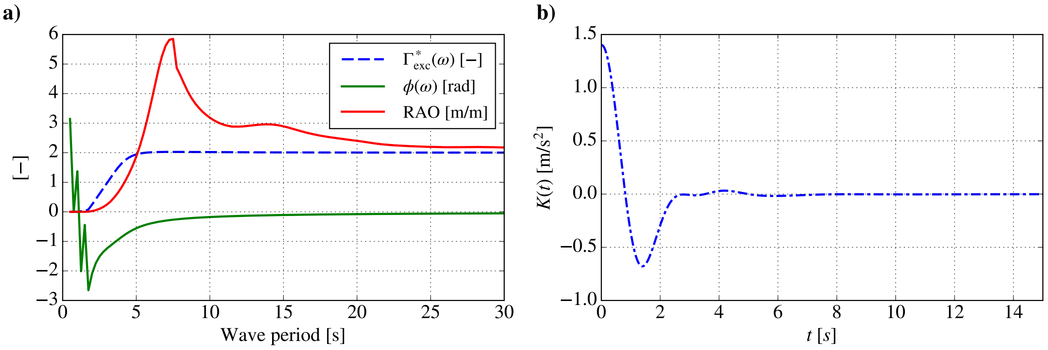

Fig. 3.4: a) Dimensionless excitation pressure, $\Gamma^*_{\mathrm{exc}}(\omega) = \Gamma_{\mathrm{exc}}(\omega)/(\rho_{\mathrm{w}} g)$, excitation pressure phase, $\phi(\omega)$, response amplitude operator (RAO) of the water column. b) Kernel of the convolution integral $K(t)$.

where

$$\rho_{\mathrm{w}} \frac{\partial \phi}{\partial t} = \frac{\rho_{\mathrm{w}} H_\infty}{A_1} \dot{Q} + \frac{\rho_{\mathrm{w}}}{A_1} \int\limits_{-\infty}^{t} K(t-\tau)\, Q(\tau)\, \mathrm{d}\tau - p_{\mathrm{exc}}. \tag{3.9}$$

Here H_∞ is the additional length at infinite frequency (related to the added mass), $K(t-\tau)$ is the retardation function, and p_{exc} is the excitation pressure computed at the centre of the U-duct opening in a diffracted wave field. For irregular waves the excitation pressure is computed from

$$p_{\mathrm{exc}} = \rho_{\mathrm{w}} g \ell \sum_{m=1}^{N} A_m(\omega_m)\, \Gamma^*(\omega_m) \sin(\omega_m t + \phi(\omega_m)). \tag{3.10}$$

where $A_m(\omega_m)$ and ω_m are the wave amplitudes and frequencies, respectively; ℓ is the characteristic length of the device, here equivalent to the air chamber width. The values ϕ, Γ^* and $K(t)$ were taken from [62] and plotted in Fig. 3.4. The response amplitude operator for the wave power is also plotted in Fig. 3.4 a).

Substitution of (3.8) and $x_1 = -h$ into (3.5) yields

$$\begin{aligned} &\tilde{m}\dot{Q} + \beta Q^2 + (p_3 - p_{\mathrm{atm}}) + \tilde{m}_\infty \dot{Q} \\ &\qquad + \frac{\rho_{\mathrm{w}}}{A_1} \int\limits_{-\infty}^{t} K(t-\tau)\, Q(\tau)\, \mathrm{d}\tau - p_{\mathrm{exc}} + \rho_{\mathrm{w}} g x_3 + \Delta p_{\mathrm{loss}} = 0, \end{aligned} \tag{3.11}$$

where

$$\tilde{m}_\infty = \frac{\rho_{\mathrm{w}} H_\infty}{A_1} + C_{\mathrm{a}} \tilde{m}. \tag{3.12}$$

The second term on the right-hand-side of (3.12) was introduced to tune the numerical method with experimental data [115], where C_{a} is an added mass coefficient. The pressure losses Δp_{loss} between sections (1) and (3) were modelled as

$$\Delta p_{\mathrm{loss}} = \alpha \,\mathrm{sign}(Q)\, Q^2, \tag{3.13}$$

with

$$\alpha = C_{\mathrm{d}}\, \rho_{\mathrm{w}} \left(\frac{(b_1 + b_3)\, l_{12}}{A_1^3} + \frac{(b_2 + b_3)\,(l_{2\mathrm{s}} + x_3)}{A_3^3} \right), \tag{3.14}$$

where C_{d} is a loss coefficient. Substituting pressure losses in (3.11), the equation of motion for the OWC is

$$(\tilde{m} + \tilde{m}_{\infty})\, \dot{Q} + (\alpha \,\mathrm{sign}(Q) + \beta)\, Q^2 + \Delta p + \frac{\rho_{\mathrm{w}}}{A_1} \int_{-\infty}^{t} K(t-\tau)\; Q(\tau)\, \mathrm{d}\tau + \rho_{\mathrm{w}} g x_3 - p_{\mathrm{exc}} = 0, \tag{3.15}$$

where $p_3 - p_{\mathrm{atm}} = p - p_{\mathrm{atm}} = \Delta p$. The dimensionless coefficients $C_{\mathrm{d}} = 0.46$ and $C_{\mathrm{a}} = 0.19$ were calibrated through experimental results [115]. β and α are coefficients related to kinetic energy and pressure losses between the U-duct and the inner chamber.

The volumetric flow rate associated with the OWC displacement Q is related to the time rate change of the chamber volume through

$$\dot{V}_{\mathrm{c}} = -Q. \tag{3.16}$$

where $V_{\mathrm{c}} = A_3\,(h_{\mathrm{c}} - x_3)$ is the instantaneous air chamber volume. Dots denote derivative with respect to time.

3.3.2 Air chamber model

The system of equations described in (3.15) and (3.16) for the oscillating water column dynamics is coupled to the air chamber equation through the pressure. The process of compression and expansion of the air in the chamber is assumed isentropic, which is a good approximation as showed in [116],

$$\rho_{\mathrm{c}} = \rho_{\mathrm{atm}} \left(\frac{p}{p_{\mathrm{atm}}} \right)^{\frac{1}{\gamma}}, \tag{3.17}$$

where ρ_{c} denotes the air density inside the chamber, ρ_{atm} is the air density in the atmosphere, and γ is the specific heats ratio.

The air chamber modelling is derived by applying a mass balance, resulting in

$$\dot{p} = -\gamma p \left(\frac{\dot{m}_{\mathrm{turb}}}{m_{\mathrm{c}}} + \frac{\dot{V}_{\mathrm{c}}}{V_{\mathrm{c}}} \right), \tag{3.18}$$

where $\dot{m}_{\text{turb}}$ is the air mass flow rate through the turbine, while $m_{\text{c}} = \rho_{\text{c}} V_{\text{c}}$ is the air mass [35].

3.4 Turbine and generator model

Dimensional analysis was used to model the performance of the air turbines [117]. For low blade-tip Mach numbers Ma_{tip}, the air compressibility effects can be ignored as shown in [118]. As discussed in [119], the viscous effects on turbine performance are independent of the Reynolds number based on the blade tip velocity if $\text{Re} > 10^6$. In this case, the performance characteristics of air turbines can be represented in a dimensionless form as

$$\Psi = \frac{\Delta p}{\rho_{\text{in}}\,\Omega^2 D^2}, \tag{3.19}$$

$$\Phi = \frac{\dot{m}_{\text{turb}}}{\rho_{\text{in}}\,\Omega D^3}, \tag{3.20}$$

and

$$\Pi = \frac{P_{\text{turb}}}{\rho_{\text{in}}\,\Omega^3 D^5}, \tag{3.21}$$

where Ψ, Φ and Π are the dimensionless pressure head, flow rate and power, respectively. Here, Ω is the turbine rotational speed (radians per unit time), P_{turb} is the turbine power output, while ρ_{in} is the stagnation air density at the turbine inlet

$$\rho_{\text{in}} = \begin{cases} \rho_{\text{c}}, & \text{if } p \geq p_{\text{atm}}, \\ \rho_{\text{atm}}, & \text{if } p < p_{\text{atm}}. \end{cases} \tag{3.22}$$

Flow rate and power coefficients may be expressed as a function of Ψ, i.e., $\Phi(\Psi)$ and $\Pi(\Psi)$. In the case of symmetrical turbines, $\Pi(\Psi)$ is an even function while $\Phi(\Psi)$ is an odd function.

The rotational speed model for the turbine/generator set is

$$\frac{\text{d}}{\text{d}t}\left(\frac{1}{2} I \Omega^2\right) = P_{\text{turb}} - P_{\text{ctrl}}, \tag{3.23}$$

where I is the moment of inertia of the rotating components, and P_{ctrl} the generator electromagnetic power.

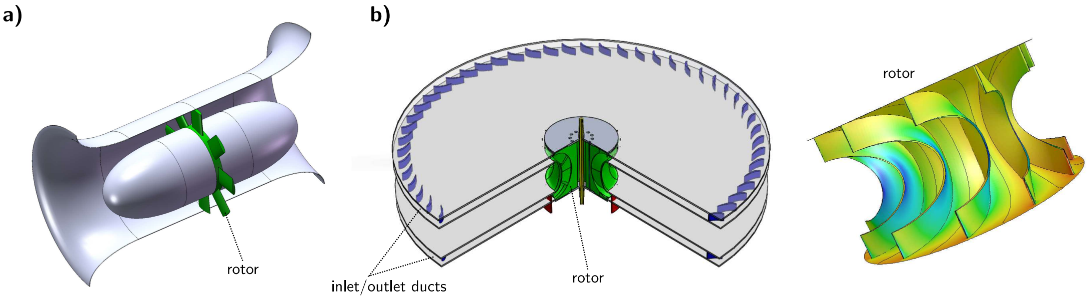

Fig. 3.5: a) The Wells turbine and b) the biradial turbine. From [9].

The turbine power may be written as

$$P_{\text{turb}} = \rho_{\text{in}}\,\Omega^3 D^5\,\Pi(\Psi). \tag{3.24}$$

The turbine efficiency is defined as

$$\eta_{\text{turb}} = \frac{P_{\text{turb}}}{P_{\text{pneu}}} = \frac{\Pi(\Psi)}{\Phi(\Psi)\,\Psi}, \tag{3.25}$$

where $P_{\text{pneu}} = \Delta p\, Q_{\text{turb}}$ is the available pneumatic power and $Q_{\text{turb}} = \dot{m}_{\text{turb}}/\rho_{\text{in}}$ is the turbine volumetric flow rate.

Two types of turbines were considered: the Wells turbine and the biradial turbine. The Wells turbine rotor consists of a set of blades symmetrical about a plane normal to its rotation axis, producing a unidirectional time-averaged torque from a reciprocating axial air flow without the need of a rectifying valve system, Fig. 3.5 a). The biradial turbine is another type of self-rectifying impulse turbine symmetrical with respect to a plane perpendicular to its axis of rotation, where the inlet flow is centripetal while the outlet flow is centrifugal, Fig. 3.5 b).

The Wells turbine used in this work is a monoplane proposed and tested at University of Siegen and code named rotor B [120]. The stall characteristics of this specific turbine appear in [98], where several turbines, with and without guide vanes, with axial and radial flow, are studied and compared for OWC devices. The biradial turbine dimensionless performance curves are the same as the ones obtained in [113], without the built-in high-speed safety valve. The performance curves of both turbines can be observed in Fig. 3.6. This figure shows that the biradial turbine operates with higher efficiency at lower rotational speed in comparison with the Wells turbine. Besides, stall flow on rotor blades is observed for the Wells turbine at low rotational speed (large values of Ψ).

The turbine power at the best efficiency point (bep) is given by

$$P_{\text{turb}}(\Omega) = a_{\text{bep}}\,\Omega^3. \tag{3.26}$$

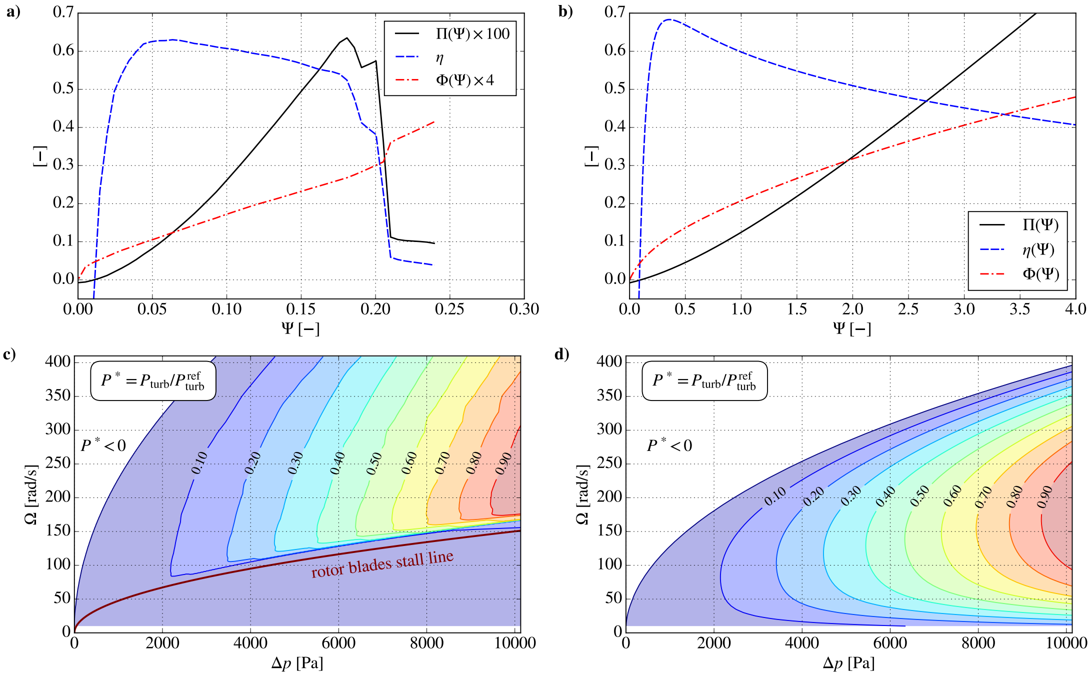

Fig. 3.6: Performance curves for a) the monoplane Wells turbine ($D = 1.20\,\mathrm{m}$) and b) the biradial turbine ($D = 0.70\,\mathrm{m}$). Plots c) and d) describe the dimensionless turbine power output, $P^* = P_{\text{turb}}/P_{\text{turb}}^{\text{ref}}$, versus the pressure head Δp and rotational speed Ω. The reference value $P_{\text{turb}}^{\text{ref}}$ is the maximum turbine power within the plot limits.

where $a_{\text{bep}} = \rho_{\text{in}} D^5 \Pi\left(\Psi_{\text{bep}}\right)$ may be considered approximately constant if the variations in the inlet air density are small, $\rho_{\text{in}} \approx \rho_{\text{atm}}$. The following generator control law was proposed by [121]

$$P_{\text{gen}} = a_{\text{bep}}\,\Omega^3, \tag{3.27}$$

that was also employed in this work (see [35] for further details). To prevent exceeding the generator rated power, $P_{\text{gen}}^{\text{rated}}$, a restriction was introduced

$$P_{\text{ctrl}} = \min\left(a_{\text{bep}}\,\Omega^3, P_{\text{gen}}^{\text{rated}}\right). \tag{3.28}$$

As a consequence, the model of the dynamics of the turbine/generator set becomes

$$\frac{\mathrm{d}}{\mathrm{d}t}\left(\frac{1}{2}\Omega^2\right) = \frac{1}{I}\left(P_{\text{turb}} - P_{\text{ctrl}}\right). \tag{3.29}$$

3.4.1 PTO maximum rotational speed

The maximum rotational speed in a turbine/generator set is limited by the maximum centrifugal stresses and the maximum Mach number of the flow on rotor blades surface. Off-the-shelf electrical generators are typically limited to $\Omega_\sigma = 314\,\mathrm{rad/s}$ (about 3000 rpm) to withstand the centrifugal stresses on the rotor. The maximum flow Mach number depends on the blade geometry, spanwise section and the

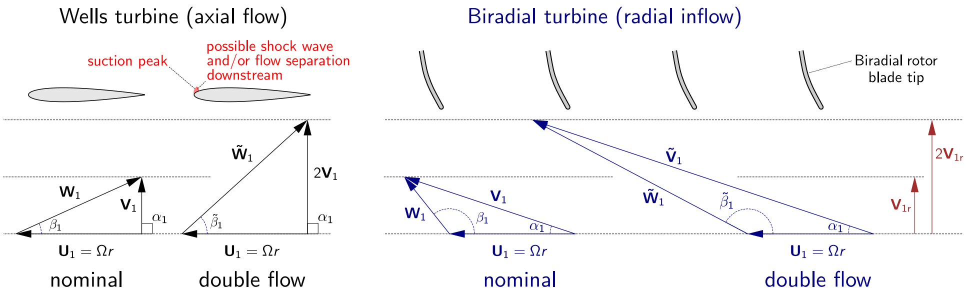

Fig. 3.7: The effect of doubling the flow in the inlet velocity triangle of the Wells turbine and biradial turbine. Here **V** is the absolute velocity, **U** is the transport velocity, **W** is the relative velocity, α is the angle of the absolute velocity, β is the angle of the relative velocity, and r is the radius.

inflow incidence angle.

Fig. 3.7 shows the effect of doubling the flow rate in the inlet velocity triangles of the Wells turbine and biradial turbine. Let us assume that β_1 is the incidence angle at nominal conditions. As found in the figure, the incidence angle changes from β_1 to $\tilde{\beta}_1 \approx 2\beta_1$ on the Wells turbine when doubling the flow rate, Fig. 3.7. This increase of β_1 implies a significant increase of the local velocity which can easily produce transonic flow and large suction peaks that are followed by strong adverse pressure gradients, thus promoting the possible appearance of shock waves [118] and aerodynamic stall. On the other hand, doubling the flow rate in the biradial turbine does not result in a large increase of the inlet angle of β_1, Fig. 3.7. This is the main reason for the smooth decrease of the efficiency of the biradial turbine for large flow rate coefficients in comparison with Wells turbine, Figs. 3.6 a) and b).

In the present work, the blade tip speed was set to $U_{\text{tip}} = \Omega D/2 = 160\,\text{m/s}$, giving a maximum tip Mach number of $\text{Ma}_{\text{tip}} = \Omega D/(2c) = 0.47$, where $c = 340\,\text{m/s}$ is the speed of sound in atmospheric conditions. The maximum rotational speed constrained to the specified Ma_{tip} is

$$\Omega_{\text{tip}}(D) \leq \frac{2c\,\text{Ma}_{\text{tip}}}{D}. \tag{3.30}$$

The rotational speed threshold that respects both the maximum generator rotational speed and the maximum tip Mach number is

$$\Omega_{\text{thr}}(D) = \min\big(\Omega_\sigma, \Omega_{\text{tip}}(D)\big). \tag{3.31}$$

3.5 Numerical results

The performance assessment of the Roccella Jonica U-OWC wave power plant was carried out through numerical simulations performed in time domain, with a time interval of 1800 s for each sea state, and a time-step of $\Delta t = 0.05\,\text{s}$. The 4th order Runge-Kutta was selected for time-integration. The convolution integral was evaluated by applying the trapezoidal rule.

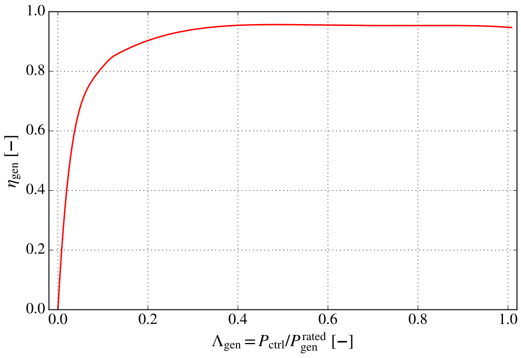

Fig. 3.8: Efficiency curve of the electrical generator as a function of the shaft load Λ. From [9].

The search for the optimal turbine was initially conducted by comparing the performance of the monoplane Wells turbine and the biradial turbine. Preliminary results showed that the rotational speed of the Wells turbine frequently exceeded the limits imposed by centrifugal stresses. To overcome this problem, multistage Wells turbines were considered to accommodate higher total blade solidity (total bladed area divided by the cross-sectional area), specially two and three rotor planes. The dimensionless performance curves for the two- and three-stage Wells turbines were derived from the curves relative to the single rotor, as in [99], by employing the following relations

$$\Phi_{\mathrm{n}}(\Psi) = \Phi\left(\frac{\Psi}{n}\right), \tag{3.32}$$

$$\Pi_{\mathrm{n}}(\Psi) = n\Pi\left(\frac{\Psi}{n}\right), \tag{3.33}$$

$$\eta_{\mathrm{n}}(\Psi) = \eta\left(\frac{\Psi}{n}\right) \tag{3.34}$$

where n is the number of stages. To prevent the efficiency drop due to the multi-stage effects, guide-vanes are required to avoid excessive swirl at turbine exit.

For the Wells turbine, a reference diameter $D_{\mathrm{ref}} = 0.75\,\mathrm{m}$ was assumed, with a reference inertia $I_{\mathrm{ref}} = 1.53\,\mathrm{kg\,m^2}$. The biradial turbine has $D_{\mathrm{ref}} = 0.5\,\mathrm{m}$ and $I_{\mathrm{ref}} = 5.01\,\mathrm{kg\,m^2}$. Both turbine rotors were assumed to be manufactured in marine grade aluminium. In this study, a range of diameters D from 0.6 to 1.4 m was selected for the simulations. By employing geometrical similarity, the turbine rotational inertia is computed as

$$I = nI_{\mathrm{ref}}\left(\frac{D}{D_{\mathrm{ref}}}\right)^5. \tag{3.35}$$

The inertia of the generator rotor was assumed to be negligible in comparison with the turbine rotor inertia.

Several air chamber scenarios were considered for the installation of a single PTO system aiming at maximizing energy production and reducing costs: single chamber; two, three and four connected chambers. For each configuration, three commercial generators were selected with rated powers ranging from 33.5 to 84.0 kW.

The assessment of the PTO performance was carried out by computing the capture width ratio based on the electrical power, $\mathrm{CWR}_{\mathrm{elec}}$, defined as

$$\mathrm{CWR}_{\mathrm{elec}} = \frac{\bar{P}_{\mathrm{elec}}}{\hat{P}_{\mathrm{wave}}\,\ell}, \tag{3.36}$$

where $\ell = b_3\, n_{\mathrm{c}}$ is the characteristic length of the OWC, here assumed equal to the air chamber transverse width b_3 times the number of connected chambers n_{c}, while $\bar{P}_{\mathrm{elec}}$ is the time-averaged electrical power output defined as

$$\bar{P}_{\mathrm{elec}} = \frac{1}{t_{\mathrm{f}} - t_{\mathrm{i}}} \int_{t_{\mathrm{i}}}^{t_{\mathrm{f}}} P_{\mathrm{elec}}(t)\,\mathrm{d}t. \tag{3.37}$$

Here t_{f} concerns the end of the simulations and $t_{\mathrm{i}} > 0$ is selected to minimize the effects of the initial transient on the average electrical power. The instantaneous electrical power output is computed through the generator efficiency, η_{elec}, with

$$P_{\mathrm{elec}}(t) = \eta_{\mathrm{elec}}(\Lambda)\, P_{\mathrm{turb}}(t), \tag{3.38}$$

where $\Lambda = P_{\mathrm{ctrl}}/P_{\mathrm{gen}}^{\mathrm{rated}}$, Fig. 3.8.

3.5.1 Turbine diameter and generator rated power selection without rotational speed constraints

Results for the annual-averaged $\mathrm{CWR}_{\mathrm{elec}}$ are plotted in Figs. 3.9 to 3.12 for each turbine and for the whole set of air chamber configurations, as a function of the rotor diameter and the generator rated power. The markers in the figures denote different maximum rotational speed $\Omega_{\max}$ ranges. The annual-averaged $\mathrm{CWR}_{\mathrm{elec}}$ is computed as a weighted sum of the time-averaged electrical power output of each of the 13 sea states that define the wave climate of Roccella Jonica, Table 3.1.

Results of the single-stage Wells turbine for a set of connected chambers $n_{\mathrm{c}} \in \{1,2,3,4\}$ are shown in Fig. 3.9. For all the cases, the optimal $\mathrm{CWR}_{\mathrm{elec}}$ is obtained for excessive rotational speeds. As an example, in the two chambers $n_{\mathrm{c}} = 2$ scenario the optimum corresponds to $D = 1.00$ m where the maximum rotational speed is achieved for sea state 13, with $\Omega_{\max} = 900$ rad/s for a generator rated power of 84.0 kW. Since the PTO cannot operate above Ω_{thr}, the wave power plant would be inoperative during the most energetic sea states, thus reducing significantly the converted energy. For this reason, the single-stage Wells turbine configuration will be discarded.

The results for the two-stage Wells turbine are depicted in Fig. 3.10. The optimal $\mathrm{CWR}_{\mathrm{elec}}$ is for two connected chambers. A diameter $D = 1.20\,\mathrm{m}$ and a generator rated power of $84\,\mathrm{kW}$ represent a good option for this configuration. For the three-stage Wells turbine, the optimal $\mathrm{CWR}_{\mathrm{elec}}$ is also for two connected chambers but occurs for a larger diameter in comparison with the previous case, Fig. 3.11. A rotor diameter $D = 1.20\,\mathrm{m}$ may be considered an effective solution for the two-chamber scenario. The three-stage Wells turbine did not enhance the performance of the power plant in comparison with the two-stage configuration and this solution was dropped.

The results presented above show that the single-stage Wells turbine has the best damping coefficient, i.e., the higher capture width ratios in comparison with the multi-stage turbines. However, the rotational speed Ω_{max} that occurs for the single-stage Wells turbine is considerably above the safety threshold. The Wells turbine maximum rotational speed decreases with increasing number of turbine stages. This behaviour is a consequence of the reduction in the pressure head per turbine stage.

The biradial turbine is characterized by lower rotational speed and higher efficiency in comparison with the Wells turbine. Results for the biradial turbine for all chamber configurations $n_{\mathrm{c}} \in \{1, 2, 3, 4\}$ are depicted in Fig. 3.12. The biradial turbine is a more complex and expensive turbomachine in comparison with the Wells turbine. Reducing the number of biradial turbines should decrease the initial investment for the power plant. As such, the best trade-off between costs and performance

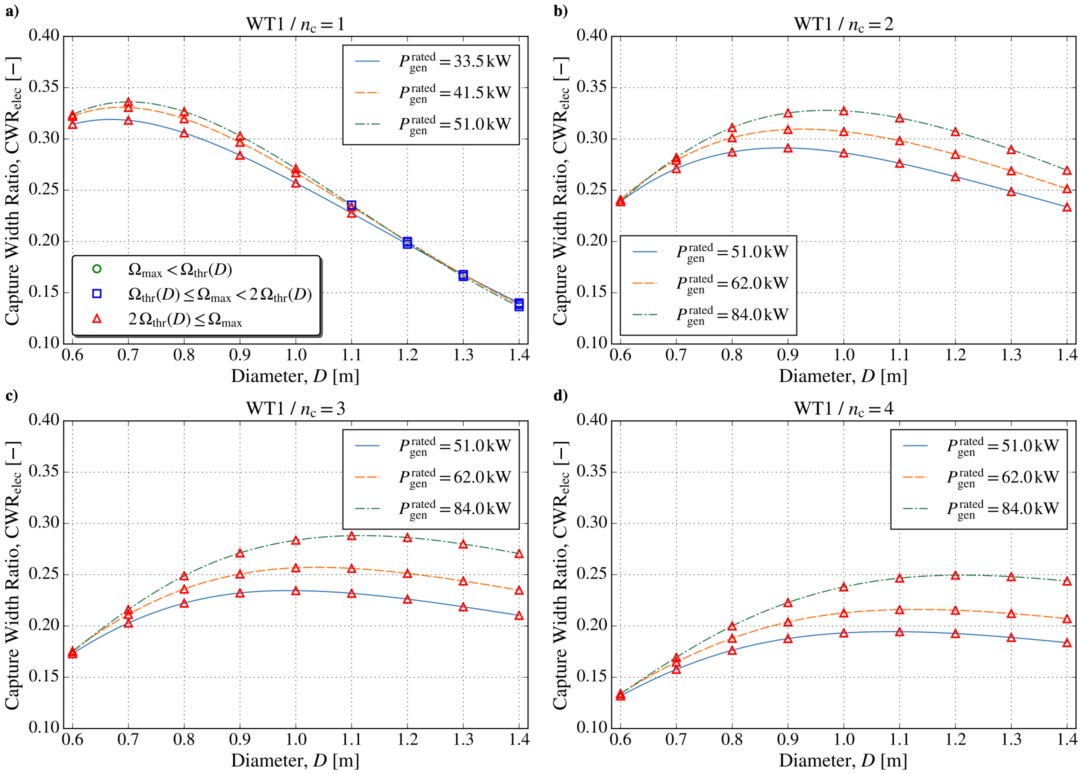

Fig. 3.9: Electrical capture width ratio for the single-stage Wells turbine versus rotor diameter and generator rated power. a) single air chamber, b) two combined air chambers, c) three combined air chambers, and d) four combined air chambers.

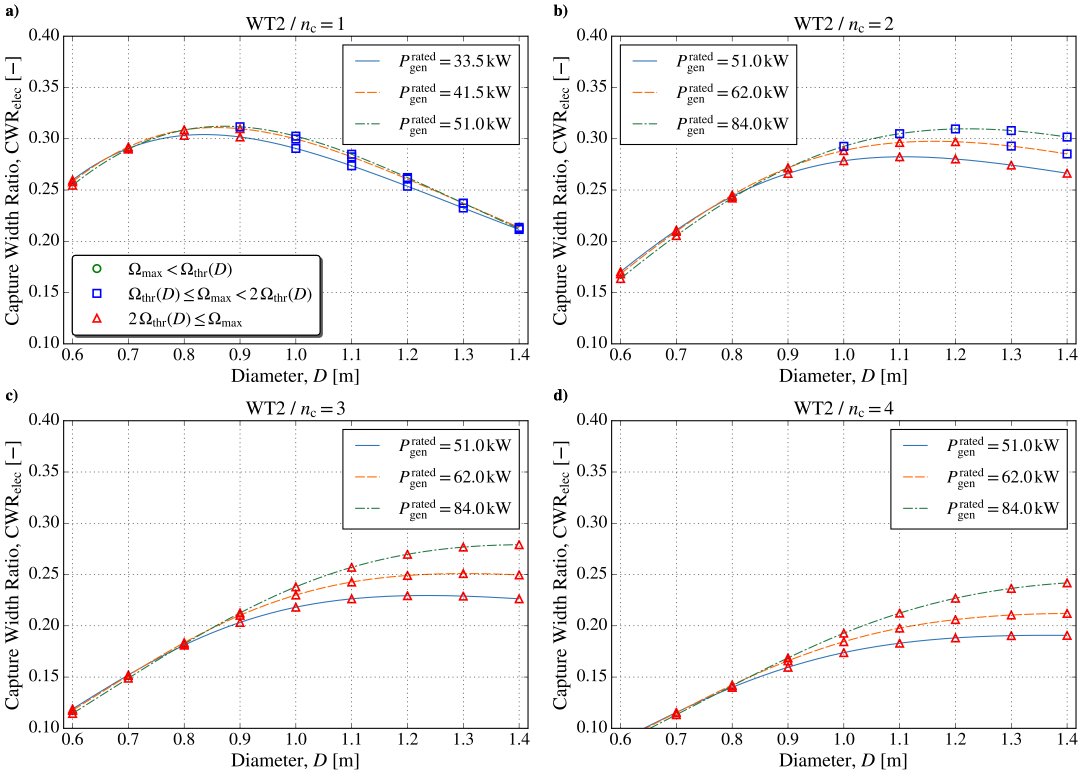

Fig. 3.10: As in Fig. 3.9, for the two-stage Wells turbine.

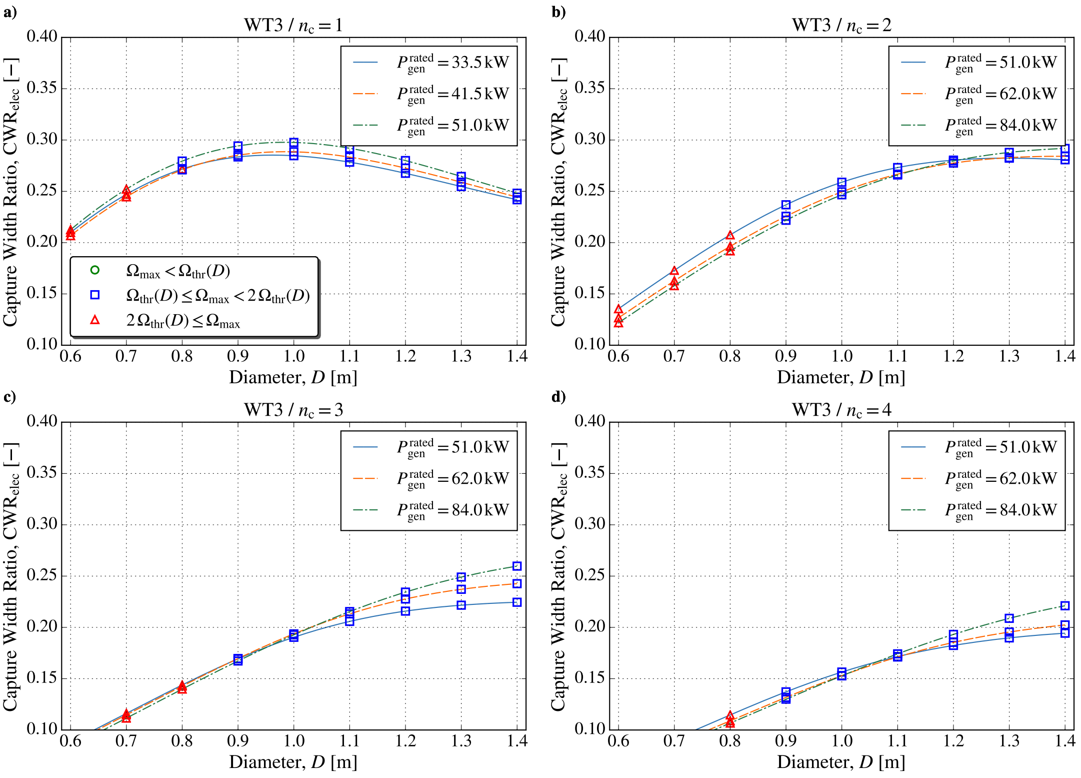

Fig. 3.11: As in Fig. 3.9, for the three-stage Wells turbine.

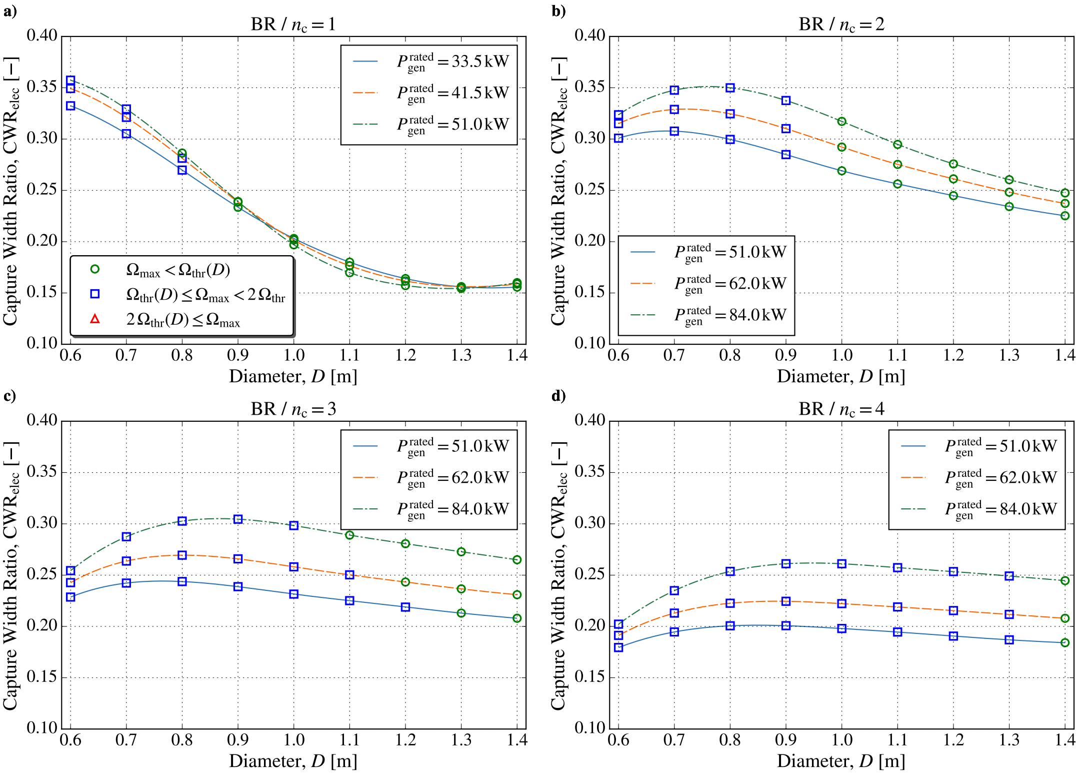

Fig. 3.12: As in Fig. 3.9, for the biradial turbine.

Table 3.2: Optimal rotor diameter and generator rated power for Wells and biradial turbines. Simulations without rotational speed constraints for two connected chambers.

Case	$D\,[\mathrm{m}]$	$P_{\mathrm{gen}}^{\mathrm{rated}}\,[\mathrm{kW}]$	$\mathrm{CWR}_{\mathrm{elec}}$
WT2	1.20	84.0	0.309
WT3	1.20	84.0	0.278
BR	0.70	84.0	0.348

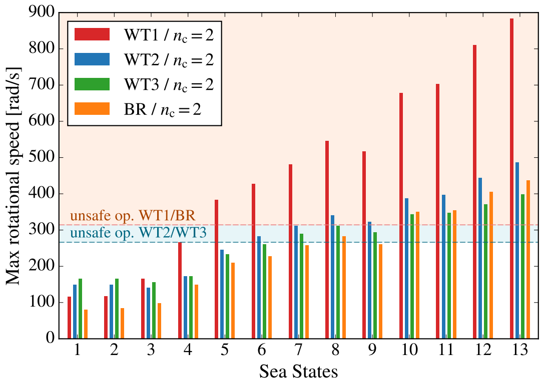

Fig. 3.13: Maximum rotational speed for the single- ($D = 1.00\,\mathrm{m}$), two- ($D = 1.20\,\mathrm{m}$) and three-stage ($D = 1.20\,\mathrm{m}$) Wells turbines and for the biradial turbine ($D = 0.70\,\mathrm{m}$) computed for each sea state. The coloured areas denote unsafe operation. The generator rated power for all cases is $P_{\mathrm{gen}}^{\mathrm{rated}} = 84.0\,\mathrm{kW}$.

should be the two chambers scenario with a rotor diameter $D = 0.70\,\mathrm{m}$ coupled to the 84 kW generator.

The list of the chosen diameters is summarized in Table 3.2 with the corresponding values of electrical capture width ratio. The turbine rotational speed for the selected diameters exceeds the allowed threshold during some sea states. This becomes more apparent in the plot of Fig. 3.13. The areas highlighted in the upper part of the plot represent unsafe operation regions, i.e., above the allowed threshold. In this case, the power plant should be shut down to guarantee the safety of the mechanical components, with consequent significant losses in the energy production.

3.5.2 Turbine diameter and generator rated power selection with a bypass relief valves system

A system of bypass relief valves was employed to allow the wave power plant to operate during highly energetic sea states by limiting the turbine rotational speed. In this section, the appropriate number of valves and the opening sequence are investigated for each turbine.

The opening of the first valve occurs upon reaching a pre-determined threshold of turbine rotational speed $\Omega_{\mathrm{v}}^{\mathrm{open}}$, as shown in Algorithm 1. The valves were actuated in a discrete sequence $[0, v_1, v_2, v_3, v_4]$ based on $\Delta\Omega$. The value of $\Delta\Omega$ depends on the type of the turbine, and is larger for the biradial turbine. It was assumed that the valves open and close instantaneously.

Algorithm 1 Control opening sequence of the relief valves.

```
$\mathbf{s} \leftarrow [0, v_1, v_2, v_3, v_4]$    ▷ zero-based vector with opening sequence of the relief valves
if Wells turbine then
    $\Omega_\mathrm{v}^\mathrm{open} \leftarrow 210\,\mathrm{rad/s}$
    $\Delta\Omega \leftarrow 20\,\mathrm{rad/s}$    ▷ Wells turbine
else
    $\Omega_\mathrm{v}^\mathrm{open} \leftarrow 230\,\mathrm{rad/s}$
    $\Delta\Omega \leftarrow 30\,\mathrm{rad/s}$    ▷ biradial turbine
end if
$n_\mathrm{f} \leftarrow \mathrm{round}\big( \big(\Omega - \Omega_\mathrm{v}^\mathrm{open}\big) / \Delta\Omega \big)$    ▷ rounds to the nearest integer
$n_\mathrm{i} \leftarrow \min(\max(n_\mathrm{f}, 0), 4)$    ▷ limit $n_\mathrm{i}$ to the entries of $\mathbf{s}$
$n_\mathrm{v} \leftarrow \mathbf{s}[n_\mathrm{i}]$    ▷ selects an entry from vector $\mathbf{s}$
```

Table 3.3: Comparison of the optimal rotor diameter and generator rated power for Wells and biradial turbines. Simulations without rotational speed constraints and with relief valves.

Case	D[m]	Ω unconstrained		Relief valves system				$\mathrm{CWR}_\mathrm{loss}$
		$P_\mathrm{gen}^\mathrm{rated}$ [kW]	$\mathrm{CWR}_\mathrm{elec}$	$P_\mathrm{gen}^\mathrm{rated}$ [kW]	$\mathrm{CWR}_\mathrm{elec}$	n_v	$\mathbf{s}$	
WT2	1.20	84.0	0.309	33.5	0.179	6	[0,2,5,6,6]	42%
BR	0.70	84.0	0.348	84.0	0.332	3	[0,1,2,3,3]	5%

In a PTO system with bypass relief valves, the mass flow rate that enters/exits the air chamber is

$$\dot{m}_\mathrm{tot} = \dot{m}_\mathrm{turb} + \dot{m}_\mathrm{v}, \tag{3.39}$$

where $\dot{m}_\mathrm{v}$ is the mass flow rate through the valves

$$\dot{m}_\mathrm{v} = n_\mathrm{v}\,\mathrm{sign}(\Delta p)\,A_\mathrm{v}\,c_\mathrm{v}\sqrt{2\rho_\mathrm{in}\,|\Delta p|}. \tag{3.40}$$

Here n_v is the number of open valves with area A_v, and c_v is the discharge coefficient. The valve diameter was $d_\mathrm{v} = 0.35\,\mathrm{m}$.

The introduction of bypass relief valves implies a reduction in the energy available to the turbine and in the turbine rotational speed. This effect has a stronger influence on the Wells turbine than on the biradial turbine. The rotational speed of the biradial turbine has just a few peaks above the threshold. In contrast, the Wells turbine exceeded the prescribed rotational speed threshold for long intervals during simulations. This explains why the number of valves required for the various turbines was different.

The computations to determine the performance of the wave power plant with the relief valves were conducted starting with the selected optimal turbine rotor diameters for the cases without rotational speed constraints. The sensitivity of the electrical capture width ratio was assessed by computing the nearest turbine rotor diameters considering a step size of 0.05 m.

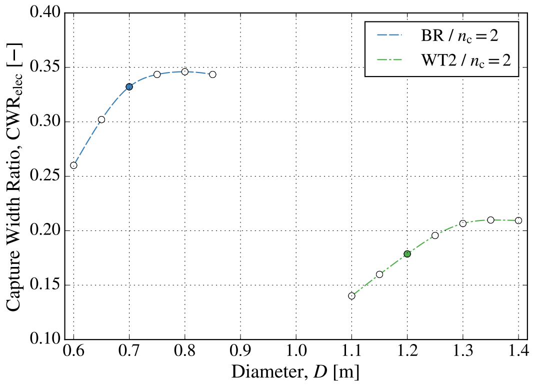

Fig. 3.14: Electrical capture width ratio for the two-stage Wells turbine and biradial turbine with relief valve system. Filled circles are the optimal diameters for the simulations without rotational speed constraints.

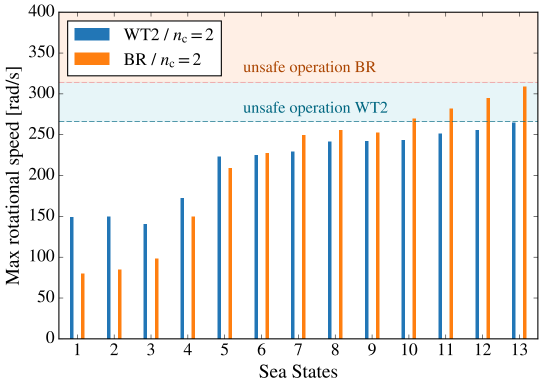

Fig. 3.15: Maximum rotational speed of the two-stage Wells turbine ($D = 1.2\,\mathrm{m}$, $P_{\mathrm{gen}}^{\mathrm{rated}} = 33.5\,\mathrm{kW}$) and biradial turbine ($D = 0.7\,\mathrm{m}$, $P_{\mathrm{gen}}^{\mathrm{rated}} = 84.0\,\mathrm{kW}$) after introduction of a relief valves system. Note that the scale of the vertical axis was reduced from 900 rad/s to 400 rad/s with respect to Fig. 3.13.

Results are shown in Fig. 3.14 where it is evident that the biradial turbine provides higher performance compared to two-stage Wells turbine. For the case of the biradial turbine, the initial rotor diameter is close to the optimal. In contrast, for the two-stage Wells turbine, a larger rotor diameter $D = 1.30\,\mathrm{m}$ enhances the energy conversion.

The effect of the relief valves on the turbine rotational speed can be observed in Fig. 3.15. Each case required different number of valves and their opening sequences which differently affected the capture width ratio. The comparison of electrical capture width ratios under conditions without and with the bypass valves is shown in Table 3.3. The biradial turbine has a small drop in the $\mathrm{CWR}_{\mathrm{elec}}$, about 5%. On the other hand, the two-stage Wells turbine shows a $\mathrm{CWR}_{\mathrm{elec}}$ reduction of around 42% and requires a larger number of relief valves. The installation of the relief valves has the advantage of reducing the turbine power peaks in the most energetic sea states. In the case of the Wells turbine, this allows lower-rated power generator selection without exceeding the rotational speed threshold.

Chapter 4

Coupling of Dielectric Elastomer Generators with U-Oscillating Water Column wave energy converters

This chapter presents two experimental activities aimed at investigating the possibility to couple the U-OWC WEC with innovative PTOs, the dielectric elastomer genetators (DEGs). The first experimental campaign was conducted at the NOEL test site in Reggio Calabria (Italy) where a small-scale metallic U-OWC is integrated into a breakwater. A U-OWC chamber was equipped with DEGs as PTO. DEGs are compliant polymeric generators able to convert mechanical energy into electrical energy by exploiting the large deformations of elastomeric membranes. This first test in real operating conditions was performed without electrical activation of the DEGs, with the objective of studying just the mechanical response of the coupled system U-OWC-DEG. The collected data were used for validating the proposed coupled model and to envisage a preliminary design of a full-scale U-OWC equipped with DEG-PTO and to predict the relative energetic performance.

The experimental setup of the tests conducted at NOEL was employed for the second research activity: a hardware-in-the-loop (HIL) simulation performed at the laboratory of the Department of Industrial Engineering, University of Trento (Italy). HIL simulations were employed to replicate the realistic operating conditions of the coupled system U-OWC/DEG in a laboratory environment in order to reduce the experimental burden compared to wave tank or sea tests. This test represents an intermediate step before proceeding with further experiments at sea including electrical control of DEGs.

4.1 Introduction

Wave energy converters based on the OWC working principle are designed to be equipped with self-rectifying air turbines to exploit the bidirectional airflow induced by the reciprocating motion of the water column inside the chamber. Traditional air turbines are represented by the Wells or impulse turbines. A more effective solution is given by the recently proposed biradial turbine [122].

Recently, innovative PTOs, the dielectric elastomer generators (DEGs), were studied as a possible alternative technology to be employed in wave energy converters [123, 124, 125]. OWCs coupled with DEGs were largely investigated in the last years through several theoretical and experimental studies [126]. DEGs are deformable capacitors made of dielectric polymeric materials. Dielectric elastomers (DEs) were originally developed for applications in the field of robotics [127, 128]. DEGs conversion process from mechanical work to eletrical energy occurs through capacitance variations related to the deformation of the membranes [129]. DEGs can be implemented according to several configurations, such as annular membranes deformed out-of-plane by oscillating loadings [130], inflating diaphragms [131], and tubular membranes [132]. Researches demonstrated the capability of DEGs to convert energy densities of up to 780 J/kg (per unit dielectric material mass) with efficiencies close to 30 % [133] and power densities over 200 W/kg (for the case of natural rubber) at operating frequencies similar to the wave frequencies [131]. Compared to traditional PTO systems, DEGs are manufactured with cheap materials and characterized by the lack of rigid/metallic moving parts. Further, they are resistant to the corrosion in the harsh marine environment and resilient [134, 135]. In the last years, several applications involving the DEGs as PTO were proposed for different WECs and demonstrated at the scale of laboratory prototype or wave-tank model [123, 136, 137, 138, 139]. Among the possible configurations of the DEGs, the circular diaphragm DEG (CD-DEG) is one of the most interesting layout. CD-DEG's performance were first assessed through theoretical analyses [124] and, later, through further studies on the optimization of the CD-DEG control aimed at maximizing the wave power extraction [140]. The characterization of the CD-DEG PTO was accomplished through dry-run laboratory tests [141] and wave-tank tests conducted on small-scale OWC prototypes [142] with rated power in the range 1-4 W. Those first experiments were useful to assess the capability of the DEGs to operate in dynamical conditions in combination with OWCs, converting a significant fraction of the input wave power into electrical power. However, those works were always conducted with controlled laboratory conditions and validated against simulated waves. None of the previous works were conducted in real operating conditions at sea.

In the first experimental activity presented in this work, a set of preliminary real sea tests is presented in order to assess the feasibility of a novel WEC that combines a U-OWC system [68] with a set of CD-DEGs as the PTO system. As a first step towards real operating conditions at sea, the tests conducted in the presented experimental campaign consider just the purely mechanical response of the coupled

U-OWC-DEG system, i.e. a passive system where the electrical components which allow the generation of electrical power were not implemented. The obtained data were employed to validate a time domain mathematical model of the system response, and they are expected to serve as a basis for future testing. Additionally, a full-scale design for the proposed WEC is presented, which relies on the mechanical model validated through experimental data and on CD-DEGs power generation outcomes obtained in the framework of previous works [142].

The experimental activity is presented through the following sections. Sect. 4.2 describes the coupled layout of a U-OWC where a set of CD-DEGs are installed as the PTO and it introduces a mathematical model for the system dynamics. Sect. 4.3 shows the experimental results and provides a validation of the proposed model. Sect. 4.4 proposes and evaluates a concept design of a larger scale U-OWC-DEG wave power plant.

4.2 Modelling of U-OWC with DEG PTO

This section describes the mathematical model of the U-OWC equipped with a CD-DEG PTO that is referred to as U-OWC-DEG. First, a general description of the plant is given. Then, the equations of motion of the system are provided.

4.2.1 U-OWC with DEG PTO: layout and features

A cross-sectional view of the system U-OWC-DEG is provided in Fig. 4.1. The system includes a U-OWC caisson that is made of a hollow chamber connected to a submerged U-shaped duct that is open to the action of the waves through an horizontal opening on the wave-beaten side. The chamber houses an oscillating water column with a volume of air located on its upper part, and presents some circular apertures on the top of the chamber and in the lateral wall where CD-DEGs can be installed to be exploited as PTO. Waves induce an oscillating pressure field on the opening of the vertical duct with consequent oscillations of the the water in the inner chamber. As a result, the air volume is cyclically compressed and expanded. Air pressure variations cause the inflation and deflation of the elastomeric membrane (i.e. the variable capacitor) of the CD-DEG that, in combination with a driving power electronics, is responsible for the conversion of mechanical energy into direct current electricity [124]. A throttle valve is installed in parallel with the CD-DEGs for limiting the air pressure in case of severe sea states in order to avoid the breaking of the membranes. Relevant geometric parameters are the width of the U-duct and of the inner chamber, respectively, b_1 and b_2; the length of the U-duct l_i; the submergence of the vertical duct h_o with respect to the mean water level; the distance h_c from the top of the air chamber to the mean water level; and the transverse width of the chamber b_3, not shown in figure.

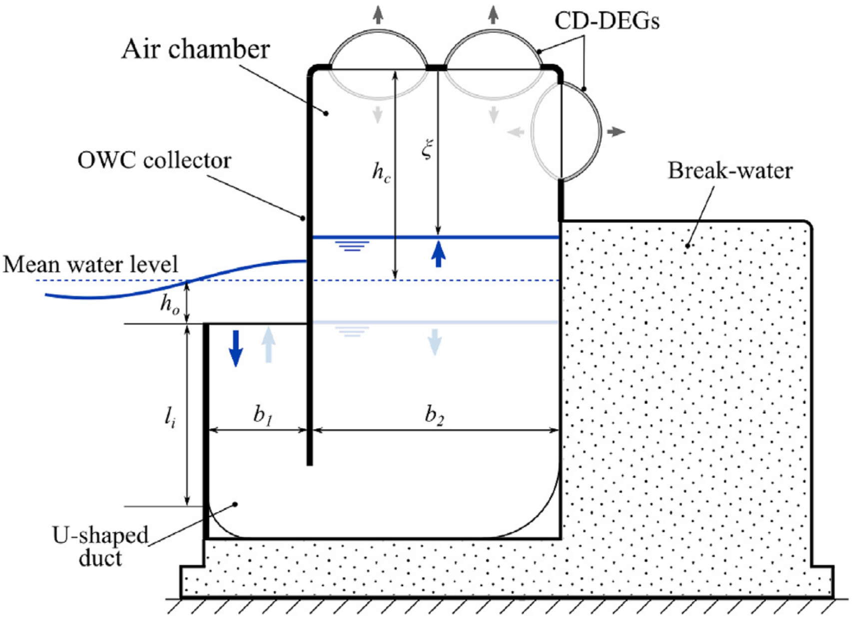

Fig. 4.1: U-OWC integrated into a breakwater equipped with CD-DEGs

4.2.2 Mathematical model

The wave-to-wire model of a U-OWC with DEGs includes different sub-models, each one describing a specific portion of the whole system. Specifically, the following models are presented:

- the U-OWC hydrodynamic model, accounting for the wave radiation and diffraction problem, the computation of the excitation on the U-OWC, and the dynamics of the water column;
- the model which describes the response of the air in the chamber;
- the DEG electro-elastic response.

These models form a system of coupled nonlinear integro-differential equations in the time domain. However, in the following section each model is presented separately.

4.2.2.1 U-OWC hydrodynamic model

The U-OWC water column oscillations are described in time domain through the extended Bernoulli theorem for unsteady flow. The equation is derived by computing the total head at the water column inlet and the total head at the free surface of the inner water column. The unknown water column displacement ξ is expressed as the distance between the instantaneous inner free surface and the top of the air chamber. Head losses, from the U-duct opening to the inner chamber, are included in the model via the instantaneous acceleration-based method, which accounts for steady head losses through a drag-type non-linearity and for unsteady head losses through an inertial term. Both quantities are proportional to constants determined in experimental tests [60, 115]. The resulting water column equation of motion is expressed as:

$$M(\xi)\ddot{\xi}+C(\xi,\dot{\xi})\dot{\xi}+(\xi-h_c)-\frac{p}{\rho g}-\frac{1}{g}\frac{b_2}{b_1}\int_0^t \dot{\xi}(t)K(t-\tau)\mathrm{d}\tau=-\frac{\Delta p^{(D)}}{\rho g}, \tag{4.1}$$

where t is the time; g is the acceleration of gravity; ρ is the water density; p is the relative pressure in the air chamber; $M(\xi)$ and $C(\xi,\dot{\xi})$ are, respectively, time-dependent mass and damping terms; $K(t)$ is a convolution term which accounts for wave radiation loads; and $\Delta p^{(D)}$ is the wave excitation pressure. The mass and damping terms read as follows:

$$M(\xi)=\frac{1+C_{\mathrm{in}}}{g}\left(\frac{b_2}{b_1}l_i+l_i+h_0+h_c-\xi\right)-\frac{b_2}{gb_1}H(\infty) \tag{4.2}$$

and

$$C(\xi,\dot{\xi})=\frac{1}{2g}\left(C_{\mathrm{dg}}\left(\frac{l_i}{R_{h1}}\left(\frac{b_2}{b_1}\right)^2+\frac{l_i+h_0+h_c-\xi}{R_{h2}}\right)+1\right)|\dot{\xi}|, \tag{4.3}$$

where $H(\infty)$ is an equivalent length accounting for the infinite frequency added mass, C_{in} and C_{dg} are coefficients accounting for the U-duct head losses, and R_{h1} and R_{h2} are hydraulic radii of the U-duct and inner chamber horizontal sections, respectively. In the previous set of equations, the wave pressure at the inlet section has been taken into account by utilizing Cummins' representation of the radiated wave field under the assumption that the surrounding wave field can be described by potential theory [143, 144]. In particular, the total wave pressure has been regarded as the sum of two contributions: the excitation pressure $\Delta p^{(D)}$ representing the wave pressure computed in a diffractive wave field; and a second contribution related to the wave field radiated by the U-OWC. This second contribution includes two terms: a term accounting for the effect of infinite-frequency added mass, $H(\infty)$ (included in the definition of $M(\xi)$), and a convolution integral accounting for the hydrodynamic memory effects. Both $H(\infty)$ and the kernel of the convolution integral $K(\tau)$ are geometric dependent parameters determined by solving pertinent boundary value problems (see Appendix and Ref. [61] for further details).

4.2.2.2 Air chamber model

The U-OWC model is coupled to the air pocket model through the air pressure in the chamber. This model is based on the air mass and energy conservation applied to the air volume in the chamber. In this regard, the equation presented in this section considers a general case in which the air chamber is connected to the atmosphere through a device, like a valve, in such a way to include a certain air flow rate $\dot{m}$ (positive if air flows out of the chamber) in the computation. Air compressibility is accounted for by assuming that the thermodynamic process is isentropic [145, 146]. In this context, the equation describing the air chamber dynamics is

$$-\gamma(p+p_{atm})\left(\frac{p+p_{atm}}{p_{atm}}\right)^{\frac{1}{\gamma}}\frac{\dot{m}}{\rho_{atm}}=\gamma\dot{\Omega}_a(p+p_{atm})+\Omega_a\dot{p}, \tag{4.4}$$

where γ is the ratio of the specific heat at constant pressure and the specific heat at constant volume; ρ_{atm} is the atmospheric air density; p_{atm} is the atmospheric pressure; and Ω_{a} is the instantaneous air pocket volume. The calculation of Ω_{a} and its derivative leads to the following equations:

$$\Omega_{\mathrm{a}} = b_2 b_3 \xi + \frac{\pi}{6} h_{\mathrm{t}} \left(h_{\mathrm{t}}^2 + 3e^2\right) N_{\mathrm{D}} \tag{4.5}$$

and

$$\dot{\Omega}_{\mathrm{a}} = b_2 b_3 \dot{\xi} + \frac{\pi}{2} \left(h_{\mathrm{t}}^2 + e^2\right) \dot{h}_{\mathrm{t}} N_{\mathrm{D}}, \tag{4.6}$$

where N_{D} represents the number of CD-DEGs installed on the U-OWC and h_{t} is the displacement of the tip of the membrane. If the chamber is equipped with a throttle valve, the air flow rate can be calculated through the equation

$$\dot{m} = C_{\mathrm{v}} \pi \frac{d_{\mathrm{v}}^2}{4} \sqrt{2\rho_{\mathrm{atm}} \left(\frac{p + p_{\mathrm{atm}}}{p_{\mathrm{atm}}}\right)^{1/\gamma} |p| \operatorname{sign}(p)} \tag{4.7}$$

where C_{v} is an empirical discharge coefficient, and d_{v} is the reference valve diameter.

4.2.2.3 DEG electro-mechanical model

The CD-DEG is an electrostatic generator that is able to convert the pneumatic work done by a pressure difference applied on its opposing faces into electrical energy. The CD-DEG is a variable capacitor made of a membrane fixed on rigid circular supports. The pressure applied on the membranes induces out-of-plane deformations with consequent capacitance variations. The membrane is generally implemented as a stack of circular layers of DE alternating with compliant electrodes arranged to form a multilayer capacitor, as shown in Fig. 4.2. Materials commonly used for the DE membranes are acrylics, natural and styrene-based rubbers and silicones, which combine the electrical properties of large dielectric strength and low conductivity with mechanical properties of large extensibility and reduced stiffness. Compliant electrodes are made of layers of electrically conductive materials able to maintain low resistivity even under large stretches. Compliant electrodes can be implemented in different ways: as thin metallic films sputtered on the DE substrates or with carbonloaded conductive elastomeric films [147].

In terms of the constitutive model, the DE material can be described as a non-linear hyperelastic continuum (i.e., an elastic solid with non-linear stress-strain response) [148] with dielectric behaviour. However, modelling the CD-DEG using local continuum electroelastic formulations [149] is rather complex and computationally expensive. In order to provide a practical formulation, suitable for design and preliminary analysis, a reduced lumped-parameter model is provided in Ref. [124]. In this work, a

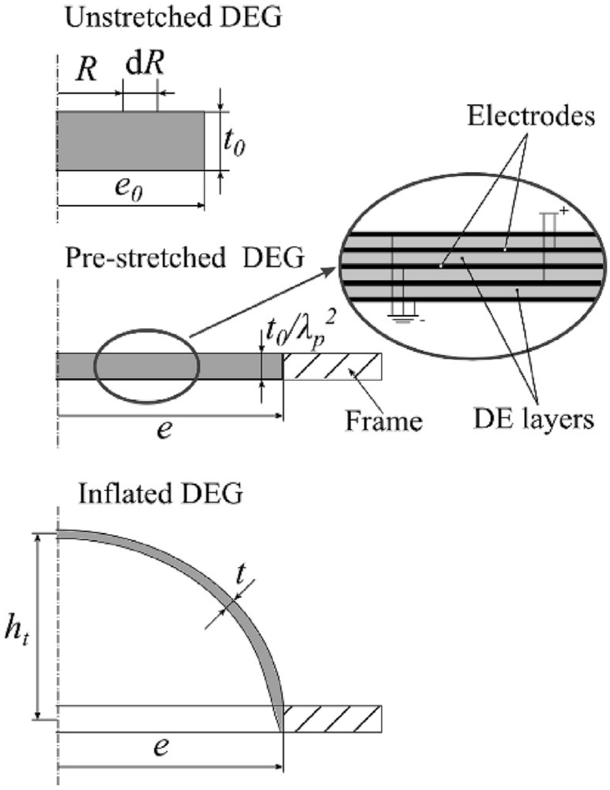

Fig. 4.2: Sketch of a CD-DEG in its undeformed state (top), pre-stretched configuration (centre) and inflated configuration (bottom). The inset shows the detail of the dielectric-electrode layers.

reduced model is employed as presented in Ref. [123]. The model is simplified through some assumptions previously validated [123, 140] and recalled in the following.

The geometrical parameters of the CD-DEG stack are described in Fig. 4.2. The symbols e_0 and t_0 represent the DEG radius and the total thickness in the undeformed configuration. The DEG is mounted on the circular frame with a certain pre-stretch, λ_p, which takes its radius to $e = \lambda_\mathrm{p} e_0$. Rubber-like materials are incompressible, that is their volume does not change with deformations. Therefore, the CD-DEG thickness after pre-stretching is t_0/λ_p^2. The application of a pressure difference p between the lower and upper faces of the DEG induces a displacement of the membrane from the flat equilibrium configuration with consequent out-of-plane deformation.

As demonstrated in Ref. [123], the equilibrium pressure p associated to a given geometric configuration and a voltage difference V applied on the DE layers is described by the following expression:

$$p = \frac{\mathrm{d}U_\mathrm{m}}{\mathrm{d}\Omega_\mathrm{c}} - \frac{V^2}{2}\frac{\mathrm{d}C}{\mathrm{d}\Omega_\mathrm{c}} \tag{4.8}$$

where U_m represents the elastic energy of the DE layers, Ω_c is the volume subtended by the deformed CD-DEG shell, and C is its capacitance. Consistent with the assumptions presented in Ref. [124], the deformed CD-DEG can be approximately described as a thin spherical shell with non-uniform thickness.

Therefore, its configuration can be uniquely identified by the displacement h_{t} of the tip element from the equilibrium plane (considered positive upwards). Using the assumption of spherical deformation, Ω_{c} relates to h_{t} as follows:

$$\Omega_c = \frac{\pi}{6} h_t \left(h_t^2 + 3e^2\right) \tag{4.9}$$

It is also assumed that the deformation state is completely equibiaxial (i.e., the stretch is the same in any direction tangent to the shell surface), though it is not uniform over the DEG. In Ref. [124], it has been shown that this assumption provides a good agreement with finite-element simulations in a wide range of DEG deformations, comprised at least between $h_{\mathrm{t}} = -e$ and $h_{\mathrm{t}} = e$. The tangential stretch in a generic point of the DEG reads as follows:

$$\lambda = e e_0 \frac{h_{\mathrm{t}}^2 + e^2}{e^2 e_0^2 + h_{\mathrm{t}}^2 R^2} \tag{4.10}$$

where R identifies a material element lying at a distance R from the axis in the unstretched state (see Fig. 4.2). Notice that, due to incompressibility of the elastomeric material, the thickness in a generic point of the deformed CD-DEG shell is given by $t = t_0/\lambda^2$.

The deformed CD-DEG layers are parallel-plate capacitors, with total capacitance given by the following expression:

$$C = \frac{\pi \varepsilon n_{\mathrm{l}}^2 \lambda_{\mathrm{p}}^2 e^2}{3 t_0} \left[\left(\frac{h_{\mathrm{t}}^2 + e^2}{e^2}\right)^3 + \left(\frac{h_{\mathrm{t}}^2 + e^2}{e^2}\right)^2 + \left(\frac{h_{\mathrm{t}}^2 + e^2}{e^2}\right) \right], \tag{4.11}$$

where ε is the DE material dielectric constant, and n_{l} is the number of dielectric layers included in the stack. The thickness of the electrodes can be neglected. Therefore, the total thickness of the dielectric layers is assumed equal to the total DEG thickness, t_0.

The DEG elastic energy is a function of stretch. Under the assumption that the DE material is hyperelastic, the volumetric elastic energy density is given by a strain-energy function, Ψ, whose dependence on λ is expressed by a given constitutive model. The Mooney-Rivlin hyperelastic model [148] is used under the assumption of incompressible solid with equibiaxial deformation. The following expression holds for Ψ:

$$\Psi = C_{1,0} \left(2\lambda^2 - \lambda^{-4}\right) + C_{0,1} \left(2\lambda^{-2} + \lambda^4\right) \tag{4.12}$$

where $C_{1,0}$ and $C_{0,1}$ are characteristic constitutive parameters. The total elastic energy, U_{m}, is obtained by integrating Ψ over the total elastomeric volume:

$$U_{\mathrm{m}} = 2\pi t_0 \int_0^{e_0} R\Psi \mathrm{d}R \tag{4.13}$$

It is worth noticing that the calculation of the derivatives in Eq. (4.8) can be performed using the chain rule, considering that U_{m}, Ω_{c} and C are functions of h_{t}. Mechanical inertia/kinetic energy of the DE material is not included into Eq. (4.8). As observed in Ref. [140], the natural frequency of the DEG is much larger than that one of the OWC. As a consequence, the DEG dynamics is expected to be much faster compared to the motion of the OWC. Therefore, the DEG response can be assumed quasistatic for this work. The electric field in the DE layers is computed as

$$E = n_{\mathrm{l}} \lambda^2 \frac{V}{t_0}. \tag{4.14}$$

Since the electric field is related to λ, it is not uniform throughout the CD-DEG. The instantaneous electrical power output of the DEG is given by:

$$P_{\mathrm{u}} = -V\dot{Q} \tag{4.15}$$

where $Q = CV$ is the charge present on the electrodes. The DEG operation can be described through control cycles, each corresponding to a full oscillation between the flat equilibrium configuration and a maximally expanded configuration, inwards or outwards according to the external excitation. DEG operation involves bidirectional electrical energy fluxes. Indeed, in each cycle, a small amount of electrical energy is initially spent by the external circuit to charge the DEG ($P_{\mathrm{u}} < 0$), and a larger amount of electrical energy is successively recovered ($P_{\mathrm{u}} > 0$) by progressively discharging the DEG. Several control strategies have been proposed for CD-DEGs installed on OWCs as PTO, including prediction-less controls [123, 124] and advanced controllers based on a statistical knowledge of the current sea state [140].

4.3 In-field experimental validation

This section presents the results of field experiments aimed at validating the proposed mathematical model of the coupled U-OWC/CD-DEG system. These experiments are the first examples of sea trials on an OWC with DEGs. At this stage, the objective of the experiments was the investigation of the purely mechanical response of the system without including electrical activation. In the following sections, details on the experimental activity is provided, and a comparison of experimental data and theoretical predictions is presented.

(*a*) (*b*)

Fig. 4.3: Metallic U-OWC caisson (a) with four CD-DEGs installed on the top of the lateral chamber (b). One of the CD-DEGs was painted black to allow post-processing of the high-speed camera frames.

4.3.1 Set-up and data acquisition

4.3.1.1 Experimental set-up

The experimental activity was carried out at the Natural Ocean Engineering Laboratory (NOEL) in Reggio Calabria (Italy). The sea states commonly recorded in the laboratory consist of pure wind waves with the typical size of a laboratory tank, characterized by significant wave heights ranging from 0.20 m to 0.80 m and peak periods between 2.0 s and 3.6 s. The generated sea states are representative, in a Froude similarity, of severe ocean sea storms. This is due to some concomitant factors: the local wind coming from NNW is highly stable, the coast is naturally protected from the swells coming from the South and the fetch is relatively short (about 10 km). The U-OWC prototype installed at the NOEL site is a metallic caisson integrated into a concrete vertical breakwater, while the CD-DEGs are installed on the ceiling of the air chamber (see Fig. 4.3). The metallic caisson includes three independent chambers. Several identical CD-DEGs are installed on one of the lateral chambers, working simultaneously as can be observed in Fig. 4.3. The chamber can be equipped wit 4 CD-DEGs, though tests with a smaller number of DEGs can be performed closing the unused DEG housings with solid steel disks and seals. On top of the air chamber, a butterfly valve with nominal diameter of 100 mm was installed for reducing the air pressure in the chamber during the most energetic sea states in order to prevent the DEGs from breaking.

A commercial acrylic material, VHB 4905, produced by 3 M, was employed for the manufacturing of the CD-DEG prototypes. This material was selected due to its low mechanical rigidity and large extensibility, thus, it is adequate for deploying small-scale DEG prototypes [123]. Each DEG was built by overlapping and bonding together different layers of VHB 4905 so as to form a single solid dielectric layer. The unstretched thickness of the resulting layer was of $4-5$ mm with a diameter of 115 mm, while the final diameter, after pre-stretching by $\lambda_p = 3.4$ and installation on a rigid polycarbonate frame, was 390 mm. In the tests carried out in these work, no electrodes were present on the CD-DEG prototypes,

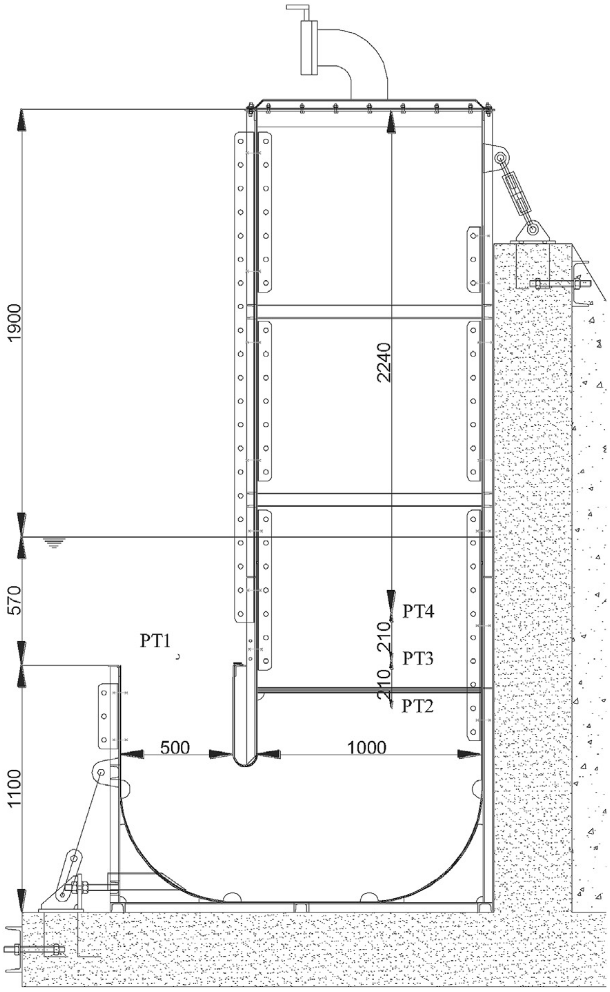

Fig. 4.4: Location of the pressure transducers (PT) in the vertical duct and inner chamber of the U-OWC

since no electrical activation was applied on the membranes and no power generation was obtained. In fact, the objective of these first tests was the characterization of the mechanical response of the system.

Constitutive models [124] and previous tests on CD-DEG samples made of VHB acrylic with carbon grease compliant electrodes [123, 142] can be employed to estimate the power theoretically achievable with the considered CD-DEG samples (if electrical activation was applied). According to those results, CD-DEGs can convert energy densities of 0.3-0.5 J/g per cycle. In the tests described here, the mass of dielectric material in each CD-DEG was about 40-50 g. Therefore, each of the employed CD-DEGs can potentially generate power outputs of 10-25 W at an operating wave frequency of 0.4-0.5 Hz. Thus, equipping the device with four DEGs would give a theoretical rated power of 40-100 W.

Measurements are obtained with pressure transducers (PT) ATM.ECO/N produced by STS. Specifically, one PT is installed at the inlet section of the collector, while three PTs are installed within the water column thanks to steel brakets. Finally, one PT is installed in the air chamber. The positions of the pressure transducers are shown in Fig. 4.4 (the PT installed in the air chamber is not shown). The figure and Table 4.1 also show the relevant geometrical parameters.

Table 4.1: Geometrical characteristics of the U-OWC chamber equipped with CD-DEGs.

h_o[m]	d[m]	b_1[m]	b_2[m]	b_3[m]	l_i[m]	h_c[m]	d_v[m]
0.57	1.9	0.5	1	1.23	0.8	1.9	0.10

4.3.1.2 Data collection and post-processing

The PTs data were recorded with a sampling frequency of 10 Hz using a NI cDAQ-9174 acquisition board by National Instrument. The data were collected in short records representative of individual sea states. Specifically, each record was composed by 3000 samples, hence, each time series has a duration of 5 min, which is the typical time resolution of a sea state at the NOEL [150]. 102 sea states were collected in the whole, which are representative of different sea conditions, spanning from wind-generated seas to mixed sea states. The corresponding significant wave heights and peak spectral periods ranged in the intervals 0.15-0.45 m and 1.8-3.3 s. The pressure transducers measurements were used to obtain the excitation and to compute the water column oscillations. In particular, the PT at the inlet section provides the wave pressure, Δp_w, including the contribution due to diffracted and radiated waves, while the PTs inside the inner chamber and in the air chamber are used to measure, indirectly, the water column displacement. For this purpose, the method described by Boccotti et al. [151] and by Malara et al. [60] is employed. Specifically, given the simultaneous measurements of two PTs under water (e.g., the upper and the lower one) and of the PT in the air chamber, the water column acceleration ($\ddot{\xi}$) is calculated by the equation

$$\ddot{\xi} = g + \frac{p_{\mathrm{u}} - p_{\mathrm{l}}}{\rho \Delta z} \tag{4.16}$$

where, p_{l} and p_{u} are the instantaneous pressures measured by the lower and the upper pressure transducers respectively, and Δz is their vertical distance between them. Then, the instantaneous displacement ξ is calculated by the equation

$$\xi = h_{\mathrm{l}} - \frac{p_{\mathrm{l}} - p}{\rho (g - \ddot{\xi})} \tag{4.17}$$

h_{l} being the distance between the lower pressure transducer and the top of the U-OWC.

The deformation of one of the CD-DEGs was acquired by means of a high-speed camera (Point Grey GS3-U3-23S6M-C with lens 250 F6C). The camera was placed at a distance of approximately 2 m from the DEGs, aligned with the top of the U-OWC, at the equilibrium plane of the CD-DEGs. Data from the camera were synchronised with the PTs acquisitions through an external analogical trigger. Only the upwards displacements were captured by the camera, as the membrane was hidden by the air chamber walls during its downwards deformation. The acquired frames were then processed to obtain time-series

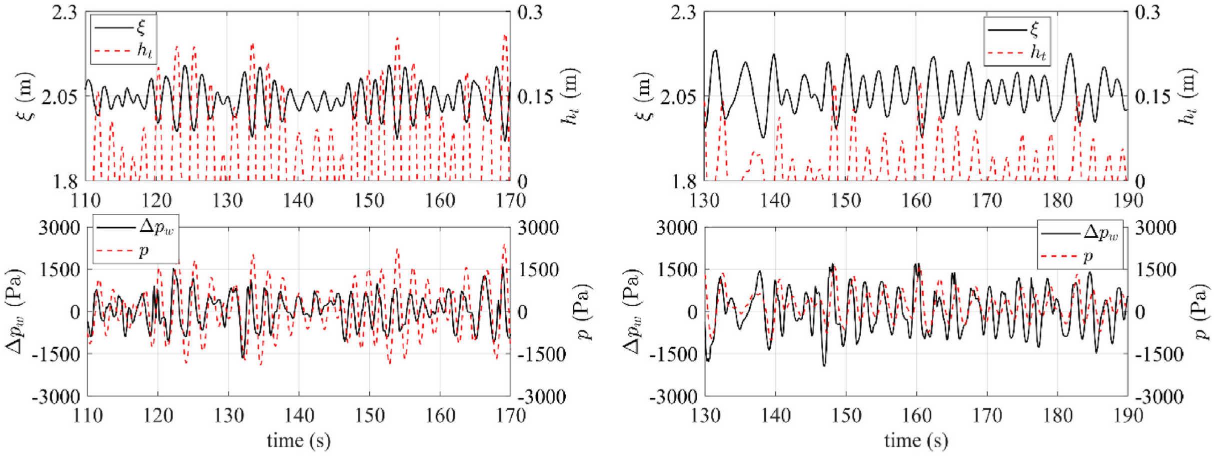

(a)

(b)

Fig. 4.5: Time-series of water column displacement ξ, CD-DEG tip displacement h_{t}, wave pressure Δp_{w}, and air relative pressure p for two tests with 4 CD-DEGs installed. In (a) tests with closed valve are shown; in (b) the valve was completely open. Time-series of h_{t} are only available during upwards membrane displacement, as the membrane was hidden by the chamber walls during downwards oscillations.

of the CD-DEG tip elevation, h_{t}, using the procedure described by Moretti et al. [123]. The effect of the DEGs on the system dynamics can be investigated through the analysis of the time-series of ξ and p. Examples of time-series of the different measured variables are reported in Fig. 4.5, which shows a comparison of two tests featuring similar sea conditions, 4 CD-DEGs with a thickness of the underformed configuration of $t_0 = 5$ mm, and two different aperture levels of the valve (closed and completely open). In the presence of closed air chamber, the oscillations in p are larger, since there is no flow through the valve, while oscillations in ξ are smaller. Indeed, the valve aperture not only introduces a damping contribution in the water column dynamics, but it also causes a reduction in the mechanical stiffness of the air chamber-DEGs system. The air pressure and the DEG tip displacement are in phase, since the DEG without activation behaves as a purely elastic component (except for viscoelastic dissipative effects). For the same reason, p and h_{t} are in phase opposition with ξ when the air chamber is closed, whereas some small phase-shifting is present when the valve is open (due to the air chamber dynamics introduced by the valve, described by Eq.(4.4)). Phase shifting among Δp_{w} and the other variables is always present, as a consequence of the water column dynamics (see Eq. (4.1)).

As can be osbserved in Fig. 4.5 the oscillation amplitude of the CD-DEG tip increases with the air pressure. The amplitude is mitigated when the valve is completely open. Therefore, the presence of a relief valve results to be a necessary safety device activated to avoid the breaking of the CD-DEGs in rough sea states. A wider analysis of experimental results and comparison of different operating conditions is reported in Ref. [68], where the effect of the CD-DEGs on the U-OWC dynamics is investigated through a frequency-domain approach.

4.3.2 Model validation

A validation of the proposed U-OWC/CD-DEG coupled model is presented in this section. The analysis is focused on the study of the coupled dynamical response of the U-OWC and the DEGs. Therefore, attention is restricted to the following set of sub-models: the water column dynamics, the air chamber response, and the CD-DEG elastic model, excluding the radiation-diffraction problem and the effect of electrical activation. The latter sub-models have been validated in the past through specific experiments [60, 142] or against numerical models [152], and they might be further explored in the future through advanced tests including fully-functional DEGs and U-OWC for the study of the wave field in proximity to the structure.

4.3.2.1 Model set-up and calibration

The time domain dynamical model of the U-OWC with DEGs has been implemented in a Matlab & Simulink environment. The numerical model includes the U-OWC dynamic equation (Eq. (4.1)), the dynamic equation of the air chamber with throttle valve (Eq. (4.4)) and the mechanical model of the CD-DEGs (Eq. (4.8), considering only the first term relative to the purely elastic response). The experimental data of the wave pressure Δp_{w} (i.e., the sum of the radiation and diffraction wave pressure) is employed as the input for the simulations. The computed outcomes are the water column displacement, ξ, the air chamber pressure, p, and the CD-DEG tip displacement, h_{t}. The parameters used in the U-OWC dynamic sub-model are the U-OWC dimensions given in Table 4.1 and the hydraulic loss parameters. Based on previous tests on the reference U-OWC prototype [60], the following loss parameters were used: $C_{\mathrm{dg}} = 0.71$ and $C_{\mathrm{in}} = 0.13$. The parameters in the CD-DEG elastic model are the Mooney-Rivlin coefficients, $C_{0,1}$ and $C_{1,0}$. Based on available tests on the VHB material [123], the following values were considered: $C_{0,1} = 3700\ \mathrm{Pa}, C_{1,0} = 380\ \mathrm{Pa}$. For the air chamber model, atmospheric air density $\rho_{\mathrm{atm}} = 1.2\ \mathrm{kg/m^3}$ and adiabatic heat ratio $\gamma = 1.4$ were assumed.

The throttle valve has 10 positions, corresponding to different levels of aperture (from 100% open to fully-closed). However, in this experimental activity, five aperture levels,including the fully open and closed states, were regarded to be sufficient for detecting the influence of the throttle valve aperture levels on the system dynamics. An experimental procedure was employed to calibrate the values of the discharge coefficient, C_{v}, corresponding to the aperture levels to be employed in the tests. Specifically, calibration tests were carried out with the valve mounted on the U-OWC lateral chamber, exploiting the air pressure variations induced by the water column oscillation. In order to investigate the role of the valve, the set of DEGs were removed and replaced with steel disks. A set of acquisitions were performed, with the valve set to the five different positions. In each test, the pressure p in the chamber and the level ξ of the water column were measured. The dynamic equation of the air chamber, Eq. (4.4), was then solved by

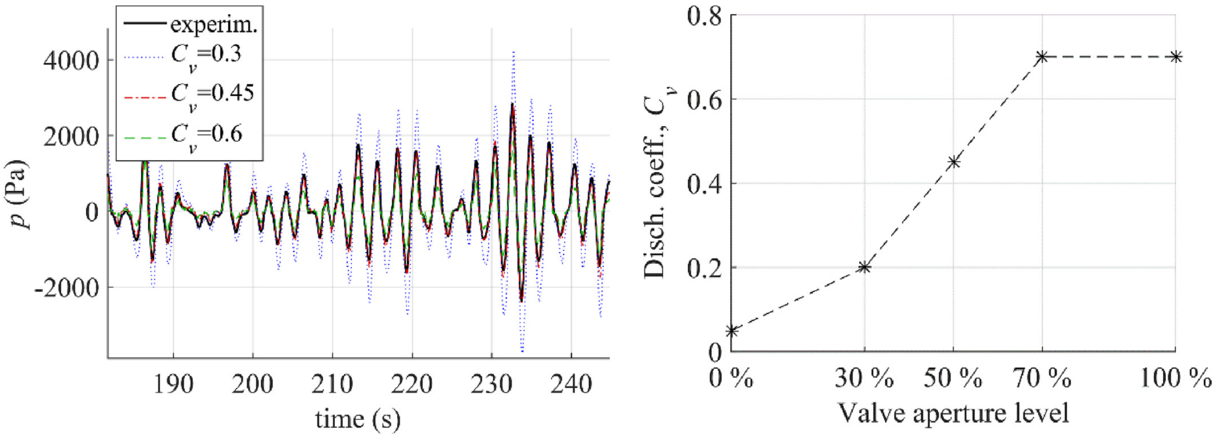

(a) (b)

Fig. 4.6: Discharge coefficient calibration: (a) comparison of the experimental air pressure time-series versus model-predicted time-series relative to different values of the discharge coefficient for a test with valve 50 % open; (b) calibrated values of C_v for the five different aperture levels used in the tests.

posing $h_\mathrm{t} = 0$ in Eqs. (4.5) and (4.6) for different values of C_v, using the measured time-series of ξ as the input. Time-series of the air pressure, p, were obtained by varying C_v. FInally, the value of C_v that minimizes the norm of the difference of experimental and model-based pressure time-series was identified. A comparison of experimental and theoretical time-series for a specific calibration test is shown in Fig. 4.6 (a). Repeating this operation for the five conditions allowed the identification of a value of C_v for each of the relevant aperture levels employed in the experiments, as shown in Fig. 4.6 (b). It should be noted that the discharge coefficient of the condition with the valve completely closed is slightly greater than 0. This is due to some air leaks in the air chamber connections and in the valve. Besides, beyond a certian level of aperture, that is 70 %, the value of C_v does not show a futher increase and becomes constant.

4.3.2.2 Comparison of model and experimental data

A set of simulations were run, using the approach described in Sect. 4.3.2.1. Each simulation has the objective to reproduce the U-OWC response in a specific experimental dataset. The simulations differ in terms of the following input parameters: wave pressure measured at the center of the U-OWC inlet, number of CD-DEGs installed on the chamber ceiling, DEGs thickness (i.e. number of used layers), discharge coefficient associated with the current valve aperture. Fig. 4.7 presents an overview of the model performance against the different tests. Vis-à-vis plots are presented comparing the measured standard deviations of the water column displacement and the air pressure in the chamber ($\sigma_{\xi,\mathrm{meas}}$ and $\sigma_{p,\mathrm{meas}}$, respectively) and those obtained through the model ($\sigma_{\xi,\mathrm{mod}}, \sigma_{p,\mathrm{mod}}$). The comparison between modelled and experimental oscillation amplitude of the CD-DEGs tip, h_t, is omitted because the tip displacement was recorder only in a few tests. Specifically, Fig. 4.7 (a) shows results relative to the scenario with 3

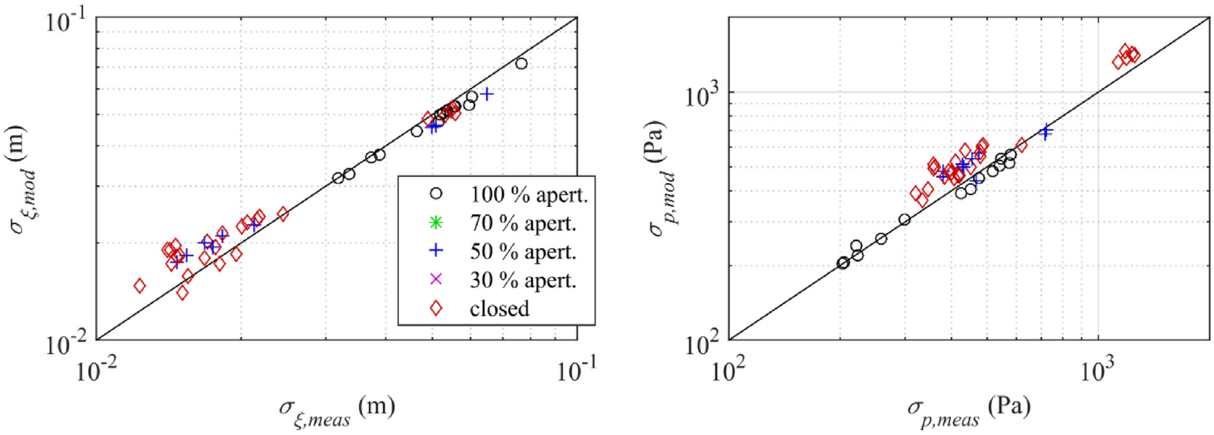

(a) Tests with 3 DEGs

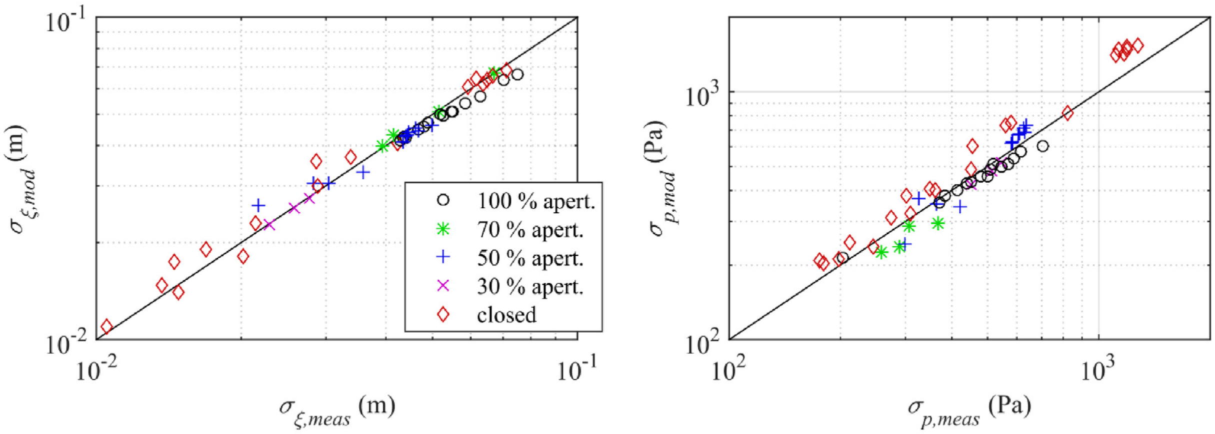

(b) Tests with 4 DEGs

Fig. 4.7: Vis-à-vis comparison of experimental and model-predicted standard deviation of the time-series of the water column oscillations on the left side of the panel and the air chamber pressure on the rigth side of the panel. Coloured markers refer to different levels of aperture of the valve. Plots (a) are relative to tests with 3 DEGs, plots (b) refer to tests with 4 DEGs.

DEGs installed on the U-OWC chamber, while Fig. 4.7 (b) shows the cases with 4 DEGs. The markers in the pltos describe datasets relative to different levels of aperture of the valve. The plots show that, in average, tests with closed air chamber exhibit lower oscillation amplitude of ξ and larger oscillation amplitude in p than the corresponding tests with fully-open valve, as already observed in Sect. 4.3.2.1. Despite the broad variety of recorded/simulated sea states and operating conditions of the different tests, the model is statistically reliable and predicts the experimental behaviour rather effectively. In particular, data are well distributed about the bisector line of the vis-à-vis plots, thus confirming that the model does not show any systematic overestimation (or underestimation) of the system oscillations.

As shown by Malara et Al. in Ref. [60], the model error for each dataset was computed based on the time-series of ξ and p through the expression:

$$\varepsilon_{\xi}=\frac{\|\xi_{\text{meas}}-\xi_{\text{mod}}\|}{\sigma_{\xi,\text{meas}}},\varepsilon_{p}=\frac{\|p_{\text{meas}}-p_{\text{mod}}\|}{\sigma_{p,\text{meas}}} \tag{4.18}$$

where the subscript meas denotes the measured time-series whereas mod denotes model time-series, and operator $\|\cdot\|$ is the norm of the argument function. Errors relative to the different scenarios considered in Fig. 4.7 are reported in Table 4.2. Values are averaged over different datasets.

Referring to the two datasets previously considered in Fig. 4.5, for which the measurements of the CD-DEGs tip height are also available, a comparison of experimental and theoretical time-series is presented in Fig. 4.8. Also in this case, both conditions, with the valve closed and completely open, are depicted. In these tests, the model tends to slightly overestimate the oscillation amplitudes of the variables in the case of closed air chamber, and to underestimate them when the valve is open. The average errors over the considered datasets are: $\varepsilon_{\xi}=0.39$ and $\varepsilon_{p}=0.50$ for the dataset shown in Fig. 4.8 (a) (greater than the average values for the different tests considered in Table 4.2); $\varepsilon_{\xi}=0.22$ and $\varepsilon_{p}=0.21$ for the dataset shown in Fig. 4.8 (b) (lower than the average error on the different tests). These small differences do not compromise the reliability of the model to predict and describe the trends and the dynamics of the physical variables, the air pressure in the chamber, the oscillations of the water column and the CD-DEGs deformations. Specifically, the possible presence of errors in correspondence with isolated oscillations does not affect the global agreement between the theoretical and experimental time-series on a statistical basis and the corresponding values of the average error.

4.4 Analysis and simulation of a full-scale U-OWC with DEG PTO

The validation of the proposed model through experimental data allowed to conduct a theoretical analysis of a full-scale application of a U-OWC equipped with a set of CD-DEGs as the PTO system. The case study for the analysis is represented by U-OWC collector installed in the port of Civitavecchia (Italy) [153, 107]. The pilot wave farm in Civitavecchia is composed by a set of U-OWC chambers (with target power of 20 kW each) integrated on bottom-fixed breakwaters. Instead of considering air turbines to be installed on the U-OWC chamber, a set of CD-DEGs is assumed to be mounted on the chamber to evaluate the potential performance of DEG PTOs in full-scale applications. For the purpose, dielectric materials more efficient than the acrylic employed for the test are adopted. Specifically, reference is made to DEGs manufactured with a silicone material, properly optimized for DE applications.

Silicone elastomers are considered among the most promising candidates for future DE applications. Compared to other DEs, they present several advantages, such as: large potential for the improvement of electro-mechanical properties through the addition of compounds as shown in Refs. [154, 155];

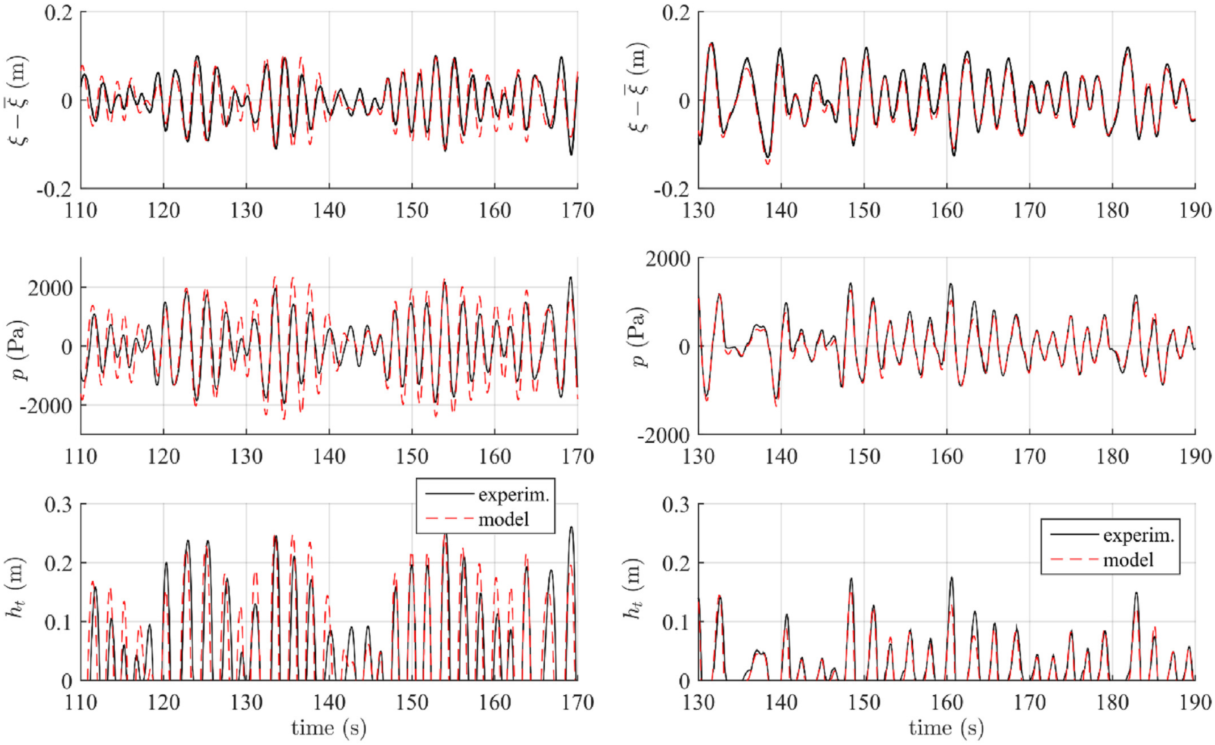

(a) (b)

Fig. 4.8: Comparison of model and experimental time-series of ξ (minus its mean value $\bar{\xi}$), p and h_{t} for two tests with 4 CD-DEGs installed. In (a) results are reported considering the valve closed; in (b) the valve is completely open.

Table 4.2: Estimate of the model error over the time-series of ξ and p.

	ε_ξ	ε_p
Tests with 3 DEGs	0.41	0.42
Tests with 4 DEGs	0.33	0.34
All tests	0.37	0.38

availability of manufacturing processes for high-quality films; and the possibility of manufacturing reliable dielectric-electrode stacks, by depositing carbon-loaded silicone electrodes on the DE layers through tested procedures including blade casting, spray coating or screen printing [141, 156].

4.4.1 Layout and assumptions

A single U-OWC chamber was considered for the simulation, whose geometrical dimensions are presented in Table 4.3 [107]. The upper part of the chamber above the water surface is equipped with four CD-DEGs with the features shown in Table 4.3, installed on top and lateral walls of the collector. The values of the hydraulic loss parameters for the Civitavecchia U-OWC chambers are $C_{\text{dg}} = 0.46$ and $C_{\text{in}} = 0.19$, as provided in Ref. [115]. The properties of the adopted silicone material are described by Madsen et al. [154]. This material is obtained by blending a commercial silicone elastomer (ELASTOSIL LR3043/50) with a silicone oil (LMS-152) in concentrations of 30 phr so as to increase the dielectric properties of the original elastomer, reduce the dielectril losses and soften its elastic stiffness. Although that material has been only investigated in the laboratory and is not a commercial product yet, it is considered to be representative of upcoming materials specifically developed for DE applications. The operating limits of the material are the ultimate rupture stretch, λ_{u}, expressing the maximum extensibility of the elastomer, and the maximum admissible value of the electric field, namely the break-down electric field, E_{BD}. Though in Ref. [154] the break-down field in the unstretched state only is measured (namely, 130 MV/m), based on literature results on different DEs [131] , E_{BD} is assumed to increase proportionally with the stretch λ to the power of r_{e} (see Table 4.3). In order to have a conservative estimate, the value at unitary stretch was considered and taken equal to 100 MV/m. The adopted silicone material is stiffer than the VHB acrylic employed for the experimental campaign conducted at NOEL. Therefore, the chosen pre-stretch is smaller, i.e. equal to 1.3. The total volume of dielectic material employed in all the 4 DEGs is 0.74 m^3. The number of layers, n_{l}, guarantees that the DEG output voltage is below 50 kV. The response of the U-OWC equipped with DEG as PTO is simulated in a set of sea states which tipically occur at the Civitavecchia site. The average wave climate at the installation site is characterized by sea states with JONSWAP spectral distribution [157] (standard peak enhancement factor of 3.3) whose peak

Table 4.3: Features of the considered full-scale U-OWC chamber with DEG PTO.

U-OWC dimensions		DEG PTO features		DE material properties	
h_0	2 m	N_D	4	Hyperelastic parameters	$C_{1,0} = 230\,\text{kPa}$; $C_{0,1} = 0$
d	14.2 m	e	1.4 m	Dielectric constant	$\varepsilon = 3.9 * 8.85 * 10^{-12}\,\text{F/m}$
b_1	1.6 m	t_0	0.05 m	Rupture stretch	$\lambda_u = 8.8$
b_2	3.2 m	λ_p	1.3	Break-down electric field	$E_0 = 100\,\text{MV/m}$
b_3	3.87 m	n_l	80	$E_{BD} = E_0 \lambda^{r_e}$	$r_e = 1$
l_i	5 m				

period, T_p, and significant wave height, H_s, are correlated as follows [150]:

$$T_p = 8.5\pi \sqrt{\frac{H_s}{(4g)}}. \tag{4.19}$$

In order to assess the response of the device in rough sea conditions, significant wave heights of up to 5 m are considered.

4.4.2 CD-DEGs control

The control adopted for the proposed full-scale simulations is based on a simple strategy which does not require the prediction of the incident waves. Only the measured DEG deformations are necessary. Such a strategy has been previously discussed in Refs. [124, 140]. The operation of a DEG is based on a four phases cycle: 1) The DEG expands from the flat configuration ($h_t = 0$) to an inflated configuration (either inwards or outwards) under the action of the external loads. In this phase no voltage is applied on its electrodes. 2) As the deformation (and, therefore, the capacitance) reaches a maximum, the DEG is rapidly charged and its voltage is increased to the maximum value compatible with the break-down limit. During this phase (called priming), a certain amount of electrical energy is initially spent to charge the DEG. 3) When the DEG returns to the flat position and its capacitance decreases, the applied voltage is kept at the maximum value allowed by the break-down condition. During this phase, the DEG generates electrical power. 4) Finally, as the DEG reaches the flat position, that is when the capacitance is minimum, it is rapidly discharged and the stored energy is harvested.

In the simulations, the voltage rise during charging phase (1) and its decrease during discharging phase (4) are simulated as quick first-order dynamics (with a characteristic time much shorter than the full cycle duration).

Based on Eq. (4.14) and Table 4.3, the limiting condition for the maximum voltage (applied during phase (3)), allowed by the break-down, is given by:

$$V \leq \frac{E_0 t_0}{n_l \lambda^{2-r_e}}. \tag{4.20}$$

The stretch λ is not uniform throughout the DEG as shown by Eq. (4.10). Therefore, the operating voltage during phase (3) is obtained by considering the maximum stretch value at the CD-DEG tip for the Eq. (4.20), namely

$$V = \frac{E_0 t_0}{n_\mathrm{l} \lambda_\mathrm{t}^{2-r_\mathrm{e}}} \tag{4.21}$$

where λ_t is the stretch calculated at the DEG tip (corresponding to the condition $R = 0$).

4.4.3 Safety mode operation

A safety valve, with nominal diameter $d_\mathrm{v} = 0.15$ m, is assumed to be installed on the U-OWC chamber. The valve is kept closed in normal operating conditions, and it is gradually opened in the presence of rough sea states to limit the CD-DEG deformation and to allow the continuous operation of the wave power plant. The level of aperture of the valve is adjusted on the basis of the knowledge of the average wave parameters, H_s and/or T_p. According to Madsen et al. [154], the maximum admissible stretch λ_u on the CD-DEGs is theoretically very large. Nevertheless, a conservative threshold value, λ_th, is here assumed that should not be exceeded but for a limited amount of time. The choice of these threshold is considered to increase the durability of the elastomeric material, which is expected to be related to the amplitude of the cyclic stretch variations of the external loads [158]. Here, the conservative value for the streth was assumed to be equal to $\lambda_\mathrm{th} = 2$. Therefore, the level of aperture of the valve and, accordingly, the discharge coefficient C_v in each sea state was selected in such a way to guarantee that the stretch does not exceed λ_th for more than 5% of the simulation time horizon. This objective is achieved in statistical terms by considering the probability that the DEG deformation surpasses a pre-determined upper bound. For a full-scale application operating in real conditions, further analysis should be conducted. The selection of the stretch streshold λ_th should be the consequence of fatigue tests on the adopted DE materials and should be trade-off between the DEG durability and the enrgy production. Indeed, a limitation of the stretch implies on one hand an increase in the membranes lifetime, but on the other hand a reduction in the power output.

4.4.4 Results and discussion

The performance of the full-scale U-OWC have been simulated in a Matlab & Simulink environment. The U-OWC hydrodynamic parameters and the exciting pressure have been computed via the two-dimensional semi-analytical approach proposed by Malara et al. [61]. The convolution integral involved in the computation of the radiation forces (see eq. (4.1)) has been approximated with a state-space model in order to reduce the computational burden [159]. In the simulations, different values of the air chamber height, h_c, were considered to evaluate the performance variations.

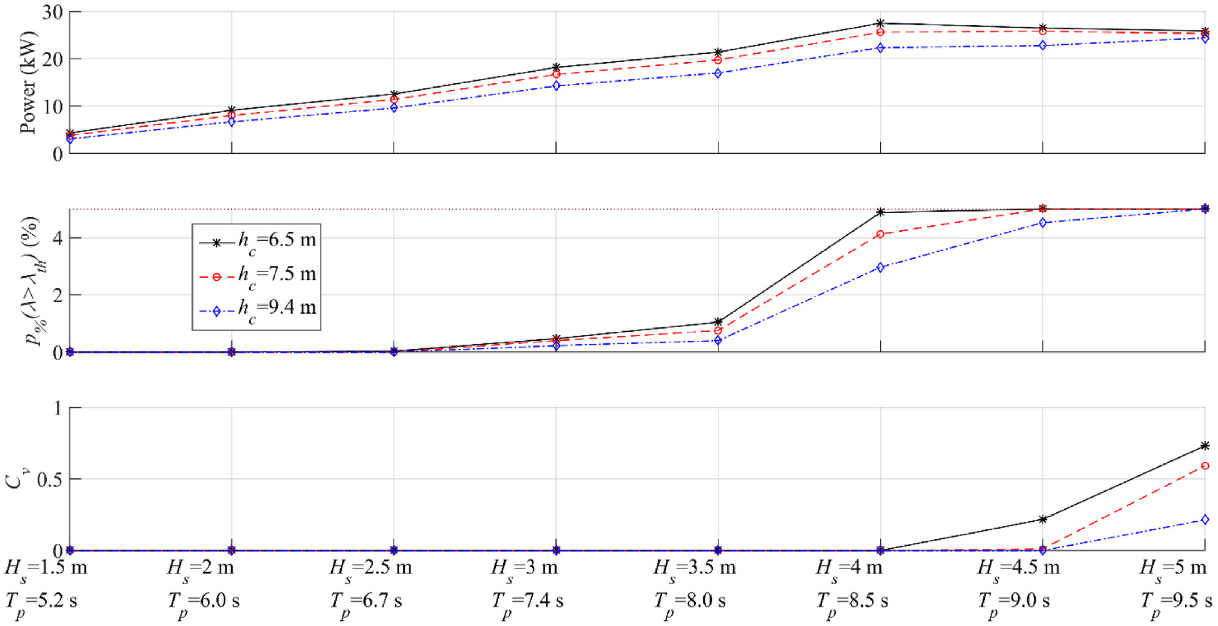

Fig. 4.9: Response and performance of a full-scale U-OWC with DEG PTO for several reference sea states. Top plot: power output. Central plot: expected percentage of operating time during which the DEGs stretch exceeds the threshold value, λ_{th}. Bottom plot: Discharge coefficient expressing the required level of aperture of the security valve in the different sea states.

Sea states with H_{s} ranging from 1.5 to 5 m, with a step of 0.5 m, were considered in the analysis. For each sea state, a simulation with a duration of 200 times the peak period was run, and the average power output was calculated from the DEG instantaneous power, P_{u} (see Eq. (4.15)). For the most energetic sea states, in which a certain degree of aperture of the security valve is required, the calculation of the power output and the valve aperture were obtained through an iterative procedure. The iterative procedure was initiated by setting $C_{\text{v}} = 0$. Then, the coefficient was gradually increased by steps of 0.1 until the percentage occurrence of stretches larger than the threshold value λ_{th} was statistically reduced below 5 %.

The outcomes of the simulations are shown in Fig. 4.9. The top plot shows the U-OWC power converting during the different sea states. The central plot shows the percentage of the simulation time, $p_{\%}$, during which the DEGs stretch λ stays above the threshold λ_{th}. The bottom plot shows the minimum level of aperture of the security valve (expressed by C_{v}) required to keep $p_{\%} \leq 5$ %. For most of the considered sea states the valve can be kept closed with $C_{\text{v}} = 0$ to obtain $p_{\%} \leq 5\%$. The proposed design of the DEG PTO for the U-OWC chamber of Civitavecchia gave rated power outputs between 20 and 30 kW. Similar power results were obtained with simulations involving air turbines as the PTO for the same wave power plant [160]. Specifically, a similar analysis conducted via Monte Carlo simulations was proposed by Malara and Arena in Ref. [67], where power output estimations are provided for four different turbine models (monoplane with and without guide vanes, biplane and contrarotating). A comparison of the power produced by the PTO in sea states with comparable significant wave height and peak period shows that the obtained converted powers are similar. The ceilings of the U-OWC air chambers are located at

$h_c = 9.4$ m above the mean water level. In the simulations the assumed smaller values for h_c proved to increase the power output of the wave energy converter. Specifically, the reduction of h_c implies a smaller air chamber volume, which in turn leads to larger DEG deformations. However, the choice of the value of h_c represents a trade-off between the energetic performance of the wave power plant and safety parameters required by the port infrastructure.

The power converted by the DEGs increases with the significant wave height untill the value of $H_s = 4$ m. In sea states with greater significant wave heigths, the power output curve becomes practically flat as a result of the influence of the security valve. The level of aperture of the valve, required to maintain the membrane stretch within the pre-determined limit, increases with the incident wave power. Besides, in simulations with h_c smaller than the design value, the level of aperture of the valve is required to be larger. In practice, an air chamber with higher ceiling and, therefore, with large compressibility, reduces the performance of the plant but guarantees greater reliability and robustess during the most energetic sea states. At the same time, it allows the achievement of a dramatic reduction in DEG deformation with relatively small diameters of the throttle valve. As it can be noted from Fig. 4.9, during mild sea states, i.e. up to $H_s = 2.5$ m , $p_{\%}$ is equal to 0 because the maximum deformations of the DEGs are constantly below the threshold value without the need to open the valve.

The results of the experimental campaign and of the full-scale simulations demonstrate that DEGs are a promising PTO solution for the U-OWC devices, as they potentially allow to obtain energetic performance similar to those achievable with air turbines. Besides, DEGs are based on a greater architectural simplicity. The presence of a throttle valve installed on the air chamber guarantees safe operation also during the most energetic sea states occurring in a given site, in order to limit the dielectric elastomer deformations.

4.5 Hardware-in-the-loop simulation of wave energy converters

The data collected during the field experimental campaign conducted at the NOEL laboratory and the relative outcomes allowed to assess the feasibility to install DEGs on a U-OWC wave energy converter. Results demonstrated a good agreement between the experimental data and the theoretical model. However, in the experiment described in the previous sections the only mechanical response of the coupled system was investigated. The electrical control of the DEGs was not initially implemented. This is due to the fact that high voltages are necessary and the electronics required to drive the DEGs and produce electricity is not commercially available, but is built ad hoc and, therefore, it is quite expensive. Moreover, the lack of a standard DEG manufacturing process poses a further problem for technologic upscaling. In order to improve the technology and have a broader understanding of the dielectric elastomeric membranes under mechanical and electrical cyclic stress, additional tests are necessary. Hardware-in-the-loop simulations are an important tool to obtain useful information with lower risks and uncertainty for the equipment compared to experiments in wave tanks or at sea. Besides, HIL simulations allow repeatability, a feature which is not found in field experiments, thus enabling to test and refine different control strategies under the same conditions.

A hardware-in-the-loop (HIL) simulator is presented in the following sections. It serves as a dry-run platform to test DEG prototypes and their power electronics, and it faithfully simulates the dynamically coupled response of DEG-OWC plants. The HIL simulations provides a more realistic representation of the DEG response with respect to theoretical models. Indeed, they are not based on mathematical assumptions/simplifications on the generator complex electro-visco-elastic behaviour. Moreover, this HIL framework provides a drastic reduction in the costs and the operational risks in comparison with sea or tank tests.

The simulator includes both software and hardware components. The software is employed to run a real-time hydrodynamic model of an OWC converter, while the hardware part is devoted to drive the physical DEG PTO, emulating the action of an OWC. The software environment solves the equations of motion of an OWC by taking as input the measured signals obtained from the physical system. The hydrodynamic model solution is, in turn, used to drive the mechanical interface.

Wave energy converters have been simulated through HIL in the past few years ([161, 162] and [163]). The objective of those tests was mainly devoted to investigate sophisticated PTO systems. The reason for the adoption of HIL simulations was due to technical and/or economical difficulties to conduct those former experiments directly in wave tank or at sea. In Refs. [161] and [162], hydraulic test rigs for HIL testing of the PTO system for heaving point-absorber WECs are proposed. In Ref. [163], the authors presents a HIL setup to replicate the action of the wave loads on some functional components of a WEC based on a gyroscope, called ISWEC. Application of HIL simulators for OWCs has been demonstrated in Refs. [164, 165], where large-scale laboratory testing of power take-off, control, and grid integration infrastructure has been pursued. A first preliminary and limited demonstration of HIL simulation for a OWC equipped with DEGs was proposed in Ref. [166]. In that work, however, consistent coupling between the hydrodynamic OWC model and the physical DEG was not included. In this research, in contrast, coupling criteria which allow studying a diversity of scenarios are proposed for the first time, including the simulation of full-scale plants equipped with several DEGs, with dimensions which largely differ from those of the tested physical samples. Moreover, compared to [166], the setup employed for the presented simulations represent a significant technological upscaling step, since it allows testing of Watt-scale DEGs, consistently with the maximum scale reached to date by the DEG PTO technology (previously the scale was in the order of 1:80 / 1:70).

The implemented Hardware-in-the-loop simulation is presented in the following sections. Section 4.6 shows an overview of the components included in the HIL simulator. Section 4.7 describes a case study, involving an existing prototype of the U-shaped OWC. The proposed application presents tests in which a fully-functional DEG prototype is coupled with a hydrodynamic model of the model of U-OWC installed at the NOEL laboratory (object of the previous experimental campaign), hence paving the way towards future sea tests on small-scale systems, with electric production, operating in a mild sea climate.

4.6 Hardware-in-the-loop testing of the DEG PTO for oscillating water columns

The OWC WEC consists in a semi-submerged collector (either fixed or floating), partly open towards the sea, housing a water column which is put into oscillation by the incident waves (see Fig. 4.10 (a)). Energy extraction is accomplished by exploiting the alternate compression and expansion of an air volume enclosed between the water column free surface and the collector (i.e., the air chamber). In a previous design, the pneumatic energy was converted into electrical energy by means of a bidirectional air turbine [5]. Recently, a special DEG layout, called a circular diaphragm DEG (CD-DEG), has been proposed as an alternative PTO system [126], which might allow overcoming problems related to the limited adaptability of the turbines to the harsh sea environment and their poor efficiency in the presence of bidirectional flows.

The CD-DEG (Fig. 4.10 (b)) is a pre-stretched multilayer structure made of a set of DE layers separated by compliant electrodes with alternate polarity, forming a deformable capacitor [126]. The multi-layer structure allows applying large electric fields and, hence, the conversion of large energy densities while limiting the operating voltage. The stack is fixed on a circular rigid frame with pre-stretch $\lambda_{\mathrm{p}} = e/e_0$, where e is the radius of the frame and e_O is the radius of the unstretched stack. Due to the elastomer incompressibility, after pre-stretching, the original stack thickness t_0 reduces to $t_0/\lambda_{\mathrm{p}}^2$ (in the flat configuration). The application of a pressure difference on the CD-DEG faces results in a bubble-like expansion of the deformable layers, i.e., an increase in the electrodes area, a decrease in the dielectric layers thickness and, hence, an increase in capacitance. In OWCs equipped with DEGs as PTO, a set of CD-DEGs are mounted on the top of the collector, so as to isolate the air chamber volume from the atmosphere as shown in Fig. 4.10 (a). The cyclic compressions/expansions of the air in the chamber cause alternate outward/inward deformations of the CD-DEG. The mechanical work related to the DEG deformations can be converted into electrical energy, upon appropriate control of the voltage on the CD-DEG [126].

In order to simulate the realistic operation of an OWC equipped with DEGs a HIL system is employed and presented. It combines: a hardware scaled implementation of the OWC air chamber and the DEG PTO, a mechanical hardware which emulates the action of the water column on the chamber, and a software

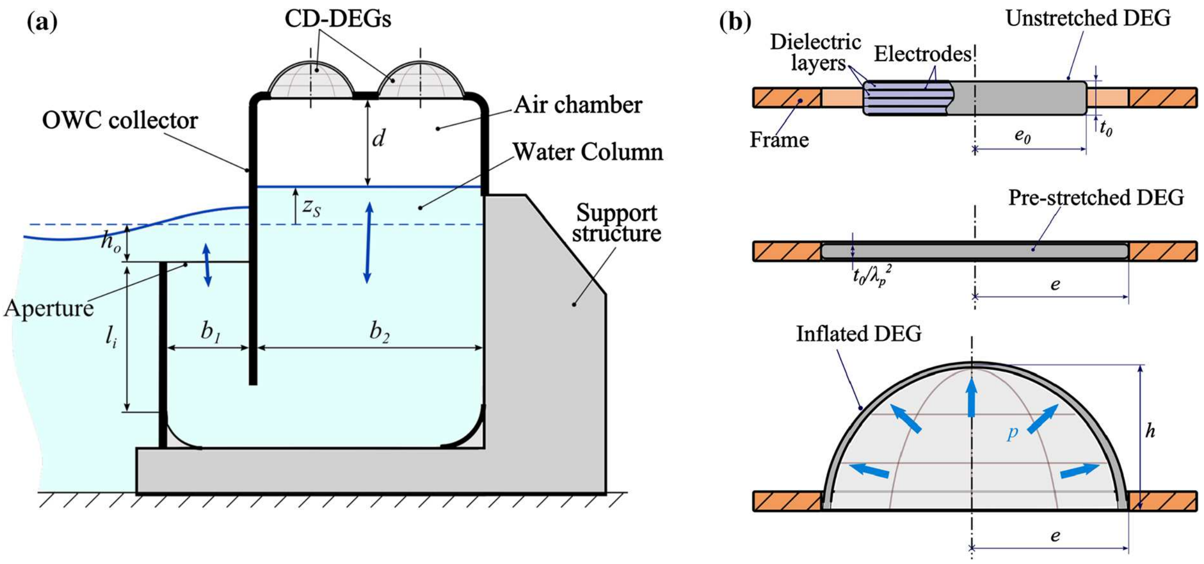

Fig. 4.10: (a) shows a schematic representation of a U-OWC equipped with a set of CD-DEGs. (b) depicts the different configurations of a CD-DEG: unstretched, pre-stretched, and inflated

environment which simulates the OWC hydrodynamic behaviour and executes the DEG's electrical control logics.

A block-diagram showing the elements and the variables flow in HIL simulations is shown in Fig. 4.11 (a). The main components of the HIL simulator are: (1) a fully-functional CD-DEG including the elastomeric unit, the driving electronics and the measuring system; (2) a mechanical driving system composed by a scaled hardware model of an OWC air chamber and position-controlled piston, which emulates the effect of the water column oscillations inside the air chamber; (3) a software environment that solves in real-time the equations of motion for a reference OWC based on a hydrodynamic model and on the instantaneous readings of sensors, and controls the CD-DEG power electronics.

The hydrodynamic model receives the wave parameters, wave height and period, as the simulation input, computes the wave loads, and solves the OWC equation of motion in real-time. The simulated displacement of the water column inside the OWC chamber is used to command the motion of the hardware piston. The relative air pressure measured in the cylinder is, in turn, fed back into the model and its contribution is accounted for in the equation of motion. The voltage applied on the DEG through the power electronics is controlled as a function of the measured control variables (here, the pressure on the CD-DEG). A coupling block is employed for scaling the measured pressure signals and commanded piston displacements. These corrections are required to guarantee a consistent coupled dynamic behaviour of the hardware and the simulated environment. Thus, the proposed HIL architecture potentially allows for the simulation of different scenarios with different OWC geometries and CD-DEG with dimensional features which differ from those of the physical prototype. In the following subsections, the main components of

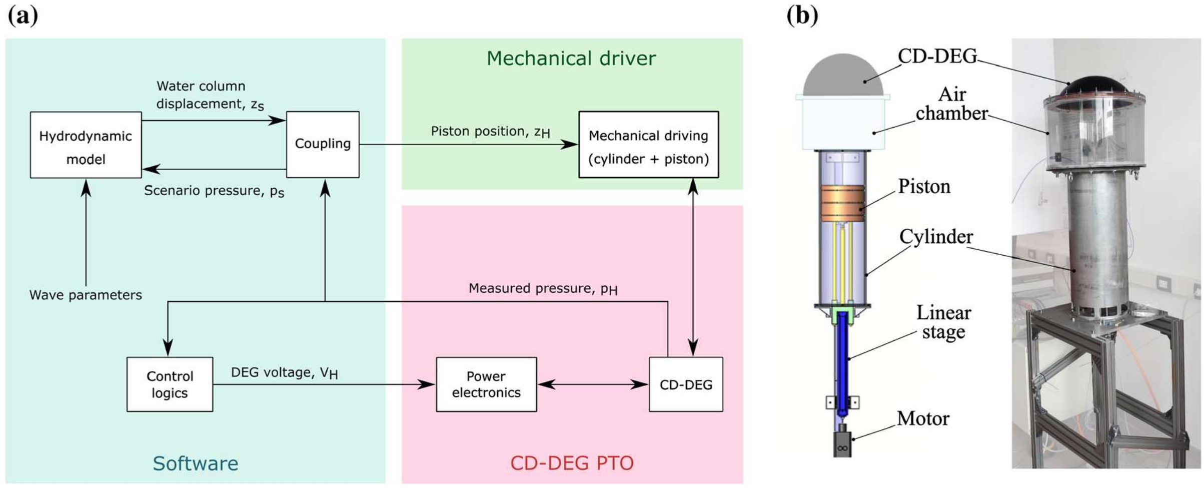

Fig. 4.11: (a) Block-diagram of HIL simulations combining a software hydrodynamic model of an OWC and a physical model of the air chamber-DEG assembly. (b) Schematic drawing and picture of the experimental setup for HIL testing

the HIL simulator are briefly described.

4.6.1 Hydrodynamic model

A nonlinear lumped-parameter hydrodynamic model is used for describing the OWC oscillations in the time domain. This modelling approach is widely used in WEC modelling, as suggested, for instance, in [66] and [61]. The model describes the water column oscillations via the extended Bernoulli equation for unsteady flow. This approach is applied under the assumptions that the OWC collector is fixed and the water column width and breadth are small compared to the wavelength, so that the water column displacement is approximated by the oscillation of a rigid vertical piston. The total head at the OWC inlet is assumed to be equal to the wave pressure head, thus neglecting other contributions. The wave field in front of the structure is described by the potential flow theory. Specifically, the computation of the wave pressure head is obtained in the framework of the linear potential wave theory [144]. The wave pressure at the center of the U-duct opening is computed via the so-called Cummins equation [143], which takes into account the effects of the hydrodynamic memory and the hydrodynamic added mass. The equation governing the water column dynamics [61] is:

$$[M(z_S)+A(\infty)]\ddot{z}_S+C(z_S,\dot{z}_S)\dot{z}_S+\frac{1}{g}\int_{-\infty}^{t}K(\tau)\dot{z}_S(t-\tau)d\tau+z_S+\frac{1}{\rho g}p_S=\frac{1}{\rho g}\Delta p^{(D)} \tag{4.22}$$

where p_S is the relative pressure in the air chamber; $A(\infty)$ is the infinite-frequency added mass; $K(t)$ is called the retardation function; $M(z_S)$ is the time-varying inertia of the water column within the collector, which includes the effect of mass transfer between the water column and the wave field: it depends on the instantaneous water column level z_S, considered as the upward elevation with respect to the mean water level, and the OWC geometry; finally, $C(z_S, \dot{z}_S)$ is a damping coefficient associated with the kinetic head of the water column, which depends on the water column position and velocity and on the geometrical parameters [61]. Commonly, the calculation of the hydrodynamic parameters $(A(\infty), K(t))$ and the excitation is obtained via boundary-element codes [167], although analytical solutions are available for some specific geometrical configurations [61].

The excitation of the system is given by the wave pressure $\Delta p^{(D)}$ calculated at the OWC inlet in a diffracted wave field. The wave pressure $\Delta p^{(D)}$ is computed as a function of the input wave parameters. $\Delta p^{(D)}$ is represented by a sinusoidal wave pressure in the case of regular waves, and as a finite sum of harmonic components for irregular waves, where the amplitudes follow a prescribed spectral distribution [168].

4.6.2 Coupling block

The general case of a OWC equipped with DEGs as PTO is considered for the simulations in the HIL. DEGs used in the HIL setup are similar to the physical prototype but present differences in several dimensional and layout features. DEG-PTOs in the simulated system and in the hardware prototype are made with the same materials. Nevertheless, they can differ in some aspects. Indeed, the simulated OWC can be equipped with several CD-DEGs installed on the same air chamber, while the HIL setup can host a single physical CD-DEG sample; the simulated CD-DEGs can have larger dimensions than those of the physical sample, which are constrained by hardware setup limits; the simulated CD-DEGs can be manufactured by using a different number of layers compared to the hardware setup; the geoemtrical parameters of the simulated OWC can be different, i.e. larger, with respect to the dimensions of the physical setup.

The dynamic equivalence between the simulated and the hardware systems can be obtained by implementing a coupling block (see Fig. 4.11 (a)) in the HIL scheme, which applies corrections to the air pressure measured in the HIL and fed into the software solver, and to the commanded piston position calculated through the simulated water column displacement obtained by solving the hydrodynamic model. These corrections are calculated so as to respect some conditions. Specifically, the procedure followed in these work has the objective to guarantee that the physical CD-DEG sample is subject to the same strain and electric field time history as the DEGs in the simulated scenario. The same time scale (e.g., operating frequencies) is adopted for the simulated scenario and for the physical experiment in the HIL. The variables of the simulated scenario and of the hardware setup were identified by denoting the first with subscript S and the latter with subscript H. The deformed CD-DEG behaves as a thin elastomeric shell. Therefore, the relative air pressure in the OWC air chamber is proportional to the CD-DEG initial thickness and the inverse of the base radius, with the proportionality factor (depending on the strain and the elastic properties) being the same in the scenario and the experiment. The relation between the air chamber pressure in the simulated scenario and the one measured in the HIL is expressed as:

$$\frac{p_{\mathrm{S}}}{p_{\mathrm{H}}} = \frac{t_{0\mathrm{S}} e_{\mathrm{H}}}{t_{0\mathrm{H}} e_{\mathrm{S}}} \tag{4.23}$$

where t_0 and e, with their subscripts relative to the HIL and the simulated scenario, indicate the thickness of the DEG in the unstretched configuration and the CD-DEG's radius (see Fig. 1 b). The right hand side of (4.23) represents the correction factor to be applied to the measured pressure p_{H} so as to obtain the pressure p_{S} to be fed in the software model, into (4.22).

The axial displacement of the CD-DEG centre in the experiment (h_{H}) and in the scenario (h_{S}) are related by assuming that the CD-DEGs strain in the experiment and in the scenario are the same:

$$\frac{h_{\mathrm{S}}}{h_{\mathrm{H}}} = \frac{e_{\mathrm{S}}}{e_{\mathrm{H}}} \tag{4.24}$$

The relationship between the water column displacement in the scenario z_{S} and the commanded piston position z_{H} is identified by assuming that the air in the OWC chamber is described by adiabatic transformations. The variations of the air chamber volume, due to the water column oscillations inside the chamber and the consequent deformation of the DEGs, are small compared to the initial volume. Therefore, the air chamber response can be described through linearized models:

$$\frac{p_{\mathrm{S}}}{p_{\mathrm{atm}}} = \frac{\gamma}{V_{\mathrm{S}}} \left(S_{\mathrm{S}} z_{\mathrm{S}} - N_{\mathrm{S}} \Omega_{\mathrm{S}} \right) \tag{4.25a}$$

$$\frac{p_{\mathrm{H}}}{p_{\mathrm{atm}}} = \frac{\gamma}{V_{\mathrm{H}}} \left(S_{\mathrm{H}} z_{\mathrm{H}} - \Omega_{\mathrm{H}} \right) \tag{4.25b}$$

where p_{atm} is the absolute atmospheric pressure; γ is the specific heat ratio of air; V_{S} and V_{H} are the initial air chamber volumes for the scenario and the HIL; S_S is the simulated water column cross section, whereas S_{H} is the hardware piston cross section; N_{S} is the number of CD-DEGs installed on the air chamber in the simulated scenario. Ω_{S} and Ω_{H} are the volumes subtended by a CD-DEG in the scenario and in the experiment (positive for outward expansions). The value of these volumes is related to the DEG strain and radius [126] as expressed by:

$$\frac{\Omega_{\mathrm{S}}}{\Omega_{\mathrm{H}}} = \frac{e_{\mathrm{S}}^3}{e_{\mathrm{H}}^3} \tag{4.26}$$

Using Eqs. from (4.23) to (4.26), leads to the following relationship for the commanded piston displacement:

$$z_{\mathrm{H}} = \frac{1}{N_{\mathrm{S}}}\frac{S_{\mathrm{S}}}{S_{\mathrm{H}}}\frac{e_{\mathrm{H}}^{3}}{e_{\mathrm{S}}^{3}} z_{\mathrm{S}} + \left(\frac{V_{\mathrm{H}}}{\gamma S_{\mathrm{H}}} - \frac{t_{0\mathrm{S}} e_{\mathrm{H}}^{4}}{t_{0\mathrm{H}} e_{\mathrm{S}}^{4}}\frac{V_{\mathrm{S}}}{\gamma N_{\mathrm{S}} S_{\mathrm{H}}}\right)\frac{p_{\mathrm{H}}}{p_{\mathrm{atm}}} \tag{4.27}$$

According to (4.27), the commanded displacement z_{H} is a sum of two terms: a kinematic term proportional to the simulated water column displacement z_{S}, and a term which includes the finite air chamber compressibility [116].

As mentioned before, the DEGs in the setup and in the simulated scenario are subject to the same electric field time-history. Since the power density (per unit dielectric material volume) converted by a CD-DEG in a cycle depends on the strain and the applied electric field [126], the DEGs generate the same electrical power density. HIL simulations allow to test DEGs with different features. For example, the CD-DEGs in the scenario and in the setup can present a different number of layers (n_{L_S} and n_{L_H} respectively). Therefore, the voltage, V_{H}, used in the HIL tests should be scaled on the basis of that envisaged in the scenario, V_{S}, according to the following relation, which guarantees that the electric field is the same:

$$\frac{V_{\mathrm{S}}}{V_{\mathrm{H}}} = \frac{n_{L_H} t_{0\mathrm{S}}}{n_{L_S} t_{0\mathrm{H}}}. \tag{4.28}$$

Eq. (4.28) allows to identify a suitable number of layers n_{L_s} for the scenario, so as to limit the output voltage V_{S} to respect the technical constraints imposed by the power electronics. The total power output P_{S} achievable in the simulation scenario is obtained by multiplying the power, P_{H}, measured in the HIL simulations, by the ratio of the total dielectric material volumes employed in the scenario and in the physical prototype:

$$\frac{P_{\mathrm{S}}}{P_{\mathrm{H}}} = \frac{N_{\mathrm{S}} e_{\mathrm{S}}^{2} t_{0\mathrm{S}}}{e_{\mathrm{H}}^{2} t_{0\mathrm{H}}}. \tag{4.29}$$

This equation implies that the efficiency of the CD-DEG is the same in the physical prototype and in the simulated scenario. Thereforem the scale-dependent effects are neglected. This represents, in general, a conservative assumption. Indeed, in these tests a low efficient material, the acrylic VHB 4905, is employed. The CD-DEGs practically developed for full-scale applications should be the result of optimization manufacturing processes, thus showing better efficiencies and performance which are more stable over time compared to the physical samples used in HIL tests.

On the basis of the presented scaling expressions, HIL simulations can be employed for testing OWCs equipped with DEGs of different scales and dimensions, including the case of full-scale wave power plant. Besides, differently from the scaling rules employed for tank testing of DEG-OWCs (based on Froude scaling) [142], the proposed procedure allows to select, independently from each other, diameter and thickness scale factors of the DEG to be used in the HIL simulator with respect to the desired simulated scenario. This advantage provides better flexibility in terms of manufacturing. The behaviour/performance obtained from HIL tests should be more reliable when the dimensions of the tested DEG prototypes are similar to those in the considered simulated scenario. However, HIL simulations of large-scale systems carried out by employing small-scale DEGs would be affected by errors related to scale-sensitive effects, such as the DEG inertia, the electrodes resistance, not included in the coupling block.

4.6.3 Mechanical driver

The mechanical driving system includes a vertical pneumatic cylinder made of steel that has been specifically designed and built. The system, shown in Fig. 4.11 (b), is made of a main driving cylinder-piston system with a nominal diameter of 300 mm (that provides $S_{\mathrm{H}} = 707\ \mathrm{cm}^2$) and stroke of 500 mm. The piston moves linearly and is driven by a ball-screw stage produced by the company Festo with pitch of 20 mm and maximum force of 4500 N. The piston is actuated by an AKM52L Kollmorgen brushless motor with a rated power of 2.4 kW, continuous torque (at stall) of 8.67 Nm, and maximum speed of 4590 rpm. The pneumatic cylinder is the base for a polycarbonate cylinder that is installed at its top, on which the CD-DEG assembly can be secured through a set of flanges. Based on the volume swept by the piston and the maximum useful force (after friction losses in the O-rings), the setup can hold CD-DEGs with diameter of up to 500 mm and thickness of up to 0.2 mm after pre-stretch (about 40 cm^3 of dielectric material volume). The CD-DEG installed on the HIL setup experiences two conversion cycles during a full oscillation of the piston, an upward and a downward deformation. If convertible energy densities of $0.1-0.2\ \mathrm{J/cm}^3$ per unit of dielectric material volume [133] are onsidered, the dielectic elastomer sample can produce power outputs in the range of 10^0-10^1 W. It is supposed that the piston oscillates with a frequency of $0.2-1$ Hz, that is a range similar to that adopted in wave tanks for the testing wave energy converter prototypes at a scale between 1:30 and 1:10 of a hypothetical full-scale wave power plant installed at sea [169].

4.6.4 Power electronics and control logics

The DEG is controlled on the basis of the instantaneous measurement of the membrane deformation. No prediction strategy of the wave field is required. The control logics implemented in this work and the power electronics adopted to drive the HIL simulator are the same as those used in Ref. [142]. A simple circuit (Fig. 4.12) is used, which includes a HV amplifier (10 / 10 B-HS by TREK), the CD-DEG prototype, three HV switches (HM12-1A69-150 by MEDER Electronics), a constant capacitor C_{a}, and a resistor R. The circuit components are necessary to drive the DEG, whose operation is based on a four-phase control cycle corresponding to a full oscillation of the DEG between the flat and the maximally

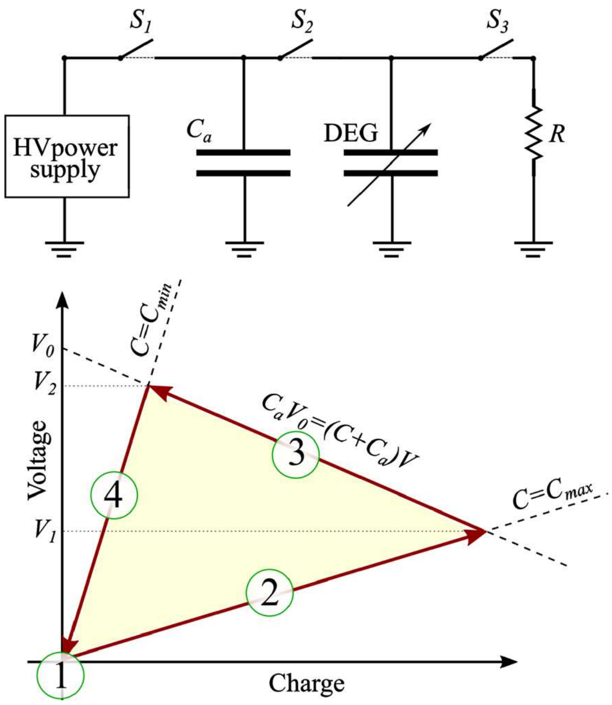

Fig. 4.12: Driving circuit for the CD-DEG and representation of the four-phase control cycle on a charge–voltage diagram

expanded(outwards or inwards) configuration. The operation phases and the relative steps to be followed in the circuit are described in the following. (1) The CD-DEG is deformed due to the oscillations of the piston which simulates the oscillations of the water column in the OWC chamber. During this phase the CD-DEG is kept electrically uncharged, while C_a is charged to a fixed voltage V_0 by the power supply. Referring to the circuit in Fig. 4.12, the switch S_1 is kept closed, while S_2 and S_3 are open. (2) When the DEG deformation, and therefore its capacitance ($C = C_\mathrm{max}$), reaches a maximum, S_1 is opened, S_2 is closed and the parallel of C_a and the CD-DEG are subject to the equilibrium voltage V_1. (3) While the membrane deformation decreases (towards the flat position), pressure makes work against the charges and mechanical energy is converted into electrostatic energy. During this phase, S_2 is kept closed, and the total charge on the DEG and C_a remains constant. (4) Finally, when the CD-DEG reaches its flat position, the maximum voltage V_2 and minimum capacitance C_min are obtained. In this phase S_2 is opened, S_3 is closed and the CD-DEG is rapidly discharged through R.

A schematic representation of the control cycle of the CD-DEG in a charge-voltage diagram is described in Fig. 4.12: during phases (2) and (4) (quick charging/discharging transients) the CD-DEG position and, tehrefore, it capacitance, remains ideally constant, whereas during phase (3) the state variables follow a trajectory which depends on the charge balance for the parallel of the CD-DEG and C_a. As a matter of fact, since the phases (2) and (4) do not occur instantaneously, the capacitance might be subject to variations. Alterations in the DEG capacitance can also be induced by the large voltage variations associated to charging/discharging operations (as in the case of DE actuators [170]). However, these variations can be neglected at the scale of the experimental CD-DEG prototypes installed in the HIL setup, but they should be included when simulating larger-scale systems [142].

The in-parallel capacitance C_{a}, as proposed in Ref. [133], has been introduced in order to increase the cyclic convertible energy. At the same time, it has the function of limiting the voltage rise on the CD-DEG during the generation phase (3). The circuit implemented for the proposed simulations does not include devices to store the converted energy. Nevertheless, the net electrical energy generated by the CD-DEG in a cycle, can be easily obtained through the following expression:

$$\mathscr{E} = \frac{1}{2}C_{\mathrm{min}}V_2^2 - \frac{1}{2}C_{\mathrm{max}}V_1^2 + \frac{1}{2}C_a\left(V_2^2 - V_1^2\right) \tag{4.30}$$

The first term in the right hand side of eq. (4.30) is the energy recovered from the DEG during the last phase, the second term represents the amount of energy that is initially spent to prime the DEG, while the third term is the energy transferred to the in-parallel capacitance C_{a} during phase (3). The maximum capacitance C_{max} reached by the CD-DEG in a cycle is related to the maximum deformation, and it can be estimated from the voltage drop relative to C_{a} during the priming phase:

$$C_{\mathrm{max}} = C_{\mathrm{a}}\left(\frac{V_0}{V_1} - 1\right) \tag{4.31}$$

The minimum capacitance C_{min} is constant and it is measured in the flat CD-DEG configuration. This implies that also the voltage V_2 is nearly constant during the whole operating cycle (apart from minor fluctuations due to the effect of charge leaks). The value of the voltage V_2 is always below the charging voltage V_0, as shown in Fig. 4.12.

The activation of the different swithces of the circuits during the cycle phases are controlled according to the measurement of the air pressure in the chamber. Other alternative measured or simulated state variables, such as charge or voltage on the DEG, can be employed to determine the transition from a phase to another. In this work, air pressure is considered because it is almost proportional to the DEG deformation and is directly measured through pressure transducers. In detail, switching from phase (1) to phase (2) occurs when the pressure reaches a maxima/minima; switching from phase (3) to phase (4) is determined by the zero-crossings of the pressure profile; the length of priming and discharging phases ((2),(4)) depends on characteristic charging/discharging times imposed by the circuit electrical dynamics. The components of the power electronics employed for the presented HIL simulations were selected due to their simplicity and capability to estimate the generated electrical energy in a straightforward way. Other power electronics, such as advanced circuits, can be employed with the adoption of devices to store the producded energy instead of draining it through the resistor.

4.6.5 Computation and measurement system

Matlab and Simulink scripts are employed to manage the software for data acquisition, to drive the piston oscillations, and to control the CD-DEG. Specifically, the Simulink Real-Time software environment is run on a real-time target machine by Speedgoat at a sampling frequency of 1 kHz. The target control machine is put into communication with the motor driver through the EtherCAT protocol.

The measurement of the voltages on the CD-DEG and on C_a is obtained through two high voltage (HV) probes. The DEG deformation is computed as the result of the postprocessing of the frames acquired by a high-speed camera (Point Grey GS3-U3-23S6M-C with lens 250 F6C). Specifically, the time history of the axial displacement of the tip of the membrane is obtained by applying the procedure described in Ref. [142]. The instantaneous position of the piston position is provided by an encoder integrated in the motor. A pressure sensor (MPX12 by Freescale Semiconductor with custom conditioning circuit) is used to measure the air pressure in the chamber.

4.7 Case study: the U-OWC plant with CD-DEG PTO

The Hardware-In-The-Loop system described in the previous sections was employed to simulate a scenario in which the CD-DEG is used as the PTO of a U-OWC chamber. The U-OWC is a special type of OWC with a U-shaped collector, provided with an inlet vertical duct, (as shown in Fig. 4.10 (a)) whose geometrical parameters are selected in order to match natural frequency of the device with target wave frequencies [66].

The reference prototype was the U-OWC pilot plant installed at NOEL laboratory of the Mediterranea University of Reggio Calabria. The U-OWC dimensions are (as shown in Fig. 4.10 (a)): $b_1 = 0.5$ m;$b_2 =$ 1 m;$h_\mathrm{o} = 0.57$ m;$l_\mathrm{i} = 0.8$ m;$d = 1.9$ m; and a width of 1.27 m The plant includes three independent chambers and it is a 1: 8 scaled hardware model of a U-OWC wave power plant meant for installation in the Mediterranean Sea. In this work, the U-OWC/DEG configuration tested at NOEL and described previously was implemented. One of the lateral chambers of the plant was equipped with $N_S = 4$ CD-DEGs made of acrylic elastomer VHB 4905 (see Fig. 4.3). As already mentioned before, those sea tests were aimed at studying only the passive mechanical response of the U-OWC/DEG system. No electrical activation and control were provided to the membranes. Here, in contrast, an electrically functional CD-DEG prototype was implemented to study the fully-coupled hydro-electro-viscoelastic response of the system in a set of sea conditions. The acrylic VHB 4905 was chosen as dielectric elastomeric material because of its ease of handling, pre-stretching and stacking which make it a suitable material for tests. The physical CD-DEG sample was built in order to have the same base radius ($e_H = e_S = 0.195$ m) and pre-stretch coefficient ($\lambda_p = 3.44$) as the CD-DEGs tested at NOEL. The CD-DEGs in the scenario had an unstretched thickness $t_{0S} = 5$ mm (0.42 mm after pre-stretch), whereas the physical sample designed for the HIL setup has unstretched thickness $t_{0H} = 3$ mm (0.25 mm after pre-stretch). This choice was motivated and limited by the possibility to use electric fields in the order of $10^1 - 10^2$kV/mm (consistent with the breakdown limits of the reference elastomer [133]) with a limited number of DE layers in the stack and operating voltages below 10 kV. Compared to the previous experimental campaign at sea, in this work a set of milder sea states was considered due to some mechanical limits of the HIL setup. Specific attention was devoted to operating conditions in which the OWC air chamber is held closed, differently from the sea tests at NOEL where a safety valve, held partly open, was present, as shown in Fig. 4.3). The response of the coupled system was obtained in the presence of both regular (sinusoidal) and irregular (stochastic) [168] wave excitation, with wave heights ranging form 5 to 15 cm and wave periods up to 3.5 s. Although these sea states are rather mild with respect to typical conditions at the NOEL test site, they allow safe operation of the CD-DEGs. Therefore, they represent reasonable realistic conditions for the implementation of pilot sea tests with electrically driven DEGs in the near future. In order to investigate the response of the system subject to more energetic sea states, the U-OWC should be equipped with CD-DEGs with larger diameter and thickness, made of more performing dielectric materials (e.g., silicone dielectric with carbon-loaded silicone electrodes [171]). However, this would require further effort in terms of technological progress, such as manufacturing and power electronics implementation. It would be a feasible test scenario only in a long-term perspective.

4.7.1 Hydrodynamic model and coupling

The U-OWC dynamics is obtained from Eq. (4.22), by properly susbstituting the mass $M(z)$ and the damping $C(z,\dot{z})$ terms with the following expressions [61]:

$$M(z_{\mathrm{S}}) = \frac{1+C_{\mathrm{in}}}{g}\left(\frac{b_2}{b_1}l_{\mathrm{i}} + l_{\mathrm{i}} + h + z_{\mathrm{S}}\right) + \frac{b_2}{gb_1}A(\infty) \tag{4.32a}$$

$$C(z_{\mathrm{S}},\dot{z}_{\mathrm{S}}) = \frac{1}{2g}\left\{1 + C_{\mathrm{dg}}\left[\frac{l_{\mathrm{i}}}{R_{h1}}\left(\frac{b_2}{b_1}\right)^2 + \frac{l_{\mathrm{i}} + h + z_{\mathrm{S}}}{R_{h2}}\right]\right\}|\dot{z}| \tag{4.32b}$$

The form presented here includes additional terms which account for hydraulic head losses according to the so-called instantaneous acceleration based model [60]. The values of the empirical coefficients appearing in (4.32) are taken from Ref. [60], where they are estimated to be $C_{\mathrm{in}} = 0.13$ and $C_{\mathrm{dg}} = 0.71$. R_{h1} and R_{h2} are called hydraulic radii of the vertical duct and of the inner chamber respectively, and they are defined as follows:

$$R_{h1} = \frac{b_1 b_3}{2(b_1+b_3)}, R_{h2} = \frac{b_2 b_3}{2(b_2+b_3)} \tag{4.33}$$

The hydrodynamic parameters $(A(\infty), K(t))$ and the excitation pressure as a function of the wave parameters are computed by employing the analytical model presented in [61]. The coupling of the simulation and the physical variables, expressed by eq. (4.27) requires the piston position z_{H} to be commanded as a function of the water column displacement in the simulated scenario, z_{S}, and the air pressure measured during the HIL simulation, p_{H}, which is naturally affected by noise. The presence of a moderate noise on the recorded p_{H} does not affect the computation of z_{S}, since the solution of (4.22) involves a double integration operation, which guarantees a smooth profile for z_{S}. On the contrary, the additional term proportional to p_{H} in the expression of z_{H} (eq. (4.27)) can lead to vibrations (which are especially critical because of the friction between the piston and the cylinder) or to close-loop instability in case signal filtering is applied. In order to overcome this issue, in this work the measured air pressure appearing in eq. (4.27) was replaced by a static averaged experimental value of the air chamber pressure, $p_{\mathrm{H}} = \tilde{p}_{\mathrm{H}}(z_{\mathrm{H}})$. In this way, z_{H} is expressed exclusively as a function of z_{S}. This choice had the effect to guarantee a smooth motion of the piston (regardless of pressure signal filtering quality), with the introduction of a tolerable error.

4.7.2 CD-DEG sample and power electronics

The CD-DEG has been built using the procedure introduced in [142]. The sample is conceived according to a multi-layer structure (as shown Fig. 4.10 (b)) with two in-parallel dielectric layers separated by three carbon grease (MG-Chemicals 846) electrodes. Two ground electrodes are connected to the outer faces of the stack, and a HV electrode is installed in the middle. Three VHB 4905 layers are bonded together to form each of the two dielectric layers (1.5 mm thick before pre-stretch).

The capacitance of the CD-DEG in the flat equilibrium configuration, $C_{\min}$, was measured and had a value of 76.5 nF. The DEG was electrically controlled through the circuit and power electronics described in the previous sections. The use of an in-parallel capacitance $C_{\mathrm{a}} = 300\mathrm{nF}$, and a resistance $R = 100\mathrm{k}\Omega$ were included. A voltage $V_0 = 9\mathrm{kV}$ was employed to prime C_{a}, leading to maximum electric fields on the CD-DEG in the order of 130 kV/mm, as described in Ref. [142].

4.7.3 HIL setup validation

Several tests were carrid out to validate the HIL setup. The reliability of the system was assess by checking the presence of possible latencies, delays in the control loop and by verifying the proper functioning related to the coupling criteria. Similarly to [161], the HIL framework and setup to reproduce the results of a reference hydroelastic model of the U-OWC and the DEG PTO were supervised. The model presented and validated via sea tests in the previous sections and reported in Ref. [102], is the same that was employed in the HIL formulation together with the numerical model of the CD-DEG. Compared to [102], in the reference model the CD-DEG elastic parameters were updated in order to better describe the deformations and the pressure response of the DEG sample under investigation, so as to reduce the effect of the elastic parameters uncertainty. The oscillation amplitudes of some relevant physical variables were investigated and a comparison between the model and the HIL results was proposed in a set of regular wave tests with periods between 1.5 s and 3.5 s, where steps of 0.5 s were adopted. In Fig. 4.13 a comparison of the oscillation amplitudes (HIL simulations vs. reference model) of the water column displacement (Fig. 4.13 (a)) and the relative air pressure (Fig. 4.13 (b)) is depicted for a wave height of 50 mm. HIL data in the plots are projected to the scenario scale by using the correction rules introduced in the coupling block. The plots confirm that the HIL simulations properly replicate the behaviour and the amplitudes of the model, thus proving the reliability and stability of the closed-loop coupling of the software model and the physical setup. However, small discrepancies between the model and the HIL results can be observed. Specifically, mismatches related to the free surface elevation data are larger than those in the air pressure data. For example, for a frequency of 0.5 Hz, the model overestimates the free surface elevation, but it estimates the pressure with a certain accuracy. This behaviour is related to inaccuracies and simplifications in the CD-DEG model, with consequences on the relationship between water surface and pressure oscillations. The simplifications introduced in the CD-DEG model are not presented in the HIL simulator, where the CD-DEG model is replaced with the physical prototype [124]. The higher differences between the reference model and the HIL results are observed at wave frequencies between 0.4 and 0.5 Hz, where the oscillation amplitudes are at their maximum because the system works close to resonance conditions. The inaccuracies are probably due to the CD-DEG viscous dissipations, which are not accounted for in the model and can affect the system response when large water column oscillations occur. Therefore, the representation of the response of the system at resonance conditions through a mathematical model is slightly inaccurate. However, the analysis of the response in resonane conditions is of paramount importance because the highest power performance occur. This aspect represents a further motivation for the employment of HIL simulations as a support to theoretical models to effectively investigate the response of a system.

4.7.4 Results

HIL simulations have been carried out to examine the response of the considered U-OWC/DEG system excited by a variety of wave conditions. The plots shown in Fig. 4.14 provide portions of time-series of the measured variables. Specifically, the behaviour of the piston position z_{H}, the air chamber pressure p_{H}, the membrane tip displacement h_{H} and the voltage V_{H}) are represented in two tests in which the U-OWC in the considered scenario was subject to incident irregular waves compatible with a JONSWAP frequency spectrum [168], similar to the sea states occurring at the NOEL site [172].

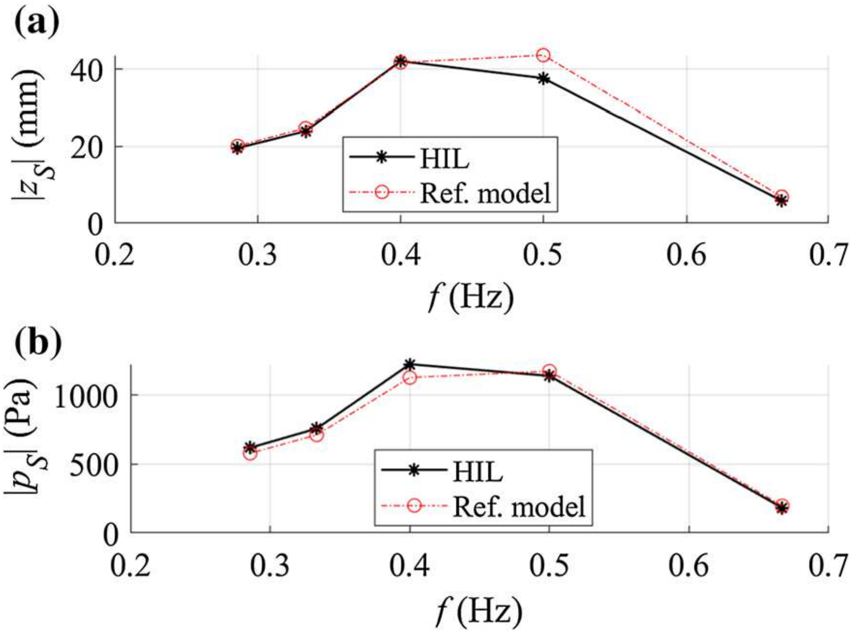

Fig. 4.13: Validation of the HIL setup against the U-OWC/ DEG model in a set of monochromatic tests with height H = 50 mm at different frequencies. (a) shows the comparison of oscillation amplitudes of the water column oscillations; (b) shows the oscillation amplitudes of the air chamber pressure

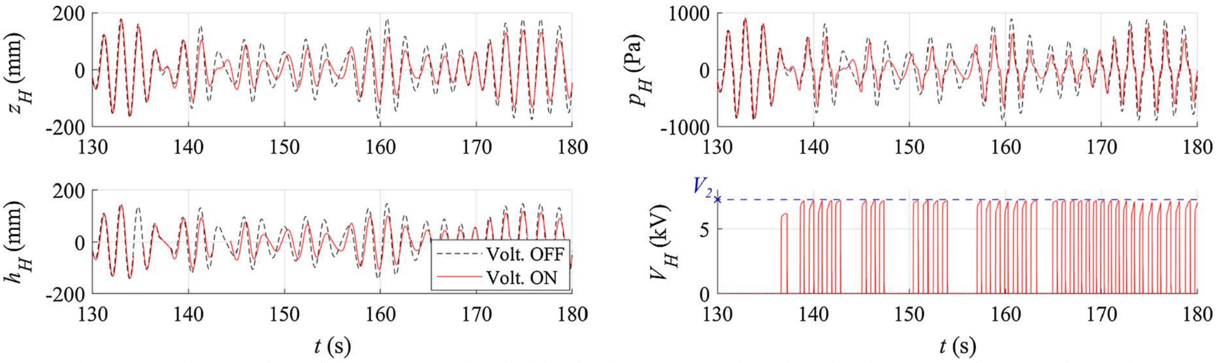

Fig. 4.14: Time-series of the measured variables in the HIL test-bench. The datasets refer to an irregular sea state with JONSWAP spectral distribution, significant wave height $H_\mathrm{s} = 150$ mm, peak period $T_\mathrm{p} = 1.65$ s. Dashed lines refer to a passive mechanical test, whereas solid lines refer to a test with active electrical control

The plots are relative to a mild sea state with significant wave height $H_\mathrm{s} = 0.15$ m, peak period $T_\mathrm{p} = 1.65$ s and peak enhancement factor of 3.3. The figure compares the results of two tests under the same excitation conditions. The first is a passive test with no voltage applied on the DEG. The second test shows the response of the system where the DEG is electrically controlled and power is converted. The two datasets shows an initial overlap in the first recorded seconds, as no voltage is initially applied on the DEG in both tests. Once the voltage is applied on the DEG the system dynamics is modified, with a consequent reduction of the average amplitude of the oscillations. This reduction is mainly due to the CD-DEG PTO damping. The analysis of the voltage time-series shows that the voltage V_1 reached by the CD-DEG after priming is different for each cycle, because it is related to the different deformation amplitudes reached by the membrane. On the other hand, the maximum voltage V_2 is almost the same (i.e., around 7 kV) for all the considered cycles with the exception of the initial transient. The voltage on the DEG was driven based on reaching a certain value of deformation, and therefore, of pressure. DEGs were not activated during small cycles where the measured air pressure module was below 200 Pa. It was estimated that with these small oscillations of the membrane the electrical losses required to prime the DEG would be larger than the produced energy. The average generated power in the test with activation of the CD-DEGs was obtained as the sum of the energies over the different cycles, as expressed by eq. (4.30), divided by the total duration of the record. The highest peaks of the generated power, recorded during the cycles with maximum deformation, were around 1.2 W with an average generated power (over a time window of 120 s) of 0.5 W. The power converted during the HIL simulations can be projected to the power achievable in the scenario by exploiting the eq. (4.29). An average power of 3.2 W can be obtained in the considered scenario, with peaks of 7.7 W. Although it seems a minimal amount of power, it represents a significant fraction (over 15 % in average) of the power available in the considered mild sea state. Several simulations were carried out to characterize the response the coupled system U-OWC/DEG under the action of regular waves. These tests allowed to study the system frequency response [142], and to obtain meaningful information that unachievable through sea tests with stochastic excitation. However, due to some mechanical limitations of the hardware setup, regular wave tests with a constant small wave height ($H = 50$ mm) and wave periods within the typical frequency range at NOEL were considered. Each simulation included a first phase in which the DEG was not electrically controlled, and a second phase in which the voltage was driven on the CD-DEG for power production. This method allowed for a whole characterization of the influence of the DEG activation on the system response.

Results of two simulations are provide in Fig. 4.15, where the system was excited by regular waves with the same wave height but considering two different periods. Specifically, the dataset shown in Fig. 4.15 (a) refers to a wave period $T = 2.5$ s (corresponding to a frequency $f = 0.4$ Hz), close to the system natural frequency, while the dataset depicted in Fig. 4.15 (b) refers to a wave period $T = 3.5$ s

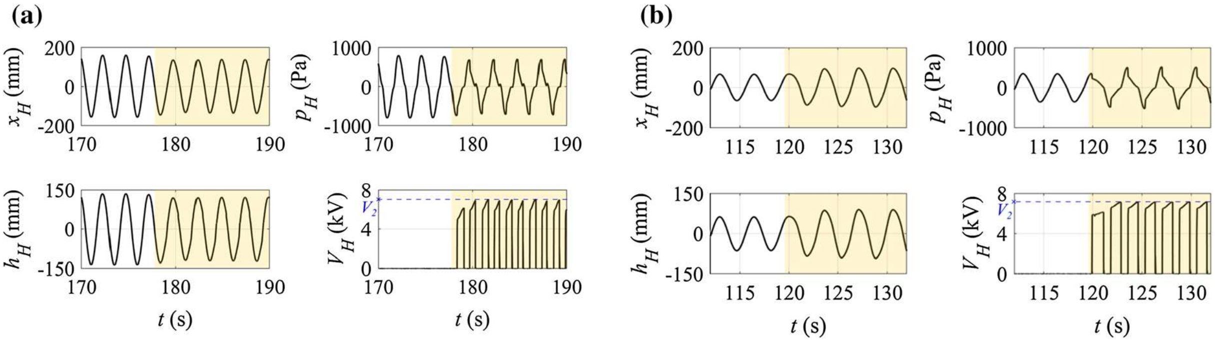

Fig. 4.15: Recorded data time-series of water column displacement, air pressure, membrane centre displacement, and CD-DEG voltage for two regular wave sea states: (a) H = 50 mm, T = 2.5 s, (b) H = 50 mm, T = 3.5 s. Coloured areas highlight the phases during which electrical control is activated

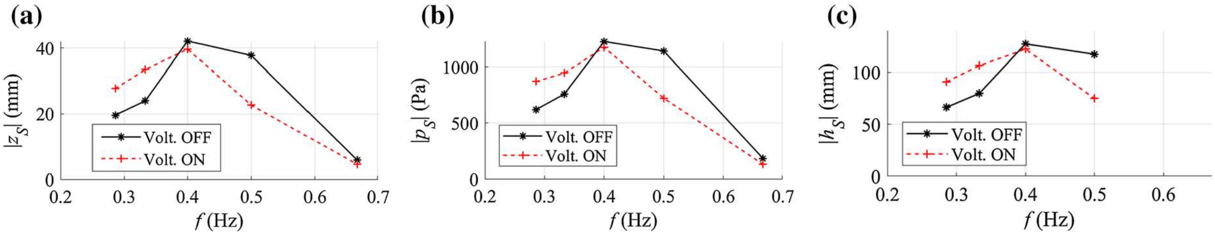

Fig. 4.16: Regular wave test results (wave height H = 50 mm). (a) Water column displacement, (b) air pressure, and (c) membrane centre displacement oscillation amplitudes with and without electrical activation. Different markers refer to different tests with excitation period T between 1.5 s and 3.5 s (spaced apart by 0.5 s). The DEG oscillation amplitudes at f = 0.67 Hz (T = 1.5 s) are not available: because of the small deformations, the membrane was hidden by the support structure and could not be detected through the camera frames

(corresponding to a frequency $f = 0.29$ Hz), below the system natural frequency. The application of the voltage on the U-OWC/DEG has a double effect. It induces a decrease in the CD-DEG stiffness, and, on the other side, it dampens the system oscillations. The consequences on the influence of the electrical activation on the system response depends upon the excitation frequecy. If the wave frequency is below the converter natural frequency, the oscillation amplitudes of the water column, pressure, membrane displacement increase upon electrical activation (Fig. 4.15 (b)). This is motivated by the fact that the presence of the voltage induces a softening of the DE layers, which causes the system natural frequency to decrease, hence getting closer to the excitation frequency. On the contrary, if the excitation wave frequency is close to the natural frequency (Fig. 4.15 (a)), the oscillation amplitudes decrease because of the electrical activation and damping. The system natural frequency is reduced with respect to the excitation frequency, thus moving away from resonance conditions. The observation of the time-series of the air pressure in the chamber shows sudden drops in corresponding to the charging instants. The electrical activation, indeed, causes as a decrease of the CD-DEG stiffness. The oscillatory behaviour of the pressure profile in the zero crossings is due to a partial loss of tension in the membrane, probably related to viscoelasticity effects.

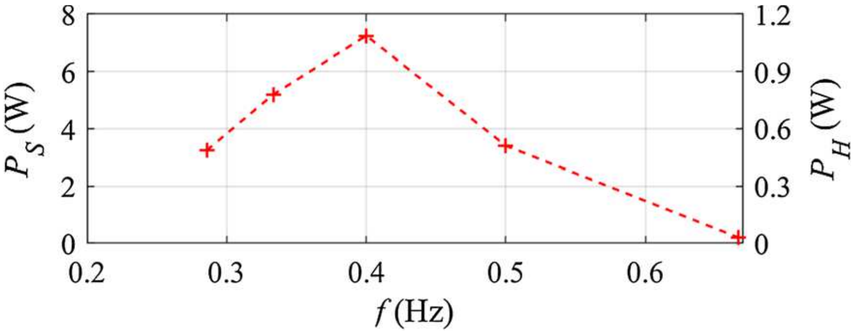

Fig. 4.17: Generated electrical power for simulated scenario (left axis), and experimental (right axis) in regular wave tests with wave height $H = 50\,\text{mm}$

A comprehensive view of the system response in regular wave tests is presented in Fig. 4.16. Specifically, the oscillation amplitudes of water column position, air pressure, and CD-DEG tip position (at the scale of the scenario) are plotted for the two cases: passive mechanical and electrically active tests. Simulations consider a wave height of 50 mm with a wide range of frequencies. As stated before, the electrical activation has the effect to reduce the natural frequency of the system. Nevertheless, in Fig. 4.16 the maxima is observed to be at 0.4 Hz, because of the low resolution of the chosen frequency grid. It can be clearly noted that the elctrical control of the DEG causes the oscillation amplitudes to increase at low frequencies (with respect to the system natural frequency) and to descrease at high frequencies (compared to the system natural frequency), because of electrically-induced variations in the system natural frequency.

The power P_{H} generated by the CD-DEG sample in the HIL simulations and the corresponding power output P_{S} of the simulated U-OWC plant are shown in Fig. 4.17. The power produced in the simulations P_{H} is computed by taking the average energy generated during the different cycles (eq. (4.30)), while P_{S} is obtained by applying the correction porposed in eq. (4.29). The CD-DEG samples generated powers over 1 W, corresponding to a few Watts at the scale of the simulated scenario. Given the dimensions of the plant at NOEL the power converted is small, but it represents a significant fraction of the input power of the mild incident waves considered in these tests. However, the results shown in this work assessed the effectiveness of the adopted control strategy for the CD-DEG and confirmed the feasibility of the DEG PTO in combination with a U-OWC wave power plant. Larger powers could be obtained (both in the scenario and with the HIL test-bench) by manufacturing DEGs with a larger thickness in such a way to consider more energetic sea states. The HIL results can be considered as the input for future sea tests to be conducted at NOEL with the scenario simulated in this work and with the implementation of the electrical control. Such tests are indeed feasible with the simplified manufacturing technology used here and in previous works [142] and with simple laboratory-scale electronics. The presented results show that, by sea states which typically occur at NOEL, it would be possible to achieve power generation greater than 10 W. This would represent the largest power generation test ever realized with DEGs, and would pave the way to further upscaling of DEG PTOs by improved electronics, the materials and the manufacturing strategies.

Chapter 5

Conclusions

In this research work attention has been devoted to the implementation of approaches for the improvement of the performance of a U-type Oscillating Water Column. Specifically, an overview of wave energy converters is given in Chapter 1, where oscillating bodies, overtopping devices and oscillating water columns are presented with their main features and deployments. Most of the chapter deals with OWCs, devices appreciated for their simple working principle and their reliability and efficiency. Typical air turbines to be installed on an OWC are described. Finally, the U-OWC wave energy converter is introduced.

The Roccella Jonica wave power plant is employed as a case study for the optimization approaches described in Chapters 2 and 3. The harbour of Roccella Jonica, located in the southern part of Italy, in the Ionian Sea, is the subject of an expansion project. A new breakwater is going to be built with the integration of U-OWC caissons for the absorption of the incoming wave energy.

In Chapter 2 a method for the optimization of the geometrical configuration of a U-Oscillating Water Column device has been presented. The statistical linearization technique has been adopted to find an approximate solution of the two coupled nonlinear differential equations governing the U-OWC dynamics, while a semi-analytical approach has been used to determine the U-OWC hydrodynamic parameters. The statistical linearization technique operates by replacing the original nonlinear system of equations via an approximate one with unknown (equivalent) parameters. The equivalent coefficients are determined by minimizing the errors between the systems' response in a mean square error sense. The use of statistical linearization was necessary to execute, in an effective way, an optimization algorithm, the genetic algorithm, for the computation of the geometrical parameters in order to maximize the energy production of the U-OWC wave power plant. The proposed method has been successfully validated through parameter sweep, that is, by considering all the possible combinations of the geometrical design parameters. The global maximum of the power produced by the turbine has been obtained for each numerical computation, thus demonstrating a significant reduction of the computational time. Next, two different approaches have been considered: a sea state and a wave climate based optimization. Computations have been carried out for different values of the submergence of the vertical duct opening. For this optimization a Wells turbine was considered as PTO for the U-OWC wave power plant. Both cases have shown that the power produced by the turbine increases progressively as the opening is closer to the mean water level, requiring the vertical duct to be wider and longer and the diameter to be slightly larger. A comparison between the two approaches has proved that the optimization based on a wave climate clearly provides better performances, even if at the price of computational cost. This is due to the fact that the whole set of sea states composing the local wave climate are considered. Nevertheless, the optimal configuration determined in the sea state based optimization has provided an average annual produced energy about 4% smaller. Thus, it is suggested to adopt the optimization based on the design sea state when a faster computation is required.

Next, a thorough study is carried out for selecting the optimal Power-Take Off system for a wave power plant, by considering all the occurring sea states, with their relative frequencies of occurrence. This procedure has been followed in the Chapter 3 where the selection of the PTO system for the Roccella Jonica wave power plant was firstly conducted by considering a monoplane Wells turbine and a biradial turbine. The turbine rotor diameter and the generator rated power were optimized by computing the capture width ratio based on the electrical power. The performance assessment for each turbine was conducted through a parametric study considering several rotor diamaters and rated powers for the generator. The possibility of several interconnected air chambers (from one to four connected chambers) sharing a single turbine was also investigated to find an effective solution to reduce the costs of the PTO system. The results of the monoplane Wells turbine have shown that the rotational speed frequently exceeds safety limits. To overcome this problem, multistage Wells turbines were considered. Indeed, the Wells turbine maximum rotational speed decreases by increasing the number of turbine stages. This behaviour is a consequence of the reduction on the pressure head per turbine stage. Two- and three-stage Wells turbines allowed the rotational speed to be reduced, although not solving the problem completely. It was found out that the two-stage Wells turbine outperforms the three-stage solution. Therefore, the option of the three-stage Wells turbine was discarded. The biradial turbine presented lower rotational speeds than all the considered Wells turbine configurations, showing just few peaks above the rotational speed threshold. Also, the biradial turbine showed higher efficiency at lower rotational speeds in comparison with the Wells turbines, and the optimal capture width ratio is obtained for smaller rotor diameters. For all the considered turbines it was observed that the electrical capture width ratio starts to decrease when more than two air chambers are connected to a single PTO.

The implementation of a system of bypass relief valves has been deemed necessary to operate the wave power plant during highly energetic sea states. The number of actuated valves and the algorithm that controls the opening/closing sequence have been customized for each turbine type. The valves were actuated in a discrete sequence based on the reaching of pre-determined speed thresholds selected in order to keep the turbine rotational speed within the limits.

The introduction of the relief valves had different effects on the performance of the turbines. The two-stage Wells turbine required the largest number of valves (six valves), and exhibited an electrical capture width ratio loss of 42% with respect to the unconstrained case, while the biradial turbine required just three valves with a reduction of 5%. The installation of relief valves with the Wells turbine has the double advantage of allowing the PTO operation within the rotational speed limits and the use of a generator with lower rated power.

The two-connected chambers scenario proved to be a good trade-off between energy performance and costs. In this configuration, the biradial turbine with relief valves was found to outperform the two-stage Wells turbine by more than 85%. Note that, the definitive power take-off of the Roccella Jonica wave power plant should be selected not only on the basis of the performance assessment but also by an economic evaluation, not addressed in this study. For this purpose, a techno-economic assessment will be carried out in future research, including the influence of several economic metrics, such as LCOE, CAPEX, OPEX, in order to determine the optimal PTO for the Roccella Jonica wave power plant from both technical and economical point of view.

In Chapter 4 the possibility to equip a U-Oscillating Water Column wave energy converter with innovative power take-off systems, such as the dielectric elastomer generators (DEGs), was evaluated and assessed. The proposed mathematical model has been obtained by combining a one-dimensional model based on the unsteady Bernoulli equation with an isentropic thermodynamic model for the air chamber dynamics, and a lumped-parameter electro-mechanical model of the DEG. Model reliability has been assessed against field data obtained from a small-scale experiment conducted in the NOEL (Natural Ocean Engineering Laboratory) benign natural basin located in Reggio Calabria (Italy). The presented experimental activity served as a first pilot investigation of a U-OWC with DEGs at sea. In this regard, the purely mechanical response of the system was initially investigated.

Based on the collected experimental data, it has been demonstrated that the model is able to capture the essential features of the system dynamics in a variety of sea states, without systematic over- or under-estimations of the relevant physical parameters. The validated model has been used for predicting the performance of a full-scale plant. For this purpose, the U-OWC wave power plant constructed in the port of Civitavecchia has been considered as a case study. The proposed mathematical model has been applied, assuming that a chamber of the plant is equipped with circular diaphragm DEGs (CD-DEGs) instead of turbines. Power output data have been obtained by running numerical simulations starting from spectrum compatible realizations of different sea states. It has been shown that a system integrating

U-OWC and CD-DEGs may provide an average power output comparable to that of a U-OWC with turbines. Further, it has been shown that the presence of the CD-DEGs does not affect the reliability of the system, as the use of throttle valves reduces the air pressure in the chamber during severe sea states, thus preventing the elastomeric membranes from breaking.

The obtained results pave the way for different future activities aimed at the advancement of the U-OWC with DEGs. However, some technological limits are slowing down the upscaling of DEGs, such as the lack of a standard DEG manufacturing process, the need for high voltage to harvest energy and the fact that the electronics is not commercially available but is made ad hoc. The gathered data and numerical models were used to allow the development of dry-run experiments aimed at evaluating control strategies and power output performance of DEG prototypes subject to loading histories similar to those recorded at sea. The implementation of a hardware-in-the-loop (HIL) framework and setup was described in the second part of Chapter 5. HIL tests were designed to simulate a wave energy converter equipped with dielectric elastomer generator (DEG) power take-off (PTO) systems. DEG based OWCs represent a promising upcoming class of low-cost and efficient WECs, which have been increasingly investigated in the recent past.

The proposed HIL framework relies on a software model of OWCs' hydrodynamics, coupled, in a closed-loop fashion, with a physical prototype of a pneumatically-driven circular diaphragm DEG (CD-DEG), and its electro-mechanical driving interface. The hydrodynamic model solves in real-time the dynamic equation of motion for the OWC plant based on simulated wave-induced loads. The solution is used to pilot the mechanical hardware that drives the deformation of the CD-DEG. The energy harvesting cycle is implemented at hardware level, through a purposely developed high voltage electronic driver that implements simple control logics based on air chamber pressure measurement. The actual pneumatic load measured on the CD-DEG is in turn fed into the software model and accounted for in the simulated dynamics. Compared to wave tank or sea tests, this HIL framework allows operating in a controlled laboratory environment, hence drastically reducing the experimental burden and cost while ensuring an exact rendering of the DEG PTO response and performance. The framework thus provides a powerful tool to test different CD-DEGs implementations and control strategies subject to realistic operating conditions. The HIL setup was applied to study the behaviour of a particular OWC/DEG implementation, based on the U-OWC layout. HIL tests were carried out at the laboratory of the Department of Industrial Engineering, University of Trento, Italy. Building upon previous sea tests, the response of a small-scale U-OWC plant equipped with a fully-functional CD-DEG PTO was charcterized, highlighting the features of the system dynamical response. Tests showed some misalignments between the model and the HIL data with reference to the oscillations inside the chamber and the air pressure. Discrepancies were observed in proximity of the resonance condition where the oscillation amplitudes are maximum. This was probably due to viscous dissipations of the elastomeric membranes, not considered in the simplified model. The influence of the electrical activation of the DEGs on the system response was analyzed and studied. Generated power obtained during the simulations was small but represents a significant fraction of the input power of the mild sea states considered in the tests (due to mechanical limitations of the HIL setup just small sea states were considered). Besides demonstrating the effectiveness of the proposed HIL framework, results were obtained which provide relevant indications for future sea tests on DEG prototypes capable of actively extracting electrical power from the presented U-OWC plant and further upscaling of the DEG PTO technology for wave energy conversion. Higher power output can be achieved by employing larger dielectric elastomer material, different materials such as silicone, and by overcoming HIL setup limitations to allow greater displacements. Future works foresee tests at the NOEL laboratory with electrical control of the CD-DEGs and the validation of HIL simulations data through field measurements.

The procedure to obtain the hydrodynamic coefficients for a U-OWC is detailed in the Appendix. Theoretical results were not part of this work but are reported in the chapter for the sake of completeness.

Appendix A

U-OWC hydrodynamic coefficients

This chapter provides the theory and the theoretical results employed in the following chapters. Specifically, it describes the fundamental concepts involved in the description of water wave mechanics applied to wave energy converter dynamics. In this context, the procedure adopted by Malara and Arena, and described in [62], for the computation of the U-OWC excitation and hydrodynamic coefficients is here summarized for completeness.

A.1 Wave field interacting with the U-OWC

This section provides the theory employed for describing the interaction between the sea waves and a U-OWC. Specifically, it describes the key concepts involved in the linearized water wave theory as described by Mei et al. [173]. In this context, the boundary value problem giving the unknown velocity potential ϕ is

$$\nabla^2\phi = 0, \tag{A.1a}$$

$$g\eta + \frac{\partial \phi}{\partial t} = 0,\ z = 0, \tag{A.1b}$$

$$\frac{\partial \eta}{\partial t} = \frac{\partial \phi}{\partial z},\ z = 0, \tag{A.1c}$$

$$\frac{\partial \phi}{\partial z} = 0,\ z = -d, \tag{A.1d}$$

where η is the free water surface displacement and g is the acceleration due to gravity. Eq. (A.1a) is the continuity equation, eq. (A.1b) is the linearized Bernoulli equation calculated at the mean water level, eq. (A.1c) is the linearized free surface condition, and eq. (A.1d) is the condition of horizontal impermeable sea bed. To account for the interaction of the waves with the U-OWC, this boundary value problem is solved in conjunction with a boundary condition enforcing an equality between the water particle velocity and the U-OWC water flow at the U-OWC inlet. Specifically, the boundary condition applied on the water column inlet S_b is

$$\frac{\partial \phi}{\partial n} = v_n(t), \text{ on } S_b \tag{A.2}$$

with n being outward normal. The equations (A.1b) and (A.1c), describing the free water surface, can be combined in one equation involving one unknonwn:

$$g\frac{\partial \phi}{\partial z} + \frac{\partial^2 \phi}{\partial t^2} = 0, \; z = 0. \tag{A.3}$$

This boundary value problem is linear. Therefore, the superposition principle can be used for representing the velocity potential as the sum of incident, $\phi^{(I)}$, scattered, $\phi^{(S)}$, and radiated $\phi^{(R)}$ waves

$$\phi = \phi^{(I)} + \phi^{(S)} + \phi^{(R)}, \tag{A.4}$$

where it is implicitly assumed that the solution (A.4) is the $Re\left\{\phi e^{(i\omega t)}\right\}$. Note that, from a mathematical perspective, eq. (A.1d) is the sum of an homogeneous solution of the boundary value problem (A.1a) and an inhomogeneous solution. The former is associated with the incident and scattered waves, while the latter is associated with the radiated waves. The next subsections elucidate the techniques used for determining analytical representations of the unknown potentials. The methodology is based on the matching of eigenfunction expansions derived as described by Linton and McIver (2001) [174]. The technique is applied by partitioning the fluid domain in two regions, Ω_1, extending from the far field to the U-OWC vertical duct, and Ω_2, located above the opening of the U-duct.

A.1.1 Diffracted wave field and U-OWC excitation

The diffraction problem is considered by assuming a still water column. Therefore, the velocity potentials due to incident and scattered waves can be included into the diffracted potential, $\phi^{(D)}$

$$\phi^{(D)} = \phi^{(I)} + \phi^{(S)}. \tag{A.5}$$

In this manner, the following system is obtained

$$\nabla^2 \phi^{(D)} = 0, \tag{A.6a}$$

$$g\frac{\partial \phi^{(D)}}{\partial z} + \frac{\partial^2 \phi^{(D)}}{\partial t^2} = 0, \; z = 0, \tag{A.6b}$$

$$\frac{\partial \phi^{(D)}}{\partial z} = 0, \; z = -d, \tag{A.6c}$$

$$\frac{\partial \phi^{(D)}}{\partial n} = 0, \text{ on the structure and on } S_\text{b}. \tag{A.6d}$$

In order to guarantee the uniqueness of the solution of the system of equations, the Sommerfeld radiation condition at the far field is considered

$$\lim_{r\to\infty} \sqrt{r}\left(\frac{\partial}{\partial r} - ik\right)\phi^{(D)} = 0, \tag{A.7}$$

with r being the horizontal polar coordinate; i being the imaginary unit; and k being the wave number. Eq. (A.7) ensures bounded waves in the far field. Replacing eq. (A.5) in the system (A.6), the following system is obtained

$$\nabla^2\phi^{(S)} = 0, \tag{A.8a}$$

$$g\frac{\partial\phi^{(S)}}{\partial z} + \frac{\partial^2\phi^{(S)}}{\partial t^2} = 0,\ z = 0, \tag{A.8b}$$

$$\frac{\partial\phi^{(S)}}{\partial z} = 0,\ z = -d, \tag{A.8c}$$

$$\frac{\partial\phi^{(S)}}{\partial n} = -\frac{\partial\phi^{(I)}}{\partial n},\ \text{on the structure}, \tag{A.8d}$$

$$\lim_{r\to\infty} \sqrt{r}\left(\frac{\partial}{\partial r} - ik\right)\phi^{(S)} = 0, \tag{A.8e}$$

in which the incident waves potential, $\phi^{(I)}$, is known. When dealing with the diffraction problem, the U-OWC is assumed to be closed and subject to the action of oblique incident waves with direction θ. If the wave is orthogonal $\theta = 0°$. In Ref. [174], for a wave field which is periodic along the direction transverse to the U-OWC, the two-dimensional velocity potential can be expressed as

$$\varphi^{(I,S)}(x,y,z) = \phi^{(I,S)}(y,z)e^{k_0 x \sin\theta}, \tag{A.9}$$

where φ is a two-dimensional velocity potential and k_0 is the positive imaginary solution of the linear dispersion rule

$$k\tan(kd) = -\frac{\omega^2}{g}. \tag{A.10}$$

The fluid domain in front of the U-OWC can be split into two domains. The domain 1 includes the portion from the far field to the outer wall of the U-duct, while the domain 2 represents the portion above the vertical duct. Therefore, the incident $\varphi^{(I)}$ and scattered wave fields $\varphi^{(1,S)}, \varphi^{(2,S)}$, can be described by the velocity potentials

$$\phi^{(I)} = iga\omega^{-1}\xi_0^{(1)}e^{-\tilde{k}_0(y+b_1)}, \tag{A.11}$$

$$\phi^{(1,S)} = iga\omega^{-1} \sum_{m=0}^{\infty} A_{\mathrm{m}}^{(S)} \frac{\cos\left[k_{\mathrm{m}}(d+z)\right]}{\cos\left(k_{\mathrm{m}}d\right)} e^{\tilde{k}_{\mathrm{m}}(y+b_1)}, \tag{A.12}$$

and

$$\phi^{(2,S)} = \mathrm{iga}\,\omega^{-1} \sum_{m=0}^{\infty} B_{\mathrm{m}}^{(S)} \frac{\cos\left[\alpha_{\mathrm{m}}(h+z)\right]}{\cos\left(\alpha_{\mathrm{m}}h\right)} \frac{\cosh\left(\tilde{\alpha}_{\mathrm{m}}y\right)}{\cosh\left(\tilde{\alpha}_{\mathrm{m}}b_1\right)}, \tag{A.13}$$

where a is the incident wave amplitude. The other terms appearing in eqs. (A.12) and (A.13) are described by the following relationships

$$\tilde{k}_{\mathrm{m}}^2 = k_{\mathrm{m}}^2 - k_0^2 \sin^2\theta, \text{for m = 0, 1, 2, } \ldots, \tag{A.14}$$

and

$$\tilde{\alpha}_{\mathrm{m}}^2 = \alpha_{\mathrm{m}}^2 - \alpha_0^2 \sin^2\theta, \text{for m = 0, 1, 2, } \ldots. \tag{A.15}$$

The terms k_{m} represent positive real solutions $(m > 0)$ of eq. (A.10), while the terms α_{m} are the positive real solutions $(m > 0)$ or positive imaginary solution $(m = 0)$ of the linear dispersion rule

$$\alpha \tan(\alpha h) = -\frac{\omega^2}{g}. \tag{A.16}$$

$A_m^{(S)}$ and $B_m^{(S)}$ are unknown constants computed by solving the linear system,

$$\begin{cases} \sum_{m=0}^{\infty} A_{\mathrm{m}}^{(S)} G_{\mathrm{mn}} - B_{\mathrm{n}}^{(S)} F_{\mathrm{n}}^{(\alpha)} = -G_{0\mathrm{n}} \quad n = 0, 1, \ldots \\ A_{\mathrm{n}}^{(S)} \tilde{k}_{\mathrm{n}} F_{\mathrm{n}}^{(k)} - \sum_{m=0}^{\infty} B_{\mathrm{m}}^{(S)} \tilde{\alpha}_{\mathrm{m}} \tanh\left(\tilde{\alpha}_{\mathrm{m}} b_1\right) G_{\mathrm{nm}} = \tilde{k}_0 F_0^{(k)} \delta_{0\mathrm{n}} \quad n = 0, 1, \ldots \end{cases} \tag{A.17}$$

where $\delta_{0\mathrm{n}}$ is the Dirac delta function, defined by $\delta_{0\mathrm{n}} = 1$ for $n = 0$ and $\delta_{0\mathrm{n}} = 0$ for $n \neq 0$. The other terms appearing in the system (A.17) are described through the following expressions

$$\begin{aligned} G_{\mathrm{nm}} =& \frac{1}{2} \frac{\sin\left[k_{\mathrm{n}}(d-h)\right] + \cos\left(k_{\mathrm{n}}d\right)\sin\left(\alpha_{\mathrm{m}}h\right) - \cos\left(\alpha_{\mathrm{m}}h\right)\sin\left(k_{\mathrm{n}}d\right)}{\left(\alpha_{\mathrm{m}} - k_{\mathrm{n}}\right)\cos\left(\alpha_{\mathrm{m}}h\right)\cos\left(k_{\mathrm{n}}d\right)} \\ &+ \frac{1}{2} \frac{\cos\left(k_{\mathrm{n}}d\right)\sin\left(\alpha_{\mathrm{m}}h\right) - \sin\left[k_{\mathrm{n}}(d-h)\right] + \cos\left(\alpha_{\mathrm{m}}h\right)\sin\left(k_{\mathrm{n}}d\right)}{\left(\alpha_{\mathrm{m}} + k_{\mathrm{n}}\right)\cos\left(\alpha_{\mathrm{m}}h\right)\cos\left(k_{\mathrm{n}}d\right)}, \end{aligned} \tag{A.18}$$

$$F_{\mathrm{n}}^{(k)} = \frac{1}{2} \frac{\sin\left(k_{\mathrm{n}}d\right)\cos\left(k_{\mathrm{n}}d\right) + k_{\mathrm{n}}d}{k_{\mathrm{n}}\cos^2\left(k_{\mathrm{n}}d\right)}, \tag{A.19}$$

and

$$F_{\mathrm{n}}^{(\alpha)} = \frac{1}{2}\frac{\sin(\alpha_{\mathrm{n}}h)\cos(\alpha_{\mathrm{n}}h) + \alpha_{\mathrm{n}}h}{\alpha_{\mathrm{n}}\cos^2(\alpha_{\mathrm{n}}h)}. \tag{A.20}$$

Finally, the wave pressure at the centre of the U-duct is given by the equation,

$$\Delta p^{(D)} = \rho g a \sum_{m=0}^{\infty} B_{\mathrm{m}}^{(S)} \frac{1}{\cos(\alpha_{\mathrm{m}}h)} \frac{\cosh(\tilde{\alpha}_{\mathrm{m}}b_1/2)}{\cosh(\tilde{\alpha}_{\mathrm{m}}b_1)}. \tag{A.21}$$

A.1.2 Wave radiation and hydrodynamic parameters

The velocity potential for the radiated waves, $\phi^{(R)}$ is computed by considering velocity oscillations at the U-OWC inlet in still water conditions. The linearized potential theory equations for this problem are

$$\nabla^2\phi^{(R)} = 0, \tag{A.22a}$$

$$g\frac{\partial\phi^{(R)}}{\partial z} + \frac{\partial^2\phi^{(R)}}{\partial t^2} = 0,\ z = 0, \tag{A.22b}$$

$$\frac{\partial\phi^{(R)}}{\partial z} = 0,\ z = -d, \tag{A.22c}$$

$$\frac{\partial\phi^{(R)}}{\partial n} = v_n(t),\ \text{on } S_b, \tag{A.22d}$$

$$\lim_{r\to\infty}\sqrt{r}\left(\frac{\partial}{\partial r} - ik\right)\phi^{(R)} = 0, \tag{A.22e}$$

where the velocity is unknown. In passing, note that superposition principle is invoked to model the case of U-OWC array, where multiple U-OWC chambers are installed in the same infrastructure, thus giving

$$\phi^{(R)} = \sum_{\alpha}\phi_{\alpha}^{(R)}, \tag{A.23}$$

where $\phi_{\alpha}^{(R)}$ is the radiated potential associated with the α-th U-OWC chamber. The radiation problem is solved by representing the radiated potential as a sequence of impulses. So that, in the case $\mathrm{d}\tau \to 0$, the radiated potential is calculated as

$$\phi_{\alpha}^{(R)} = \int_{-\infty}^{\infty}\phi^{\Delta}\mathrm{d}\tau, \tag{A.24}$$

where ϕ^{Δ} is defined as the velocity potential of the radiated waves due to an impulse at the instant $t = \tau$. In this context, the boundary condition on the structure is expressed as

$$\frac{\partial\phi^{\Delta}}{\partial n} = v_{\alpha}(\tau)\,\delta(t-\tau)\,n_{\alpha}, \tag{A.25}$$

where $\delta(t-\tau)$ is the Dirac delta function, while $v_\alpha(\tau)$ is the velocity of α-th U-OWC water column at the time instant τ. Cummins [143] introduced the following representation of ϕ^Δ:

$$\phi^\Delta(x,y,z,t) = v_\alpha(\tau)\left[H_\alpha(x,y,z)\,\delta(t-\tau) + \Gamma_\alpha(x,y,z,t)\,\Theta(t-\tau)\right], \tag{A.26}$$

where H_α and Γ_α are velocity potentials, while $\Theta(t-\tau)$ is the Heaviside step function defined as [175]

$$\Theta(t-\tau) = \begin{cases} 0, \ t < \tau \\ 1, \ t \geqslant \tau \end{cases} \tag{A.27}$$

H_α and Γ_α can be computed by substituting ϕ^Δ into the linearized potential theory equations. Focusing on the substitution of equation (A.26) into the conditon on the free surface (A.22b), the two terms that are obtained are

$$g\frac{\partial \phi^{(\Delta)}}{\partial z} = g\left[\frac{\partial H_\alpha(\mathbf{x})}{\partial z}\delta(t-\tau) + \frac{\partial \Gamma_\alpha(\mathbf{x},t)}{\partial z}\Theta(t-\tau)\right]v_\alpha(\tau), \tag{A.28}$$

and

$$\begin{aligned} \frac{\partial^2 \phi^{(\Delta)}}{\partial t^2} = v_\alpha(\tau)&\left[H_\alpha(\mathbf{x})\ddot{\delta}(t-\tau) + \frac{\partial^2 \Gamma_\alpha(\mathbf{x},t)}{\partial t^2}\Theta(t-\tau) + \right. \\ &\left. + \dot{\Theta}(t-\tau)\frac{\partial \Gamma_\alpha(\mathbf{x},t)}{\partial t} + \ddot{\Theta}(t-\tau)\Gamma_\alpha(\mathbf{x},t) + \frac{\partial \Gamma_\alpha(\mathbf{x},t)}{\partial t}\dot{\Theta}(t-\tau)\right], \end{aligned} \tag{A.29}$$

where $\mathbf{x} = (x,y,z)$. Considering the Heaviside step function property

$$\frac{\partial \Theta_x}{\partial x} = \delta(x), \tag{A.30}$$

and summing the two terms into equation (A.22b) the following expression is derived

$$\begin{aligned} g\left[\frac{\partial H_\alpha(\mathbf{x})}{\partial z}\delta + \frac{\partial \Gamma_\alpha(\mathbf{x},t)}{\partial z}\Theta\right] + \\ + \left[H_\alpha(\mathbf{x})\ddot{\delta} + \frac{\partial^2 \Gamma_\alpha(\mathbf{x},t)}{\partial t^2}\Theta + \dot{\Theta}\frac{\partial \Gamma_\alpha(\mathbf{x},t)}{\partial t} + \ddot{\Theta}\,\Gamma_\alpha(\mathbf{x},t) + \frac{\partial \Gamma_\alpha(\mathbf{x},t)}{\partial t}\dot{\Theta}\right] = 0. \end{aligned} \tag{A.31}$$

The argument $(t-\tau)$ of Θ, δ, $\dot{\delta}$ and $\ddot{\delta}$ has been omitted for the sake of simplicity. Their coefficients can be equated to zero individually, thus obtaining the boundary conditions on the free surface. Finally the problem to compute $H_\alpha(\mathbf{x})$ and $\Gamma_\alpha(\mathbf{x},t)$ is derived as follow. Note that the velocity potential H_α is time independent. Specifically,

$$\nabla^2 H_\alpha = 0, \tag{A.32a}$$

$$H_\alpha = 0,\ z = 0, \tag{A.32b}$$

$$\frac{\partial H_\alpha}{\partial z} = 0,\ z = -d, \tag{A.32c}$$

$$\frac{\partial H_\alpha}{\partial n} = n_\alpha,\ \text{on } S_\text{b}, \tag{A.32d}$$

$$\frac{\partial H_\alpha}{\partial n} = 0,\ \text{on the structure}, \tag{A.32e}$$

$$H_\alpha \to 0,\ r \to \infty. \tag{A.32f}$$

Instead, Γ_α is time dependent. Therefore, initial conditions need to be set. Thus,

$$\nabla^2 \Gamma_\alpha = 0, \tag{A.33a}$$

$$\Gamma_\alpha = 0,\ z = 0,\ \tau = t_0, \tag{A.33b}$$

$$\frac{\partial \Gamma_\alpha}{\partial t} + g\frac{\partial H_\alpha}{\partial z} = 0,\ z = 0,\ \tau = t_0, \tag{A.33c}$$

$$\frac{\partial^2 \Gamma_\alpha}{\partial t^2} + g\frac{\partial \Gamma_\alpha}{\partial z} = 0,\ z = 0,\ t_0 < \tau < +\infty, \tag{A.33d}$$

$$\frac{\partial \Gamma_\alpha}{\partial z} = 0,\ z = -d, \tag{A.33e}$$

$$\frac{\partial \Gamma_\alpha}{\partial n} = 0,\ \text{on the structure and on } S_\text{b}. \tag{A.33f}$$

Once the velocity potentials are computed, $\phi_\alpha^{(R)}$ can be integrated over a sequence of impulses from $-\infty$ to ∞

$$\begin{aligned}\phi_\alpha^{(R)} &= \int_{-\infty}^{\infty} v_\alpha(\tau)\left[H_\alpha(x,y,z)\delta(t-\tau) + \Gamma_\alpha(x,y,z,t)\Theta(t-\tau)\right]\mathrm{d}\tau = \\ &= v_\alpha(t)H_\alpha(x,y,z) + \int_{-\infty}^{t} v_\alpha(\tau)\Gamma_\alpha(x,y,z,t-\tau)\mathrm{d}\tau,\end{aligned} \tag{A.34}$$

where the property of the Dirac delta function

$$\int_{-\infty}^{\infty} f(x)\delta(x-a)\,\mathrm{d}x = f(a), \tag{A.35}$$

has been used. Pressures on the structure due to the radiated waves can be computed as

$$\Delta p = -\rho\frac{\partial}{\partial t}\phi_\alpha^{(R)} = -\rho\frac{\partial}{\partial t}\left[v_\alpha(t)H_\alpha + \int_{-\infty}^{t} v_\alpha(\tau)\Gamma_\alpha(x,y,z,t-\tau)\mathrm{d}\tau\right]. \tag{A.36}$$

The derivative of the integral term in the right hand side of equation (A.36) can be solved by considering the Leibniz integral rule

$$\begin{aligned}\frac{\partial}{\partial t}\int_{-\infty}^{t}\Gamma_\alpha(x,y,z,t-\tau)v_\alpha(\tau)\mathrm{d}\tau = \int_{-\infty}^{t}\frac{\partial}{\partial t}\Gamma_\alpha(x,y,z,t-\tau)v_\alpha(\tau)\mathrm{d}\tau + \\ -\Gamma_\alpha(x,y,z,0)v_\alpha(t)+\Gamma_\alpha(x,y,z,\infty)v_\alpha(-\infty).\end{aligned} \tag{A.37}$$

Since $v_\alpha(-\infty)=0$ and considering equation (A.33b) it yields

$$\frac{\partial}{\partial t}\phi_\alpha^{(R)} = H_\alpha \ddot{x}_\alpha + \int_{-\infty}^{t}\Gamma_\alpha(x,y,z,t-\tau)\ddot{x}_\alpha(\tau)\mathrm{d}\tau. \tag{A.38}$$

Here the dots denote time derivatives, so that $v_\alpha = \dot{x}_\alpha$. Substituting eq. (A.38) into eq. (A.36), the wave pressure at any point of the wave field can be computed. Therefore, for each velocity potential $\phi_\alpha^{(R)}$ it is possible to compute the pressure, and consequently the force, acting on the U-OWC inlets.

Consider now the force $F_{\beta\alpha}$ on the U-OWC β due to the wave propagated by the U-OWC α,

$$\begin{aligned}F_{\beta\alpha} = -\rho\int_{S_\mathrm{b}}\frac{\partial}{\partial t}\phi_\alpha^{(R)} n_\beta\, \mathrm{d}S_\mathrm{b} = \\ = -\left[\rho\int_{S_\mathrm{b}} H_\alpha(x,y,z)n_\beta\,\mathrm{d}S\right]\ddot{x}_\alpha(t) - \int_{-\infty}^{t}\left[\rho\int_{S_\mathrm{b}}\Gamma_\alpha(x,y,z,t-\tau)n_\beta\,\mathrm{d}S\right]\ddot{x}_\alpha(t).\end{aligned} \tag{A.39}$$

The term $\left[\rho\int_{S_\mathrm{b}} H_\alpha(x,y,z)n_\beta\,\mathrm{d}S\right]$ is defined as the infinite frequency added mass $H_{\beta\alpha}(\infty)$, while the term $\left[\rho\int_{S_\mathrm{b}}\Gamma_\alpha(x,y,z,t-\tau)n_\beta\,\mathrm{d}S\right]$ is the hydrodynamic memory, $L_{\beta\alpha}(t-\tau)$. To clarify the role of these parameters, consider the Newton's law for a body interacting with the wave field

$$\mathbf{M}\ddot{\mathbf{x}} = \mathbf{F_e} + \mathbf{F^{(D)}} + \mathbf{F^{(R)}}, \tag{A.40}$$

where $\mathbf{M}$ is the mass of the body, $\mathbf{F_e}$ are all the external forces but the wave forces, such as the mooring forces, wind forces, etc; $\mathbf{F^{(D)}}$ is the force due to the diffracted waves; $\mathbf{F^{(R)}}$ is the force due to the radiated waves as computed before. Substituting eq. (A.39) in (A.40) it yields

$$\left[\mathbf{M}+\mathbf{H}(\infty)\right]\ddot{\mathbf{x}} + \int_{-\infty}^{t}\mathbf{L}(t-\tau)\ddot{\mathbf{x}}(\tau)\mathrm{d}\tau = \mathbf{F_e} + \mathbf{F^{(D)}}. \tag{A.41}$$

It is seen that $\mathbf{H}(\infty)$ is proportional to the body acceleration, therefore it is a mass. The notation "infinite frequency added mass" relates to the fact that the boundary value problem (A.32) is equivalent to a radiation problem in the limiting case of $\omega \to \infty$. The convolution integral accounts for the influence of the past acceleration values on the current system response. Therefore, it is called hydrodynamic memory effect. Note that, in this representation, the acceleration $\ddot{\mathbf{x}}(\tau)$ is unknow at the considered time instant. Thus, the numerical implementation of eq. (A.41) can be tedious. For circumventing this issue, it is observed that, the hydrodynamic memory can be expressed equivalently as a velocity based convolution integral, whose kernel $\mathbf{K}(t)$ is related to $\mathbf{L}(t)$ by the equation [176]

$$\mathbf{L}(t-\tau) = \int_0^t \mathbf{K}(t-\tau)\,\mathrm{d}\tau. \tag{A.42}$$

This representation of the hydrodynamic memory effect accommodates the implementation of classical numerical integration schemes for solving eq. (A.41) as the velocity is a (known) state of the system. Regarding the determination of the kernel of the convolution integral, it is noteworthy that it can be computed directly by the equation

$$\mathbf{K}(t) = \frac{2}{\pi}\int_0^\infty \mathbf{B}(\omega)\cos(\omega t)\,\mathrm{d}\omega, \tag{A.43}$$

with $\mathbf{B}(\omega)$ being the frequency dependent radiation damping. The procedure for computing the radiation damping is described in the next section. Eq. (A.43) shows that the computation of $\mathbf{K}(t)$ is straightforward if $\mathbf{B}(\omega)$ is known. For calculating $\mathbf{B}(\omega)$, the particular case of harmonic system response is studied. In this case, the velocity is harmonic and can be expressed as

$$v_\alpha(t) = \mathrm{Re}\left\{V_\alpha e^{-i\omega t}\right\}. \tag{A.44}$$

Substituting eq. (A.44) in eq. (A.34) and assuming the initial time to be $t=-\infty$, it results

$$\phi_\alpha^{(R)}(x,y,z,t) = \mathrm{Re}\left\{\left[H_\alpha(x,y,z) + \int_0^\infty \Gamma_\alpha(x,y,z,\tau)e^{i\omega\tau}d\tau\right]V_\alpha e^{-i\omega t}\right\}. \tag{A.45}$$

The terms in [ ] represent the amplitude of an harmonic oscillation due to the radiation force with $\partial\phi_\alpha/\partial n = n_\alpha$ on S_b. Therefore,

$$\phi_\alpha(x,y,z,\omega) = \mathrm{Re}\,\phi_\alpha + i\,\mathrm{Im}\,\phi_\alpha = H_\alpha(x,y,z) + \int_0^\infty \Gamma_\alpha(x,y,z,\tau)e^{i\omega\tau}d\tau. \tag{A.46}$$

$\Gamma_\alpha = 0$ for $\tau \leq 0$. Therefore, the integral appearing in eq. (A.46) is the Fourier transform of Γ_α. Once the values of ϕ_α and H_α are known for a set of frequencies, $\Gamma_\alpha(x,y,z,t)$ can be obtained by applying the inverse Fourier transform to eq. (A.46). Once ϕ_α is known, the component $F_{\beta\alpha}$ can be obtained. It represents the hydrodynamic reaction of the U-OWC caisson α due to the displacement of the caisson β. It should be considered that the α-th component of the generalized hydrodynamic force on the body can be expressed as [144]

$$F_\alpha = i\rho\omega\iint_{S_b}\phi n_\alpha dS \tag{A.47}$$

Considering that $\phi = \phi^D + \sum_\alpha v_\alpha \phi_\alpha$ and substituting it into (A.47), it is obtained

$$F_\alpha = i\rho\omega \iint_{S_b} \phi^D n_\alpha dS + \sum_\beta i\rho\omega v_\beta \iint_{S_b} \phi_\beta n_\alpha dS, \tag{A.48}$$

where the quantities in the right-hand side represent the exciting force on a stationary body due to diffraction F_α^D, and the hydrodynamic reaction $F_{\beta\alpha}$

$$\begin{aligned} &F_\alpha^{(D)} = i\rho\omega \textstyle\iint_{S_b} \phi^{(D)} n_\alpha dS, \\ &F_{\beta\alpha} = i\rho\omega \textstyle\iint_{S_b} \phi_\beta n_\alpha dS. \end{aligned} \tag{A.49}$$

Therefore, the hydrodynamic force on the body appears as

$$F_\alpha = F_\alpha^{(D)} + \sum_\beta v_\beta F_{\beta\alpha} \tag{A.50}$$

By analyzing the restoring force, it results

$$\begin{aligned} &\operatorname{Re}\left(v_\beta F_{\beta\alpha} e^{-i\omega t}\right) \\ &= \operatorname{Re}\left[\left(\operatorname{Re} F_{\beta\alpha} + i \operatorname{Im} F_{\beta\alpha}\right) v_\beta e^{-i\omega t}\right] \\ &\quad = \operatorname{Re}\left[\left(i\rho\omega \textstyle\iint_{S_b} \operatorname{Re}\phi_\beta n_\alpha dS - \rho\omega \iint_{S_b} \operatorname{Im}\phi_\beta n_\alpha dS\right) \cdot v_\beta e^{-i\omega t}\right] \\ &= -\left(\rho \textstyle\iint_{S_b} \operatorname{Re}\phi_\beta n_\alpha dS\right) \operatorname{Re} \frac{d}{dt}\left(v_\beta e^{-i\omega t}\right) \\ &\quad -\left(\rho\omega \textstyle\iint_{S_b} \operatorname{Im}\phi_\beta n_\alpha dS\right) \operatorname{Re}\left(v_\beta e^{-i\omega t}\right) \\ &= -\left(\rho \textstyle\iint_{S_b} \operatorname{Re}\phi_\beta n_\alpha dS\right) \ddot{x}_\beta - \left(\rho\omega \iint_{S_b} \operatorname{Im}\phi_\beta n_\alpha dS\right) \dot{x}_\beta \end{aligned} \tag{A.51}$$

The first integral above is proportional to the body acceleration and is the hydrodynamic inertia, called added mass

$$H_{\beta\alpha} = \rho \iint_{S_b} \operatorname{Re}\phi_\beta n_\alpha dS = \frac{1}{\omega} \operatorname{Im} F_{\beta\alpha}. \tag{A.52}$$

The second integral is, instead, proportional to the body velocity and is called radiation damping

$$B_{\beta\alpha}(\omega) = \rho\omega \iint_{S_b} \operatorname{Im}\phi_\beta n_\alpha dS = -\operatorname{Re} F_{\beta\alpha}. \tag{A.53}$$

A.2 Added mass and radiation damping of a U-OWC

A.2.1 Infinite frequency added mass

The velocity potential associated with the infinite frequency added mass is determined by solving, in both fluid domains, the following boundary value problems:

$$\nabla^2 H^{(1)} = 0, \tag{A.54a}$$

$$\frac{\partial H^{(1)}}{\partial y} = 0,\ y = -b_1, \tag{A.54b}$$

$$\frac{\partial H^{(1)}}{\partial z} = 0,\ z = -d, \tag{A.54c}$$

$$H^{(1)} = 0,\ z = 0, \tag{A.54d}$$

$$H^{(1)} \to 0,\ y \to -\infty, \tag{A.54e}$$

for the region 1, and

$$\nabla^2 H^{(2)} = 0, \tag{A.55a}$$

$$\frac{\partial H^{(2)}}{\partial y} = 0,\ y = 0, \tag{A.55b}$$

$$\frac{\partial H^{(2)}}{\partial z} = \Theta\left(x + \frac{b_3}{2}\right) - \Theta\left(x - \frac{b_3}{2}\right),\ z = -h, \tag{A.55c}$$

$$H^{(2)} = 0,\ z = 0, \tag{A.55d}$$

for region 2. Eq. (A.55c) describes the condition of the vertical velocity near the U-OWC exploiting the Heaviside step function Θ and incorporating the following two requirements

$$\frac{\partial H^{(2)}}{\partial z} = 0,\ -\infty < x < -\frac{b_3}{2},\ -b_1 < y < 0,\ z = -h, \tag{A.56a}$$

$$\frac{\partial H^{(2)}}{\partial z} = 1,\ -\frac{b_3}{2} < x < \frac{b_3}{2},\ -b_1 < y < 0,\ z = -h. \tag{A.56b}$$

Additionally, the following equations are included to impose the continuity of $H(x,y,z)$ and its derivative $\frac{\partial H}{\partial y}$ on the boundary between the two domains:

$$H^{(1)} = H^{(2)},\ y = -b_1, \tag{A.57a}$$

$$\frac{\partial H^{(1)}}{\partial y} = \frac{\partial H^{(2)}}{\partial y},\ y = -b_1. \tag{A.57b}$$

The boundary value problem can be solved in the Fourier domain transformed with respect to variable x and the velocity potential can be expressed as

$$\tilde{H}(k_{\mathrm{x}},y,z) = \int_{-\infty}^{\infty} H(x,y,z) e^{-ik_{\mathrm{x}}x} \mathrm{d}x \tag{A.58}$$

with k_{x} being the Fourier variable. Then, the boundary value problem for the regions Ω_1 and Ω_2 becomes, respectively,

$$\frac{\partial^2 \tilde{H}^{(1)}}{\partial y^2} + \frac{\partial^2 \tilde{H}^{(1)}}{\partial z^2} - k_{\mathrm{x}}^2 \tilde{H}^{(1)} = 0, \tag{A.59a}$$

$$\frac{\partial \tilde{H}^{(1)}}{\partial y} = 0, \; y = -b_1, \tag{A.59b}$$

$$\frac{\partial \tilde{H}^{(1)}}{\partial z} = 0, \; z = -d, \tag{A.59c}$$

$$\tilde{H}^{(1)} = 0, \; z = 0, \tag{A.59d}$$

$$\tilde{H}^{(1)} \to 0, \; y \to -\infty, \tag{A.59e}$$

and

$$\frac{\partial^2 \tilde{H}^{(2)}}{\partial y^2} + \frac{\partial^2 \tilde{H}^{(2)}}{\partial z^2} - k_{\mathrm{x}}^2 \tilde{H}^{(2)} = 0, \tag{A.60a}$$

$$\frac{\partial \tilde{H}^{(2)}}{\partial y} = 0, \; y = 0, \tag{A.60b}$$

$$\frac{\partial \tilde{H}^{(2)}}{\partial z} = 2sin\left(\frac{k_{\mathrm{x}}\frac{b_3}{2}}{k_{\mathrm{x}}}\right) = c\left(k_{\mathrm{x}}\right), \; z = -h, \tag{A.60c}$$

$$\tilde{H}^{(2)} = 0, \; z = 0. \tag{A.60d}$$

Here again, the continuity between the two domains is guaranteed by the equations:

$$\tilde{H}^{(1)} = \tilde{H}^{(2)}, \; y = -b_1, \tag{A.61a}$$

$$\frac{\partial \tilde{H}^{(1)}}{\partial y} = \frac{\partial \tilde{H}^{(2)}}{\partial y}, \; y = -b_1. \tag{A.61b}$$

The solutions of these problems are obtained through eigenfunction expansions with unknown coefficients. For the domain Ω_1, the eigenfunction expansion corresponding to the Helmholtz equation (A.59a) in the fluid domain is expressed in the form [174]

$$\tilde{H}^{(1)} = h^2 \sum_{m=1}^{\infty} \left[A_{\mathrm{m}}^{(h)} e^{\tilde{k}_m^{(h)}(y+b_1)} + B_{\mathrm{m}}^{(h)} e^{-\tilde{k}_m^{(h)}(y+b_1)} \right] \Psi_{\mathrm{m}}(z), \tag{A.62}$$

where $\Psi_{\mathrm{m}}(z)$ is the vertical eigenfunction, $A_m^{(h)}$ and $B_m^{(h)}$ unknown constants and

$$\tilde{k}_m^{(h)} = \sqrt{k_m^{(h)^2} + k_x^2}, \tag{A.63}$$

with $k_{\mathrm{m}}^{(h)}(m > 0) = \frac{(m-\frac{1}{2}\pi)}{d}$. Applying the radiation condition (A.59e) it is immediately seen that $B_{\mathrm{m}}^{(h)} = 0$. Thus it follows that

$$\tilde{H}^{(1)} = h^2 \sum_{m=1}^{\infty} \left[A_{\mathrm{m}}^{(h)} e^{\tilde{k}_m^{(h)}(y+b_1)} \right] \cos \left[k_{\mathrm{m}}^{(h)}(d+z) \right]. \tag{A.64}$$

For the region Ω_2 the velocity potential can be expressed in the form

$$\tilde{H}^{(2)} = h^2 \varphi(y,z) - \frac{z^2}{2h} c(k_{\mathrm{x}}). \tag{A.65}$$

Substituting it in eq. (A.60a) and dividing by h^2, it is obtained

$$\frac{\partial^2 \varphi^{(2)}}{\partial y^2} + \frac{\partial^2 \varphi^{(2)}}{\partial z^2} - k_{\mathrm{x}}^2 \varphi^{(2)} = \frac{1}{h^2}\frac{c(k_{\mathrm{x}})}{h} - k_{\mathrm{x}}^2 \frac{z^2}{2h^2}\frac{c(k_{\mathrm{x}})}{h}. \tag{A.66}$$

Separable solutions of φ may be found in the form

$$\varphi(y,z) = \sum_{m=1}^{\infty} \Psi_{\mathrm{m}}(y) Z_{\mathrm{m}}(z), \tag{A.67}$$

with $Z(z)$ the vertical eigenfunction written as

$$Z_{\mathrm{m}}(z) = C cos \left[\alpha_{\mathrm{m}}^{(h)}(z+h) \right] + D sin \left[\alpha_{\mathrm{m}}^{(h)}(z+h) \right], \tag{A.68}$$

with $\alpha_{\mathrm{m}}^{(h)} = \frac{(m-\frac{1}{2}\pi)}{h}$. Thus,

$$\varphi(y,z) = \sum_{m=1}^{\infty} \Psi_{\mathrm{m}}(y) cos \left[\alpha_{\mathrm{m}}^{(h)}(z+h) \right]. \tag{A.69}$$

Substituting this expression into eq. (A.66), it results

$$\begin{aligned} \sum_{m=1}^{\infty} \left\{ \Psi''_{\mathrm{m}}(y) cos \left[\alpha_{\mathrm{m}}^{(h)}(z+h) \right] - \alpha_{\mathrm{m}}^{(h)^2} \Psi_{\mathrm{m}}(y) cos \left[\alpha_{\mathrm{m}}^{(h)}(z+h) \right] - k_{\mathrm{x}}^2 \Psi_{\mathrm{m}}(y) cos \left[\alpha_{\mathrm{m}}^{(h)}(z+h) \right] \right\} = \\ \frac{1}{h^2}\frac{c(k_{\mathrm{x}})}{h} - k_{\mathrm{x}}^2 \frac{z^2}{2h^2}\frac{c(k_{\mathrm{x}})}{h}. \end{aligned} \tag{A.70}$$

Denoting $\alpha_{\mathrm{m}}^{(h)^2} + k_{\mathrm{x}}^2 = \tilde{\alpha}_{\mathrm{m}}^{(h)^2}$ it is obtained

$$\sum_{m=1}^{\infty} \left\{ \Psi_{\mathrm{m}}''(y) cos\left[\alpha_{\mathrm{m}}^{(h)}(z+h)\right] - \tilde{\alpha}_{\mathrm{m}}^{(h)^2} \Psi_{\mathrm{m}}(y) cos\left[\alpha_{\mathrm{m}}^{(h)}(z+h)\right] \right\} = \frac{1}{h^2}\frac{c(k_{\mathrm{x}})}{h} - k_{\mathrm{x}}^2 \frac{z^2}{2h^2}\frac{c(k_{\mathrm{x}})}{h}. \tag{A.71}$$

Exploiting the orthogonality property of the vertical eigenfunction for which it is

$$\int_{-h}^{0} cos\left[\alpha_{\mathrm{m}}^{(h)}(z+h)\right] cos\left[\alpha_{\mathrm{n}}^{(h)}(z+h)\right] \mathrm{d}z = 0, \text{ for } m \neq n, \tag{A.72}$$

multiplying each term by $cos\left[\alpha_{\mathrm{n}}^{(h)}(z+h)\right]$ and integrating over the depth from h to 0 it is obtained, for $m = n$

$$\begin{aligned} &\int_{-h}^{0} \left\{ \Psi_{\mathrm{n}}''(y) cos^2\left[\alpha_{\mathrm{n}}^{(h)}(z+h)\right] - \tilde{\alpha}_{\mathrm{n}}^{(h)^2} \Psi_{\mathrm{n}}(y) cos^2\left[\alpha_{\mathrm{n}}^{(h)}(z+h)\right] \right\} \mathrm{d}z = \\ &\int_{-h}^{0} cos\left[\alpha_{\mathrm{n}}^{(h)}(z+h)\right] \frac{1}{h^2}\frac{c(k_{\mathrm{x}})}{h} \mathrm{d}z - \int_{-h}^{0} cos\left[\alpha_{\mathrm{n}}^{(h)}(z+h)\right] k_{\mathrm{x}}^2 \frac{z^2}{2h^2}\frac{c(k_{\mathrm{x}})}{h} \mathrm{d}z. \end{aligned} \tag{A.73}$$

The integral terms are computed as

$$F_{\mathrm{n}}^{\alpha} = \int_{-h}^{0} \cos^2\left[\alpha_{\mathrm{n}}^{(h)}(z+h)\right] \mathrm{d}z = \frac{2\alpha_{\mathrm{n}}^{(h)} h + \sin(2\alpha_{\mathrm{n}}^{(h)} h)}{4\alpha_{\mathrm{n}}^{(h)}}, \tag{A.74}$$

$$F_{\mathrm{n}}^{\beta} = \int_{-h}^{0} z^2 \cos\left[\alpha_{\mathrm{n}}^{(h)}(z+h)\right] \mathrm{d}z = \frac{2\alpha_{\mathrm{n}}^{(h)} h - 2\sin(\alpha_{\mathrm{n}}^{(h)} h)^{3}}{\alpha_{\mathrm{n}}^{(h)}}, \tag{A.75}$$

$$F_{\mathrm{n}}^{\gamma} = \int_{-h}^{0} cos\left[\alpha_{\mathrm{n}}^{(h)}(z+h)\right] \mathrm{d}z = \frac{\sin(\alpha_{\mathrm{n}}^{(h)} h)}{\alpha_{\mathrm{n}}^{(h)}}. \tag{A.76}$$

By substituting these integrals into eq. (A.71) it is obtained

$$\begin{aligned} &\Psi_{\mathrm{n}}''(y) - \tilde{\alpha}_{\mathrm{n}}^{(h)^2} \Psi_{\mathrm{n}}(y) = \\ &\frac{4\alpha_{\mathrm{n}}^{(h)}}{2\alpha_{\mathrm{n}}^{(h)} h + sin(2\alpha_{\mathrm{n}}^{(h)} h)} \left[\frac{1}{h^2}\frac{c(k_{\mathrm{x}})}{h}\frac{\sin(\alpha_{\mathrm{n}}^{(h)} h)}{\alpha_{\mathrm{n}}^{(h)}} - k_{\mathrm{x}}^2 \frac{1}{2h^2}\frac{c(k_{\mathrm{x}})}{h}\frac{2\alpha_{\mathrm{n}}^{(h)} h - 2\sin(\alpha_{\mathrm{n}}^{(h)} h)^{3}}{\alpha_{\mathrm{n}}^{(h)}} \right]. \end{aligned} \tag{A.77}$$

The solution to the differential equation (A.73) is

$$\begin{aligned} \Psi_{\mathrm{n}}(y) = B_{\mathrm{n}}^{(h)} \frac{\cosh(\tilde{\alpha}_{\mathrm{n}}^{(h)} y)}{\cosh(\tilde{\alpha}_{\mathrm{n}}^{(h)} b_1)} &- 4\frac{c(k_{\mathrm{x}})}{h}\frac{\sin(\alpha_{\mathrm{n}}^{(h)} h)}{2\alpha_{\mathrm{n}}^{(h)} h + \sin(2\alpha_{\mathrm{n}}^{(h)} h)}\frac{1}{(\tilde{\alpha}_{\mathrm{n}}^{(h)} h)^2} + \\ &+ \frac{c(k_{\mathrm{x}})}{h}\frac{\alpha_{\mathrm{n}}^{(h)} h - \sin(\alpha_{\mathrm{n}}^{(h)} h)}{2\alpha_{\mathrm{n}}^{(h)} h + \sin(2\alpha_{\mathrm{n}}^{(h)} h)}\frac{1}{\alpha_{\mathrm{n}}^{(h)^2}}\frac{k_{\mathrm{x}}^2}{\tilde{\alpha}_{\mathrm{n}}^{(h)^2}}, \end{aligned} \tag{A.78}$$

where $B_{\mathrm{n}}^{(h)}$ is an unknown constant. Substituting the solution in eq. (A.69), it results

$$\begin{aligned}\varphi(y,z) = \sum_{m=1}^{\infty}\Bigg(& B_{\mathrm{m}}^{(h)}\frac{\cosh(\tilde{\alpha}_{\mathrm{m}}^{(h)}y)}{\cosh(\tilde{\alpha}_{\mathrm{m}}^{(h)}b_1)} - 4\frac{c(k_{\mathrm{x}})}{h}\frac{\sin(\alpha_m^{(h)}h)}{2\alpha_m^{(h)}h+\sin(2\alpha_m^{(h)}h)}\frac{1}{(\tilde{\alpha}_m h)^2} + \\ & + \frac{c(k_{\mathrm{x}})}{h}\frac{\alpha_m^{(h)}h-\sin(\alpha_m^{(h)}h)}{2\alpha_m^{(h)}h+\sin(2\alpha_m^{(h)}h)}\frac{1}{(\alpha_{\mathrm{m}}^{(h)}h)^2}\frac{k_{\mathrm{x}}^2}{\tilde{\alpha}_{\mathrm{m}}^{(h)2}}\Bigg)\cos\left[\alpha_{\mathrm{m}}^{(h)}(h+z)\right].\end{aligned} \tag{A.79}$$

This expression of $\varphi(y,z)$ is then employed to finally compute the velocity potential of eq. (A.65)

$$\begin{aligned}\tilde{H}^{(2)} = h^2\sum_{m=1}^{\infty}\Bigg(& B_{\mathrm{m}}^{(h)}\frac{\cosh(\tilde{\alpha}_{\mathrm{m}}^{(h)}y)}{\cosh(\tilde{\alpha}_{\mathrm{m}}^{(h)}b_1)}\cos\left[\alpha_{\mathrm{m}}^{(h)}(h+z)\right] + \\ & -4\frac{c(k_{\mathrm{x}})}{h}\frac{\sin(\alpha_m^{(h)}h)}{2\alpha_m^{(h)}h+\sin(2\alpha_m^{(h)}h)}\frac{1}{(\tilde{\alpha}_m^{(h)}h)^2}\cos\left[\alpha_{\mathrm{m}}^{(h)}(h+z)\right] + \\ & + \frac{c(k_{\mathrm{x}})}{h}\frac{\alpha_m^{(h)}h-\sin(\alpha_m^{(h)}h)}{2\alpha_m^{(h)}h+\sin(2\alpha_m^{(h)}h)}\frac{1}{(\alpha_m^{(h)}h)^2}\frac{k_{\mathrm{x}}^2}{\tilde{\alpha}_{\mathrm{m}}^{(h)2}}\cos\left[\alpha_{\mathrm{m}}^{(h)}(h+z)\right]\Bigg) - \frac{z^2}{2h}c(k_{\mathrm{x}}).\end{aligned} \tag{A.80}$$

The unknown constants of this problem, $A_{\mathrm{m}}^{(h)}$ and $B_{\mathrm{m}}^{(h)}$ are determined by enforcing continuity of the velocity potentials and their derivatives along the common boundary between region Ω_1 and Ω_2. Consider the condition (A.61a) for $y=-b_1$ and $-h<z<0$. It results

$$\begin{aligned}h^2\sum_{m=1}^{\infty}A_{\mathrm{m}}^{(h)}\cos\left[k_{\mathrm{m}}^{(h)}(d+z)\right] = h^2\sum_{m=1}^{\infty}\Bigg(& B_{\mathrm{m}}^{(h)}\cos\left[\alpha_{\mathrm{m}}^{(h)}(h+z)\right] + \\ & -4\frac{c(k_{\mathrm{x}})}{h}\frac{\sin(\alpha_{\mathrm{m}}^{(h)}h)}{2\alpha_{\mathrm{m}}^{(h)}h+\sin(2\alpha_{\mathrm{m}}^{(h)}h)}\frac{1}{(\tilde{\alpha}_m^{(h)}h)^2}\cos\left[\alpha_{\mathrm{m}}^{(h)}(h+z)\right] + \\ & + \frac{c(k_{\mathrm{x}})}{h}\frac{\alpha_m^{(h)}h-\sin(\alpha_{\mathrm{m}}^{(h)}h)}{2\alpha_{\mathrm{m}}^{(h)}h+\sin(2\alpha_{\mathrm{m}}^{(h)}h)}\frac{1}{(\alpha_{\mathrm{m}}^{(h)}h)^2}\frac{k_{\mathrm{x}}^2}{\tilde{\alpha}_{\mathrm{m}}^{(h)2}}\cos\left[\alpha_{\mathrm{m}}^{(h)}(h+z)\right]\Bigg) - \frac{z^2}{2h}c(k_{\mathrm{x}}).\end{aligned} \tag{A.81}$$

Applying the orthogonality property of the vertical eigenfunctions, that is multiplying by *cos* $\left[\alpha_{\mathrm{n}}^{(h)}(h+z)\right]$ and integrating over the depth it is obtained

$$\begin{aligned}\int_{-h}^{0}h^2\sum_{m=1}^{\infty}A_{\mathrm{m}}^{(h)}\cos\left[k_{\mathrm{m}}^{(h)}(d+z)\right]\cos\left[\alpha_{\mathrm{n}}^{(h)}(h+z)\right]\mathrm{d}z = h^2\Bigg(& \int_{-h}^{0}B_{\mathrm{n}}^{(h)}\cos^2\left[\alpha_{\mathrm{n}}^{(h)}(h+z)\right]\mathrm{d}z + \\ & -4\frac{c(k_{\mathrm{x}})}{h}\frac{\sin(\alpha_{\mathrm{n}}^{(h)}h)}{2\alpha_{\mathrm{n}}^{(h)}h+\sin(2\alpha_{\mathrm{n}}^{(h)}h)}\frac{1}{(\tilde{\alpha}_{\mathrm{n}}^{(h)}h)^2}\int_{-h}^{0}cos^2\left[\alpha_{\mathrm{n}}^{(h)}(h+z)\right]\mathrm{d}z + \\ & + \frac{c(k_{\mathrm{x}})}{h}\frac{\alpha_{\mathrm{n}}^{(h)}h-\sin(\alpha_{\mathrm{n}}^{(h)}h)}{2\alpha_{\mathrm{n}}^{(h)}h+\sin(2\alpha_{\mathrm{n}}^{(h)}h)}\frac{1}{(\alpha_{\mathrm{n}}^{(h)}h)^2}\frac{k_{\mathrm{x}}^2}{\tilde{\alpha}_{\mathrm{n}}^{(h)2}}\int_{-h}^{0}\cos^2\left[\alpha_{\mathrm{n}}^{(h)}(h+z)\right]\mathrm{d}z\Bigg) + \\ & -\int_{-h}^{0}\frac{z^2}{2h}c(k_{\mathrm{x}})\cos\left[\alpha_{\mathrm{n}}^{(h)}(h+z)\right]\mathrm{d}z,\end{aligned} \tag{A.82}$$

where the integral in the left-hand side is denoted by $G^{(h)}_{\mathrm{m,n}}$ and it is evaluated as

$$
\begin{aligned}
G^{(h)}_{\mathrm{m,n}} &= \int_{-h}^{0} \cos\left[k^{(h)}_{\mathrm{m}}(d+z)\right]\cos\left[\alpha^{(h)}_{\mathrm{n}}(h+z)\right]\mathrm{d}z = \\
&= \frac{\alpha^{(h)}_{\mathrm{n}}\cos(k^{(h)}_{\mathrm{m}}d)\sin(\alpha^{(h)}_{\mathrm{n}}h) + k^{(h)}_{\mathrm{m}}\left[-\cos(\alpha^{(h)}_{\mathrm{n}}h)\sin(k^{(h)}_{\mathrm{n}}d) + \sin\left[k^{(h)}_{\mathrm{n}}(d-h)\right]\right]}{{\alpha^{(h)}_{\mathrm{n}}}^2 - {k^{(h)}_{\mathrm{m}}}^2}.
\end{aligned}
\tag{A.83}
$$

Substituting $G^{(h)}_{\mathrm{m,n}}$, F^{α}_{n} and F^{β}_{n} it is obtained

$$
\begin{aligned}
\sum_{m=1}^{\infty} A^{(h)}_{\mathrm{m}} G^{(h)}_{\mathrm{m,n}} - B^{(h)}_{\mathrm{n}} F^{\alpha}_{\mathrm{n}} &= -4\frac{c(k_{\mathrm{x}})}{h}\frac{\sin(\alpha^{(h)}_{\mathrm{n}}h)}{2\alpha^{(h)}_{\mathrm{n}}h + \sin(2\alpha^{(h)}_{\mathrm{n}}h)}\frac{1}{(\tilde{\alpha}^{(h)}_{\mathrm{n}}h)^2}F^{\alpha}_{\mathrm{n}} + \\
&+ \frac{c(k_{\mathrm{x}})}{h}\frac{\alpha^{(h)}_{\mathrm{n}}h - \sin(\alpha^{(h)}_{\mathrm{n}}h)}{2\alpha^{(h)}_{\mathrm{n}}h + \sin(2\alpha^{(h)}_{\mathrm{n}}h)}\frac{1}{(\alpha^{(h)}_{\mathrm{n}}h)^2}\frac{k_{\mathrm{x}}^2}{{\tilde{\alpha}^{(h)}_{\mathrm{n}}}^2}F^{\alpha}_{\mathrm{n}} - \frac{1}{h^2}\frac{c(k_{\mathrm{x}})}{2h}F^{\beta}_{\mathrm{n}}.
\end{aligned}
\tag{A.84}
$$

Consider now the continuity of the velocity potentials between the two regions, described by the relation (A.61b) for $y = -b_1$ and $-h < z < 0$. Substituting in it the expression for the two obtained velocity potentials, it results

$$
\sum_{m=1}^{\infty} A^{(h)}_{\mathrm{m}}\tilde{k}^{(h)}_{\mathrm{m}}\cos\left[k^{(h)}_{\mathrm{m}}(d+z)\right] = -\sum_{m=1}^{\infty} B^{(h)}_{\mathrm{m}}\tilde{\alpha}^{(h)}_{\mathrm{m}}\frac{\sinh(\tilde{\alpha}^{(h)}_{\mathrm{m}}b_1)}{\cosh(\tilde{\alpha}^{(h)}_{\mathrm{m}}b_1)}\cos\left[\alpha^{(h)}_{\mathrm{m}}(h+z)\right]. \tag{A.85}
$$

Applying the orthogonality property for the vertical eigenfunction, that is multiplying by $cos\left[k^{(h)}_{\mathrm{n}}(d+z)\right]$ and integrating over the depth it is obtained

$$
\int_{-h}^{0} A^{(h)}_{\mathrm{n}}\tilde{k}^{(h)}_{\mathrm{n}}\cos^2\left[k^{(h)}_{\mathrm{n}}(d+z)\right]\mathrm{d}z = -\sum_{m=1}^{\infty} B^{(h)}_{\mathrm{m}}\tilde{\alpha}^{(h)}_{\mathrm{m}} tanh(\tilde{\alpha}^{(h)}_{\mathrm{m}}b_1)\int_{-h}^{0}\cos\left[\alpha^{(h)}_{\mathrm{m}}(h+z)\right]\cos\left[k^{(h)}_{\mathrm{n}}(d+z)\right]\mathrm{d}z. \tag{A.86}
$$

The integral in the left-hand side of eq (A.86) is denoted by F^{k}_{n} and is computed as

$$
\int_{-h}^{0}\cos^2\left[k^{(h)}_{\mathrm{n}}(d+z)\right]\mathrm{d}z = \frac{2k^{(h)}_{\mathrm{n}}h + \sin(2k^{(h)}_{\mathrm{n}}h)}{4k^{(h)}_{\mathrm{n}}}. \tag{A.87}
$$

Considering the expressions for F^{k}_{n} and $G^{(h)}_{\mathrm{n,m}}$ the equality between the derivatives of the velocity potentials is

$$
A^{(h)}_{\mathrm{n}}\tilde{k}^{(h)}_{\mathrm{n}}F^{k}_{\mathrm{n}} + \sum_{m=1}^{\infty} B^{(h)}_{\mathrm{m}}\tilde{\alpha}^{(h)}_{\mathrm{m}}\tanh(\tilde{\alpha}^{(h)}_{\mathrm{m}}b_1)G^{(h)}_{\mathrm{n,m}} = 0. \tag{A.88}
$$

The system of equations (A.84) - (A.88) can be solved numerically, as a function of k_{x}, by truncating the infinite series representation. Then, the added mass term is obtained by applying the inverse Fourier transform

$$H\left(x_\mathrm{c}, y_\mathrm{c}, -h\right) = \frac{1}{2\pi}\int_{-\infty}^{\infty} \widetilde{H}\left(k_\mathrm{x}, y_\mathrm{c}, -h\right) e^{ik_\mathrm{x}x_\mathrm{c}} \mathrm{d}k_\mathrm{x} \tag{A.89}$$

where x_c, y_c and $-h$ are the coordinates of the centre of the U-duct. In passing, note that the added mass calculated by eq. (A.89) has the units of a length. Such a definition relates to the fact that the U-OWC response is determined by solving the unsteady Bernoulli equation.

A.2.2 Radiation damping

The eigenfunction expansions matching is used for determining the radiation damping, as well. The boundary value problem for the computation of the radiation damping coefficient is described by the following systems for the two regions of the domain where the radiation potentials, $\phi^{(R,1)}$ and $\phi^{(R,2)}$, are considered:

$$\nabla^2\phi^{(R,1)} = 0, \tag{A.90a}$$

$$\frac{\partial\phi^{(R,1)}}{\partial z} = \frac{\omega^2}{g}\phi^{(R,1)},\ z = 0, \tag{A.90b}$$

$$\frac{\partial\phi^{(R,1)}}{\partial z} = 0,\ z = -d, \tag{A.90c}$$

$$\frac{\partial\phi^{(R,1)}}{\partial y} = 0,\ -d < z < 0,\ -\infty < y < -b_1, \tag{A.90d}$$

and

$$\nabla^2\phi^{(R,2)} = 0, \tag{A.91a}$$

$$\frac{\partial\phi^{(R,2)}}{\partial z} = \frac{\omega^2}{g}\phi^{(R,2)},\ z = 0, \tag{A.91b}$$

$$\frac{\partial\phi^{(R,2)}}{\partial y} = 0,\ y = 0, \tag{A.91c}$$

$$\frac{\partial\phi^{(R,2)}}{\partial z} = \Theta\left(x + \frac{b_3}{2}\right) - \Theta\left(x - \frac{b_3}{2}\right),\ z = -h, \tag{A.91d}$$

$$\phi^{(R,1)} = \phi^{(R,2)},\ y = -b_1, \tag{A.91e}$$

$$\frac{\partial\phi^{(R,1)}}{\partial y} = \frac{\partial\phi^{(R,2)}}{\partial y},\ y = -b_1. \tag{A.91f}$$

As before, the boundary value problem can be solved in the Fourier domain where the velocity potential is expressed as

$$\tilde{\phi}^{(R)}(k_\mathrm{x}, y, z) = \int_{-\infty}^{\infty} \phi^{(R)}(x, y, z) e^{-ik_\mathrm{x}x} \mathrm{d}x. \tag{A.92}$$

The boundary value problems in the freqeuncy domain appear as

$$\frac{\partial^2\tilde{\phi}^{(R,1)}}{\partial y^2}+\frac{\partial^2\tilde{\phi}^{(R,1)}}{\partial z^2}-k_{\mathrm{x}}^2\tilde{\phi}^{(R,1)}=0, \tag{A.93a}$$

$$\frac{\partial\tilde{\phi}^{(R,1)}}{\partial z}=\frac{\omega^2}{g}\tilde{\phi}^{(R,1)},\ z=0, \tag{A.93b}$$

$$\frac{\partial\tilde{\phi}^{(R,1)}}{\partial z}=0,\ z=-d, \tag{A.93c}$$

$$\frac{\partial\tilde{\phi}^{(R,1)}}{\partial y}=0,\ -d<z<0,\ -\infty<y<-b_1, \tag{A.93d}$$

for region Ω_1, and

$$\frac{\partial^2\tilde{\phi}^{(R,2)}}{\partial y^2}+\frac{\partial^2\tilde{\phi}^{(R,2)}}{\partial z^2}-k_{\mathrm{x}}^2\tilde{\phi}^{(R,2)}=0 \tag{A.94a}$$

$$\frac{\partial\tilde{\phi}^{(R,2)}}{\partial z}=\frac{\omega^2}{g}\tilde{\phi}^{(R,2)},\ z=0 \tag{A.94b}$$

$$\frac{\partial\tilde{\phi}^{(R,2)}}{\partial y}=0,\ y=0 \tag{A.94c}$$

$$\frac{\partial\tilde{\phi}^{(R,2)}}{\partial z}=2sin\left(\frac{k_{\mathrm{x}}\frac{b_3}{2}}{k_{\mathrm{x}}}\right)=c\left(k_{\mathrm{x}}\right),\ z=-h \tag{A.94d}$$

$$\tilde{\phi}^{(R,1)}=\tilde{\phi}^{(R,2)},\ y=-b_1 \tag{A.94e}$$

$$\frac{\partial\tilde{\phi}^{(R,1)}}{\partial y}=\frac{\partial\tilde{\phi}^{(R,2)}}{\partial y},\ y=-b_1 \tag{A.94f}$$

for region Ω_2. The velocity potential for region Ω_1 is described by the following expression

$$\tilde{\phi}^{(R,1)}=h^2\sum_{m=0}^{\infty}A_{\mathrm{m}}^{(R)}\zeta^{(1)}e^{\left[\tilde{k}_{\mathrm{m}}^{(R)}(y+b_1)\right]}, \tag{A.95}$$

where

$$\zeta^{(1)}=\frac{\cos\left[k_{\mathrm{m}}^{(R)}(d+z)\right]}{\cos(k_{\mathrm{m}}^{(R)}d)}. \tag{A.96}$$

For the region Ω_2 the velocity potential can be conveniently expressed in the form

$$\tilde{\phi}^{(R,2)}=h^2\varphi(y,z)-\frac{z^2}{2h}c(k_{\mathrm{x}}). \tag{A.97}$$

Considering the relation (A.94a) and substituting the expression of $\tilde{\phi}^{(R,2)}$ it is obtained

$$\frac{\partial^2\varphi^{(2)}}{\partial y^2}+\frac{\partial^2\varphi^{(2)}}{\partial z^2}-k_{\mathrm{x}}^2\varphi^{(2)}=\frac{1}{h^2}\frac{c(k_{\mathrm{x}})}{h}-k_{\mathrm{x}}^2\frac{z^2}{2h^2}\frac{c(k_{\mathrm{x}})}{h}. \tag{A.98}$$

Separable solutions of $\varphi(y,z)$ may be found in the form

$$\varphi(y,z) = \sum_{m=0}^{\infty} \Upsilon_{\mathrm{m}}(y) Z_{\mathrm{m}}(z), \tag{A.99}$$

where

$$Z_{\mathrm{m}}(z) = \zeta_{\mathrm{m}}^{2} = \frac{\cos\left[\alpha_{\mathrm{m}}^{(R)}(h+z)\right]}{\cos(\alpha_{\mathrm{m}}^{(R)} h)}. \tag{A.100}$$

Substituting eq. (A.99) in (A.98) it is obtained

$$\sum_{m=0}^{\infty}\left(\Upsilon_{\mathrm{m}}''(y)\zeta_{\mathrm{m}}^{(2)} - \alpha_{\mathrm{m}}^{(R)^2}\Upsilon_{\mathrm{m}}(y)\zeta_{\mathrm{m}}^{(2)} - k_{\mathrm{x}}^2\Upsilon_{\mathrm{m}}(y)\zeta_{\mathrm{m}}^{(2)}\right) = \frac{1}{h^2}\frac{c(k_{\mathrm{x}})}{h} - k_{\mathrm{x}}^2\frac{z^2}{2h^2}\frac{c(k_{\mathrm{x}})}{h}. \tag{A.101}$$

Reminding that

$$\alpha_{\mathrm{m}}^{(R)^2} + k_{\mathrm{x}}^2 = \tilde{\alpha}_{\mathrm{m}}^{(R)^2}, \tag{A.102}$$

it results

$$\sum_{m=0}^{\infty}\left(\Upsilon_{\mathrm{m}}''(y)\zeta_{\mathrm{m}}^{(2)} - \tilde{\alpha}_{\mathrm{m}}^{(R)^2}\Upsilon_{\mathrm{m}}(y)\zeta_{\mathrm{m}}^{(2)}\right) = \frac{1}{h^2}\frac{c(k_{\mathrm{x}})}{h} - k_{\mathrm{x}}^2. \tag{A.103}$$

Making use of the orthogonality property and therefore multiplying by $\frac{\cos[\alpha_{\mathrm{n}}(h+z)]}{\cos(\alpha_{\mathrm{n}} h)}$ and integrating from $-h$ to 0 over the depth, it is obtained

$$\begin{aligned}
&\int_{-h}^{0}\Upsilon_{\mathrm{m}}''(y)\frac{\cos^2\left[\alpha_{\mathrm{n}}^{(R)}(h+z)\right]}{\cos^2(\alpha_{\mathrm{n}}^{(R)}h)}\mathrm{d}z - \int_{-h}^{0}\tilde{\alpha}_{\mathrm{m}}^{(R)^2}\Upsilon_{\mathrm{m}}(y)\frac{\cos^2\left[\alpha_{\mathrm{n}}^{(R)}(h+z)\right]}{\cos^2(\alpha_{\mathrm{n}}^{(R)}h)}\mathrm{d}z = \\
&= \int_{-h}^{0}\frac{1}{h^2}\frac{c(k_{\mathrm{x}})}{h}\frac{\cos\left[\alpha_{\mathrm{n}}^{(R)}(h+z)\right]}{\cos(\alpha_{\mathrm{n}}^{(R)}h)}\mathrm{d}z - \int_{-h}^{0}k_{\mathrm{x}}^2\frac{z^2}{2h^2}\frac{c(k_{\mathrm{x}})}{h}\frac{\cos\left[\alpha_{\mathrm{n}}^{(R)}(h+z)\right]}{\cos(\alpha_{\mathrm{n}}^{(R)}h)}\mathrm{d}z.
\end{aligned} \tag{A.104}$$

The integral terms are computed as follow

$$F_{\mathrm{n}}^{(\alpha,2)} = \int_{-h}^{0}\frac{\cos^2\left[\alpha_{\mathrm{n}}^{(R)}(h+z)\right]}{\cos^2(\alpha_{\mathrm{n}}^{(R)}h)}\mathrm{d}z = \frac{2\alpha_{\mathrm{n}}^{(R)}h + \sin(2\alpha_{\mathrm{n}}^{(R)}h)}{4\alpha_{\mathrm{n}}^{(R)}\cos^2(\alpha_{\mathrm{n}}^{(R)}h)}, \tag{A.105}$$

$$F_{\mathrm{n}}^{(\gamma,2)} = \int_{-h}^{0}\frac{\cos\left[\alpha_{\mathrm{n}}^{(R)}(h+z)\right]}{\cos(\alpha_{\mathrm{n}}^{(R)}h)}\mathrm{d}z = \frac{\tan(\alpha_{\mathrm{n}}^{(R)}h)}{\alpha_{\mathrm{n}}^{(R)}}, \tag{A.106}$$

$$F_{\mathrm{n}}^{(\beta,2)} = \int_{-h}^{0} z^2 \frac{\cos\left[\alpha_{\mathrm{n}}^{(R)}(h+z)\right]}{\cos(\alpha_{\mathrm{n}}^{(R)}h)} \mathrm{d}z = \frac{2\alpha_{\mathrm{n}}^{(R)}h - 2\sin(\alpha_{\mathrm{n}}^{(R)}h)}{{\alpha_{\mathrm{n}}^{(R)}}^3 \cos(\alpha_{\mathrm{n}}^{(R)}h)}, \tag{A.107}$$

By employing these terms, after some adjustments, eq. (A.104) becomes

$$\begin{aligned} \Upsilon_{\mathrm{m}}''(y) - {\tilde{\alpha}_{\mathrm{m}}^{(R)}}^2 \Upsilon_{\mathrm{m}}(y) = \frac{4}{h^2} \frac{c(k_{\mathrm{x}})}{h} \frac{\cos(\alpha_{\mathrm{n}}^{(R)}h)\sin(\alpha_{\mathrm{n}}^{(R)}h)}{2\alpha_{\mathrm{n}}^{(R)}h\sin(2\alpha_{\mathrm{n}}^{(R)}h)} + \\ + k_{\mathrm{x}}^2 \frac{c(k_{\mathrm{x}})}{h} \frac{2\cos(\alpha_{\mathrm{n}}^{(R)}h)}{(\alpha_{\mathrm{n}}^{(R)}h)^2} \left[\frac{2\alpha_{\mathrm{n}}^{(R)}h - 2\sin(\alpha_{\mathrm{n}}^{(R)}h)}{2\alpha_{\mathrm{n}}^{(R)}h + \sin(2\alpha_{\mathrm{n}}^{(R)}h)}\right]. \end{aligned} \tag{A.108}$$

The solution to this differential equation is

$$\begin{aligned} \Upsilon_{\mathrm{n}}(y) = B_{\mathrm{n}}^{(R)} \frac{\cosh(\tilde{\alpha}_{\mathrm{n}}^{(R)}y)}{\cosh(\tilde{\alpha}_{\mathrm{n}}^{(R)}b_1)} - \frac{4}{(\tilde{\alpha}_{\mathrm{n}}^{(R)}h)^2} \frac{c(k_{\mathrm{x}})}{h} \frac{\cos(\alpha_{\mathrm{n}}^{(R)}h)\sin(\alpha_{\mathrm{n}}^{(R)}h)}{2\alpha_{\mathrm{n}}^{(R)}h + \sin(2\alpha_{\mathrm{n}}^{(R)}h)} + \\ + \left(\frac{k_{\mathrm{x}}}{\tilde{\alpha}_{\mathrm{n}}^{(R)}}\right)^2 \frac{c(k_{\mathrm{x}})}{h} \frac{2\cos(\alpha_{\mathrm{n}}^{(R)}h)}{(\alpha_{\mathrm{n}}^{(R)}h)^2} \left[\frac{2\alpha_{\mathrm{n}}^{(R)}h - 2\sin(\alpha_{\mathrm{n}}^{(R)}h)}{2\alpha_{\mathrm{n}}^{(R)}h + \sin(2\alpha_{\mathrm{n}}^{(R)}h)}\right], \end{aligned} \tag{A.109}$$

where $B_{\mathrm{n}}^{(R)}$ is an unknown constant. Substituting the solution obtained in eq. (A.99) it results

$$\begin{aligned} \varphi(y,z) = \Bigg(\sum_{m=0}^{\infty} B_{\mathrm{m}}^{(R)} \frac{\cosh(\tilde{\alpha}_{\mathrm{m}}^{(R)}y)}{\cosh(\tilde{\alpha}_{\mathrm{m}}^{(R)}b_1)} - \frac{4}{(\tilde{\alpha}_{\mathrm{n}}^{(R)}h)^2} \frac{c(k_{\mathrm{x}})}{h} \frac{\cos(\alpha_{\mathrm{n}}^{(R)}h)\sin(\alpha_{\mathrm{n}}^{(R)}h)}{2\alpha_{\mathrm{n}}^{(R)}h + \sin(2\alpha_{\mathrm{n}}^{(R)}h)} + \\ + \left(\frac{k_{\mathrm{x}}}{\tilde{\alpha}_{\mathrm{n}}^{(R)}}\right)^2 \frac{c(k_{\mathrm{x}})}{h} \frac{2\cos(\alpha_{\mathrm{n}}^{(R)}h)}{(\alpha_{\mathrm{n}}^{(R)}h)^2} \left[\frac{2\alpha_{\mathrm{n}}^{(R)}h - 2\sin(\alpha_{\mathrm{n}}^{(R)}h)}{2\alpha_{\mathrm{n}}^{(R)}h + \sin(2\alpha_{\mathrm{n}}^{(R)}h)}\right] \Bigg) \zeta_{\mathrm{m}}^{(2)}. \end{aligned} \tag{A.110}$$

Thus, the velocity potential $\tilde{\phi}^{(R,2)}$ becomes

$$\begin{aligned} \tilde{\phi}^{(R,2)} = h^2 \Bigg[\sum_{m=0}^{\infty} B_{\mathrm{m}}^{(R)} \frac{\cosh(\tilde{\alpha}_{\mathrm{m}}^{(R)}y)}{\cosh(\tilde{\alpha}_{\mathrm{m}}^{(R)}b_1)} \zeta_{\mathrm{m}}^{(2)} - \frac{4}{(\tilde{\alpha}_{\mathrm{n}}^{(R)}h)^2} \frac{c(k_{\mathrm{x}})}{h} \frac{\cos(\alpha_{\mathrm{n}}^{(R)}h)\sin(\alpha_{\mathrm{n}}^{(R)}h)}{2\alpha_{\mathrm{n}}^{(R)}h + \sin(2\alpha_{\mathrm{n}}^{(R)}h)} \zeta_{\mathrm{m}}^{(2)} + \\ + \left(\frac{k_{\mathrm{x}}}{\tilde{\alpha}_{\mathrm{n}}^{(R)}}\right)^2 \frac{c(k_{\mathrm{x}})}{h} \frac{2\cos(\alpha_{\mathrm{n}}^{(R)}h)}{(\alpha_{\mathrm{n}}^{(R)}h)^2} \left[\frac{2\alpha_{\mathrm{n}}^{(R)}h - 2\sin(\alpha_{\mathrm{n}}^{(R)}h)}{2\alpha_{\mathrm{n}}^{(R)}h + \sin(2\alpha_{\mathrm{n}}^{(R)}h)}\right] \zeta_{\mathrm{m}}^{(2)} \Bigg] - \frac{z^2}{2h^2} \frac{c(k_{\mathrm{x}})}{h}. \end{aligned} \tag{A.111}$$

The unknown constants, $A_{\mathrm{m}}^{(R)}$ and $B_{\mathrm{m}}^{(R)}$, of the boundary value problem for the evaluation of the radiation damping are determined by exploiting the continuity of the potentials and their derivatives along the common boundary between the two regions for $y = -b_1$. Considering first eq. (A.94e) it results

$$\begin{aligned} h^2 \sum_{m=0}^{\infty} A_{\mathrm{m}}^{(R)} \zeta^{(1)} = h^2 \Bigg[\sum_{m=0}^{\infty} B_{\mathrm{m}}^{(R)} \zeta_{\mathrm{m}}^{(2)} - \frac{4}{(\tilde{\alpha}_{\mathrm{n}}^{(R)}h)^2} \frac{c(k_{\mathrm{x}})}{h} \frac{\cos(\alpha_{\mathrm{n}}^{(R)}h)\sin(\alpha_{\mathrm{n}}^{(R)}h)}{2\alpha_{\mathrm{n}}^{(R)}h + \sin(2\alpha_{\mathrm{n}}^{(R)}h)} \zeta_{\mathrm{m}}^{(2)} + \\ + \left(\frac{k_{\mathrm{x}}}{\tilde{\alpha}_{\mathrm{n}}^{(R)}}\right)^2 \frac{c(k_{\mathrm{x}})}{h} \frac{2\cos(\alpha_{\mathrm{n}}^{(R)}h)}{(\alpha_{\mathrm{n}}^{(R)}h)^2} \left[\frac{2\alpha_{\mathrm{n}}^{(R)}h - 2\sin(\alpha_{\mathrm{n}}^{(R)}h)}{2\alpha_{\mathrm{n}}^{(R)}h + \sin(2\alpha_{\mathrm{n}}^{(R)}h)}\right] \zeta_{\mathrm{m}}^{(2)} \Bigg] - \frac{z^2}{2h^2} \frac{c(k_{\mathrm{x}})}{h}. \end{aligned} \tag{A.112}$$

Substituting the values of the terms $\zeta^{(1)}$ and $\zeta^{(2)}$ and applying the orthogonality property, multiplying by $\frac{\cos\left[\alpha_{\mathrm{n}}^{(R)}(h+z)\right]}{\cos(\alpha_{\mathrm{n}}^{(R)}h)}$ and integrating it is obtained

$$\begin{aligned}
&\int_{-h}^{0} h^2 \sum_{m=0}^{\infty} A_{\mathrm{m}}^{(R)} \frac{\cos\left[k_{\mathrm{m}}^{(R)}(d+z)\right]}{\cos(k_{\mathrm{m}}^{(R)}d)} \frac{\cos\left[\alpha_{\mathrm{n}}^{(R)}(h+z)\right]}{\cos(\alpha_{\mathrm{n}}^{(R)}h)} \mathrm{d}z = \\
&= \int_{-h}^{0} h^2 B_{\mathrm{n}}^{(R)} \frac{\cos^2\left[\alpha_{\mathrm{n}}^{(R)}(h+z)\right]}{\cos^2(\alpha_{\mathrm{n}}^{(R)}h)} \mathrm{d}z - \int_{-h}^{0} \frac{4}{(\tilde{\alpha}_{\mathrm{n}}^{(R)}h)^2} \frac{c(k_{\mathrm{x}})}{h} \frac{\cos(\alpha_{\mathrm{n}}^{(R)}h)\sin(\alpha_{\mathrm{n}}^{(R)}h)}{2\alpha_{\mathrm{n}}^{(R)}h+\sin(2\alpha_{\mathrm{n}}^{(R)}h)} \frac{\cos^2\left[\alpha_{\mathrm{n}}^{(R)}(h+z)\right]}{\cos^2(\alpha_{\mathrm{n}}^{(R)}h)} \mathrm{d}z + \\
&+ \int_{-h}^{0} \left(\frac{k_{\mathrm{x}}}{\tilde{\alpha}_{\mathrm{n}}^{(R)}}\right)^2 \frac{c(k_{\mathrm{x}})}{h} \frac{2\cos(\alpha_{\mathrm{n}}^{(R)}h)}{(\alpha_{\mathrm{n}}^{(R)}h)^2} \left[\frac{2\alpha_{\mathrm{n}}^{(R)}h - 2\sin(\alpha_{\mathrm{n}}^{(R)}h)}{2\alpha_{\mathrm{n}}^{(R)}h+\sin(2\alpha_{\mathrm{n}}^{(R)}h)}\right] \frac{\cos^2\left[\alpha_{\mathrm{n}}^{(R)}(h+z)\right]}{\cos^2(\alpha_{\mathrm{n}}^{(R)}h)} \mathrm{d}z + \\
&- \int_{-h}^{0} \frac{z^2}{2h^2} \frac{c(k_{\mathrm{x}})}{h} \frac{\cos\left[\alpha_{\mathrm{n}}^{(R)}(h+z)\right]}{\cos(\alpha_{\mathrm{n}}^{(R)}h)} \mathrm{d}z,
\end{aligned} \tag{A.113}$$

where the integral in the left-hand side is denoted by $G_{\mathrm{m,n}}^{(R)}$ and its value is given by the following expression

$$\begin{aligned}
G_{\mathrm{m,n}}^{(R)} &= \int_{-h}^{0} \frac{\cos\left[k_{\mathrm{m}}^{(R)}(d+z)\right]}{\cos(k_{\mathrm{m}}^{(R)}d)} \frac{\cos\left[\alpha_{\mathrm{n}}^{(R)}(h+z)\right]}{\cos(\alpha_{\mathrm{n}}^{(R)}h)} \mathrm{d}z = \\
&= \frac{\alpha_{\mathrm{n}}^{(R)}\cos(k_{\mathrm{m}}^{(R)}d)\sin(\alpha_{\mathrm{n}}^{(R)}h) + k_{\mathrm{m}}^{(R)}\left[-\cos(\alpha_{\mathrm{n}}^{(R)}h)\sin(k_{\mathrm{m}}^{(R)}d) + \sin\left[k_{\mathrm{m}}^{(R)}(d-h)\right]\right]}{({\alpha_{\mathrm{n}}^{(R)}}^2 - {k_{\mathrm{m}}^{(R)}}^2)\left[\cos(k_{\mathrm{m}}^{(R)}d)\cos(\alpha_{\mathrm{n}}^{(R)}h)\right]}.
\end{aligned} \tag{A.114}$$

Thus, employing the terms $G_{\mathrm{m,n}}^{(R)}$, $F_{\mathrm{n}}^{(\alpha,2)}$ and $F_{\mathrm{n}}^{(\beta,2)}$, and dividing by h^2, eq. (A.113) becomes

$$\begin{aligned}
\sum_{m=0}^{\infty} A_{\mathrm{m}}^{(R)} G_{\mathrm{m,n}}^{(R)} - B_{\mathrm{n}}^{(R)} F_{\mathrm{n}}^{(\alpha,2)} &= -\frac{4}{(\tilde{\alpha}_{\mathrm{n}}^{(R)}h)^2} \frac{c(k_{\mathrm{x}})}{h} \frac{\cos(\alpha_{\mathrm{n}}^{(R)}h)\sin(\alpha_{\mathrm{n}}^{(R)}h)}{2\alpha_{\mathrm{n}}^{(R)}h+\sin(2\alpha_{\mathrm{n}}^{(R)}h)} F_{\mathrm{n}}^{(\alpha,2)} + \\
&+ \left(\frac{k_{\mathrm{x}}}{\tilde{\alpha}_{\mathrm{n}}^{(R)}}\right)^2 \frac{c(k_{\mathrm{x}})}{h} \frac{2\cos(\alpha_{\mathrm{n}}^{(R)}h)}{(\alpha_{\mathrm{n}}^{(R)}h)^2} \left[\frac{2\alpha_{\mathrm{n}}^{(R)}h - 2\sin(\alpha_{\mathrm{n}}^{(R)}h)}{2\alpha_{\mathrm{n}}^{(R)}h+\sin(2\alpha_{\mathrm{n}}^{(R)}h)}\right] F_{\mathrm{n}}^{(\alpha,2)} - \frac{c(k_{\mathrm{x}})}{2h} \frac{F_{\mathrm{n}}^{(\beta,2)}}{h^2}.
\end{aligned} \tag{A.115}$$

Consider now the second relation for the continuity of the derivatives of the two potentials, (A.94f), for which it is

$$\sum_{m=0}^{\infty} A_{\mathrm{m}}^{(R)} \zeta_{\mathrm{m}}^{(1)} \tilde{k}_{\mathrm{m}}^{(R)} + \sum_{m=0}^{\infty} B_{\mathrm{m}}^{(R)} \tilde{\alpha}_{\mathrm{m}}^{(R)} \tanh(\tilde{\alpha}_{\mathrm{m}}^{(R)} b_1) \zeta_{\mathrm{m}}^{(2)} = 0. \tag{A.116}$$

By exploiting the ortoghonality property of the vertical eigenfunction, considering the values of $\zeta^{(1)}$ and $\zeta^{(2)}$ and multiplying by $\frac{\cos\left[k_{\mathrm{n}}^{(R)}(d+z)\right]}{\cos(k_{\mathrm{n}}^{(R)}d)}$ it is obtained

$$\int_{-h}^{0} A_{\mathrm{n}}^{(R)}\tilde{k}_{\mathrm{n}}^{(R)}\frac{\cos^2\left[k_{\mathrm{n}}^{(R)}(d+z)\right]}{\cos^2(k_{\mathrm{n}}^{(R)}d)}\mathrm{d}z+\int_{-h}^{0}\sum_{m=0}^{\infty}B_{\mathrm{m}}\tilde{\alpha}_{\mathrm{m}}^{(R)}\tanh(\tilde{\alpha}_{\mathrm{m}}^{(R)}b_1)\frac{\cos\left[\alpha_{\mathrm{m}}^{(R)}(h+z)\right]}{\cos(\alpha_{\mathrm{m}}^{(R)}h)}\frac{\cos\left[k_{\mathrm{n}}^{(R)}(d+z)\right]}{\cos(k_{\mathrm{n}}^{(R)}d)}\mathrm{d}z=0 \tag{A.117}$$

Then, substituting the integral terms by $F_{\mathrm{n}}^{(k,2)}$ and $G_{\mathrm{n,m}}^{(R)}$, it finally results

$$A_{\mathrm{n}}^{(R)}\tilde{k}_{\mathrm{n}}^{(R)}F_{\mathrm{n}}^{(k,2)}+\sum_{m=0}^{\infty}B_{\mathrm{m}}^{(R)}\tilde{\alpha}_{\mathrm{m}}^{(R)}\tanh(\tilde{\alpha}_{\mathrm{m}}^{(R)}b_1)G_{\mathrm{n,m}}^{(R)}=0 \tag{A.118}$$

Thus, the potentials $\tilde{\Phi}^{(\mathrm{R},1)}$ and $\tilde{\Phi}^{(R,2)}$ are obtained by inverse Fourier transform and the radiation damping coefficient is calculated by the equation [144]

$$B(\omega)=\omega\mathrm{Im}\left(\tilde{\Phi}^{(R,2)}(x_{\mathrm{c}},y_{\mathrm{c}},-h;\omega)\right) \tag{A.119}$$

Bibliography

[1] J. P. Kofoed, P. Frigaard, E. Friis-Madsen, H. C. Sørensen, Prototype testing of the wave energy converter wave dragon, Renewable Energy 31 (2) (2006) 181–189. `doi:10.1016/j.renene.2005.09.005`.

[2] D. Vicinanza, P. Frigaard, Wave pressure acting on a seawave slot-cone generator, Coastal Engineering 55 (6) (2008) 553–568. `doi:doi.org/10.1016/j.coastaleng.2008.02.011`.

[3] H. Polinder, M. Scuotto, Wave energy converters and their impact on power systems, in: 2005 International Conference on Future Power Systems, 2005, pp. 9 pp.–9. `doi:10.1109/FPS.2005.204210`.

[4] A. F. de O. Falcão, Wave energy utilization: A review of the technologies, Renewable and Sustainable Energy Reviews 14 (3) (2010) 899 – 918. `doi:10.1016/j.rser.2009.11.003`.

[5] A. F. O. Falcão, J. C. C. Henriques, Oscillating-water-column wave energy converters and air turbines: A review, Renewable Energy 85 (2016) 1391 – 1424. `doi:10.1016/j.renene.2015.07.086`.

[6] T. V. Heath, A review of oscillating water columns, Philosophical Transactions of the Royal Society of London A: Mathematical, Physical and Engineering Sciences 370 (1959) (2012) 235–245. `doi:10.1098/rsta.2011.0164`.

[7] A. F. O. Falcão, L. M. C. Gato, Air Turbines, in: A. Sayigh (Ed.), Comprehensive Renewable Energy, Vol. 8: Ocean Energy, Elsevier, Oxford, 2012, pp. 111 – 149. `doi:10.1016/B978-0-08-087872-0.00805-2`.

[8] A. F. O. Falcão, L. M. C. Gato, E. P. A. S. Nunes, A novel radial self-rectifying air turbine for use in wave energy converters, Renewable Energy 50 (2013) 289 – 298. `doi:10.1016/j.renene.2012.06.050`.

[9] J. C. C. Henriques, J. C. C. Portillo, L. M. C. Gato, R. P. F. Gomes, D. N. Ferreira, A. F. O. Falcão, Design of oscillating-water-column wave energy converters with an application to self-powered sensor buoys, Energy 112 (2016) 852 – 867. doi:10.1016/j.energy.2016.06.054.

[10] Wavenergy.it, The wave climate at the Roccella Jonica wave power plant, Private communication (2019).

[11] K. Gunn, C. Stock-Williams, Quantifying the global wave power resource, Renewable Energy 44 (2012) 296 – 304. doi:10.1016/j.renene.2012.01.101.

[12] S. Barstow, G. Mørk, D. Mollison, J. Cruz, Ocean Wave Energy. Green Energy and Technology, Springer, Berlin, Heidelberg, 2008.

[13] S. Salter, Wave power, Nature 249 (1974) 720 – 724. doi:10.1038/249720a0.

[14] E. Mehlum, Tapchan, in: F. A. d. O. Evans D.V. (Ed.), Hydrodynamics of Ocean Wave-Energy Utilization, Springer, Berlin, Heidelberg, 1986, pp. 51 – 55.

[15] S. A. Noren, Plant for utilizing kinetic energy, U.S. patent No. 4277690 (1981).

[16] A. Weinstein, G. Fredrikson, L. Claeson, J. Forsberg, M. Parks, K. Nielsen, M. Jensen, K. Zandiyeh, P. Frigaard, M. Kramer, T. Andersen, Aquabuoy: The offshore wave energy converter numerical modeling and optimization, in: IEEE Conference Proceeding, Electrical Engineering/Electronics, Computer, Communications and Information Technology Association, 2003, pp. 1988–1995.

[17] M. G. de Sousa Prado, F. Gardner, M. Damen, H. Polinder, Modelling and test results of the Archimedes wave swing, Proceedings of the Institution of Mechanical Engineers, Part A: Journal of Power and Energy 220 (8) (2006) 855–868. doi:10.1243/09576509JPE284.

[18] D. J. Pizer, C. Retzler, R. M. Henderson, F. L. Cowieson, M. G. Shaw, B. Dickens, R. Hart, Pelamis WEC—recent advances in the numerical and experimental modelling programme, in: Proceedings of 6th European Wave Tidal Energy Conference, 2005, pp. 373–378.

[19] A. P. McCabe, A. Bradshaw, J. A. C. Meadowcroft, G. Aggidis, Developments in the design of the PS Frog Mk 5 wave energy converter, Renewable Energy 31 (2) (2006) 141–151. doi:10.1016/j.renene.2005.08.

[20] A. Babarit, A. H. Clement, J. Gilloteaux, Optimization and Time-Domain Simulation of the SEAREV Wave Energy Converter, in: Proceedings of the ASME 2005 24th International Conference on Ocean, Offshore and Arctic Engineering, Halkidiki, Greece, 2005. doi:10.1115/OMAE2005-67286.

[21] T. Whittaker, D. Collier, M. Folley, M. Osterried, A. Henry, M. Crowley, The development of Oyster–A shallow water surging wave energy converter, Proceedings of 7th European Wave Tidal Energy Conference (01 2007).

[22] Y. Masuda, An Experience of Wave Power Generator through Tests and Improvement, in: F. A. d. O. Evans D.V. (Ed.), Hydrodynamics of Ocean Wave-Energy Utilization, Springer, Berlin, Heidelberg, 1986, pp. 445 – 452. `doi:10.1007/978-3-642-82666-5_36`.

[23] C. Grove-Palmer, Wave energy in the United Kingdom: A review of the programme June 1975-March 1982, The Second International Symposium on Wave Energy Utilization (Trondheim), 1982.

[24] J. Falnes, Research and development in ocean-wave energy in Norway, in: Proceedings of International Symposium on Ocean Energy Development, Muroran, Hokkaido, Japan, 1993, pp. 27 – 39.

[25] T. V. Heath, Chapter 334 - The Development and Installation of the Limpet Wave Energy Converter, in: A. A. M. Sayigh (Ed.), World Renewable Energy Congress VI, Pergamon, Oxford, 2000, pp. 1619 – 1622. `doi:10.1016/B978-008043865-8/50334-2`.

[26] S. Takahashi, H. Nakada, H. Ohneda, M. Shikamori, Wave Power Conversion by a Prototype Wave Power Extracting Caisson in Sakata Port, in: Coastal Engineering, 2000, pp. 3440–3453. `doi:10.1061/9780872629332.261`.

[27] V. Raju, M. Ravindran, Wave energy: Potential and programme in India, Renewable Energy 10 (2) (1997) 339 – 345, world Renewable Energy Congress IV Renewable Energy, Energy Efficiency and the Environment. `doi:10.1016/0960-1481(96)00090-0`.

[28] A. F. O. Falcão, A. J. N. A. Sarmento, L. M. C. Gato, A. Brito-Melo, The Pico OWC wave power plant: Its lifetime from conception to closure 1986–2018, Applied Ocean Research 98 (2020) 102104. `doi:10.1016/j.apor.2020.102104`.

[29] C. B. Boake, T. J. T. Whittaker, M. Folley, H. Ellen, Overview and initial operational experience of the LIMPET wave energy plant, in: Proceedings of the 12th International Offshore and Polar Engineering Conference, Kitakyushu, Japan, 2002.

[30] D. Zhang, W. Li, Y. Lin, Wave energy in China: Current status and perspectives, Renewable Energy 34 (10) (2009) 2089 – 2092. `doi:10.1016/j.renene.2009.03.014`.

[31] T. W. Thorpe, An assessment of the art Osprey wave energy device. final report (December 1995).

[32] G. Kim, M. E. Lee, K. S. Lee, J.-S. Park, W. M. Jeong, S. K. Kang, J.-G. Soh, H. Kim, An overview of ocean renewable energy resources in Korea, Renewable and Sustainable Energy Reviews 16 (4) (2012) 2278–2288. doi:10.1016/j.rser.2012.01.04.

[33] B. M. Count, D. V. Evans, The influence of projecting sidewalls on the hydrodynamic performance of wave-energy devices, Journal of Fluid Mechanics 145 (1984) 361–376. doi:10.1017/S0022112084002962.

[34] Y. Torre-Enciso, I. Ortubia, L. I. I. López de Aguileta, J. Marqués, Mutriku Wave Power Plant: From the Thinking out to the reality, in: Proc 8th European Wave Tidal Energy Conf, Uppsala, Sweden, 2009, pp. 319–329.

[35] J. C. C. Henriques, J. C. C. Portillo, W. Sheng, L. M. C. Gato, A. F. O. Falcão, Dynamics and control of air turbines in oscillating-water-column wave energy converters: Analyses and case study, Renewable and Sustainable Energy Reviews 112 (2019) 571 – 589. doi:10.1016/j.rser.2019.05.010.

[36] F. Arena, A. Romolo, G. Malara, V. Fiamma, V. Laface, The First Full Operative U-OWC Plants in the Port of Civitavecchia, in: Proceedings of the 36th International Conference on Ocean, Offshore and Arctic Engineering, OMAE 2017, Trondheim, Norway, 2017. doi:10.1115/OMAE2017-62036.

[37] P. Boccotti, On a new wave energy absorber, Ocean Engineering 30 (9) (2003) 1191 – 1200. doi:10.1016/S0029-8018(02)00102-6.

[38] A. Scialò, J. C. C. Henriques, G. Malara, A. F. O. Falcão, L. M. C. Gato, F. Arena, Power take-off selection for a fixed U-OWC wave power plant in the Mediterranean Sea: The case of Roccella Jonica, Energy 215 (2021) 119085. doi:10.1016/j.energy.2020.119085.

[39] M. E. McCormick, Analysis of a wave energy conversion buoy, Journal of Hydronautics 8 (3) (1974) 77–82. doi:10.2514/3.62983.

[40] A. F. Falcão, J. C. Henriques, J. J. Cândido, Dynamics and optimization of the owc spar buoy wave energy converter, Renewable Energy 48 (2012) 369 – 381. doi:10.1016/j.renene.2012.05.009.

[41] Y. Masuda, T. Yamazaki, Y. Outa, M. McCormick, Study of Backward Bent Duct Buoy, in: OCEANS '87, 1987, pp. 384–389. doi:10.1109/OCEANS.1987.1160750.

[42] D. Bull, C. Smith, D. S. Jenne, P. Jacob, A. Copping, S. Willits, A. Fontaine, D. Brefort, G. Copeland, M. Gordon, et al., Reference Model 6 (RM6): Oscillating Wave Energy Converter, Sandia National Laboratories 6 (2014).

[43] A. Lewis, Modeling the Backward Bent Duct Device-B2D2 A Comparison between physical and numerical models, in: Proceeding of Fifth European Wave Energy Conference, 2003, 2003.

[44] W. Sheng, Motion and performance of BBDB OWC wave energy converters: I, hydrodynamics, Renewable Energy 138 (2019) 106–120. doi:10.1016/j.renene.2019.01.016.

[45] J. C. C. Portillo, P. F. Reis, J. C. C. Henriques, L. M. C. Gato, A. F. O. Falcão, Backward bent-duct buoy or frontward bent-duct buoy? Review, assessment and optimisation, Renewable and Sustainable Energy Reviews 112 (2019) 353–368. doi:10.1016/j.rser.2019.05.026.

[46] J.-H. Kim, J.-M. Lew, D.-C. Hong, Y.-S. Kim, H.-S. Choi, S.-W. Hong, A Study on Motion of a BBDB type OWC Wave Energy Device considering Pneumatic Damping Coefficients in the Duct, in: 17th International offshore and polar engineering, ISOPE;, California, 2007, pp. 483–488.

[47] Y. Washio, H. Osawa, Y. Nagata, F. Fujii, H. Furuyama, T. Fujita, The offshore floating type wave power device "Mighty Whale": Open sea tests, in: Proceedings of the 10th International Offshore and Polar Engineering Conference, Seattle, Washington, USA, 2000.

[48] J. L. Lye, D. T. Brown, F. Johnson, An investigation into the non-linear effects resulting from air cushions in the Orecon Oscillating Water Column (OWC) device, in: Proceedings of the ASME 2009 28th International Conference on Ocean, Offshore and Arctic Engineering, Honolulu, Hawaii, USA, 2009. doi:10.1115/OMAE2009-79115.

[49] L. Li, C. Ruzzo, M. Collu, Y. Gao, G. Failla, F. Arena, Analysis of the coupled dynamic response of an offshore floating multi-purpose platform for the Blue Economy, Ocean Engineering 217 (2020) 107943. doi:10.1016/j.oceaneng.2020.107943.

[50] J. C. C. Henriques, L. M. C. Gato, A. F. O. Falcão, E. Robles, F. X. Faÿ, Latching control of a floating oscillating-water-column wave energy converter, Renewable Energy 90 (2016) 229–241. doi:10.1016/j.renene.2015.12.065.

[51] J. C. C. Henriques, L. M. C. Gato, J. M. Lemos, R. P. F. Gomes, A. F. O. Falcão, Peak-power control of a grid-integrated oscillating water column wave energy converter, Energy 109 (2016) 378–390. doi:10.1016/j.energy.2016.04.098.

[52] A. A. Wells, Fluid driven rotary transducer, British Patent Spec. No 1595700 (1976).

[53] S. Raghunathan, C. P. Tan, Performance of biplane Wells turbine, Journal of Energy 7 (6) (1983) 741–742. doi:10.2514/3.62727.

[54] R. Arlitt, H. U. Banzhaf, R. Startzmann, F. Biskup, Air turbine for a wave power station, WO 2009/089902 (2009).

[55] L. M. C. Gato, R. Curran, Performance of the Biplane Wells Turbine, Journal of Offshore Mechanics and Arctic Engineering–Transactions of the American Society of Mechanical Engineers 118 (3) (1996) 210–215. doi:10.1115/1.2828836.

[56] I. A. Babintsev, Apparatus for converting sea wave energy into electrical energy, U.S. patent No. 3922739 (1975).

[57] T. Setoguchi, K. Kaneko, H. Maeda, T. Kim, M. Inoue, Impulse turbine with self-pitch-controlled guide vanes for wave power conversion: Performance of mono- vane type, International Journal of Offshore and Polar Engineering 3 (1993).

[58] A. Sarmento, L. Gato, A. de O. Falcão, Turbine-controlled wave energy absorption by oscillating water column devices, Ocean Engineering 17 (5) (1990) 481–497. doi:10.1016/0029-8018(90)90040-D.

[59] P. Boccotti, Comparison between a U-OWC and a conventional OWC, Ocean Engineering 34 (5) (2007) 799 – 805. doi:10.1016/j.oceaneng.2006.04.005.

[60] G. Malara, A. Romolo, V. Fiamma, F. Arena, On the modelling of water column oscillations in U-OWC energy harvesters, Renewable Energy 101 (2017) 964 – 972. doi:10.1016/j.renene.2016.09.051.

[61] G. Malara, R. P. F. Gomes, F. Arena, J. C. C. Henriques, L. M. C. Gato, A. F. O. Falcão, The influence of three-dimensional effects on the performance of U-type oscillating water column wave energy harvesters, Renewable Energy 111 (2017) 506 – 522. doi:10.1016/j.renene.2017.04.038.

[62] G. Malara, F. Arena, Response of U-Oscillating Water Column arrays: semi-analytical approach and numerical results, Renewable Energy 138 (2019) 1152 – 1165. doi:10.1016/j.renene.2019.02.018.

[63] F. Arena, A. Romolo, G. Malara, V. Fiamma, V. Laface, The first worldwide application at full-scale of the REWEC3 device in the Port of Civitavecchia: Initial energetic performances, in: Proceedings of Renew 2016, 2nd International Conference on Renewable Energies Offshore, Lisbon, Portugal, 2016. doi:10.1201/9781315229256-38.

[64] P. Boccotti, Design of breakwater for conversion of wave energy into electrical energy, Ocean Engineering 51 (2012) 106–118. doi:10.1016/j.oceaneng.2012.05.011.

[65] D. Ning, G. Baoming, W. Rongquan, T. Vyzikas, D. Greaves, Geometrical investigation of a U-shaped oscillating water column wave energy device, Applied Ocean Research 97 (2020) 102105. doi:10.1016/j.apor.2020.102105.

[66] P. Boccotti, Caisson breakwaters embodying an OWC with a small opening-Part I: Theory, Ocean Engineering 34 (5) (2007) 806 – 819. doi:10.1016/j.oceaneng.2006.04.006.

[67] G. Malara, F. Arena, Analytical modelling of an U-Oscillating Water Column and performance in random waves, Renewable Energy 60 (2013) 116–126. doi:10.1016/j.renene.2013.04.016.

[68] F. Arena, L. Daniele, V. Fiamma, M. Fontana, G. Malara, G. Moretti, A. Romolo, G. P. R. Papini, A. Scialò, R. Vertechy, Field Experiments on Dielectric Elastomer Generators Integrated on a U-OWC Wave Energy Converter, in: Proceedings of the ASME 2018 37th International Conference on Ocean, Offshore and Arctic Engineering, Madrid, Spain, 2018. doi:10.1115/OMAE2018-77830.

[69] A. Garcia-Teruel, D. Forehand, A review of geometry optimisation of wave energy converters, Renewable and Sustainable Energy Reviews 139 (2021) 110593. doi:10.1016/j.rser.2020.110593.

[70] M. d. N. Gomes, C. D. d. Nascimento, B. L. Bonafini, E. D. d. Santos, L. A. Isoldi, L. A. O. Rocha, Two-dimensional geometric optimization of an oscillating water column converter in laboratory scale, Revista de Engenharia Térmica 11 (1-2) (2012) 30–36.

[71] M. Shadman, S. F. Estefen, C. A. Rodriguez, I. C. Nogueira, A geometrical optimization method applied to a heaving point absorber wave energy converter, Renewable Energy 115 (2018) 533–546. doi:10.1016/j.renene.2017.08.055.

[72] A. Clément, A. Babarit, J.-c. Gilloteaux, C. Josset, G. Duclos, The SEAREV wave energy converter, Proceedings of the 6th Wave and Tidal Energy Conference, Glasgow, UK (01 2005).

[73] A. McCabe, G. Aggidis, M. Widden, Optimizing the shape of a surge-and-pitch wave energy collector using a genetic algorithm, Renewable Energy 35 (12) (2010) 2767–2775. doi:10.1016/j.renene.2010.04.029.

[74] J. H. Holland, et al., Adaptation in natural and artificial systems: an introductory analysis with applications to biology, control, and artificial intelligence, MIT press, 1992.

[75] R. P. F. Gomes, J. C. C. Henriques, L. M. C. Gato, A. F. O. Falcão, Hydrodynamic optimization of an axisymmetric floating oscillating water column for wave energy conversion, Renewable Energy 44 (2012) 328–339. doi:10.1016/j.renene.2012.01.105.

[76] C. Sharp, A. Miller, V. Ferrero, M. Bentivoglio, M. Ebrahimi, B. L. DuPont, Characterizing the Use of Heuristic Optimization Methods for Renewable Energy Systems Design. doi:10.2514/6.2018-1369.

[77] J. Lyu, O. Abdelkhalik, L. Gauchia, Optimization of dimensions and layout of an array of wave energy converters, Ocean Engineering 192 (2019) 106543. doi:10.1016/j.oceaneng.2019.106543.

[78] S. A. Sirigu, L. Foglietta, G. Giorgi, M. Bonfanti, G. Cervelli, G. Bracco, G. Mattiazzo, Techno-Economic Optimisation for a Wave Energy Converter via Genetic Algorithm, Journal of Marine Science and Engineering 8 (7) (2020). doi:10.3390/jmse8070482.

[79] M. Giassi, M. Göteman, Layout design of wave energy parks by a genetic algorithm, Ocean Engineering 154 (2018) 252–261. doi:10.1016/j.oceaneng.2018.01.096.

[80] P. D. Spanos, F. M. Strati, G. Malara, F. Arena, An approach for non-linear stochastic analysis of U-shaped OWC wave energy converters, Probabilistic Engineering Mechanics 54 (2018) 44–52. doi:10.1016/j.probengmech.2017.07.001.

[81] J. B. Roberts, P. D. Spanos, Random vibration and statistical linearization, Courier Corporation, 2003.

[82] P. D. Spanos, F. Arena, A. A. Richichi, G. Malara, Efficient Dynamic Analysis of a Nonlinear Wave Energy Harvester Model, Journal of Offshore Mechanics and Arctic Engineering 138 (03 2016). doi:10.1115/1.4032898.

[83] L. S. P. Silva, N. Y. Sergiienko, C. P. Pesce, B. Ding, B. Cazzolato, H. M. Morishita, Stochastic analysis of nonlinear wave energy converters via statistical linearization, Applied Ocean Research 95 (2020) 102023. doi:10.1016/j.apor.2019.102023.

[84] G. Malara, P. D. Spanos, Efficient determination of nonlinear response of an array of Oscillating Water Column energy harvesters exposed to random sea waves, Nonlinear Dynamics 98 (3) (2019) 2019–2034. doi:10.1007/s11071-019-05303-z.

[85] M. Abramowitz, I. A. Stegun, R. H. Romer, Handbook of Mathematical Functions with Formulas, Graphs, and Mathematical Tables, American Journal of Physics 56 (10) (1988) 958–958. doi:10.1119/1.15378.

[86] F. Arena, V. Laface, G. Malara, A. Romolo, A. Viviano, V. Fiamma, G. Sannino, A. Carillo, Wave climate analysis for the design of wave energy harvesters in the Mediterranean Sea, Renewable Energy 77 (2015) 125–141. doi:10.1016/j.renene.2014.12.002.

[87] R. Curran, L. M. C. Gato, The energy conversion performance of several types of Wells turbine designs, Proceedings of the Institution of Mechanical Engineers, Part A: Journal of Power and Energy 211 (2) (1997) 133–145. doi:10.1243/0957650971537051.

[88] T. Aderinto, H. Li, Ocean wave energy converters: Status and challenges, Energies 11 (2018) 1250. doi:10.3390/en11051250.

[89] A. Babarit, A database of capture width ratio of wave energy converters, Renewable Energy 80 (2015) 610 – 628. doi:10.1016/j.renene.2015.02.049.

[90] V. Sundar, T. Moan, J. Hals, Conceptual design of OWC wave energy converters combined with breakwater structures, in: Proceedings of the 29th International Conference on Ocean, Offshore and Arctic Engineering, OMAE 2010, Shanghai, China, 2010. doi:10.1115/OMAE2010-20508.

[91] T. Cabral, D. Clemente, P. Rosa-Santos, F. Taveira-Pinto, T. Morais, F. Belga, H. Cestaro, Performance Assessment of a Hybrid Wave Energy Converter Integrated into a Harbor Breakwater, Energies 13 (2020) 236. doi:10.3390/en13010236.

[92] P. Rosa-Santos, F. Taveira-Pinto, D. Clemente, T. Cabral, F. Fiorentin, F. Belga, T. Morais, Experimental Study of a Hybrid Wave Energy Converter Integrated in a Harbor Breakwater, Journal of Marine Science and Engineering 7 (2019) 33. doi:10.3390/jmse7020033.

[93] A. Scialò, G. Malara, F. Arena, Geometrical optimization of U-Oscillating Water Columns in random waves, in: Proceedings of the 38th International Conference on Ocean, Offshore and Arctic Engineering, OMAE 2019, Glasgow, Scotland, UK, 2019. doi:10.1115/OMAE2019-95973.

[94] S. Raghunathan, The Wells air turbine for wave energy conversion, Progress in Aerospace Sciences 31 (4) (1995) 335 – 386. doi:10.1016/0376-0421(95)00001-F.

[95] T. H. Kim, T. Setoguchi, M. Takao, K. Kaneko, S. Santhakumar, Study of turbine with self-pitch-controlled blades for wave energy conversion, International Journal of Thermal Sciences 41 (1) (2002) 101 – 107. doi:10.1016/S1290-0729(01)01308-4.

[96] M. Folley, R. Curran, T. Whittaker, Comparison of LIMPET contra-rotating Wells turbine with theoretical and model test predictions, Ocean Engineering 33 (8) (2006) 1056 – 1069. doi:10.1016/j.oceaneng.2005.08.001.

[97] A. S. Shehata, Q. Xiao, K. M. Saqr, D. Alexander, Wells turbine for wave energy conversion: A review, International journal of energy research 41 (1) (2017) 6–38. doi:10.1002/er.3583.

[98] A. F. O. Falcão, J. C. C. Henriques, L. M. C. Gato, Self-rectifying air turbines for wave energy conversion: A comparative analysis, Renewable and Sustainable Energy Reviews 91 (2018) 1231–1241. doi:10.1016/j.rser.2018.04.019.

[99] A. F. O. Falcão, J. C. C. Henriques, L. M. C. Gato, Air turbine optimization for a bottom-standing column wave energy converter, Journal of Ocean Engineering and Marine Energy 2 (2016) 459–472. doi:10.1007/s40722-016-0045-7.

[100] Y. Imai, K. Toyota, S. Nagata, T. Setoguchi, M. Takao, An experimental study on generating efficiency of a wave energy converter Backward Bent Duct Buoy, in: Proceedings of the 9th European Wave and Tidal Energy Conference, 2011, pp. 5–9.

[101] M. Suzuki, M. Takao, E. Satoh, S. Nagata, K. Toyota, T. Setoguchi, Performance prediction of OWC type small size wave power device with impulse turbine, Journal of Fluid Science and Technology 3 (3) (2008) 466–475. doi:10.1299/jfst.3.466.

[102] G. Moretti, G. Malara, A. Scialò, L. Daniele, A. Romolo, R. Vertechy, M. Fontana, F. Arena, Modelling and field testing of a breakwater-integrated U-OWC wave energy converter with dielectric elastomer generator, Renewable Energy 146 (2020) 628 – 642. doi:10.1016/j.renene.2019.06.077.

[103] R. A. Arinaga, K. F. Cheung, Atlas of global wave energy from 10 years of reanalysis and hindcast data, Renewable Energy 39 (1) (2012) 49 – 64. doi:10.1016/j.renene.2011.06.039.

[104] L. Liberti, A. Carillo, G. Sannino, Wave energy resource assessment in the Mediterranean, the Italian perspective, Renewable Energy 50 (2013) 938 – 949. doi:10.1016/j.renene.2012.08.023.

[105] A. F. O. Falcão, J. C. C. Henriques, L. M. C. Gato, Rotational speed control and electrical rated power of an oscillating-water-column wave energy converter, Energy 120 (2017) 253 – 261. doi:10.1016/j.energy.2016.11.078.

[106] P. A. P. Justino, A. F. de O. Falcão, Rotational speed control of an OWC wave power plant, Journal of Offshore Mechanics and Artic Engineering 121(2) (1999) 65–70. doi:10.1115/1.2830079.

[107] F. M. Strati, G. Malara, F. Arena, Performance optimization of a U-Oscillating-Water-Column wave energy harvester, Renewable Energy 99 (2016) 1019 – 1028. doi:10.1016/j.renene.2016.07.080.

[108] S. Ceballos, J. Rea, I. Lopez, J. Pou, E. Robles, D. L. O'Sullivan, Efficiency optimization in low inertia Wells turbine-oscillating water column devices, IEEE Transactions on Energy Conversion 28 (3) (2013) 553–564. doi:10.1109/TEC.2013.2265172.

[109] A. Brito-Melo, L. M. C. Gato, A. J. N. A. Sarmento, Analysis of Wells turbine design parameters by numerical simulation of the OWC performance, Ocean Engineering 29 (12) (2002) 1463 – 1477. doi:10.1016/S0029-8018(01)00099-3.

[110] F. R. Torres, P. R. Teixeira, E. Didier, A methodology to determine the optimal size of a Wells turbine in an oscillating water column device by using coupled hydro-aerodynamic models, Renewable Energy 121 (2018) 9 – 18. doi:10.1016/j.renene.2018.01.003.

[111] P. A. P. Justino, A. F. de O. Falcão, Active relief-valve control for an OWC wave energy device, in: Proceedings of the 4th European Wave and Tidal Energy Conference, Aalborg, Denmark, 2000.

[112] J. C. C. Henriques, R. P. F. Gomes, L. M. C. Gato, A. F. O. Falcão, E. Robles, S. Ceballos, Testing and control of a power take-off system for an oscillating-water-column wave energy converter, Renewable Energy 85 (2016) 714–724. doi:10.1016/j.renene.2015.07.015.

[113] A. A. D. Carrelhas, L. M. C. Gato, J. C. C. Henriques, A. F. O. Falcão, J. Varandas, Test results of a 30 kW self-rectifying biradial air turbine-generator prototype, Renewable and Sustainable Energy Reviews 109 (2019) 187 – 198. doi:10.1016/j.rser.2019.04.008.

[114] P.

and Wave Loads on Marine Structures, Butterworth-Heinemann, Oxford, 2015, pp. 1 – 23. doi:10.1016/B978-0-12-800343-5.00001-9.

[115] F. Arena, A. Romolo, G. Malara, V. Fiamma, V. Laface, Validation of the U-Oscillating Water Column model by full-scale experimental data, in: Proceedings of the 12th European Wave and Tidal Energy Conference, Cork, Ireland, 2017, pp. 1038–1 – 1038–5.

[116] A. F. O. Falcão, J. C. C. Henriques, The spring-like air compressibility effect in oscillating-water-column wave energy converters: Review and analyses, Renewable and Sustainable Energy Reviews 112 (2019) 483 – 498. doi:10.1016/j.rser.2019.04.040.

[117] S. L. Dixon, C. A. Hall, Fluid mechanics and thermodynamics of turbomachinery, 7th Edition, Butterworth-Heinemann, Oxford, 2013.

[118] J. C. C. Henriques, L. M. C. Gato, Use of a Residual Distribution Euler solver to study the occurrence of transonic flow in Wells turbine rotor blades, Computational Mechanics 29 (2002) 243 – 253. doi:10.1007/s00466-002-0337-8.

[119] A. F. O. Falcão, J. C. C. Henriques, Model-prototype similarity of oscillating-water-column wave energy converters, International Journal of Marine Energy 6 (2014) 18 – 34. doi:10.1016/j.ijome.2014.05.002.

[120] R. Starzmann, T. Carolus, Model-based selection of full-scale Wells turbines for ocean wave energy conversion and prediction of their aerodynamic and acoustic performances, Proceedings of the Institution of Mechanical Engineers, Part A: Journal of Power and Energy 228 (1) (2014) 2–16. doi:10.1177/0957650913503153.

[121] A. F. de O. Falcão, Control of an oscillating-water-column wave power plant for maximum energy production, Applied Ocean Research 24 (2) (2002) 73 – 82. doi:10.1016/S0141-1187(02)00021-4.

[122] A. F. O. Falcão, L. M. C. Gato, J. C. C. Henriques, J. E. Borges, B. Pereiras, F. Castro, A novel twin-rotor radial-inflow air turbine for oscillating-water-column wave energy converters, Energy 93 (2015) 2116–2125. doi:10.1016/j.energy.2015.10.046.

[123] G. Moretti, G. P. R. Papini, M. Righi, D. Forehand, D. Ingram, R. Vertechy, M. Fontana, Resonant wave energy harvester based on dielectric elastomer generator, Smart Materials and Structures 27 (3) (2018) 035015. doi:10.1088/1361-665x/aaab1e.

[124] R. Vertechy, G. P. P. Rosati, M. Fontana, Reduced Model and Application of Inflating Circular Diaphragm Dielectric Elastomer Generators for Wave Energy Harvesting, ASME Journal of Vibration and Acoustics 137 (1) (2015) 011004. doi:10.1115/1.4028508.

[125] S. Chiba, M. Waki, Innovative power generator using dielectric elastomers (creating the foundations of an environmentally sustainable society), Sustainable Chemistry and Pharmacy 15 (2020) 100205. doi:10.1016/j.scp.2019.100205.

[126] G. Moretti, M. Santos Herran, D. Forehand, M. Alves, H. Jeffrey, R. Vertechy, M. Fontana, Advances in the development of dielectric elastomer generators for wave energy conversion, Renewable and Sustainable Energy Reviews 117 (2020) 109430. doi:10.1016/j.rser.2019.109430.

[127] F. Carpi, D. De Rossi, R. Kornbluh, R. Pelrine, P. Sommer-Larsen, Dielectric Elastomers as Electromechanical Transducers: Fundamentals, Materials, Devices, Models and Applications of an

Emerging Electroactive Polymer Technology, in: Dielectric Elastomers as Electromechanical Transducers, Elsevier, Amsterdam, 2008. doi:10.1016/B978-0-08-047488-5.00033-2.

[128] R. Pelrine, R. Kornbluh, Q. Pei, J. Joseph, High-Speed Electrically Actuated Elastomers with Strain Greater Than 100%, Science 287 (5454) (2000) 836–839. doi:10.1126/science.287.5454.836.

[129] G. Thomson, D. Yurchenko, D. V. Val, Dielectric Elastomers for Energy Harvesting, in: R. Manyala (Ed.), Energy Harvesting, IntechOpen, Rijeka, 2018, Ch. 4. doi:10.5772/intechopen.74136.

[130] E. Bortot, M. Gei, Harvesting energy with load-driven dielectric elastomer annular membranes deforming out-of-plane, Extreme Mechanics Letters 5 (2015) 62–73. doi:10.1016/j.eml.2015.09.009.

[131] R. Kaltseis, C. Keplinger, S. J. Adrian Koh, R. Baumgartner, Y. F. Goh, W. H. Ng, A. Kogler, A. Tröls, C. C. Foo, Z. Suo, S. Bauer, Natural rubber for sustainable high-power electrical energy generation, RSC Adv. 4 (2014) 27905–27913. doi:10.1039/C4RA03090G.

[132] R. D. Kornbluh, R. Pelrine, H. Prahlad, A. Wong-Foy, B. McCoy, S. Kim, J. Eckerle, T. Low, From Boots to Buoys: Promises and Challenges of Dielectric Elastomer Energy Harvesting, Springer US, Boston, MA, 2012, pp. 67–93. doi:10.1007/978-1-4614-0878-9_3.

[133] S. Shian, J. Huang, S. Zhu, D. R. Clarke, Optimizing the Electrical Energy Conversion Cycle of Dielectric Elastomer Generators, Advanced Materials 26 (38) (2014) 6617–6621. doi:10.1002/adma.201402291.

[134] R. Pelrine, R. D. Kornbluh, J. Eckerle, P. Jeuck, S. Oh, Q. Pei, S. Stanford, Dielectric elastomers: generator mode fundamentals and applications, in: Y. Bar-Cohen (Ed.), Smart Structures and Materials 2001: Electroactive Polymer Actuators and Devices, Vol. 4329, International Society for Optics and Photonics, SPIE, 2001, pp. 148 – 156. doi:10.1117/12.432640.

[135] S. J. A. Koh, C. Keplinger, T. Li, S. Bauer, Z. Suo, Dielectric Elastomer Generators: How Much Energy Can Be Converted?, IEEE/ASME Transactions on Mechatronics 16 (1) (2011) 33–41. doi:10.1109/TMECH.2010.2089635.

[136] S. Chiba, M. Waki, K. Fujita, K. Masuda, T. Ikoma, Simple and Robust Direct Drive Wave Power Generation System Using Dielectric Elastomers, Journal of Materials Science and Engineering B 7 (02 2017). doi:10.17265/2161-6221/2017.1-2.005.

[137] S. Chiba, M. Waki, T. Wada, Y. Hirakawa, K. Masuda, T. Ikoma, Consistent ocean wave energy harvesting using electroactive polymer (dielectric elastomer) artificial muscle generators, Applied Energy 104 (2013) 497–502. doi:10.1016/j.apenergy.2012.10.052.

[138] G. Moretti, M. Fontana, R. Vertechy, Model-based design and optimization of a dielectric elastomer power take-off for oscillating wave surge energy converters, Meccanica 50 (2015) 2797–2813. doi:10.1007/s11012-015-0235-8.

[139] A. Babarit, J. Singh, C. Mélis, A. Wattez, P. Jean, A linear numerical model for analysing the hydroelastic response of a flexible electroactive wave energy converter, Journal of Fluids and Structures 74 (2017) 356–384. doi:10.1016/j.jfluidstructs.2017.06.003.

[140] G. Rosati, G. Moretti, R. Vertechy, M. Fontana, Control of an oscillating water column wave energy converter based on dielectric elastomer generator, Nonlinear Dynamics 92 (04 2018). doi:10.1007/s11071-018-4048-x.

[141] G. Moretti, M. Righi, R. Vertechy, M. Fontana, Fabrication and Test of an Inflated Circular Diaphragm Dielectric Elastomer Generator Based on PDMS Rubber Composite, Polymers 9 (7) (2017). doi:10.3390/polym9070283.

[142] G. Moretti, G. P. Rosati Papini, L. Daniele, D. Forehand, D. Ingram, R. Vertechy, M. Fontana, Modelling and testing of a wave energy converter based on dielectric elastomer generators, Proceedings of the Royal Society A: Mathematical, Physical and Engineering Sciences 475 (2222) (2019) 20180566. doi:10.1098/rspa.2018.0566.

[143] W. Cummins, The impulse response function and ship motions, Tech. rep., David Taylor Model Basin Washington DC (1962).

[144] C. C. Mei, M. Stiassnie, D. K.-P. Yue, Theory and applications of ocean surface waves: nonlinear aspects, Vol. 23, World scientific, 2005.

[145] A. J. N. A. Sarmento, A. F. d. O. Falcão, Wave generation by an oscillating surface-pressure and its application in wave-energy extraction, Journal of Fluid Mechanics 150 (1985) 467–485. doi:10.1017/S0022112085000234.

[146] A. F. de O. Falcão, P. A. P. Justino, OWC wave energy devices with air flow control, Ocean Engineering 26 (12) (1999) 1275–1295. doi:10.1016/S0029-8018(98)00075-4.

[147] S. Rosset, H. R. Shea, Flexible and stretchable electrodes for dielectric elastomer actuators, Applied Physics A: Materials Science & Processing 110 (2) (2013) 281–307. doi:10.1007/s00339-012-7402-8.

[148] G. A. Holzapfel, Nonlinear Solid Mechanics: A Continuum Approach for Engineering Science, Meccanica 37 (4) (2002) 489–490. doi:10.1023/A:1020843529530.

[149] L. Dorfmann, R. W. Ogden, Nonlinear theory of electroelastic and magnetoelastic interactions, Vol. 1, Springer, 2014. doi:10.1007/978-1-4614-9596-3.

[150] P. Boccotti, Chapter 3 - Random Wind-Generated Waves: Basic Concepts, in: P. Boccotti (Ed.), Wave Mechanics and Wave Loads on Marine Structures, Butterworth-Heinemann, Oxford, 2015, pp. 43–61. doi:10.1016/B978-0-12-800343-5.00003-2.

[151] P. Boccotti, P. Filianoti, V. Fiamma, F. Arena, Caisson breakwaters embodying an OWC with a small opening—Part ii: A small-scale field experiment, Ocean Engineering 34 (5) (2007) 820–841. doi:10.1016/j.oceaneng.2006.04.016.

[152] G. Malara, R. Gomes, F. Arena, J. Henriques, L. Gato, A. Falcao, Hydrodynamic characteristics of a U-OWC plant: Comparison between analytical and numerical results, in: Proc. 11th Eur. Wave Tidal Energy Conf, Nantes, France, 2015.

[153] F. Arena, A. Romolo, G. Malara, A. Ascanelli, On design and building of a U-OWC wave energy converter in the mediterranean sea: A case study, Vol. 8, 2013. doi:10.1115/OMAE2013-11593.

[154] F. B. Madsen, L. Yu, P. Mazurek, A. L. Skov, A simple method for reducing inevitable dielectric loss in high-permittivity dielectric elastomers, Smart Materials and Structures 25 (7) (2016) 075018. doi:10.1088/0964-1726/25/7/075018.

[155] P. Caspari, S. J. Dünki, F. A. Nüesch, D. M. Opris, Dielectric elastomer actuators with increased dielectric permittivity and low leakage current capable of suppressing electromechanical instability, J. Mater. Chem. C 6 (2018) 2043–2053. doi:10.1039/C7TC05562E.

[156] B. Fasolt, M. Hodgins, G. Rizzello, S. Seelecke, Effect of screen printing parameters on sensor and actuator performance of dielectric elastomer (DE) membranes, Sensors and Actuators A: Physical 265 (2017) 10–19. doi:10.1016/j.sna.2017.08.028.

[157] K. Hasselmann, T. Barnett, E. Bouws, H. Carlson, D. Cartwright, K. Enke, J. Ewing, H. Gienapp, D. Hasselmann, P. Kruseman, A. Meerburg, P. Muller, D. Olbers, K. Richter, W. Sell, H. Walden, Measurements of wind-wave growth and swell decay during the Joint North Sea Wave Project (JONSWAP), Deut. Hydrogr. Z. 8 (1973) 1–95.

[158] P. Y. Le Gac, M. Arhant, P. Davies, A. Muhr, Fatigue behavior of natural rubber in marine environment: Comparison between air and sea water, Materials and Design 65 (2015) 462–467. `doi:10.1016/j.matdes.2014.09.032`.

[159] Z. Yu, J. Falnes, State-space modelling of a vertical cylinder in heave, Applied Ocean Research 17 (5) (1995) 265–275. `doi:10.1016/0141-1187(96)00002-8`.

[160] F. Arena, G. Malara, A. Romolo, A U-OWC wave energy converter in the Mediterranean Sea: Preliminary results on the monitoring system of the first prototype, 2015, pp. 417–421. `doi:10.1201/b18973-59`.

[161] C. Signorelli, C. Villegas, J. Ringwood, Hardware-In-the-Loop simulation of a heaving wave energy converter, Proceedings of the 9th European Wave and Tidal Energy Conference (EWTEC) (September 2011).

[162] A. F. de O. Falcão, P. E. R. Pereira, J. C. C. Henriques, L. M. C. Gato, Hydrodynamic simulation of a floating wave energy converter by a u-tube rig for power take-off testing, Ocean Engineering 37 (14) (2010) 1253–1260. `doi:10.1016/j.oceaneng.2010.05.007`.

[163] G. Bracco, E. Giorcelli, G. Mattiazzo, V. Orlando, M. Raffero, Hardware-In-the-Loop test rig for the ISWEC wave energy system, Mechatronics 25 (2015) 11–17. `doi:10.1016/j.mechatronics.2014.10.007`.

[164] J. Rea, J. F. Kelly, R. Alcorn, D. O'Sullivan, Development and operation of a power take off rig for ocean energy research and testing, 2011.

[165] J. F. Kelly, R. Christie, Applying Hardware-in-the-Loop capabilities to an ocean renewable energy device emulator, in: 2017 Twelfth International Conference on Ecological Vehicles and Renewable Energies (EVER), 2017, pp. 1–7. `doi:10.1109/EVER.2017.7935943`.

[166] G. Moretti, G. P. P. Rosati, M. Fontana, R. Vertechy, Hardware in the loop simulation of a dielectric elastomer generator for oscillating water column wave energy converters, in: OCEANS 2015 - Genova, 2015, pp. 1–7. `doi:10.1109/OCEANS-Genova.2015.7271571`.

[167] J. N. Newman, C. Lee, Boundary-element methods in offshore structure analysis, ASME. Journal of Offshore Mechanics and Arctic Engineering 124 (2) (2002) 81–89. `doi:10.1115/1.1464561`.

[168] P. Boccotti, Wave mechanics for ocean engineering, Elsevier, 2000.

[169] D. Ingram, R. Wallace, A. Robinson, I. Bryden, The design and commissioning of the first, circular, combined current and wave test basin, in: OCEANS 2014 - TAIPEI, 2014, pp. 1–7. `doi:10.1109/OCEANS-TAIPEI.2014.6964577`.

[170] P. Zanini, J. Rossiter, M. Homer, Modelling the effect of actuator-like behavior in dielectric elastomer generators, Applied Physics Letters 107 (15) (2015) 153906. `doi:10.1063/1.4933315`.

[171] F. B. Madsen, A. E. Daugaard, S. Hvilsted, A. L. Skov, The current state of silicone-based dielectric elastomer transducers, Macromolecular Rapid Communications 37 (5) (2016) 378–413. `doi:10.1002/marc.201500576`.

[172] F. Arena, G. Barbaro, The Natural Ocean Engineering Laboratory, NOEL, in Reggio Calabria, Italy: A Commentary and Announcement, Journal of Coastal Research 29 (5) (2013). `doi:10.2112/13A-00004`.

[173] C. Mei, M. Stiassnie, D. Yue, Theory and Applications of Ocean Surface Waves, Vol. 23, 2005.

[174] C. M. Linton, P. McIver, Handbook of mathematical techniques for wave/structure interactions, CRC Press, 2001.

[175] M. Abramowitz, I. A. Stegun, Handbook of mathematical functions with formulas, graphs, and mathematical tables, Vol. 55, US Government printing office, 1964.

[176] E. Jefferys, Simulation of wave power devices, Applied Ocean Research 6 (1) (1984) 31–39. `doi:10.1016/0141-1187(84)90026-9`.